Studies of the Hot Interstellar Medium in the Large Magellanic Cloud

Dissertation
der Mathematisch-Naturwissenschaftlichen Fakultät
der Eberhard-Karls Univsersität Tübingen
zur Erlangung des Grades eines
Doktors der Naturwissenschaften
(Dr. rer. nat.)

vorgelegt von
Gabriele Warth
aus Reutlingen

Tübingen
2014

Tag der mündlichen Qualifikation:	10.12.2014
Dekan:	Prof. Dr. Wolfgang Rosenstiel
1. Berichterstatter:	Dr. Manami Sasaki
2. Berichterstatter:	Prof. Dr. Andrea Santangelo

Zusammenfassung

Der Raum zwischen den Sternen einer Galaxie ist keinesfalls leer, sondern gefüllt mit heißem interstellaren Medium (ISM) – ein Plasma, welches Temperaturen von $\sim 10^6 - 10^7$ K besitzt und größtenteils aus ionisiertem Wasserstoff besteht. Es erreicht diese hohen Temperaturen aufgrund von Aufheizung durch Supernova Explosionen und stellaren Winden. In der Milchstraße sowie in benachbarten Galaxien ist dieses Plasma als ausgedehnte, diffuse Röntgenstrahlung beobachtbar, welche Informationen über die Entwicklung von Sternen, den Materiezyklus, und selbst über die Entwicklung ganzer Galaxien liefert. Zu finden ist das heiße ISM beispielsweise in Supernova Überresten sowie im Innern von Superbubbles und Supergiant Shells, welches Hüllen aus kaltem und warmen ISM darstellen, die mit heißem ISM gefüllt sind und durch stellare Winde und Supernova Explosionen erzeugt wurden. Während Superbubbles eine Größe von ~ 100 pc besitzen und durch die Sternenpopulation eines oder mehrerer Sternhaufen erzeugt wurden, werden Supergiant Shells durch mehrere Generationen von Sternpopulationen vieler Sternhaufen erzeugt und erreichen enorme Ausmaße von bis zu ~ 1 kpc.

Ziel dieser Dissertation ist die Untersuchung des heißen interstellaren Mediums in einer Region rundum Supergiant Shell LMC-SGS 2. Diese Supergiant Shell befindet sich in der Großen Magellanschen Wolke, welche eine unserer nächsten Nachbargalaxien darstellt. In dieser LMC-SGS 2-Region ist ebenfalls die H II-Region DEM L299 zu finden. Sie liegt am nord-westlichen Rand der Supergiant Shell und beherbergt den Supernova Überrest SNR B0543-68.9. Sowohl für LMC-SGS 2 als auch für DEM L299 wurden im Rahmen dieser Dissertation detaillierte Studien durchgeführt. Im Laufe dieser Studien konnte eine neue Superbubble identifiziert werden, welche gegen DEM L299 projiziert ist und Hinweise auf einen Ausbruch heißen Gases aus ihrem Inneren in die Umgebung zeigt.
Im Zuge dieser Arbeit wurde eine Multi-Wellenlängenanalyse für LMC-SGS 2 und für DEM L299 im Röntgen-, optischen, und Radiowellenlängenbereich durchgeführt, welche das Studium der Verteilung des heißen, warmen und kalten ISMs in dieser Region zum Ziel hatte. Hierfür wurden Daten des Satelliten *XMM-Newton* verwendet, um Mosaike von der Supergiant Shell in verschiedenen Energiebändern im Röntgenbereich zu erstellen. Diese Mosaike zeigen ein sehr viel detaillierteres Bild der Region als dies in früheren Studien der Fall war. Während der morphologischen Studie von DEM L299 wurde die exakte Position des Supernova Überrestes

SNR B0543-68.9 bestimmt, was zur Identifikation der DEM L299-Superbubble führte. So konnte gezeigt werden, dass DEM L299 neben dem Supernova Überrest noch zusätzlich eine Superbubble in Projektion beherbergt. Des Weiteren wurden Hinweise dafür gefunden, dass der Supernova Überrest und die Superbubble von einer gemeinsamen Hülle aus neutralem Wasserstoff umgeben sind, was darauf hindeutet, dass beide Objekte in der Tat nahe beieinander liegen und es sich hierbei nicht nur um einen Projektionseffekt handelt.
Eine spektrale Analyse im Röntgenbereich wurde für LMC-SGS 2, SNR B0543-68.9, DEM L299-Superbubble und deren Ausbruch durchgeführt. Darin wurden Eigenschaften der Objekte wie deren Temperatur und Wasserstoffsäulendichte bestimmt. Darüber hinaus wurde die Leuchtkraft des Supernova Überrestes, der Superbubble, und deren Ausbruches berechnet. Die Ergebnisse der spektralen Analyse wurden verwendet, um weitere Eigenschaften der Objekte zu bestimmen. So wurde beispielsweise die Masse, der Druck und der thermische Energiegehalt des heißen Gases der Supergiant Shell, der Superbubble und deren Ausbruchs bestimmt sowie das dynamische Alter der Superbubble. Für SNR B0543-68.9 wurden Parameter wie seine Expansionsgeschwindigkeit, die ursprüngliche Explosionsenergie, die seit der Explosion vergangene Zeit und die Masse des durch ihn aufgeschwemmten ISMs berechnet. Hierbei wurden für SNR B0543-68.9 die Effekte des nicht vorhandenen Ionisationsgleichgewichtes berücksichtigt, was sich aus dessen spektraler Analyse ergeben hatte.
Eine Sternenpopulationsstudie wurde für die DEM L299-Region durchgeführt, in welcher gezeigt werden konnte, dass es sich bei der detektierten diffusen Röntgenemission aus dieser Himmelsregion tatsächlich um diffuse Emission handelt und nicht lediglich um eine Überlagerung vieler Punktquellen. Dies geschah durch eine Abschätzung der Anzahl massearmer und massereicher Sterne sowie deren Beitrag zur Röntgenleuchtkraft dieser Region, welcher sich als vernachlässigbar herausstellte. Des Weiteren wurde die Anzahl der in dieser Region bereits geschehenen Supernova Explosionen bestimmt sowie das Alter der stellaren Population. Zudem wurde der Energie- und Massenbeitrag berechnet, welchen die stellare Population auf die Superbubble gehabt haben muss. Die dabei erhaltenen Werte sind konsistent mit den Resultaten der spektralen Röntgenanalyse.

Die im Rahmen dieser Dissertation durchgeführten Studien über LMC-SGS 2 und DEM L299 haben zu dem Verständnis dieser interessanten und vielschichtigen Region aus heißem ISM in der Großen Magellanschen Wolke beigetragen und das Wissen über diese Region erweitert. Die erhaltenen Resultate für die Supergiant Shell, den Supernova Überrest und die Superbubble liefern neue Informationen über die Zusammensetzung dieser Region und bieten einen Überblick über die Eigenschaften der Region und dieser Objekte, was zu dem Verständnis vom Ursprung dieser Strukturen im heißen ISM beiträgt und das Wissen über jene Prozesse erweitert, welche zu deren Erzeugung geführt haben.

Abstract

The hot interstellar medium (ISM) is defined as the plasma which can be found between the stars of a galaxy and has a temperature of $\sim 10^6 - 10^7$ K. The material is heated to these temperatures through supernova explosions and stellar winds and can be observed as an extended, diffuse X-ray emission in the Milky Way and in our neighboring galaxies. Thus, it provides information about stellar evolution and the matter cycle as well as about the evolution of whole galaxies. The hot ISM can be found for example in supernova remnants and in the interior of superbubbles or supergiant shells, the latter two being shells of cold and warm ISM which are filled with hot ISM, blown by stellar winds and supernova explosions. While superbubbles have a size of ~ 100 pc and are created through the stellar winds and supernovae of clusters of stars and stellar associations, supergiant shells are created by generations of clusters of stars and reach enormous sizes of ~ 1 kpc.

Within the scope of this thesis, the hot ISM in the region of the supergiant shell LMC-SGS 2 has been studied. This supergiant shell is located in the Large Magellanic Cloud – a satellite galaxy of the Milky Way and one of our closest neighbor galaxies. Within the LMC-SGS 2 region lies DEM L299, which is an H II region located at the north-western rim of the supergiant shell and which is known to harbor the supernova remnant SNR B0543-68.9. Both LMC-SGS 2 and DEM L299 have been studied in detail within this thesis. In addition, a new superbubble was identified during these analyses. This superbubble is projected towards DEM L299, and indications for a blowout of hot gas from its interior were found.

For LMC-SGS 2 and DEM L299, a multi-frequency morphological study was performed in X-ray, optical, and radio wavelengths in order to study the distribution of the hot, the warm, and the cold ISM of this region. For these analyses, X-ray data of the *XMM-Newton* satellite have been used to create mosaics of LMC-SGS 2 in several X-ray energy bands. These mosaics show the region in much more detail than previous X-ray studies did. During the morphological study of DEM L299, the exact position of SNR B0543-68.9 was determined, which lead to the identification of the DEM L299 superbubble. Thus, it was shown that DEM L299 harbors not only a supernova remnant in projection, as believed up to now, but also a superbubble. In addition, evidence was found for a common shell of neutral hydrogen around the supernova remnant and the superbubble, indicating that they indeed lie close to each other.

An X-ray spectral analysis has been performed for LMC-SGS 2, SNR B0543-68.9, the DEM L299 superbubble, and the superbubble blowout. In these studies, the properties of these objects were determined, like their temperature and their hydrogen column density. For the latter three objects, also their luminosities were calculated. The results of the spectral analysis were used to determine further properties of all objects, like the mass, pressure and thermal energy content of the hot gas of LMC-SGS 2, the superbubble, and its blowout, and the dynamic age of the superbubble. Additional parameters were calculated for the supernova remnant, like its expansion velocity, the initial energy of its explosion, the time passed since the explosion, and the mass of the swept-up ambient ISM. This was done while considering the effects of collisional non-equilibrium ionization (NEI) for SNR B0543-68.9, which resulted from the X-ray spectral analysis of the hot gas of the supernova remnant.
During the performed population study, it was shown that the diffuse X-ray emission of DEM L299 is truly diffuse emission. This result was obtained by estimating the contribution of low- and high-mass stars to the X-ray emission of this region. DEM L299 has been further characterized by determining the age of its stellar population and the number of already occurred supernovae in this region. During the population study, the energy and mass input of the stellar population has been determined for the superbubble, which is in agreement with the results obtained during the X-ray spectral analysis.

The studies performed within the scope of this thesis for LMC-SGS 2 and DEM L299 enhance the understanding of this interesting and complex region of hot ISM within the Large Magellanic Cloud. The obtained results provide new information about the actual composition of this region and yield an overview of its properties, which helps to understand the origin of these ISM structures and of the processes which lead to their creation.

Contents

Chapter 1

Introduction to X-ray Astronomy

1.1 History of X-ray Astronomy

The field of X-ray astronomy is a relatively young field, not older than ~ 50 years – the age, in which the technology was available for scientific purposes to unbind astronomy from the surface of the Earth and take it into the upper atmosphere and space. Operation in space was a necessity required to bring X-ray astronomy to live, since, due to absorption and interaction of the electromagnetic radiation with atmospheric molecules and gases, X-rays cannot penetrate Earth's atmosphere and thus cannot be measured from ground. Before the age of balloon-, rocket-, and finally space-born science began, astronomy was limited to the investigation of optical, near-infrared, and radio emission (see Table 1.1 for the energy range of the different regimes) which are hardly absorbed by the atmosphere and thus are the only wavelengths which can be observed from ground (see Fig. 1.1). Space-born astronomy opened a new window not only to X-rays, but also to γ rays, ultraviolet, and infrared emission, thus drastically increasing the observable range of wavelengths.

Table 1.1: Overview of the corresponding energy band and wavelength range of the different regimes of electromagnetic radiation.

	Energy	Wavelength
Radio	$< 10^{-3}\,\mathrm{eV}$	$> 1\,\mathrm{mm}$
Infrared	$10^{-3} - 1\,\mathrm{eV}$	$10^{3} - 0.8\,\mu\mathrm{m}$
Optical	$1 - 5\,\mathrm{eV}$	$800 - 400\,\mathrm{nm}$
Ultraviolet	$5 - 100\,\mathrm{eV}$	$400 - 10\,\mathrm{nm}$
X-rays	$100 - 4 \times 10^{5}\,\mathrm{eV}$	$10 - 0.01\,\mathrm{nm}$
γ rays	$> 4 \times 10^{5}\,\mathrm{eV}$[a]	$< 0.01\,\mathrm{nm}$

[a] The current energy limit for detected photons lies at $\sim 10^{12}\,\mathrm{keV}$, i.e. in the TeV regime.

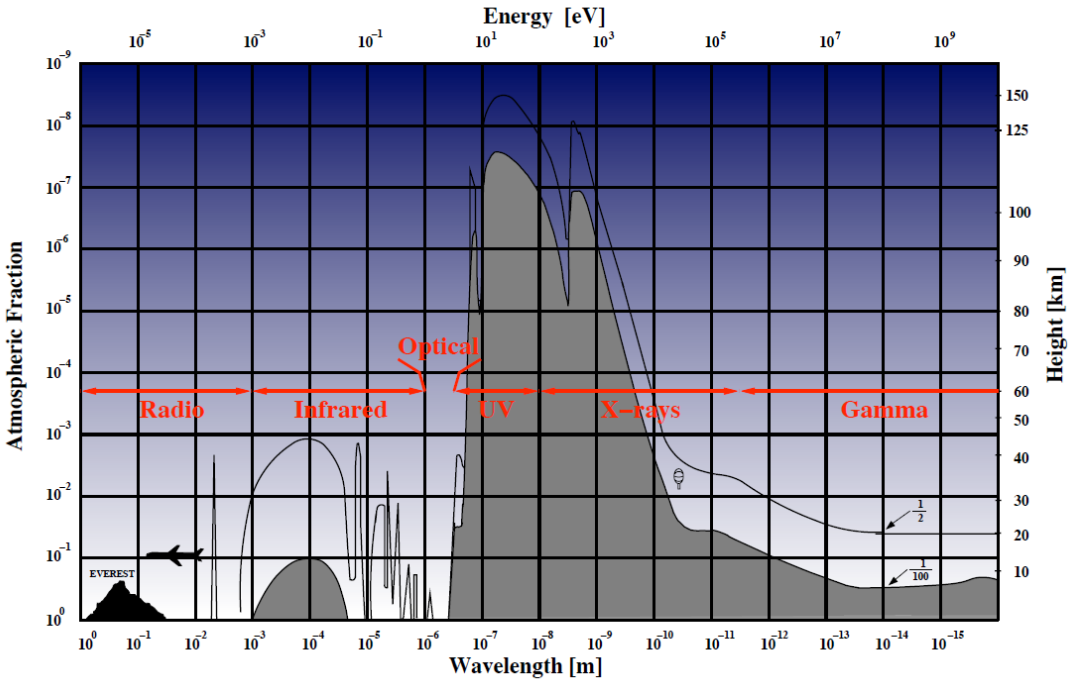

Figure 1.1: Attenuation of electromagnetic radiation through Earth's atmosphere. The upper black curve indicates the height (right-hand scale) which is reached within the atmosphere by only 50 % of the incident radiation, depending on the photon energy. The lower curve shows the same for the 1 % limit. The surface of the Earth is reached by more than 1 % of the incident radiation only at optical, near-infrared, and radio wavelengths. Credit: Giacconi et al. (1968); modified by Schanz/Tenzer (IAAT).

The first experiment which successfully measured X-ray emission from space was performed in the year 1949 by Friedman et al. (1951). They equipped a rocket with an X-ray detector, which reached high enough altitudes to take the first X-ray image of the Sun. Since the intensity of the Sun's X-ray emission was taken as a typical value for a star, stellar X-ray emission was then believed to be too weak to be observed for more distant stars and thus, the X-ray sky was considered to be quite empty. This picture only changed 13 years later with the rocket flight performed by Giacconi et al. (1962), which is generally considered as the birth of X-ray astronomy. This rocket flight was supposed to study the X-ray emission from the Moon. Surprisingly, Giacconi et al. (1962) found an X-ray source in their data which was much stronger than the expected emission from the Moon. Today, it is known that they observed the X-ray emission of Scorpius X-1 (Giacconi et al., 1964), a low-mass X-ray binary, which is the brightest X-ray source in our

sky apart from the Sun. For this discovery and for opening the field of X-ray astronomy, Giacconi was awarded the Nobel Prize in Physics in the year 2002. This discovery of the existence of unpredicted X-ray sources outside of our solar system was the beginning of X-ray astronomy. It is driven by the desire to find new sources, to study the nature of their X-ray emission, and to understand the processes which produce huge amounts of high-energetic radiation.
This trailblazing discovery was followed by a whole set of balloon flights, which have the great advantage of longer observation time of many hours and even days, compared to short-lived rocket flights which only allowed data acquisition for minutes. In the year 1970, a new area of X-ray astronomy was opened with *UHURU*[1] (Jagoda et al., 1972), the first dedicated X-ray satellite. Within its first day of operation, *UHURU* collected more X-ray data than obtained in all rocket and balloon flights before (Arnaud et al., 2011b) and performed the first all-sky survey in X-rays in the energy range of $2-20\,\mathrm{keV}$. In the year 1978, the *Einstein* Observatory (Giacconi, 1980) was launched which was the first satellite to use X-ray focusing optics, providing an unprecedented sensitivity. In the year 1990, the German satellite *ROSAT* (**Ro**entgen **Sat**ellit) was launched (Trümper, 1982), which observed more than 150 000 sources during its all-sky survey in the energy range of $0.1-2.5\,\mathrm{keV}$. An image of the X-ray sky as detected by *ROSAT* during this survey is shown in Figure 1.2.

Today, with the further development of X-ray imaging detectors, spectroscopic detectors, and focusing optics, great advances have been achieved in the spectral, spatial, and timing resolution as well as in the sensitivity of X-ray telescopes. Modern X-ray observatories like *XMM-Newton* (Jansen et al., 2001) or *Chandra* (Weisskopf et al., 2002) offer unprecedented possibilities in the study of the high-energetic Universe in the still young field of X-ray astronomy, and more are to come, with missions like *eROSITA* (**e**xtended **Ro**entgen **S**urvey with an **I**maging **T**elescope **A**rray) which will reveal more of the X-ray sky to higher energies (up to $10\,\mathrm{keV}$) with yet unmatched spectral and spatial resolution (Predehl et al., 2006). More about the history and future of X-ray astronomy can be found, for example, in Santangelo and Madonia (2014).

In this chapter, an introduction about the physical processes which produce X-rays will be given. Furthermore, various X-ray detectors as well as non-focusing and focusing optics will be described.

[1] UHURU is the Swahili word for 'freedom'.

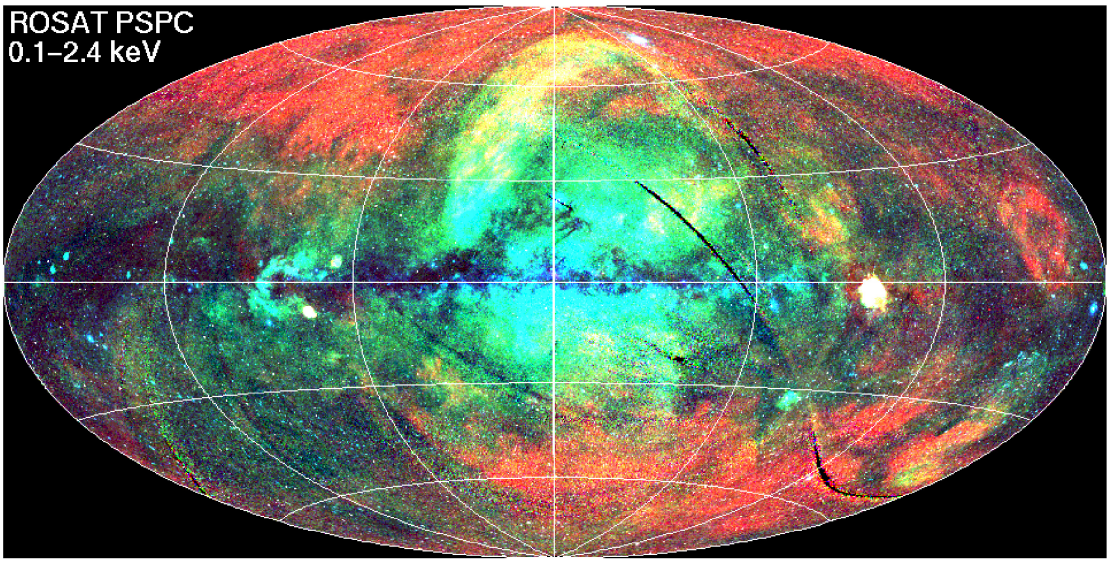

Figure 1.2: Image of the X-ray sky as observed by *ROSAT* during its all-sky survey (RASS). Red indicates soft X-rays (0.1 – 0.4 keV), green shows the emission in the energy range of 0.5 – 0.9 keV, and blue stands for harder photons with energies between 0.9 – 2.0 keV. Credit: *ROSAT* and Max-Planck-Institute for Extraterrestrial Physics (MPE), Garching, Germany.

1.2 X-ray Producing Processes

There are various high-energetic mechanisms, which can produce X-rays. These mechanisms can be divided into thermal processes, non-thermal processes, and non-thermal processes of thermally distributed particles. In this section, an introduction is given to some of those mechanisms which play a crucial role in the field of X-ray astrophysics (see Seward and Charles, 2010).

1.2.1 Processes Occurring in Thermal Gases

Black-Body Radiation

Black-body radiation can be one type of thermal X-ray emission. A black body is an idealized object that possesses zero reflectivity and is in thermodynamic equilibrium. An object which absorbs all incoming radiation consequently also has to re-emit it. This emitted spectrum of a black body is radiated away isotropically in all directions and has a characteristic shape which is described by Planck's law:

$$B_\nu(T) = \frac{2h\nu^3}{c^2} \frac{1}{\exp(h\nu/k_\mathrm{B}T) - 1}\,, \tag{1.1}$$

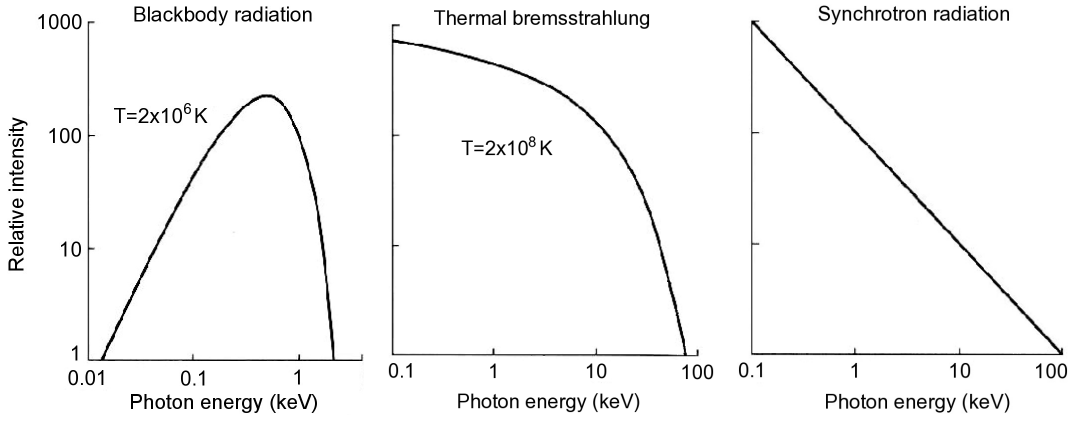

Figure 1.3: Example of a spectrum as created through (a): black-body radiation, (b): thermal bremsstrahlung, and (c): synchrotron radiation as produced by a population of electrons which follow a power law distribution. Credit: Seward and Charles (2010).

with the following definitions:

B_ν : spectral radiance in W sr^{-1} Hz^{-1} m^{-2},
ν : frequency of the emitted radiation,
T : temperature of the black body,
h : Planck constant,
k_B : Boltzmann constant,
c : speed of light in vacuum.

The shape of this spectrum (see Fig. 1.3a) depends only on the temperature of the black body and is therefore independent of the frequency and the incident angle of the incoming radiation which is absorbed by the black body. The temperature of the black body can be calculated out of the position of the maximum of the emitted spectrum, according to Wien's displacement law, which states that the position of the maximum, ν_max, can be described as $\nu_\mathrm{max} = 5.879 \times 10^{10} \times T\,\mathrm{Hz/K}$ (or depending on the wavelength λ, as $\lambda_\mathrm{max} = \frac{0.002898}{T}\,\mathrm{K\,m}$). Many astrophysical objects emit black-body radiation, like for example stellar photospheres. For the maximum of the emitted spectrum to lie in the X-ray regime, a temperature of the black body of $\sim 10^6 - 10^8\,\mathrm{K}$ is necessary. Such high temperatures are reached for example on the surface of young neutron stars.

Thermal Bremsstrahlung

Whenever a charged particle is deflected by an electric field, it emits bremsstrahlung. This happens for example when an electron passes by an ion close enough for electromagnetic interaction to take place. This interaction forces the electron to change its direction, which causes the emission of bremsstrahlung in the form of a photon. Since the electron loses energy due to this radiation, its kinetic energy decreases. Thermal bremsstrahlung is produced if the plasma which emits bremsstrahlung is in thermal equilibrium – i.e. that all its particle species have the same temperature and follow a Maxwell-Boltzmann velocity distribution. The emitted radiation is a continuum with an exponential cutoff at higher energies (see Fig. 1.3b). The intensity I of this emission is defined as

$$I \propto Z^2 n_\mathrm{e} n_\mathrm{i} \sqrt{k_\mathrm{B} T} \exp(-h\nu / k_\mathrm{B} T)\,, \tag{1.2}$$

with the following definitions:

Z : atomic number of the ions,
n_e : electron density of the plasma,
n_i : ion density of the plasma,
k_B : Boltzmann constant,
T : temperature of the plasma,
h : Planck constant,
ν : frequency of the generated radiation.

Through thermal bremsstrahlung, considerable amounts of X-rays are produced when the plasma has a temperature of $\gtrsim 10^6\,\mathrm{K}$. In addition to continuum bremsstrahlung, such a plasma typically also shows line emission created through fluorescence emission.

Fluorescence Lines

In a plasma in which the heavier elements are not fully ionized, i.e. a plasma with temperatures $\lesssim 5 \times 10^7\,\mathrm{K}$, a considerable amount of energy can be radiated away through fluorescence lines. Fluorescence lines are created through the de-excitation of an electron into a lower energetic level of an atom via the emission of a photon. These lines lie in the X-ray regime if the temperature of the plasma is $\gtrsim 2 \times 10^6\,\mathrm{K}$. X-ray line emission can be produced through energy transitions in the inner shells of heavy elements. This can happen for example through an electron capture of a highly ionized particle in an upper shell and the subsequent de-excitement of the electron under emission of a photon. Another possibility to produce line emission is given as a consequence of the collision of a particle with a high-energetic electron. Through this collision, an electron can be knocked

out from an inner shell of the particle and X-rays can be produced through the subsequent transition of an electron from an outer shell to fill up the inner gap. The energy of these transition lines is characteristic for each atom, and certain temperatures are required for each transition. Therefore, these lines represent a diagnostics for the chemical composition and for the temperature of a plasma in thermal equilibrium.

1.2.2 Non-Thermal Processes

Synchrotron Radiation

When a charged particle moves in a magnetic field with a velocity close to the speed of light and with a velocity component perpendicular to the magnetic field lines, it emits synchrotron radiation. The radiation is caused by the Lorentz force, which makes the charged particle move on circles around the field lines. Due to the change in the direction of motion, the particles emits radiation. The resulting spectrum of a population of charged particles in a magnetic field depends on the energy of the charged particles and on the strength of the magnetic field. If the underlying population of charged particles are electrons which follow a power law distribution, then the resulting spectrum will also follow a power law (see Fig. 1.3c) with a maximum intensity at a frequency ν of

$$\nu = 2\pi \frac{eB}{m_\mathrm{e} c} \left(\frac{E}{m_\mathrm{e} c^2} \right)^2 , \tag{1.3}$$

with the following definitions:

e : elementary charge of an electron,
B : magnetic field strength,
m_e : mass of an electron,
c : speed of light,
E : energy of the electron.

For the creation of X-ray synchrotron radiation, a relativistic population of electrons is necessary in addition to a strong magnetic field of $\sim 10^6$ G.

Comptonization

Another non-thermal process which plays an important role in many astrophysical environments is comptonization, which is a consequence of the inverse Compton effect. The Compton effect itself describes the scattering of a photon by a charged particle – typically electrons – through which the photon loses energy and the

charged particle gains energy due to its recoil. This happens whenever the energy of the photon ($E = h\nu$) is bigger than the energy of the charged particle ($E = \gamma mc^2$, with $\gamma = \sqrt{\frac{1}{1-v/c^2}}$ being the Lorentz factor). The energy loss of the photon can be described through an increase of its wavelength λ, whereas

$$\Delta\lambda = \lambda_\mathrm{f} - \lambda_\mathrm{i} = \frac{h}{mc}(1 - \cos\phi)\,, \tag{1.4}$$

with the following definitions:

$\Delta\lambda$: change in wavelength of the photon,
λ_f : wavelength of the photon after the scattering,
λ_i : wavelength of the photon before the scattering,
h : Planck constant,
m : mass of the particle,
c : speed of light,
ϕ : scattering angle of the photon.

Interestingly, this change in wavelength depends on the scattering angle of the photon, but not on its initial energy.
If the particle energy is bigger than the photon energy, the opposite takes place: the photon gets up-scattered and the particle loses energy. This process is referred to as inverse Compton effect and can often be found in astrophysical hot plasmas or populations of hot electrons like in the coronae of black holes. When inverse Compton scattering occurs repeatedly and when the scattered photons can subsequently escape the population of hot particles, an effective cooling of the plasma is possible. This effect, which is called comptonization, leads to a characteristic shape of the observed spectrum of a comptonized population of hot particles, showing a power-law with an exponential cutoff.

All the physical processes introduced in this section play an important role in the physics of many cosmic sources of X-ray emission. Different ways of how to detect this radiation are discussed in the following section.

1.3 Detection of X-ray Emission

In this section, different techniques and technologies are discussed which are used for the detection of X-rays. The first part is dedicated to different non-focusing and focusing imaging techniques, while in the second part, X-ray detectors are discussed with special emphasis on modern, imaging semiconductor detectors.

1.3.1 Imaging Techniques

The imaging of X-rays is a challenging task since they are absorbed by traditional glass lenses and since the reflection of these high-energetic photons from the surface of a mirror requires very small incident angles (Staubert, 2008). In the following paragraphs, different non-focusing and focusing techniques are discussed which can be used in X-ray imaging systems.

Non-Focusing Optics

The first optical systems which were used for the imaging of X-rays were non-focusing optics. They consist of collimators, which are tubes made out of X-ray blocking materials. These tubes were put in front of the detector in order to limit its field of view (FOV) to a certain area of the sky. They were used for example on the *UHURU* satellit. To reduce the large size of collimators, honeycomb collimators can be used, which consist of a large number of small collimator tubes which are arranged in a comb-like structure. This decreases the size of the collimator considerably, but with the trade-off of a smaller sensitive detector area due to the honeycomb structure in front of the detector.
Since these optics provide no information about the position of the source within the FOV, one-pixel detectors can be used without any additional loss of information. Still, even without spatially resolving detectors, information about the number of sources within the FOV and about their position can be obtained by using rotation modulation collimators. These collimators consist of two grids of X-ray absorbing material which are rotated with respect to each other in front of the detector. The thus created light curve which is observed by the one-pixel detector has a specific frequency and modulation which depend on the position of the source within the FOV. The frequency of this signal allows to determine the distance of the projected source image from the rotational axes of the collimator, while the phase of the modulation curve provides information about the position angle of the projected source image. This technique was a great improvement in the imaging of cosmic X-ray sources since it allows for the distinction between different point sources within the same FOV. This type of optics was used for example on the High Energy X-ray Experiment (HEXE) onboard the space station MIR (Reppin et al., 1985).

Another way to identify individual sources and to determine their position within the FOV is provided by using coded masks. For this imaging technique, spatially resolving detectors are required. The coded masks are attached in front of the detectors and consist of complicated patterns of an X-ray absorbing material (e.g. tungsten) with X-ray-transmissive gaps. The pattern is chosen in a way that the

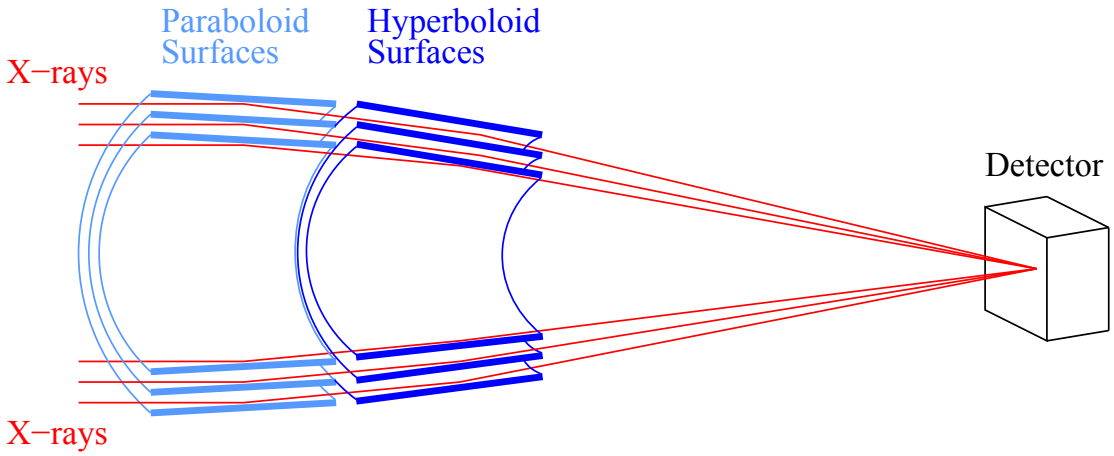

Figure 1.4: Schematic illustration of a Wolter-I mirror telescope. The X-rays are reflected from the paraboloid and hyperboloid mirror shells and focused onto the detector. Credit: C. Tenzer, IAAT; modified by J. Bayer, IAAT.

shape of the shadow which is cast upon the detector by an X-ray source depends on the position of the source within the FOV. Thus, the position of the source can be calculated by deconvolving the cast shadow. This technique is still used today for the imaging of hard X-rays ($\gtrsim 20\,\mathrm{keV}$), which are reflected only under very small incidence angles and therefore require a large focal length which is difficult to realize in satellite missions. For softer X-rays, focusing optics are used in combination with imaging detectors, which are discussed in the following section.

Focusing Optics

A big improvement in the sensitivity and resolution of X-ray imaging systems was obtained with the launch of the first X-ray focusing optics on the X-ray satellite *Einstein* Observatory in the year 1978 (Giacconi, 1980). Focusing X-rays by using mirrors is a non-trivial task due to the small incident angles required for their reflection. This angle increases with the atomic number and density of the reflecting material and with the wavelength of the incident radiation. To increase this angle, the reflective surface of X-ray mirrors is coated with elements like gold or iridium, which have a large atomic number and a high density.
For photons with energies of 1 keV, this critical angle for the reflection is only $\sim 1°$. Since such low reflection angles would lead to very large focal lengths, a special mirror configuration is used in X-ray astronomy which is called a Wolter-I mirror (Wolter, 1952; Giacconi et al., 1968; Aschenbach, 1985). In this configuration, the X-rays are reflected twice: first from a paraboloid mirror shell and then from a

hyperboloid mirror shell (see Fig. 1.4). Through this double-reflection, the focal length can be decreased considerably, e.g. to $\sim 7\,\mathrm{m}$ for photons with an energy of $\sim 15\,\mathrm{keV}$. To compensate for the small effective area of each mirror shell which is a result of the small reflection angle for X-rays, several of these mirror shells of different radii are nested within each other coaxially and confocally.
Wolter-I mirror telescopes are commonly used in modern X-ray astronomy, e.g. for the X-ray telescopes of *XMM-Newton*, each of which consists of 58 nested mirror shells with a minimum packing distance of 1 mm for the individual shells (see Sect. 3.1). Most often, such focusing optics are used in combination with a spatially resolving X-ray detector for accurate image reconstruction. Some of these detectors are introduced in the following section.

1.3.2 X-ray Detectors

Since the discovery of X-rays in 1895 (Röntgen, 1896), X-ray detectors have undergone a fast development. The used devices have undergone a huge development and are permanently improving in performance. In this section, a brief overview of the different kinds of detectors is given, with a focus on modern semiconductor detectors.

The Beginning of X-ray Detectors

The first X-rays discovered by Röntgen (1896) were recorded on ordinary, optical film plates which are also sensible to X-ray photons. Starting from 1908, proportional counters were developed which are basically capacitors filled with a noble gas (Rutherford and Geiger, 1908; Pfeffermann, 2008). When X-rays enter the proportional counter, electron-ion pairs are generated by the photoeffect. A voltage is applied to the capacitor which separates the electron-ion pairs and accelerates mainly the electrons which subsequently collide with other atoms. Through this, further free electrons are produced, which are attracted by the anode and can be measured as a current. When applying the correct voltage, the number of the thus created electrons is proportional to the energy of the incident photon.
For the detection of hard X-rays with energies $> 15\,\mathrm{keV}$, inorganic scintillation counters can be used (Kendziorra, 2008). These consist of a scintillator crystal and a photomultiplier. When an incident X-ray photon hits the scintillator, it can be absorbed through the photoeffect and the resulting photoelectron can excite several atoms. When they subsequently de-excite radiatively, photons are emitted which posses optical wavelengths. These photons interact with the photomultiplier and create free electrons due to the photoeffect. The photoelectrons are then accelerated and amplified through electric fields within the photomultiplier. Out

of the resulting current, the intensity and the energy of the incoming radiation can be measured.
These days, the most widespread detectors which are used in astronomy for the detection of X-rays are semiconductor detectors, which will be discussed in the following section.

Semiconductor Detectors

In modern X-ray astronomy, semiconductor detectors are the most commonly used type of detectors. In this device, the detection of photons is based upon the inner photoeffect within a doped semiconductor material (e.g. silicon). Incident photons with energies greater or similar to the energy of the material's band-gap can create electron-hole pairs in the semiconductor. To avoid immediate recombination, a voltage is applied which separates the electron-hole pairs and stores the electrons in a potential well which is present in each pixel.[2]
This concept is realized in different kinds of semiconductor detectors, with the main difference lying in the readout of the devices. A widespread detector type is the so-called charge-coupled device (CCD), which is read out by shifting the photon-induced charges through the device until a readout node is reached. In a CCD, each pixel consists typically of three electrodes onto which different voltages can be applied (see Fig. 1.5a). During the exposure time of the detector, the photoelectrons are gathered under the middle electrode of each pixel. After the integration time, the voltage of the electrodes is shifted in a way that causes the collected electrons to shift from pixel to pixel through a pixel row, until they reach a readout node. After each pixel of a row has been read out one by one using this method, the readout cycle is complete and a new integration time can follow. The time needed for a complete readout cycle depends on the number of pixels per row and is a trade-off between energy resolution and timing resolution. This readout method has the advantage that a large number of pixels can be read out by the same readout node and readout electronics. For more information about CCDs, see for example Strüder et al. (2001) or Strüder and Meidinger (2008).

Another type of semiconductor detectors are the so-called active pixel sensors. In these devices, every pixel is read out individually, e.g., by measuring the locally amplified voltage created by the electrons gathered in a pixel without shifting them. Since the readout preserves the gathered electrons, a signal can be read out multiple times to increase the energy resolution. Afterwards, the pixel is actively cleared from these electrons. A pixel as described here is often placed within

[2] In most detectors, the electrons are stored in the potential wells while the signal from the holes is discarded, but there are also some detectors where the information (arrival time, energy) of the holes is used to achieve better resolution.

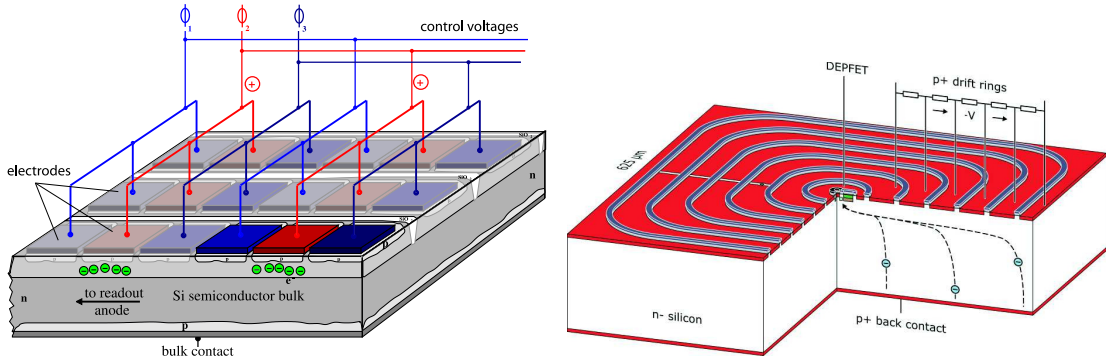

(a) (b)

Figure 1.5: Two different kinds of semiconductor devices used in astronomy for the detection of X-rays: (a) a charge-coupled device (CCD), in which the readout of a pixel occurs by shifting the collected electrons through a pixel row. Credit: T. Schanz, IAAT; (b) a macropixel with an active pixel sensor at its center, which can be read out individually. Credit: Treis et al. (2009).

the center of a so-called macropixel (see Fig. 1.5b). A macropixel consists of a selectable number of drift rings which are attached around a pixel center. The drift rings are cathodes with a decreasingly negative potential towards the pixel center. Through this structure, the collected electrons within a macropixel are gathered beneath the pixel center, where the readout occurs. Due to the variable number and shape of drift rings, this design leads to a high flexibility in the size of a macropixel. The big advantage of active pixel sensors is their high readout speed ($\sim 2\,\mu$s/line), which is a result of the direct readout without the necessity of shifting the charges. Further, the local amplification of the signal before the readout leads to a better energy resolution. More information about active pixel sensors can be found for example in Treis et al. (2009) or Strüder and Meidinger (2008).

In this chapter, an introduction to X-ray astronomy was given. The history of X-ray astronomy was described briefly, from the first cosmic X-rays to be detected up to modern space observatories. Various thermal and non-thermal processes were introduced which can produce X-ray emission. In the last part of this chapter, detection techniques were introduced, the challenges in the focusing of X-rays were described, and examples of different devices used for the detection of X-ray emission were given.

In Chapter 2, an introduction into the interstellar medium will be given, which was the driving science topic for the studies performed within this thesis. Main topics discussed in this chapter are supernova remnants, superbubbles, and supergiant shells. In the following chapter (Chapt. 3), the X-ray observatory *XMM-Newton*

will be introduced, whose data has been used for the morphological and spectral X-ray analyses performed within the scope of this thesis. Chapter 4 provides a detailed discussion about the different background components present in (*XMM-Newton*) X-ray data and shows the ways to eliminate, reduce, or model these components. In Chapter 5, the technical details of the performed X-ray analyses are described, in particular the used *XMM-Newton* data, the data handling and processing, and the model used for the spectral fitting of the observational data. This is followed by a detailed discussion of the results of the morphological and spectral analyses which have been performed within the scope of this thesis for supergiant shell LMC-SGS 2. Chapter 6 provides the same for the studies performed for DEM L299, for which the same basic techniques as for supergiant shell LMC-SGS 2 have been used. Chapter 7 concludes the thesis by giving a summary of the most important results.

Chapter 2

The Interstellar Medium

At first glance, in particular in the optical, the space between the stars of a galaxy might appear to be empty, but it is not: it is filled with gas and dust, which – in the case of the Milky Way – account for 10 % of the visible mass of the galaxy (Seward and Charles, 2010). This material is defined as the interstellar medium (ISM) and mainly consists of hydrogen. The major part of the ISM has much lower densities than the best vacuum which can currently be produced on Earth and is therefore only visible when the observed structure has a large depth. As an example, Figure 2.1 shows an area of $\sim 2\,\mathrm{kpc} \times 2\,\mathrm{kpc}$ around the star-forming region 30 Doradus. In this image, the ISM can be observed in the form of H II regions, supernova remnants, bubbles, superbubbles, and supergiant shells (see respective sections for zoom-ins onto these individual objects).
The ISM plays an important role in many astrophysical processes. New stars are being formed out of it, and these stars later give their material back to the ISM through stellar winds and supernovae. Thus, the ISM provides information about star formation, stellar evolution, and supernova explosions. It allows to study the galactic matter cycle and provides insight into galaxy evolution (see Sect. 2.4). The ISM provides the possibility to improve our knowledge of various fields of astronomy and to test current models and theories.

In this Chapter, the different properties of the ISM as well as its different manifestations will be discussed. After a general introduction about the ISM, an overview about H II regions, wind-blown bubbles, and supernova remnants will be provided, with a special emphasis on their similarities and differences. The information given in this Chapter is based upon Dyson and Williams (1997), where further details can be found.

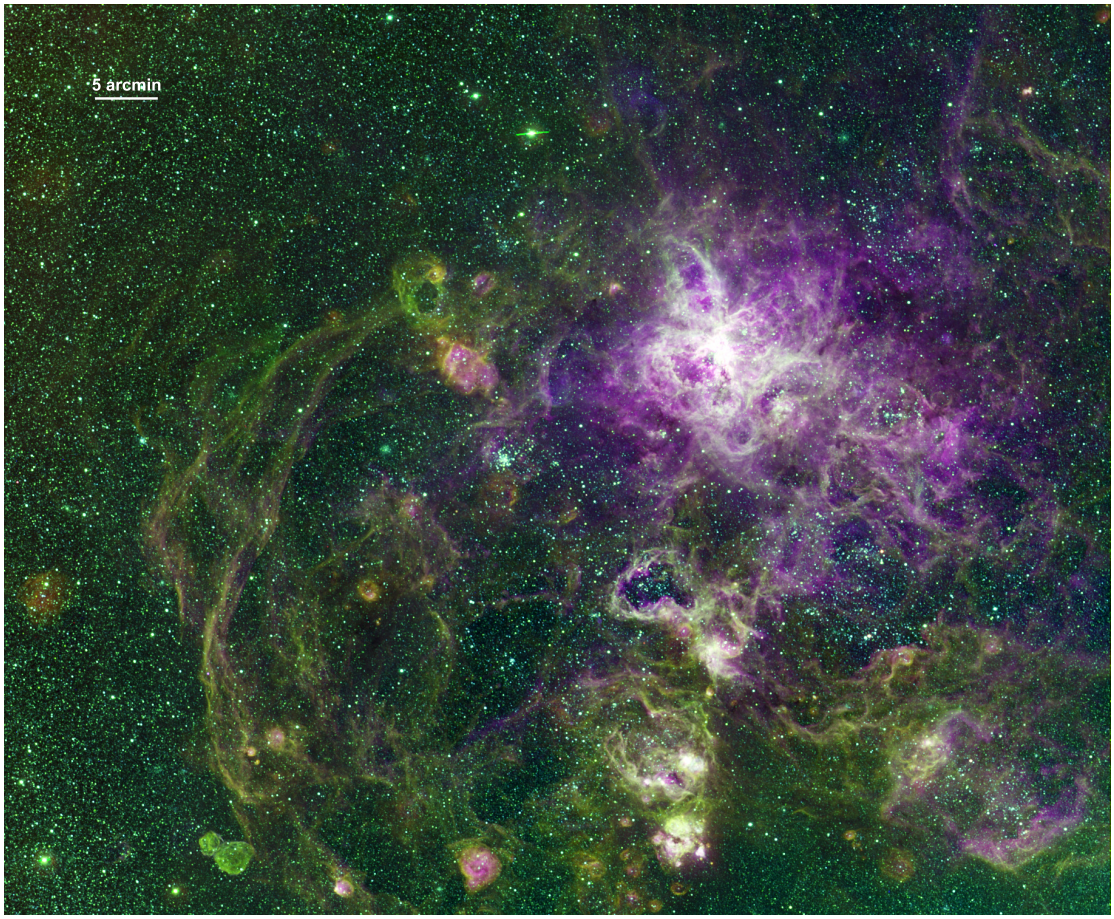

Figure 2.1: The 30 Doradus region in the Large Magellanic Cloud as an example of interstellar medium, shown in the light of three optical emission lines. The image is created out of data of the Magellanic Cloud Emission Line Survey (MCELS) and is a three-color image which shows the Hα emission in red, the [S II] emission in green, and the [O III] emission in blue. Credit: Jörg Bayer, IAAT.

2.1 Introduction to the Interstellar Medium

By far the most abundant element in the ISM is hydrogen, with an abundance of 89 %. The remaining matter consists to 9 % of helium, and to only 2 % of heavier elements. The ISM can mainly be found as gas or plasma, which fills the interstellar space, while only 1 % of the mass of the ISM is bound as dust or molecules. Its abundances, which globally reflect cosmic abundances, can strongly differ locally. Its composition represents the composition of future stars and provides information about the mechanisms occurring in, e.g., supernova explosions or within massive stars – mechanisms which are otherwise not directly observable as they occur within the interiors of these objects. Despite the great diversity of the ISM, there are properties and mechanisms that describe the ISM globally, which will be discussed in this section. In addition, cooling and heating processes occurring in the ISM will be described, and the characteristics of shocked ISM will be introduced.

2.1.1 The Three-Phase Model of the ISM

The ISM exists mainly in three different temperature regimes: in a dense, cold phase with temperatures of $< 100\,\mathrm{K}$, a less dense, warm phase with temperatures of $\sim 10\,000\,\mathrm{K}$, and a tenuous, hot phase with temperatures of $\sim 10^6 - 10^7\,\mathrm{K}$. The model of a three-phase ISM has first been introduced by McKee and Ostriker (1977). According to this model, the three different phases are supposed to be in a global pressure equilibrium, i.e. that two phases which lie next to each other in a stable configuration are of equal pressure, with a typical pressure of $p/k_\mathrm{B} \approx 10^4\,\mathrm{cm^{-3}\,K}$ (Weigert et al., 2009). Thus, to obtain pressure equilibrium, the hot phase has a very low density, while the cold phase shows high densities. Another consequence of this model is that the whole space between the stars of a galaxy is supposed to be filled with ISM, in order to obtain pressure equilibrium. Otherwise, no small-scale structures would be observable in the ISM, since for example an interstellar cloud which is located in complete vacuum – i.e. which is not in pressure equilibrium with its surroundings – would soon completely dissolve due to its inner gas pressure.[1] McKee and Ostriker (1977) gave a volume-filling factor for the hot ISM of 70 %, for the warm ISM of 30 %, and for the cold ISM of 2×10^{-3} %. An overview of the different properties of the three phases given in Table 2.1.

The cold phase ($< 100\,\mathrm{K}$) consists of neutral atoms and molecules and has densities of $50 - 10^6\,\mathrm{particles/cm^3}$. It forms molecular clouds or H I regions for example,

[1] This does not hold for structures, for which gravitation has a significant effect. One example are galaxy clusters, in which the intracluster medium – i.e. the gas between the galaxies of the cluster – is gravitationally bound to the cluster and therefore does not evaporate.

Table 2.1: Overview of the main properties of the cold, warm, and hot phase of the ISM.

	Cold ISM	Warm ISM	Hot ISM
Temperature	a few – 100 K i.e. 10^{-3} – 10^{-2} eV	5 000 – 10 000 K i.e. 0.4 – 0.9 eV	10^6 – 5×10^7 K i.e. 85 – 4 000 eV
Composition	neutral H, molecules	(partially) ionized H	ionized H
Density	50 – 10^6 particles/cm^3	$\sim$ 0.5 particles/cm^3	10^{-4} particles/cm^3
Filling factor	2×10^{-3} %	30 %	70 %
Sound speed	1 km/s	10 km/s	$>$ 120 – 600 km/s
Examples	molecular clouds, H I regions	H II regions, Strömgen spheres	interior of SNRs, superbubbles, & supergiant shells
Observable through	H I 21 cm radio line emission	recombination (e.g. Hα), forbidden-line cooling	thermal bremsstrahlung, line emission

which consist of neutral hydrogen. In this phase, the formation of molecules takes place, and star formation can be triggered. It can be observed for example through the 21 cm radio emission line of neutral hydrogen. This is a hyperfine structure transition line which is created due to an electron spin flip and can be used, e.g., to determine the velocity of a cold gas cloud through the Doppler shift of the line.
The warm phase ($5\,000 - 10\,000$ K) consists of partially or fully ionized gas with densities of ~ 0.5 particles/cm^3. It forms H II regions for example (see Sect. 2.2), which are ionized through the ultraviolet (UV) radiation of OB-stars. This phase can be observed in optical wavelengths through, e.g., the Hα line which is a recombination line from the state of principle quantum number $n = 2$ to the $n = 3$ state of neutral hydrogen, or through forbidden-line emission of [S II] or [O III] (see Sect. 2.1.1). This phase also emits continuum radio emission due to thermal bremsstrahlung.
The hot phase ($10^6 - 10^7$ K) is a plasma which is highly ionized and has very low densities of 10^{-4} particles/cm^3. It is observable in X-rays through thermal bremsstrahlung and through line emission, which originates from transitions in the inner energy levels of heavy elements. This phase, which has been heated through supernova explosions and stellar winds, fills for example the interior of supernova remnants, bubbles, superbubbles, or supergiant shells.
The temperature of the ISM is not homogeneous over the whole temperature range, but is observed to exist mainly at the three temperatures regimes of the cold, the warm, and the hot ISM. The temperatures between these regimes are hardly observed. To explain this, it is necessary to understand the cooling and heating mechanisms which take place in the ISM. These processes are discussed in the following section.

Heating and Cooling Mechanisms

Two of the most important physical processes occurring in the ISM are heating and cooling, since the temperature is a critical quantity for many fundamental processes taking place in the ISM, like molecule formation or star formation.

Heating of the ISM occurs through an increase of the kinetic energy of the gas, e.g., through the transformation of radiation energy. This can happen for example as a consequence of the photoeffect: a photon is absorbed and the kinetic energy of the emitted photoelectron can increase the temperature of the gas through further collisions. Other possibilities for heating are photodissociation of molecules, in which the fragments of the molecule carry away the energy of the absorbed photon as kinetic energy, or the ionization of an atom through a collision with a cosmic-ray particle (mainly electrons and protons) and the subsequent sharing of the free electron's kinetic energy with the gas. The most efficient heating mechanism is

heating via shock, which will be discussed in Section 2.1.2. Possible sources of heating of the ISM are for example starlight, cosmic rays, supernova explosions, and stellar winds.

Cooling of the ISM follows the inverse principles as heating: Cooling occurs through the transformation of kinetic energy into radiation, which escapes the gas and therefore leads to a reduction of the energy of the gas. This transformation occurs through the collisional excitation of an atom, ion, or molecule, which subsequently de-excites radiatively by emitting photons. Since the number of collisions depends on the density of the colliding partners, the most abundant atoms and molecules play an important role in the cooling. Another important parameter is the kinetic energy – i.e. the temperature – of the colliding partners, since an excitation can only occur when the kinetic energy of the colliding particle is equal to or larger than the energy required for the transition. Recombination can also cool the gas since electrons often recombine in a highly excited state and subsequently cascade down to the ground state. The thus emitted photons have too low energies to re-ionize the atom and can therefore escape the gas, which leads to a cooling of the gas.

Both cooling and heating can also occur through dust grains. They cool the ISM when a particle sticks to their surface via adsorption and thus loses its kinetic energy, which can be emitted by the dust grain through black-body radiation. A heating of the ISM occurs when a photoelectron is emitted after the absorption of a photon, which shares its kinetic energy with the gas. More information about this can be found for example in Dyson and Williams (1997).

Forbidden-Line Cooling

Forbidden-line cooling is a very important cooling mechanism in the ISM and the most important mechanism in the temperature range of $\sim 5\,000 - 10\,000\,\mathrm{K}$ (i.e. in the warm ISM). It is a consequence of line transitions which are quantum mechanically forbidden to occur through the fast electric-dipole transitions (typical rate: $\sim 10^8\,\mathrm{s}^{-1}$). Instead, they occur through electric-quadruple or magnetic-dipole transitions which have much lower transition rates of $\sim 1\,\mathrm{s}^{-1}$ (Dyson and Williams, 1997). The upper energy level of a forbidden transition is called a metastable state. These metastable states are populated through collisions with electrons. Two possible ways exist in which they are able to de-excite: collisional de-excitation and radiative de-excitation. On Earth, only collisional de-excitation is observed, since the collision rate is much higher than the rate for radiative de-excitation. This is different in the ISM, where the densities are so low that radiative de-excitation is the much more probable mechanism. The thus emitted photons – which are exclusively observed in space – can freely escape the ISM (Dyson and Williams, 1997). In fact, the ISM often shows strong forbidden line

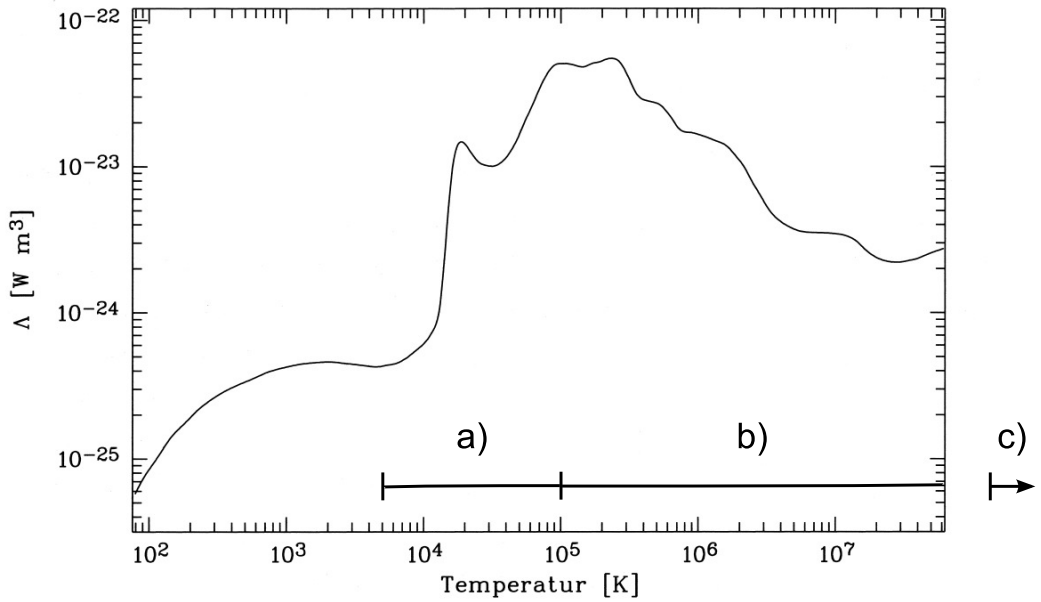

Figure 2.2: The cooling function Λ of the ISM plotted over the temperature. Three main minima can be recognized in the plot at < 100 K, 10 000 K, and 10^7 K – at the same temperatures at which the cold, warm, and hot ISM can be found. Credit: Weigert et al. (2009); modified.

emission, since the absorption of these photons through electric-dipole transition is quantum mechanically forbidden. Thus, forbidden-line transitions are a very efficient cooling mechanism for the ISM and an important tool used for astronomical studies. Important examples of ions or atoms producing forbidden-line emission are [S II] and [O III] in the optical energy band, and neutral hydrogen atoms.

The Cooling Function

The ISM is almost exclusively observed at the temperature of the cold, warm, or hot phase. This dominance of only three temperature regimes can be understood when looking at the cooling function of the ISM. The cooling function Λ can be used to determine the cooling rate $\mathscr{L}$ by which a gas loses its energy:

$$\mathscr{L} = n^2 \Lambda(T_e)\,, \tag{2.1}$$

with the number density n of the interacting species in m^{-3} and the cooling function Λ in Wm^3. Thus, the cooling rate depends only on the density of the species and – through $\Lambda(T_e)$ – on the electron temperature. Furthermore, the

electron temperature depends only on the shock velocity and the molecular mass of the gas. The cooling function is shown in Figure 2.2 as a function of temperature. In this figure, three regimes with different temperature dependencies are marked, which shall be discussed in this section:

- regime *a)*: $\sim 5 \times 10^3 - 10^5\,\mathrm{K}$,
- regime *b)*: $\sim 10^5 - 10^8\,\mathrm{K}$,
- regime *c)*: $\gtrsim 10^8\,\mathrm{K}$.

In regime *a)*, the cooling function increases with temperature. Forbidden-line cooling is the dominant process in this regime, which produces photons mainly at optical and infrared wavelengths. At higher temperatures, the metastable states needed for these forbidden-line transitions become more and more rare, due to higher ionization states of the ions. At $\sim 10^5\,\mathrm{K}$, the cooling function reaches its maximum, which is created due to the collisional excitation or ionization of hydrogen. At this temperature, the emission mainly occurs in optical and UV energy bands.
In regime *b)*, the cooling function decreases. Here, the cooling occurs due to the collisional excitation and subsequent radiative decay of more highly ionized particles (resonance lines). This regime emits photons in far UV and soft X-rays. The cooling function decreases with temperature in this regime because less particles are available at higher temperatures which can still be excited or ionized.
In regime *c)*, above $\sim 10^8\,\mathrm{K}$, almost all particles are fully ionized and bremsstrahlung is the remaining main cooling process, producing photons in the X-ray energy band.

The cooling function possesses three main minima: at $< 10^2\,\mathrm{K}$, around $8 \times 10^3\,\mathrm{K}$, and at $\sim 10^7\,\mathrm{K}$. These are exactly the three temperatures at which the cold, the warm, and the hot ISM are found. When considering for example the minimum at $\sim 8 \times 10^3\,\mathrm{K}$, a small increase of the temperature results in a strong increase of the cooling function and therefore of the cooling rate (see Fig. 2.2). The increase of the cooling rate leads to a decrease of the temperature, which is thus stabilized at $\sim 8 \times 10^3\,\mathrm{K}$ due to this thermostat effect. In contrast, when considering a gas with a temperature of $\sim 5 \times 10^5\,\mathrm{K}$, a small increase of the temperature leads to a decrease of the cooling function, which in turn further speeds up the increase of the temperature, until the hot phase of the ISM is reached at $\sim 10^7\,\mathrm{K}$. Through this, the temperature of the ISM is kept stable at the minima of the cooling function, which define the three phases of the ISM.

2.1.2 Shocked ISM: the Rankine-Hugoniot Jump Conditions

Many astrophysical processes like supernovae (SNe) cause a shock wave in the ISM. Since shocked ISM can be found in many interstellar regions, it represents an important state of the ISM which will be discussed in this section.
A shock front (also referred to as a shock wave) can be described as a discontinuity in the parameters of a system, like velocity, density, and pressure. A shock front is formed whenever the velocity of a sound wave is larger than the adiabatic[2] sound speed of the medium in which it propagates, i.e. whenever it has a Mach number of $\mathcal{M}_\mathrm{a} = v/v_\mathrm{sound} > 1$. In the ISM, these shock fronts have typical velocities of $\sim 50\,\mathrm{km/s} - 3\,000\,\mathrm{km/s}$. They are created for example through a supernova explosion, during which the ambient gas is heated very quickly and thus expands strongly and abruptly, which causes a shock front to moves into the ISM. Since a sound wave has a finite length, it possesses a density gradient. The discontinuity is formed because the 'front parts' of the sound wave reach the ISM first and compress it. Thus, the 'rear parts' of the sound wave hit a denser ISM than the 'front parts' did. Through this, the sound wave of the explosion expands into a medium with continuously increasing density, which in turn increases the speed of sound. Thus, the 'rear parts' of the sound wave travels with a higher velocity than the 'front parts', and will be catching up with them, through which a shock front is created.

The conservation of mass flux, momentum flux, and energy flux across the shock front can be used to derive the Rankine-Hugoniot jump conditions (Rankine, 1870; Hugoniot, 1887, 1889). These jump conditions can be used to correlate the properties of the unshocked gas in front of the shock (ρ_0, T_0, v_0) with the properties of the shocked gas behind the shock front (ρ_1, T_1, v_1). The Rankine-Hugoniot jump conditions can be used for strong shocks (i.e. for shocks with a high Mach number) within a monatomic, ideal gas without magnetic fields. The Rankine-Hugoniot jump conditions show an increase of the inner energy of the gas (and thus an increase of its temperature) across the shock front. Also, the entropy of the gas increases, and the gas is 'dragged' in the direction of the leaving shock front, meaning that the shock hits the gas supersonically and leaves the gas with a subsonical velocity in respect to the shocked gas. For such monatomic gases with $\mathcal{M}_\mathrm{a} \gg 1$, the density of the shocked gas behind the shock front is four times the density of the unshocked gas, independent from the strength of the shock (i.e.

[2] An adiabatic gas is a gas which does not exchange any heat with its surroundings. An energy transfer with its surroundings occurs therefore only by work (e.g. mechanical work). This means that an adiabatic gas does not have an energy input or energy loss through radiation or thermal conduction.

from its Mach number). Higher densities are prevented due to increased translation movement of the gas particles which leads to a high pressure that prevents further compression of the gas even for high Mach numbers (Dyson and Williams, 1997). In a frame of reference in which the unshocked gas is at rest, this leads to the following equations for an adiabatic gas and a strong shock, with the subscripts 0 and 1 denoting pre- and post-shock values, respectively:

$$\begin{aligned} v_1 &= \frac{3}{4} v_{\text{shock}} \,, \\ \rho_1 &= 4\rho_0 \,, \\ p_1 &= \frac{3}{4} \rho_0 v_{\text{shock}} \,, \\ T_1 &= \frac{3\mu m}{16 k_{\text{B}}} v_{\text{shock}}^2 \,, \end{aligned} \tag{2.2}$$

with the following definitions:

v_{shock} : velocity of the shock,
p_1 : post-shock pressure of the gas,
μ : molecular mass of the gas (with $\mu = \frac{1}{2}$ for a totally ionized hydrogen gas),
m : particle mass,
k_{B} : Boltzmann constant.

These equations change when considering an isothermal (i.e. radiative) shock wave. An isothermal shock wave can be described as a shock wave which does not modify the temperature of the gas, although the other properties of the gas change discontinuously.[3] This is achieved by loss of energy, e.g., through the processes describe in Section 2.1.1. Since an isothermally shocked gas is able to lose inner energy through radiation, a higher compression of the gas can be achieved than in the adiabatic case (Dyson and Williams, 1997). The post-shock density of an isothermally shocked gas can thus reach values larger than four times the pre-shock density and depends on the isothermal pre-shock Mach number $\mathcal{M}_{\text{isothermal}}$. In a fixed frame of reference, the Rankine-Hugoniot jump conditions result in the following equations for an isothermal shock, with the subscript f denoting the post-shock values after the cooling zone:

$$\begin{aligned} v_{\text{f}} &= v_{\text{shock}} \,, \\ \rho_{\text{f}} &= \rho_0 \mathcal{M}_{\text{isothermal}}^2 \,, \\ p_{\text{f}} &= \rho_0 v_{\text{shock}}^2 \,, \\ T_{\text{f}} &= T_0 \,. \end{aligned} \tag{2.3}$$

[3] Actually, an isothermal shock wave is an adiabatic shock wave plus a thin cooling zone.

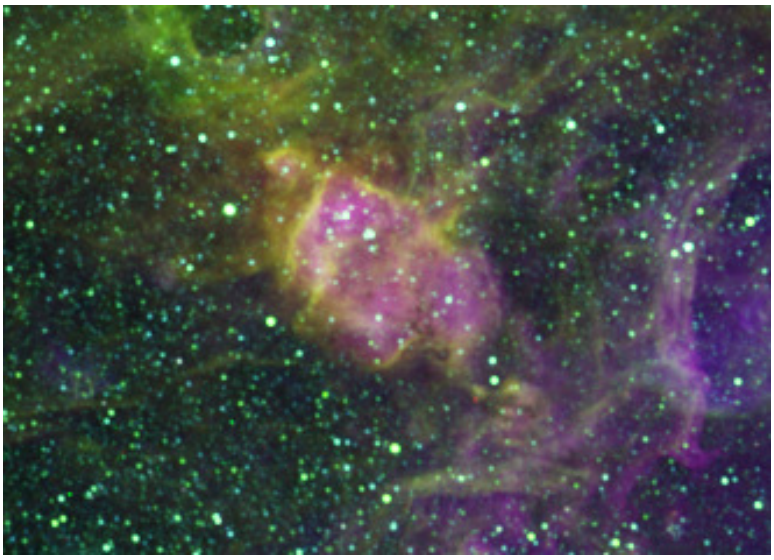

Figure 2.3: Zoom-in of Figure 2.1 onto LHA 120-N 164 as an example of an H II region.

2.2 H II Regions

H II regions – also referred to as diffuse nebulae or radiatively excited regions – consist of a thin gas with densities of $\sim 0.5\,\mathrm{particles/cm^3}$ which is heated to a temperature of $\sim 5\,000\,\mathrm{K} - 10\,000\,\mathrm{K}$ by the radiation of early-type stars (OB-stars). These stars emit a considerable amount of their energy as UV photons, which have wavelengths needed for the ionization of hydrogen or oxygen, for example. The thus produced photoelectrons distribute their kinetic energy within the gas which leads to a heating of the gas. An example of an H II region can be seen in Figure 2.3.
The emission of H II regions is mainly caused by hydrogen, although some of the heavier elements like oxygen, sulfur, and nitrogen also play an important role for the properties of the gas since they allow the very efficient forbidden-line cooling. H II regions emit optical emission lines as a result of collisions (e.g. forbidden lines) or recombination. In addition, optical continuum emission is produced through recombination of continuously distributed electrons with ions and the subsequent emission of photons, which carry away the excess energy of the electrons. At radio frequencies, H II regions emit continuum emission due to thermal bremsstrahlung, and line emission originating from recombination in very high energy levels (principle quantum number $n \approx 100$) of hydrogen.

In an H II region with a temperature of $\sim 10\,000\,\mathrm{K}$, the ionization degree of hydrogen is almost unity ($n_{\mathrm{H,ionized}}/n_{\mathrm{H,total}} \approx 1$), i.e. almost all hydrogen atoms are

ionized.[4] The UV radiation of an OB-star ionizes its ambient ISM, with the radius of this ionized region depending on the flux of ionizing photons and the density of the gas. The thus defined sphere is called a Strömgen sphere. The transition of almost completely ionized hydrogen within this sphere to neutral hydrogen outside the sphere is sharp-edged. This is a combined effect of the geometrical decrease of the flux of the ionizing radiation with $1/r^2$ and the subsequent increase of the number of neutral hydrogen atoms, which lead to a further decrease of the ionizing radiation, which in turn increases the number of neutral hydrogen atoms, and so on.

A typical OB-star will produce a Strömgen sphere with a radius of $\sim 1-3\,\mathrm{pc}$. However, the gas inside this sphere is heated up from initially 100 K to 10 000 K. This plus the ionization of the gas will increase the pressure of the gas by a factor of ~ 200. Subsequently, the sphere of ionized gas expands and reaches a radius of ~ 34 times the radius of the initial Strömgen sphere. OB-stars produce a stable flux of ionizing photons only during their main-sequence phase, which lasts about $3 \times 10^6\,\mathrm{yr}$. Since this time span is shorter than the time needed for the sphere to reach pressure equilibrium with its surrounding neutral ISM, this equilibrium is never reached and a Strömgen sphere will therefore always be observed as an expanding sphere.
The ionization front of the sphere moves with a velocity of initially $\sim 2\,500\,\mathrm{km/s}$ and slows down to $\sim 11\,\mathrm{km/s}$ as the sphere expands. Thus, it is faster than the sound speed of the ionized gas of $v_\mathrm{i} \approx 10\,\mathrm{km/s}$. At the beginning of the evolution of such a bubble, the gas around the star will be ionized without any expansion occurring, since the ionization front moves too fast for the bubble to react on it. After this short initial phase, the bubble will expand due to its increased pressure. Since the bubble expands supersonically into the ambient interstellar medium ($v_\mathrm{n} \approx 1\,\mathrm{km/s}$), it forms a shock front which creates a thick shell of swept-up neutral ISM around it.
The efficiency to transform the radiation energy inherent to the UV photons into kinetic energy (i.e. into the expansion) or into thermal energy (i.e into the temperature increase) is only 1 %. The major part of the energy is radiated away, e.g., through forbidden-line cooling, since the cooling function has its maximum at these temperatures. The temperature of the star only has a weak influence onto the electron temperature of the gas (and thus on the gas temperature): if the stellar temperature increases, the density of the neutral hydrogen decreases, which leads to a less efficient heating of the gas. This thermostat effect stabilizes the temperature of the H II region at $5\,000\,\mathrm{K} - 10\,000\,\mathrm{K}$.

[4] This might be different in a gas of the same temperature which has been heated by shock ionization: compared to a photo-ionized gas, a shock-ionized gas might show a lower ionization degree.

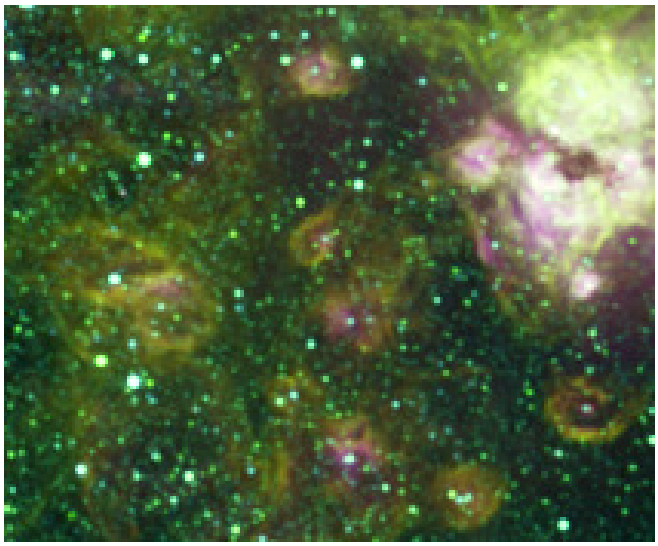

Figure 2.4: Zoom-in of Figure 2.1 showing several stellar bubbles.

2.3 Wind-Blown Bubbles

In addition to their ionizing radiation, OB-stars also produce a high-velocity stellar wind of particles originating from the stellar atmosphere. These winds create a bubble of hot gas in the ambient ISM (see Fig. 2.4). Stellar winds are created through radiation pressure, i.e. through the momentum transfer onto a particle after the absorption of a photon. These stellar winds have typical velocities of $\sim 2\,000\,\mathrm{km/s}$ and lead to a mass loss of $10^{-6}\mathrm{M}_{\odot}/\mathrm{yr}$ for the star.
These high-velocity particles hit the ISM highly supersonically and act therefore as a piston pushing on the ISM, which can be assumed to be ionized due to the UV radiation of the star (see Sect. 2.2). Therefore, a shock is created which compresses and sweeps up the ionized ISM, thus creating a shell. In contrast to H II regions which are expanding only due to their increased pressure, a permanent mass input exists for wind-blown bubbles through the stellar winds. The fast stellar wind bumps into this slower moving shell and is reflected, through which a reverse shock is created, oriented in opposite direction than the forward shock.
The structure of a wind-blown bubble is sketched in Figure 2.5. It consists of

a) a region of unshocked stellar wind,

b) a region of shocked stellar wind,

c) a region of shocked ISM, and

d) is surrounded by unshocked ISM.

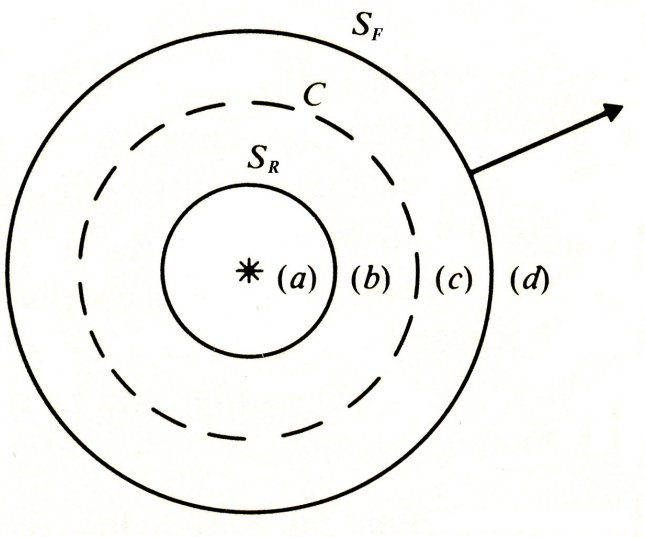

Figure 2.5: Schematic illustration of the structure of a wind-blown bubble around an OB-star. From smaller to larger radii, it consists of *(a)* unshocked stellar wind, *(b)* shocked stellar wind, *(c)* shocked ISM, and is surrounded by *(d)* unshocked ISM. A contact discontinuity C exists between region *(b)* and *(c)*. S_F and S_R represent the forward shock and the reverse shock. Credit: Dyson and Williams (1997); modified.

These regions can be approximated to have a spherical, concentric shape with the OB-star at their center. Region *a)*, which is the innermost region, consists of high-velocity stellar wind which is expanding freely with a velocity of $\sim 2\,000\,\mathrm{km/s}$. This region is bound by the reverse shock S_R which is directed towards the star. This strong shock (i.e., with high Mach number) has shocked the stellar wind in region *b)* which is heated to temperatures of $4 \times 10^7\,\mathrm{K}$ through the transformation of the kinetic energy of the shock front to thermal energy of the stellar wind region. Since the density of the stellar wind is low, the shock is believed to be collisionless. The likely mechanism responsible for the formation of a shock is magnetic interaction. At these temperatures, the cooling function is at its minimum (see Sect. 2.1.1) and thus, the shocked material cools only slowly and can be assumed to be adiabatic. This region is spatially extended and can be observed in X-rays through thermal bremsstrahlung and line emission. This region can be approximated to be in pressure equilibrium due to its large speed of sound of $\sim 600\,\mathrm{km/s}$. This is a result of the high temperature, the constant energy input, and the fast decrease of the expansion velocity of this shell, which lead to a sound crossing time which is shorter than the expansion time scale. The sudden pressure increase through the increasing temperature causes this region to expand and to sweep up the ISM around it, which is called an energy-driven flow.

A contact discontinuity exists at the boundary of this region *b)* of shocked stellar wind (shocked by S_R) and region *c)* of shocked ISM (shocked by the forward shock S_F). Since both regions have the same pressure, no mass flow occurs between them (therefore its name). Unlike the pressure, other parameters like temperature, density, and ionization states still change discontinuously at this contact surface. Region *c)* consists of ISM which has been shocked by the forward shock. Since the forward shock S_F is much weaker than the reverse shock S_R[5], the shocked ISM of region *c)* has lower temperatures than the shocked stellar wind of region *b)*. Therefore, it can cool very efficiently, e.g., through forbidden-line cooling, and consequently decreases its volume and forms a thin, but dense shell of shocked ISM. A cooling to very low temperatures is prevented by the constant flux of ionizing radiation originating from the star, which keeps the gas in this region at a constant temperature of $\sim 10\,000\,\mathrm{K}$. It has a high density due to the higher compression which is possible for an isothermal gas (cf. Eq. 2.3), compared to the adiabatic gas of region *b)* (cf. Eq. 2.2). Due to its large density and low thickness, this shell is in pressure equilibrium. At the contact region between the colder shell and the hot interior of the bubble, a part of the colder gas of the shell will evaporate into the interior of the bubble due to thermal conduction, creating a mass-increase of the bubble. While the mass loss of the shell is negligible, the mass increase of its interior has an important impact on the amount of gas inside the bubble (Castor et al., 1975).
The wind-blown bubble expands into an unshocked ISM (region *d*). Initially, this ISM is ionized due to the stellar UV radiation and has a temperature of $\sim 10\,000\,\mathrm{K}$. Eventually, the growing shell of shocked ISM gets thick enough to prevent the flux of ionizing radiation from reaching the unshocked ISM of region *d)*, which therefore becomes neutral again.

The properties of the hot gas inside a wind-blown bubble can be calculated by using the ideal gas equations, since this gas can be assumed to be in thermal equilibrium as the particles have enough time to exchange their energy. The ideal gas equation is defined as

$$pV = n_{\mathrm{tot}} k_{\mathrm{B}} T \,, \tag{2.4}$$

with n_{tot} being the total number density of particles. Out of this equation, the total thermal energy content E_{th} of the hot gas inside the wind-blown bubble can be determined by using the equation

$$E_{\mathrm{th}} = \frac{3}{2} n_{\mathrm{tot}} k_{\mathrm{B}} T_{\mathrm{x}} \phi \,, \tag{2.5}$$

[5] Since the reverse shock and the stellar wind move towards each other and collide, the relative speed of the reverse shock is higher than that of the forward shock, which moves into a resting ISM. Further, the forward shock loses velocity through a loss of internal energy which is put into the expansion of the gas.

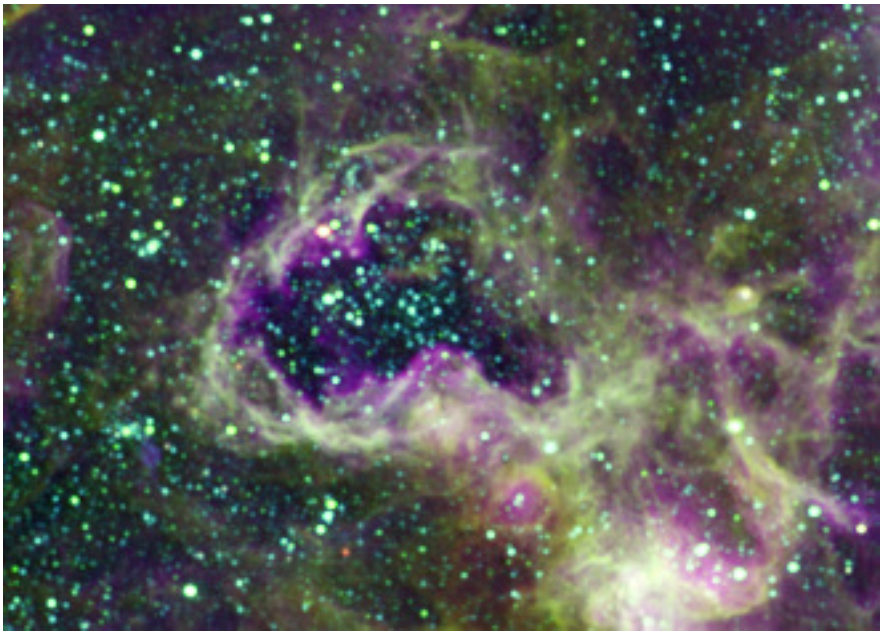

Figure 2.6: Zoom-in of Figure 2.1 showing the superbubble LHA 120-N 158.

with the X-ray temperature T_{x} of the hot gas and its filling factor ϕ within the bubble. The dynamic age t_{dyn} of the wind-blown bubble can be calculated out of the equation

$$R = \alpha (E_{\mathrm{th}}/\rho)^{1/5} t_{\mathrm{dyn}}^{2/5} \,, \tag{2.6}$$

with R being the radius of the bubble and α being a constant, which can be set to $\alpha = 0.76$ for an interstellar bubble in an intermediate evolutionary stage (Weaver et al., 1977).

2.4 Superbubbles and Supergiant Shells

Like wind-blown bubbles, superbubbles (Fig. 2.6) and supergiant shells (Fig. 2.7) are bubble-like structures within the ISM which are created through the energy input of massive stars. They follow the same physical principles as wind-blown bubbles and possess the same basic structure. Thus, the same equations can be applied to all three objects. While superbubbles and supergiant shells have many similarities with wind-blown bubbles, they have a much larger spatial extent and an additional energy input through supernovae (see Sect. 2.5). While a wind-blown bubble is formed by a single OB-star and has a radius of some parsec, a superbubble is blown by the stellar winds and the supernova explosions of a whole group of stars. Since a group of stars produces stellar winds over a much larger

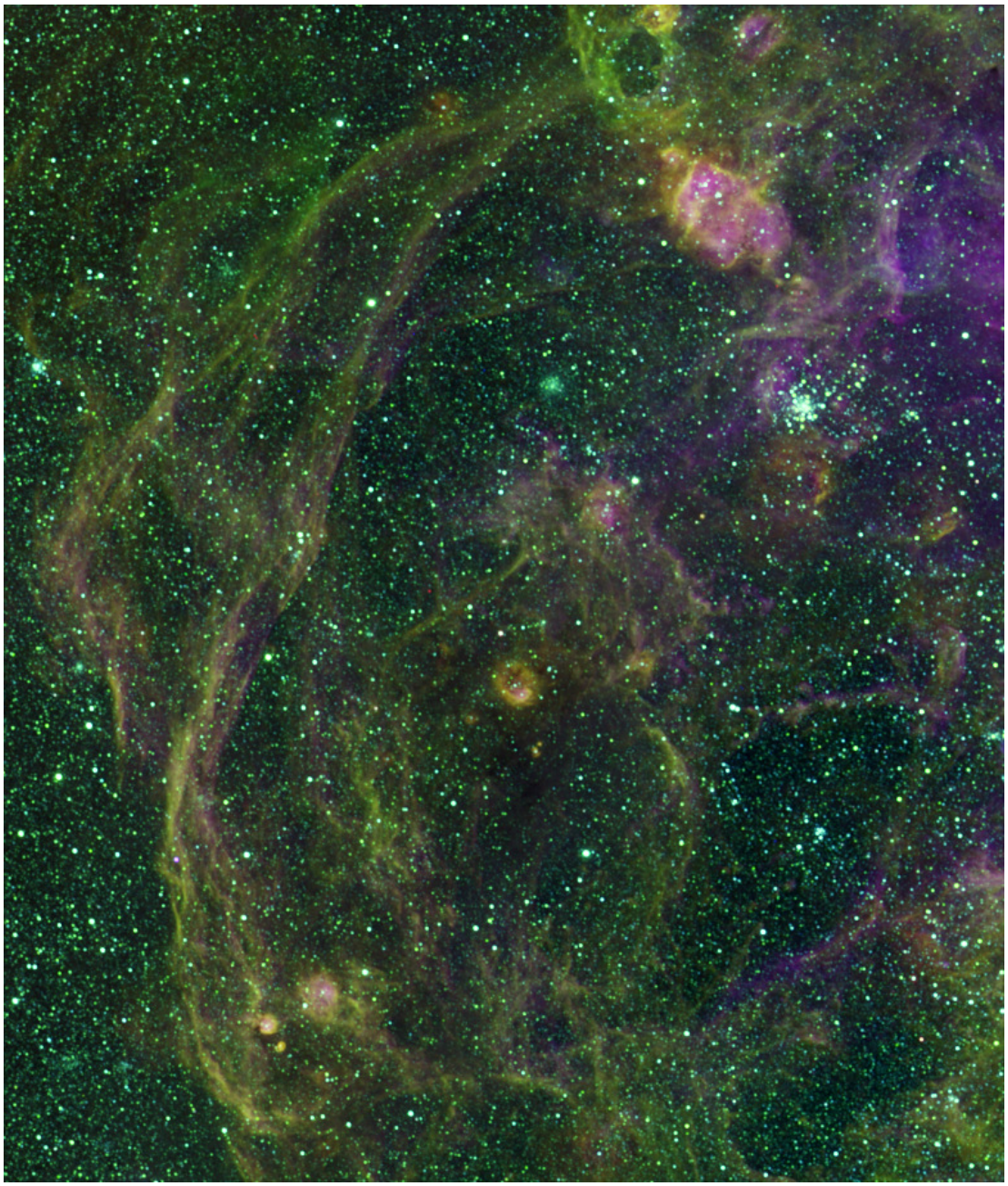

Figure 2.7: Zoom-in of Figure 2.1 showing the supergiant shell LMC-SGS 2.

Table 2.2: Comparison of wind-blown bubbles, superbubbles, and supergiant shells.

	Wind-blown bubbles	Superbubbles	Supergiant shells
Typ. radius	10 pc	100 pc	1 000 pc
Caused by	one OB-star	group/cluster of stars (10 – 100 OB-stars)	generations of clusters of stars
Energy input through	stellar winds	stellar winds, supernovae	stellar winds, supernovae
Typ. age	$< 3 \times 10^6$ yr	several $10^6 - 10^7$ yr	$> 10^7$ yr

time scale than a single OB-star, superbubbles are the much older objects (see Table 2.2). In such close groups or association, which can contain 10 – 100 OB-stars and thousands of low- and intermediate-mass stars, the wind-blown bubbles of the individual OB-stars combine and merge to form a superbubble. As soon as supernovae start to occur in such a group, they seem to dominate the energy input of the superbubble (Dyson and Williams, 1997). At typical densities of 1 particle/cm^3 of the ambient ISM, a superbubble of an age of 10^7 yr will have a radius of 270 pc and an expansion velocity of 16 km/s.

Supergiant shells are formed when superbubbles recombine over large time and spatial scales through the influence of many groups of stars over many generations. These supergiant shells can reach enormous sizes of 1 kpc (Goudis and Meaburn, 1978) and require 10^{52} erg – 10^{53} erg for their creation (Meaburn, 1980). Several supergiant shells have been observed in the Large Magellanic Cloud. Due to their large size, their detailed examination is challenging, since many observations are necessary to cover their whole extent, and detailed knowledge about a large number of stars and stellar association is required to calculate their energy input. Both can be achieved more easily for the much smaller superbubbles.

Since the shape of all kinds of interstellar bubbles depends strongly on the density of the ambient ISM, the large size of superbubbles and supergiant shells requires the consideration of density gradients present in galaxies: in spiral galaxies for example, the density will decrease when moving away from the galactic disk. Furthermore, local pressure or density gradients can often be found in star-forming regions. If one part of an interstellar bubble expands into a region with a lower density, its expansion velocity and radius are much larger in this direction than in the other directions. This leads to a non-spherical, often elliptical shape of the bubble and might also cause its ‘eruption’ and a blowout of its hot gas into

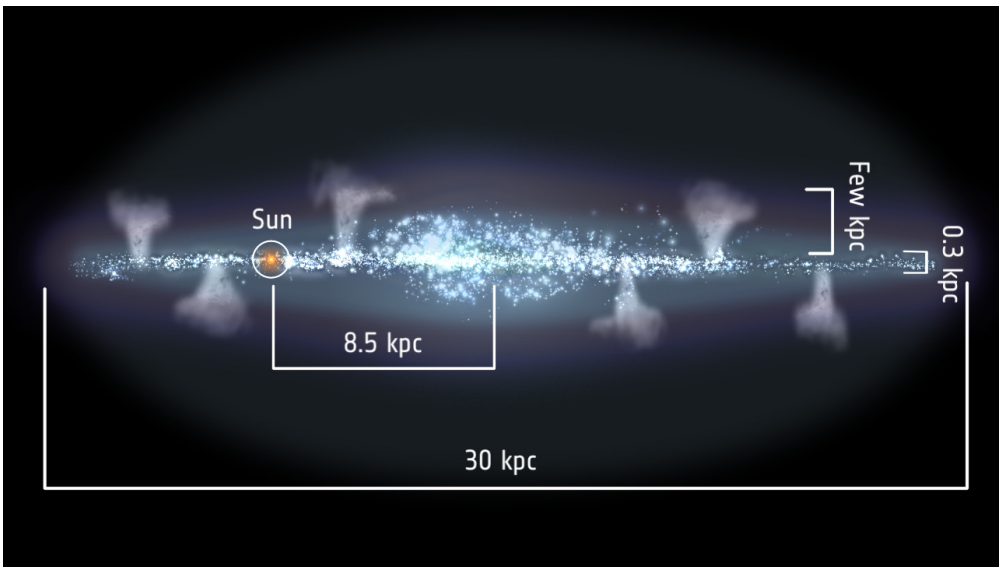

Figure 2.8: Schematic illustration of galactic fountains which release gas into the halo of a galaxy, thus producing the hot corona of a galaxy. Credit: ESA.

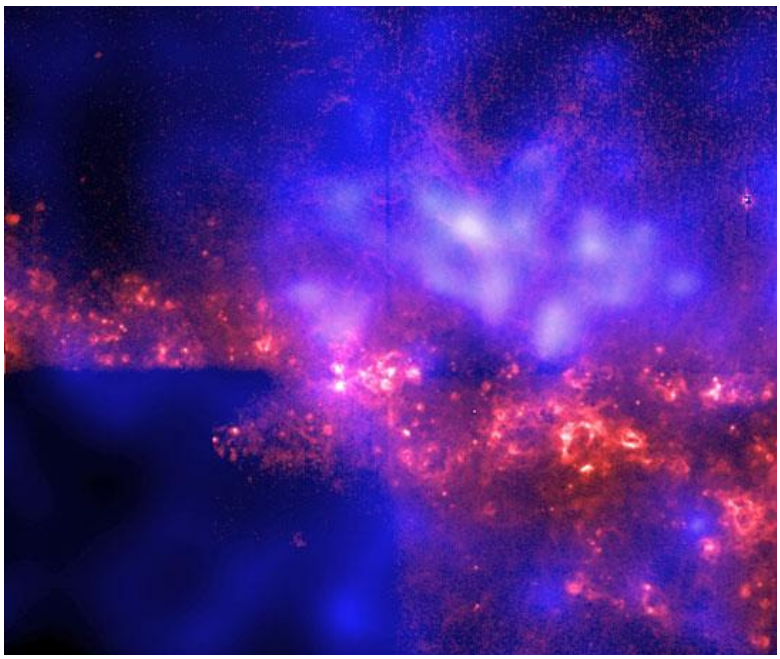

Figure 2.9: Image of the hot halo around the galaxy NGC 4631. Diffuse X-ray emission as observed with *Chandra* is shown in blue, while massive stars as observed with the *Hubble* Space Telescope are shown in red. Credit: Daniel Wang (U. Mass.) et al., *Chandra*, NASA, HST.

the ambient ISM. When supergiant shells break through a galactic disk and 'erupt', they blow their gas into intergalactic space. This phenomenon is called a galactic fountain or a galactic wind. The escaped hot gas forms the corona of a galaxy and can 'rain' down again into the galactic disk due to gravity. Thus, they play a crucial role in the evolution of galaxies. A schematic illustration of galactic fountains and an example of a galactic corona are shown in Figures 2.8 and 2.9. An overview about the different properties of wind-blown bubbles, superbubbles, and supergiant shells can be found in Table 2.2. Further information can be found for example in Tenorio-Tagle and Bodenheimer (1988) or McCray and Snow (1979).

2.4.1 Growth-Rate Discrepancy

When applying the ideal gas equations to determine the properties of superbubbles as described in Section 2.3, the resulting dynamic ages (see Eq. 2.6) found for several superbubbles are too small compared to the ages of the stellar population which blew the superbubbles, and which often have ages of several million years (e.g. Sasaki et al., 2011; Cooper et al., 2004; Warth et al., 2014). These dynamic ages are determined by using the model of Weaver et al. (1977), which is the standard model for interstellar bubbles and uses a coefficient of $\alpha = 0.76$. The growth-rate discrepancy, which is also discussed by, e.g., Cooper et al. (2004) and Jaskot et al. (2011), states that the observed growth rates of superbubbles are too low in respect to the stellar energy input. This becomes manifest in the failing energy budget: the thermal energy of the superbubble plus the kinetic energy of its shell are too low to balance the energy input of supernovae and stellar winds (Cooper et al., 2004; Maddox et al., 2009). Thus, part of the mechanical energy seems to be converted into other forms of energy (Cooper et al., 2004). Several models for possible explanations for this discrepancy exist. Two possibilities are an energy loss through a blowout, which already has been observed in several superbubbles, and the evaporation of denser, cooler cloudlets which lie within the superbubble (e.g. Jaskot et al., 2011; Silich et al., 1996). Although these mechanisms can partially account for the missing energy, none of the current models has been proven to completely explain the deviation up to now, and an interplay of several scenarios is likely.

2.5 Supernova Remnants

A supernova remnant (SNR) is the remainder of the supernova explosion of a star (see Fig. 2.10). In such an event, the star is destroyed and distributes its material in a violent explosion into the interstellar space. While a supernova is

observable for some weeks, its supernova remnant – i.e. the ejecta of the explosion and the interstellar medium which is swept-up by the shock front – can exist up to $\sim 100\,000$ yr, before the gas cools down again to temperatures and velocities of the ambient ISM.
Both supernovae and SNRs have strong effects on the ISM of a galaxy. They supply the ISM with energy and – together with wind-blown bubbles – they are responsible for the production of the hot phase of the ISM. Thus, they play a crucial role in the dynamics of the ISM, shape it into various structures, and are responsible for the production of galactic fountains (see Sect. 2.4) which influence the evolution of whole galaxies. Supernovae can also trigger star formation by compressing clumps of cold ISM, which thus collapse and recombine to form new stars. All heavier elements are created within stars or during supernovae and are distributed into the ISM through stellar winds and supernova explosions. Therefore, supernovae and stellar winds play a crucial role in the chemical composition of the ISM. Since the ISM is the material out of which future stars are being formed, its composition mirrors the composition of the next generation of stars. In this section, the evolution and properties of supernovae and supernova remnants will be discussed and basic information about their spectra and their identification will be given.

2.5.1 Supernovae

Some stars end their life in an enormous explosion: a supernova (SN). This name historically originates from their appearance as a new, bright star on the night sky, although in fact they represent the death of a star. A huge amount of energy of 10^{53} erg (or 10^{46} J) is released in such an explosion. Up to 99 % of this energy is carried away by neutrinos, while only $\sim 1\,\%$ (i.e. 10^{51} erg or 10^{44} J) is released as kinetic energy. In general, supernovae are caused by an enhancement of the stellar mass that finally leads to the instability of the star and to its subsequent explosion. According to their spectra and light curves, supernovae are separated into two major groups – type I SNe and type II SNe – which are in turn separated into different sub-groups. The main difference between the two groups of supernovae are hydrogen lines in their spectra, which are absent for type I SNe and present for type II SNe. From a physical point of view, supernovae can be separated into a group caused by the detonation of a white dwarf (type Ia SNe) and a group caused by the core-collapse of a massive star (all the rest).
In this section, the two physical (sub)groups of supernovae will be discussed, which are type Ia SNe and core-collapse SNe. The given information are based upon Unsöld and Baschek (1999), Seward and Charles (2010), and Vink (2012), where also further details can be found.

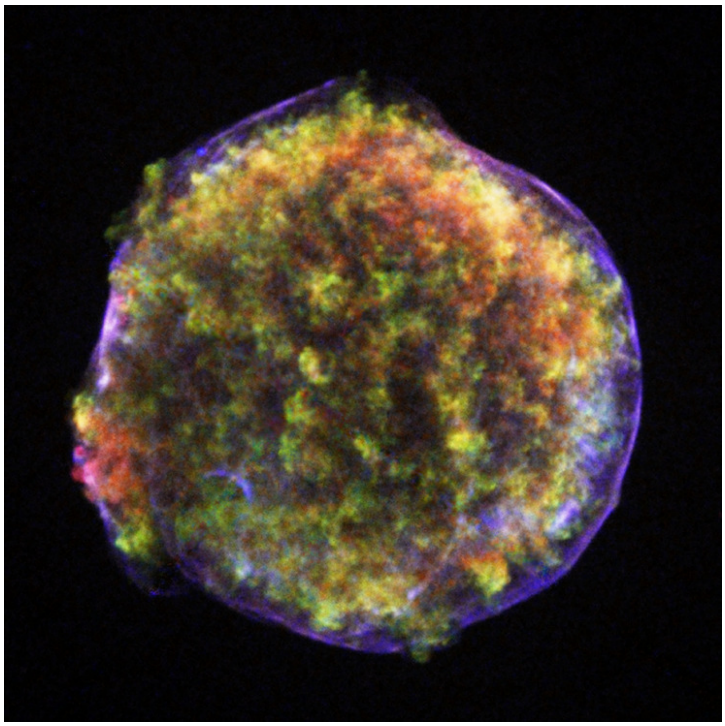

Figure 2.10: Tycho's SNR as imaged with *Chandra*. Visible are the stellar ejecta of the explosion (in red and green) which are shocked by the reverse shock, and synchrotron emission (in blue) originating from highly relativistic electrons which are accelerated through the forward shock. Credit: NASA/CXC/Rutgers/J.Warren & J.Hughes et al.

Type Ia SNe

Type Ia SNe are observed in all kind of galaxies, including old galaxies and galactic halos where no star formation occurs. Therefore, they are supposed to have old, less massive[6] progenitors. This also explains the absence of hydrogen lines in the spectra of these supernovae, since a star loses its hydrogen in the course of its evolution. Thus, white dwarfs[7] are believed to be the progenitors of this kind of

[6] Since the speed of evolution of a star scales with its mass, low-mass stars reach much older ages than high-mass stars.

[7] A white dwarf is the final stage in the evolution of a star which had an initial mass of $< 8\,\mathrm{M}_\odot$. These stars do not develop high enough temperatures to start carbon burning and therefore end their lives as cool white dwarfs, which mainly consist of carbon and oxygen. They have masses of $\sim 1\,\mathrm{M}_\odot$ and are Earth-sized ($R \approx 10^4\,\mathrm{km}$). Thus, they are compact objects with high densities of $\sim 10^{12}\,\mathrm{g\,m^{-3}}$. When the nuclear burning of these low-mass stars ends after He burning, its center starts to cool and gravity becomes the dominant force, leading to a contraction of the star that is only stopped by the degeneracy pressure of the electrons. This degeneracy pressure can be explained through the Pauli principle, which states that two

supernovae. The two most favored scenarios which lead to a type Ia SN are the mass accretion onto a white dwarf from a red giant – or in some cases also from a main-sequence star – in a close binary system, in which the initial masses of the stars where $\sim 1\,M_\odot$ and $\sim 3\,M_\odot$, and the merger of two white dwarfs in a white dwarf-white dwarf binary system.
When the mass of the white dwarf is enhanced beyond the Chandrasekhar limit, the degeneracy pressure of electrons is no longer capable of stabilizing the white dwarf against gravitational collapse. Subsequently, the white dwarf collapses, which increases its temperature to a point where C/O burning can take place. Since a white dwarf consists almost exclusively of carbon and oxygen, the burning deflagrates throughout the white dwarf within seconds. This enormous release of energy completely disrupts the white dwarf, and thus can be observed as a type Ia SN. In the sudden release of energy, radioactive ^{56}Ni is created, whose decay is responsible for a slow, exponential decrease of the light curve, since it causes the debris to glow.
Since this type of supernova is always ignited as soon as the Chandrasekhar limit is reached, i.e., when the white dwarf reaches a mass of $1.4\,M_\odot$, the light curves of these supernovae all look extremely similar and can be used to estimate the total luminosity and therefore the distance of a supernova. These light curves have a sharp maximum with luminosities of $\sim 10^9\,L_\odot$, which is reached after only ~ 2 weeks, followed by a quick exponential decay, which flattens with time. After typically ~ 55 days, the luminosity of the supernova has decreased significantly. Compared to core-collapse SNe, this type of supernova is much less frequent and shows a higher absolute magnitude in the optical energy band (Seward and Charles, 2010).

Core-collapse SNe

Core-collapse SNe are observed almost exclusively in the arms of spiral galaxies and in irregular galaxies – two places in which star formation occurs. Thus, since they are exclusively found in young galaxies and at the sites of star formation, they are believed to have young progenitor stars.
The light curves of core-collapse SNe show a broader, lower maximum than type Ia SNe and an exponential decay. In contrast to type Ia SNe, their light curves are more individual and differ from each other. This leads to the assumption of different progenitors for different core-collapse SNe. The underlying mechanism is assumed to be the core collapse of a massive star with an initial mass of $> 8\,M_\odot$. Depending on the initial mass and on the state of evolution at which the star becomes a supernova, different light curves are produced.

fermions cannot occupy the same quantum mechanical state. A white dwarf can be stabilized by degeneracy pressure only up to a mass of $1.4\,M_\odot$, which is called the Chandrasekhar limit.

The progenitor stars of core-collapse SNe are massive enough to perform the whole chain of nuclear burning, from H-, He-, C-, Ne-, O-, to Si-burning, during its lifetime. As an end product of Si-burning, ^{56}Fe is produced, which possesses the maximum binding energy of all elements. Therefore, no Fe-burning occurs, since a further fusion would not lead to an energetically preferred state. At this stage, the star possesses a degenerate Fe-core, which has a mass of $\sim 1\,\mathrm{M}_\odot$ and the density of a white dwarf. As Si-burning continues in a shell around the core, the Fe-core permanently gains mass, until the Chandrasekhar limit is exceeded and the degeneracy pressure of the electrons can no longer support the core against gravity. Consequently, the core starts to contract, which leads to an increase of its temperature. This leads to the decomposition of iron into lighter nuclei, through which energy is consumed and free protons are produced. These protons can combine with electrons through the inverse beta-decay, producing neutrons and neutrinos. The number of electrons which stabilize the core against gravity is thus reduced. In addition, the neutrinos leave the star and carry away energy which would otherwise support the core through thermal pressure. This leads to a runaway process in which the core collapses to a neutron star, which is stabilized through the degeneracy pressure of the neutrons. The collapsed core has a radius of $\sim 10\,\mathrm{km}$ and an extreme density of $\sim 10^{20}\,\mathrm{g\,m^{-3}}$, similar to the density within the nucleus of an atom. The collapse of the core occurs within seconds, and the thus unsupported shell of the star falls onto the neutron star, which in turn bounces due to the rapid collapse and catapults the infalling matter outside. The shell of the star is expelled, and a shock wave is moving outwards, which is a consequence of the energy loss through neutrinos escaping the core. If this shock wave reaches the surface of the star (i.e. if the star was not too massive), it blows away the stellar envelope and no further mass accretion can occur onto the neutron star. Otherwise, if the star was so massive ($\gtrsim 40\,\mathrm{M}_\odot$) that the shock front does not succeed to blow away its shell, further mass can be accreted onto the neutron star, until the mass limit of $\sim 2\,\mathrm{M}_\odot$ is reached. Above this limit, the degeneracy pressure of the neutrons cannot stabilize the neutron star against gravity anymore and the neutron star collapses to a black hole.

By studying supernovae, much information can be obtained about the progenitor stars and about the ambient ISM. Thus, studies about the evolution of the light curves of supernovae and the spectra of SNRs provide information about the distribution and composition of the ISM around the progenitor star and about the matter the progenitor lost in stellar winds. Out of this, conclusions can be drawn upon the properties of the progenitor at the time of the explosion. Furthermore, it provides a test for stellar evolution theories. For example, some neutrinos of SNR 1987A were detected, which occurred in the Large Magellanic Cloud. The measured neutrino flux was in agreement with core-collapse SNe models, which provided an excellent test for the appropriateness of these models.

Table 2.3: Comparison of H II regions, wind-blown bubbles, and supernova remnants.

	H II regions	Wind-blown bubbles	SNRs
Temperature	gas inside bubble: $\sim 10\,000\,\mathrm{K}$	shocked stellar wind: $\sim 4 \times 10^7\,\mathrm{K}$	initial: $\sim 6 \times 10^7\,\mathrm{K}$
Radius	100 pc	~ 10 pc	some pc – 50 pc
Typ. density of ambient ISM	10^2 particles/cm^3	10^2 particles/cm^3	1 particle/cm^3
Ionization mechanism	photo ionization	photo ionization	shock ionization
Reverse shock	no	yes	yes
Distribution of	gas inside bubble: homogenous	shocked stellar wind: (almost) homogenous	shocked ejecta & shocked stellar wind: inhomogeneous, in shell
Mass input by star	none	continuous	instantaneous
Energy input	continuous	continuous	instantaneous
Expansion velocity	initial: 2 000 km/s, typical: 20 km/s	stellar wind: 2 000 km/s, typical: 20 km/s	initial: 5 000 km/s, typical: 200 km/s

2.5.2 Evolution and Properties of SNRs

Comparison of SNRs and Wind-Blown Bubbles

The basic structure of an SNR is very similar to that of a wind-blown bubble as discussed in Section 2.3 and shown in Figure 2.5, with the difference that the unshocked and shocked stellar winds of regions *a)* and *b)* are replaced by unshocked and shocked ejecta of the explosion. The 'bubble' which is blown through a supernova explosion is called a supernova remnant. Despite many similarities between wind-blown bubbles and supernova-blown bubbles (i.e. SNRs), there are also some distinct difference (see Table 2.3 for an overview). In contrast to the energy input of wind-blown bubbles in which a constant stellar wind blows for several million years, the energy of a supernova is released instantaneously into the ambient ISM. Furthermore, the amount of energy differs: the energy which is

released by a supernova explosion is the same as 100 O-stars release through their stellar winds within 300 000 yr. In addition, the typical density of the ambient ISM differs between wind-blown bubbles (100 particles/cm^3) and supernova remnants (1 particle/cm^3) due to the different stage of evolution of the star. The lower ambient density of SNRs causes longer cooling times and therefore, the consideration of the adiabatic phase becomes necessary, before the SNR shell becomes radiative. For wind-blown bubbles, this adiabatic phase is so short that it was omitted in their discussion in Section 2.3.
Another difference is that wind-blown bubbles expand with a velocity which is supersonic in respect to the ambient ISM, but subsonic in respect to the ionized gas inside the bubble. This allows for a homogeneous pressure inside the bubble. This changes for SNRs, in which the expansion velocity is larger than the speed of sound for both the ambient ISM and the hot gas in its interior. This allows for a pressure gradient within the SNR. In SNRs, the hot gas lies therefore mainly in a thin shell within its interior and consists of shocked ISM and shocked ejecta, while superbubbles can be assumed to be completely filled with hot gas. This is also a consequence of the different age of both types of objects: while SNRs have an age of $\lesssim 10^5$ yr and are often observed at much younger ages, superbubbles form during the evolution of a population of stars and can therefore have an age as high as several 10^6 yr.

Phases of SNR Evolution

The evolution of an SNR can be separated into three different phases, which are introduced in this section. The underlying physics of shocked ISM have been introduced in Section 2.1.2 and shall be applied here for supernova remnants.

Free Expansion Phase

The first phase in the evolution of an SNR is the free expansion phase, in which the SNR can be found for the first couple of hundred years after the supernova explosion. In this phase, the ejecta of the explosion move freely into the ambient interstellar medium and sweep it up without taking notice of it, since the mass of the swept-up medium is less than the mass of the ejecta ($\sim 4\,M_\odot$). During this phase, the expansion velocity of the SNR of $\sim 5\,000$ km/s does not change and the temperature within the remnant stays constant. After ~ 600 yr, the swept-up mass of ISM equals the mass of the ejecta, and the SNR, which has now a radius of $\sim 3\,\mathrm{pc} - 4\,\mathrm{pc}$, enters the adiabatic phase.

Adiabatic Phase

In the adiabatic phase, which is also called the Sedov phase, the SNR starts to 'feel' the swept-up mass of ISM, which has now a non-negligible mass and stands in

its way of expansion. Through this swept-up mass, ejecta are decelerated and the following ejecta bump into this decelerated material, which causes a reverse shock to move in reverse direction. The same structure is formed as for wind-blown bubbles as described in Section 2.3. Only the shocked material is hot, i.e. the material between the forward and the reverse shock. Shocked ejecta and shocked ISM get mixed up due to turbulence, and Rayleigh-Taylor instabilities can form which can be observed as clumps. These instabilities, which cause a mixing of two fluids of different densities, occur at the contact discontinuity between the shocked ejecta and the shocked ISM (see Sect. 2.3).
In this phase, which lasts $1-2\times10^4\,\mathrm{yr}$, the properties of the SNR can be calculated by using the Sedov solution (see following section). The expansion occurs adiabatically, since the radiated energy is negligible compared to the total energy of the SNR. This changes in the last evolutionary phase, which is called the radiative phase.

Radiative Phase

In this phase, the SNR has cooled down so far ($<10^6\,\mathrm{K}$) through its expansion that it enters now a temperature regime in which cooling becomes very efficient (see Sect. 2.1.1). As a consequence of the lower temperatures, heavy ions and electrons starts to recombine, which enables radiative cooling through line emission. The lower temperatures cause the shell to become thinner, which in turn increases the cooling through the increased densities. This leads to a thin, dense shell which radiates in optical wavelengths. In this phase, which lasts $\sim10^5\,\mathrm{yr}$, the SNR radiates away its energy until its velocity and temperature become similar to the turbulent velocity and the temperature of the ISM. Thus, the SNR finally merges with the ISM and dissolves.

Sedov-Taylor-von Neumann Similarity Solution

Enormous explosions like supernovae or atomic bombs can be described by a blast wave model which predicts their basic parameters and their evolution. The standard model for this is the Sedov-Talyor-von Neumann similarity solution (in short: Sedov solution or Sedov model) which has been independently developed by Taylor (1950), von Neumann (1947), and Sedov (1959). It describes the adiabatic phase of an explosion and is valid at any time and radius. In the Sedov model, the evolution of an SNR in its adiabatic phase – or of an explosion in general – depends only on the initial energy E_0 of the explosion and on the density n_0 of the ambient medium. Out of these parameters, further properties like the time passed since the explosion or the swept-up mass of the ambient medium can be determined. In the adiabatic phase, not much energy is radiated away, so that the whole energy of the explosion can be assumed to be enclosed within and inside the shock front.

Energy conservation is the underlying principle of the mathematical description of this phase. (This changes in the radiative phase, in which the calculations are based upon momentum conservation.) In addition to adiabaticity, further necessary assumptions are

- a point-like release of the energy, i.e. a point explosion;
- a spherical symmetric shock front, indicating a homogeneous medium, i.e. an one-dimensional problem; and
- a monatomic ambient gas, i.e. the absence of, e.g., rotational energy states.

The Sedov model allows the connection between the initial energy of the supernova explosion, the age of the SNR, and its radius. This relation is described through

$$R_{\mathrm{SNR}} = \left(\frac{2.02 E_0 t_{\mathrm{SNR}}^2}{\bar{m}_{\mathrm{n}} n_0} \right)^{1/5} , \tag{2.7}$$

with the following definitions:

R_{SNR} : radius of the SNR,
E_0 : initial energy of the supernova explosion,
t_{SNR} : age of the SNR,
$\bar{m}_{\mathrm{n}}$: mean mass per nucleus,
n_0 : pre-shock density of nuclei.

Further, the shock velocity v_{S} can be determined through the relation

$$v_{\mathrm{S}} = \frac{2}{5} \frac{R_{\mathrm{SNR}}}{t_{\mathrm{SNR}}} . \tag{2.8}$$

Thus, only the initial energy E_0 of the explosion and the density n_0 of the ambient medium are required to determine the basic parameters of an SNR, like its radius, age, and the shock velocity. Out of these parameters, further properties like the swept-up mass of the ambient medium can be determined.

Temperature Equilibration and Collisional Ionization Equilibrium

The concepts of temperature equilibration and collisional ionization equilibrium (CIE) are important to be considered in the study of SNRs, since they influence the interpretation of the observed spectrum. Temperature equilibration (i.e. thermal equilibrium) exists, when the ion temperature corresponds to the electron temperature of the plasma. If, in addition to temperature equilibration, the ionization states of the ions correspond to their temperature (i.e. to their kinetic energy), then the plasma is in CIE. A plasma can be in temperature equilibration long before CIE takes place. The reason for this is the extremely large mean free path (in the order of 100 pc) for the particles in the warm and hot ISM, which leads to

low ionization rates, since ionization occurs through collisions. The time needed for a plasma to create CIE depends on the temperatures and the densities of the different species of particles present in the plasma. When these parameters are disturbed by a shock, both CIE and temperature equilibration are destroyed and replaced by collisional non-equilibrium ionization (NEI). This can be understood easily:
A shock which runs through a low-density medium like the warm and hot ISM is a collisionless shock, in which the energy is transmitted only through the magnetic field. The shock can increase the temperature (i.e. the velocity) of the particles only until the thermal velocity of a species of particles is about the same as the shock velocity (Heiles, 1964). Since the thermal velocity v_{thermal} of a species is proportional to $\sqrt{(k_{\mathrm{B}}T)/m}$ and therefore increases with the temperature T and decreases with the mass m of the species, the ions can reach temperatures which are, e.g., $\sim 1\,800$ times higher for protons than for electrons, owing to their different masses. In consequence, the ions gain much more kinetic energy through the shock than the electrons, and thus, temperature equilibration (i.e. thermal equilibrium) between the ions and electrons is destroyed. The electrons can thus create an ionization state which only corresponds to the electron temperature, but not to the much higher ion temperature. Thus, the ionization stage does not correspond anymore to the temperature of the ions, and with this, ionization equilibrium is destroyed.
With time, the electrons gain slowly higher temperatures through collisions with the ions, until thermal equilibrium is restored. Now, further ionization can occur through the electrons and finally, CIE is restored. The time needed for this depends on the temperature and on the density of the gas and is usually longer than typical SNR ages (Shklovskij, 1969), so that in most SNRs, CIE is not or only partially re-established.
In X-ray spectral analysis, NEI is important to be considered when fitting ionization lines and X-ray continua, since otherwise, the deduced electron and ion temperatures will be wrong. Furthermore, the degree of re-established CIE provides information about the time passed since the shock occurred, or about the density of the gas.

A first indicator of how well CIE has been re-established again is given through the ionization time scale τ, which is the product of the time passed since the explosion and the electron density. It is often a parameter in NEI models (e.g. in the *vpshock* and *vnei* models of Xspec). A low ionization time scale of $\tau \approx 10^{10}\,\mathrm{s\,cm^{-3}}$ indicates a poorly re-established CIE, while a high value of $\tau \approx 10^{12} - 10^{13}\,\mathrm{s\,cm^{-3}}$ implies a well re-established CIE. Smith and Hughes (2010) provided a maximum-ionization time scale plot for different elements which can be used for comparison with fitted X-ray temperatures and ionization time scales. Through this, they provided a mean to decide how well collisional ionization equilibrium has been

re-established and which ions are most meaningful in a certain temperature and time scale regime. They state that for most ions, ionization equilibrium is already re-established at an ionization time scale τ of some $10^{12}\,\mathrm{s\,cm^{-3}}$, and not only at some $10^{13}\,\mathrm{s\,cm^{-3}}$ as formerly assumed.

A way to test for temperature equilibration is given by Itoh (1978). He provided a method to estimate a lower limit for how well temperature equilibration is re-established. This can be used to calculate a limit for the properties of an SNR in its adiabatic phase in the case of an incompletely re-established temperature equilibration. Itoh took the Sedov solution as a starting point and assumed that electrons are not heated much in the shock front, resulting in a two-fluid blast wave model. The calculations are done for a homogeneous ISM with the chemical composition of the Milky Way taken from Allen (1973). When the results of these calculations are used for extragalactic SNRs like SNR B0543-68.9 (see Sect. 6.5.1), resulting estimates should be handled with caution and be regarded as approximations, since the differing extragalactic abundances are not taken into account and might have an impact on the resulting lower limit for temperature equilibration.
Itoh shows that in a two-fluid blast wave model, the fitted X-ray temperature $T_{\mathrm{x,SNR}}$ and the average electron temperature $< T_{\mathrm{e}} >$ can be considered to be equal. Normalized to the mean post-shock temperature T_{S}, the ratio f_{T} can be calculated:

$$\frac{< T_{\mathrm{e}} >}{T_{\mathrm{S}}} \approx \frac{T_{\mathrm{x,SNR}}}{T_{\mathrm{S}}} := f_{\mathrm{T}}\,. \tag{2.9}$$

Itoh obtained the ratio f_{T} by determining the intersection point of the curve for Coulomb interaction, $< T_{\mathrm{e}} > /T_{\mathrm{S}}$, with the curve defined by $T_{\mathrm{x,SNR}}/T_{\mathrm{S}} = 0.043 T_{\mathrm{x}}(R_{\mathrm{SNR}} n_0)^{-1/2}\nu^{7/5}$, derived from the Sedov solution, with $T_{\mathrm{x,SNR}}$ in $10^6\,\mathrm{K}$, the radius R_{SNR} in pc, and the reduced time variable $\nu = t_3(n_0^8/E_{51}^3)^{1/14} < 12$, with t_3 being the time since the explosion in units of $10^3\,\mathrm{yr}$, E_{51} the initial energy of the explosion in $10^{51}\,\mathrm{erg}$, and n_0 the pre-shock density in $\mathrm{H\,cm^{-3}}$. The ratio f_{T} indicates how well temperature equilibration has been re-established again, with $f_{\mathrm{T}} = 1$ implying a well-established temperature equilibration. Lower values of f_{T} indicate that the electron temperature is still below the mean post-shock temperature, which means temperature equilibration is not yet re-established. Equation 2.9 can be used to substitute the shock temperature with the fitted X-ray temperature in the equations discussed in the previous section and thus determine a limit for the SNR properties in the case of NEI. The two methods introduced in this section have been used in the studies of SNR B0543-68.9 performed within the scope of this thesis (see Sect. 6.5.1).

Cosmic Ray Acceleration in Supernova Remnants

An SNR can lose a considerable amount of its energy through high-energetic particles which leave the SNR after being accelerated to relativistic velocities. The thus dissipated energy can be as much as 50% of the kinetic energy of the SNR and leads to an explicitly lower temperature of its thermal gas (Borkowski et al., 2001).
A way to accelerate particles to such high velocities is provided by the first order Fermi mechanism. This is a mechanism in which high-energetic, charged particles are accelerated by magnetic inhomogeneities in the shock to highly relativistic velocities and become cosmic rays. Requirements for this mechanism are the presence of high-energetic particles as well as turbulences in the magnetic field in front of and behind the shock front of a collisionless shock. These are shocks which have a much smaller width than the mean free path of the material into which they move. This is the case in most phases of the ISM, and all shocks discussed in this chapter are collisionless. In such a shock front, the interaction of the particles occurs through the magnetic field instead of Coulomb collisions. Due to the lack of collisions, the energy of the particles is not distributed thermally during the shock, and single particles can consequently gain an energy which is much higher than the thermal energy of the gas. During the Fermi mechanism, these particles are reflected back and forth across the shock front by diffusion. Since these particles gain energy with each transition of the shock front, they finally reach relativistic velocities. While electrons which are accelerated through this mechanism to energies in the GeV range (10^{12} eV) emit synchrotron radiation in the radio regime, X-ray synchrotron radiation is emitted by electrons in the TeV range (10^{15} eV), which can be observed as non-thermal emission from SNRs.

2.5.3 Diagnostics of SNRs

An SNR emits in a wide range of wavelengths – from radio to TeV emission. It emits a continuum of thermal bremsstrahlung which has its bulk emission in X-rays. Line emission can be observed especially in optical wavelengths through forbidden-line emission and in soft X-rays. Non-thermal radiation can be observed in particular in young SNRs due to synchrotron radiation emitted by high-energetic electrons which have been acceleration by the magnetic field (see Sect. 2.5.2). If a pulsar is located within the SNR as a remainder of the stellar explosion, a pulsar wind nebula is another source of non-thermal X-ray emission. It can be observed in the energy range of X-rays up to TeV due to synchrotron radiation of relativistic electrons, which are accelerated through interaction with the pulsar's strong and quickly rotating magnetic field.

Observational Indicators of SNRs

For the analysis of SNRs, multi-frequency studies of soft X-ray, optical, and radio data is most useful, since they provide an overview of the hot, the warm, and the cold phase of the ISM. As discussed in Sections 2.1.2 and 2.5.2, an SNR comprises all three phases, since it consists of a hot bubble which sweeps up a shell of warm and cold ISM around it.

There are three main indicators which can be used to identify an SNR and to distinguish it from objects which show similarities in their observational data, like H II regions and superbubbles. The first indicator of an SNR is the presence of diffuse X-ray emission. This emission is produced by the shocked ISM and the shocked ejecta within the SNR, which reach temperatures of several $10^6 - 10^7$ K (see Sect. 2.5.2). This diffuse X-ray emission is already sufficient to distinguish SNRs from H II regions, which appear similar in optical wavelengths, but show no X-ray emission (see Sect. 2.2). A second indicator is the observation of non-thermal radio synchrotron emission of electrons. Due to the lower shock strength, this emission is usually not found in superbubbles and can therefore be used to distinguish them from SNRs. The third indicator of an SNR is an enhanced flux ratio of the [S II] to the Hα emission line. Such an enhanced ratio with a value of > 0.67 indicates shock-ionized material, in contrast to photoionized material, which typically shows lower ratios (Fesen et al., 1985). These three indicators have been used within the scope of this thesis to identify and study SNR B0543-68.9, as described in Section 6.3.

Spectral Diagnostics in X-rays

The X-ray spectrum of an SNR is determined by two major features: continuum emission and line emission. The continuum emission is created by recombination emission, two-photon emission, and thermal bremsstrahlung. The slope of the continuum helps to determine the temperature of the plasma: since it is created through thermal emission, the spectrum gets steeper with higher plasma temperatures.
Below ~ 2 keV, the spectrum is dominated by line emission and by interstellar absorption, which causes a decrease of the spectrum at low energies. The emission lines originate from abundant elements like C, N, O, Ne, Mg, Si, S, Ca, Fe, and Ni. Many hydrogen- and helium-like ions are present in SNRs, i.e. elements which are highly ionized, with only one or two remaining electrons. If the resolution of the spectrum is well enough, these lines allow to draw conclusions about the chemical composition of the ISM and – for young remnants – of the ejecta of the star. They are also means of estimating the temperature and the ionization state

Figure 2.11: Image showing the LMC in optical wavelengths. The 30 Doradus region, which is shown in Figure 2.1, is visible as a bright area in the upper left of the galaxy's bar. Credit: ESO.

of the gas through the examination of line ratios, if these lines are sensitive to the temperature or the ionization time scale. If they are not, they can be used to estimate the degree of interstellar absorption (Hamilton et al., 1983).

SNR Observation in the Large Magellanic Cloud

The Large Magellanic Cloud (LMC) – our neighbor galaxy – represents a perfect site for the observation of SNRs, superbubbles, supergiant shells, and the ISM in general. It is a dwarf SB type[8] galaxy with indications for a spiral structure (see Fig. 2.11). The LMC is rich of ISM and harbors many sites of supernova explosions and star formation. It is a satellite galaxy of the Milky Way and our closest neighbor with a distance of $\sim 50\,\mathrm{kpc}$ (Pietrzyński et al., 2013). Many observations of the LMC are available in various wavelength regimes, and due to its proximity, the its ISM can be well resolved. With a diameter of $\sim 10\,\mathrm{kpc}$, it has only 1/10 of the Milky Way's size. Since it is orientated almost face-on in respect to us and is located at low Galactic latitudes, it can be well observed from the Earth without significant absorption of the soft X-rays emitted by SNRs,

[8] SB type galaxies are galaxies which show a spiral structure as well as a central bar.

superbubbles, and supergiant shells. Within the Milky Way, these objects are difficult to observe since the Galactic disk causes interstellar extinction and often completely absorbes this soft emission. The LMC is therefore a perfect site for the study of these objects, since the observations are not disturbed by heavy extinction by neither the Milky Way nor the LMC.

In this Chapter, an introduction about the interstellar medium and about some of its manifold manifestations were given. After discussing its basic properties, with special emphasis on cooling and heating processes and on shocked ISM, a closer look on H II regions, wind-blown bubbles, and supernova remnants was taken. In the following Chapter, the X-ray satellite *XMM-Newton* will be introduced, whose data was used within the scope of this thesis to perform the X-ray studies of supergiant shell LMC-SGS 2, SNR B0543-68.9, and the DEM L299 superbubble.

Chapter 3

The *XMM-Newton* Space Observatory

The **X**-ray **M**ulti-**M**irror space observatory *XMM-Newton* (Jansen et al., 2001) is an X-ray satellite launched and operated by the European Space Agency (ESA), which is observing the Universe in X-rays for already more than 14 years. Its high timing and moderate spatial and spectral resolution allows imaging spectroscopy of bright and variable sources, and an optical telescope on board the satellite enables simultaneous X-ray and optical/UV observations. The satellite is able to perform high-resolution X-ray spectroscopy as well and is equipped with a large effective area which allows high sensitivity imaging. Through *XMM-Newton*, new insights have been gained in a great variety of astronomical fields like star formation, properties of neutron stars, and galaxy cluster evolution (e.g. Schartel, 2012). With its high sensitivity and large field of view, *XMM-Newton* is optimally suited for the observation of faint and extended sources like the interstellar medium.
In this Chapter, an overview of *XMM-Newton* is given, in which the instrumentation of the satellite is described. In the scope of this thesis, data of *XMM-Newton* has been used to perform the morphological and spectral X-ray analysis of the supergiant shell LMC-SGS 2 and the H II region DEM L299.

3.1 Set-Up and Instrumentation

XMM-Newton was launched on December 10, 1999 from Kourou in French Guiana and is since then performing astrophysical observations by orbiting around the Earth (Fig. 3.1). With a period of 48 hours, it follows a highly elliptic orbit with a perigee of $\sim$6 000 km and an apogee of $\sim$115 000 km (XMM-Newton Users Handbook, 2013), which corresponds to almost one third of the distance between the Earth and the Moon (see Fig. 3.2). This makes low-background observations possible, since the satellite is shielded against charged particles from the solar

Figure 3.1: Artist's impression of the X-ray observatory *XMM-Newton* orbiting around the Earth. Credit: Image courtesy of ESA.

wind through Earth's magnetosphere. At the same time, it is located outside of the Earth's radiation belts for the most part of the orbit. In addition, the large distance to the Earth in apogee allows long and uninterrupted observations since the time intervals in which observations are not possible because the Earth is too close to the FOV is relatively short.

One of the most outstanding features of *XMM-Newton* is the large geometric effective area of 1 500 cm^2 for each of its three X-ray mirror modules (Turner et al., 2001). Each X-ray mirror module consists of 58 nested Wolter-I (see Sect. 1.3.1) mirror shells (Fig. 3.3), with a diameter of 70 cm for the largest mirror shell and a minimum packing distance of 1 mm (Jansen et al., 2001). The X-ray mirror modules have a focal length of 7.5 m, with one detector of the European Photon Imaging Camera (see Sect. 3.1.3 for a more detailed description) situated at the focal point of each module. An illustration of the satellite's set-up is shown in Figure 3.4. Besides the European Photon Imaging Camera, there are two further scientific instruments on board *XMM-Newton*: the Reflection Grating Spectrometer (see Sect. 3.1.1) and the Optical/UV Monitor Telescope (see Sect. 3.1.2). All three instruments can be operated in parallel, allowing for simultaneous, time resolved X-ray and optical/UV imaging and spectroscopy. In the remainder of this section, an overview of *XMM-Newton*'s scientific instruments will be given, with special emphasis on the European Photon Imaging Camera (see Sect. 3.1.3), with which the X-ray data analyzed within the scope of this thesis have been taken. In addi-

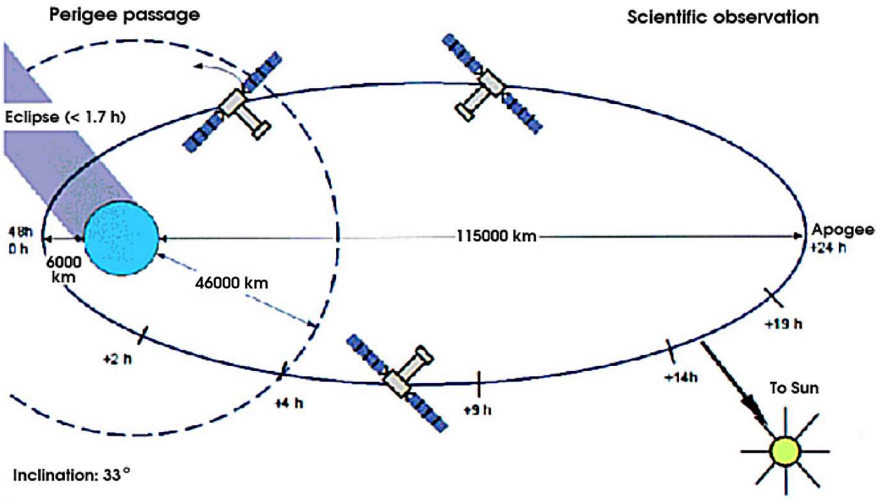

Figure 3.2: Illustration of the orbit of *XMM-Newton* around Earth. Credit: Dornier Satellitensysteme GmbH, (XMM-Newton Users Handbook, 2013).

tion, a discussion of the different background components of this camera can be found in Chapter 4.

3.1.1 Reflection Grating Spectrometer (RGS)

The Reflection Grating Spectrometer (den Herder et al., 2001) provides dispersed high-resolution spectra in an energy range of $0.3-2.1\,\mathrm{keV}$. It consists of two identical grating stacks located in the converging X-ray beam behind two of the mirror modules, and of a detector array of nine back-illuminated charge-coupled devices (CCDs) which can perform single-photon counting. Each grating stack diverts $\sim 50\,\%$ of the photon flux emanating from the mirror module (den Herder et al., 2001).

3.1.2 Optical/UV Monitor Telescope (XMM-OM)

The Optical/UV Monitor Telescope (XMM-OM, Mason et al., 2001) is an additional telescope on board *XMM-Newton* which enhances the observable range of the electromagnetic spectrum to optical/UV wavelengths and thus enables simultaneous observations in an energy range of $170-650\,\mathrm{nm}$ $(0.007-0.002\,\mathrm{keV})$ and X-ray wavelengths. It is located on the mirror support platform of the

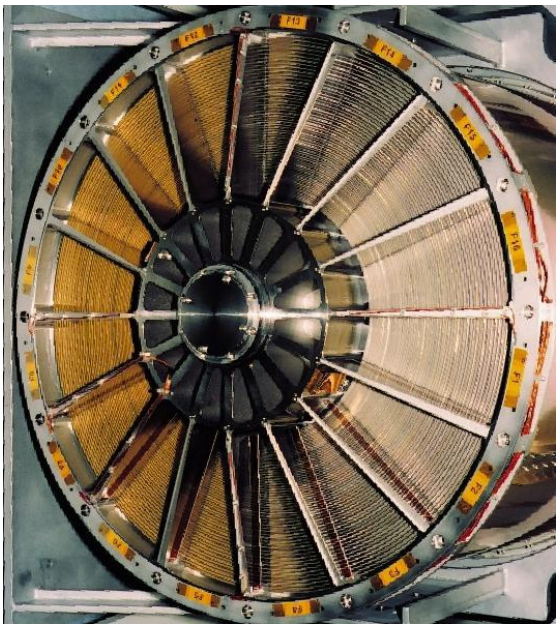

Figure 3.3: Image showing one of the three X-ray mirror modules of *XMM-Newton*. Each X-ray mirror module consists of 58 nested mirror shells. These Wolter-I mirror shells are gold-coated nickel shells with diameters ranging from 30.6 – 70 cm, a thickness of 0.47 – 1.07 mm, and a common length of 60 cm. The mirror shells are attached to a spider wheel for mechanical stability. Credit: Image courtesy of Dornier Satellitensysteme GmbH and ESA.

XMM-Newton Service Module and consists of a Ritchey Chrétien telescope[1] and a microchannelplate-intensified CCD[2] (Fordham et al., 1992).

3.1.3 European Photon Imaging Camera (EPIC)

The European Photon Imaging Camera (Strüder et al., 2001; Turner et al., 2001) provides time-resolved, high-sensitivity spectroscopy and imaging in an X-ray energy range of 0.15 – 15 keV. It consists of three CCD cameras: two EPIC-MOS cameras (Turner et al., 2001) and one EPIC-pn camera (Strüder et al., 2001). Each camera is located at the focal point of one of the three X-ray mirror modules and has a field of view (FOV) of $\sim 30'$. The sensitivity of each camera, which

[1] A Ritchey Chrétien telescope is a telescope whose mirrors – both the primary and the secondary one – are hyperbolic mirrors. This configuration is used to minimize optical errors.

[2] Microchannelplate-intensified CCD: Before the incident photons hit the CCD, they are converted to photoelectrons, which are amplified and afterwards reconverted to photons by a phosphor screen. Microchannel-plates are used to amplify the signal while maintaining the initial position of the incident photons.

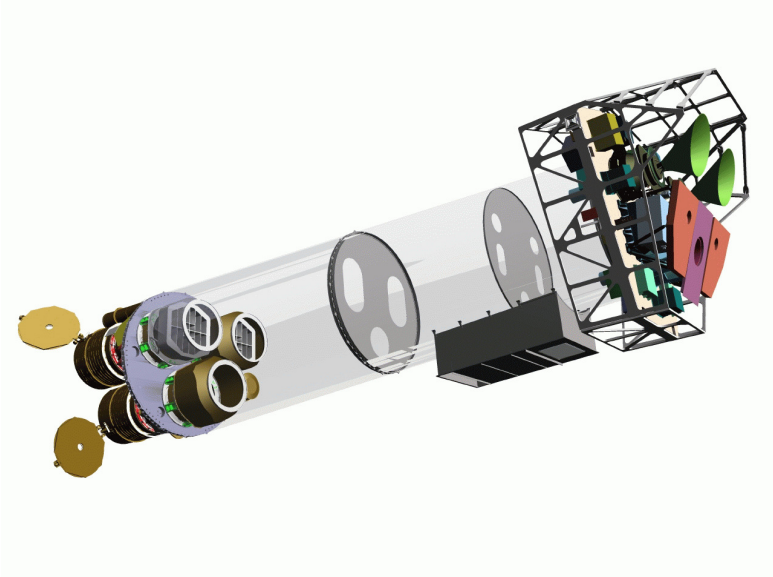

Figure 3.4: Schematic drawing of *XMM-Newton*. The spacecraft has a length of 10 m and an initial mass of $\sim 4\,000$ kg at the time of launch. On the left side of the image, the Service Module is visible which comprises the three X-ray mirror modules, the two grating stacks of the RGS, and the XMM-OM. A carbon fibre tube connects this module with the Focal Plane Assembly (visible on the right side), which contains the *XMM-Newton* EPIC and RGS detectors. Credit: Image courtesy of Dornier Satellitensysteme GmbH and ESA.

is defined here as the minimum detectable flux at $5\,\sigma$ after 10 ks of integration, is $\sim 10^{-14}\,\mathrm{erg\,s^{-1}\,cm^{-2}}$ in an energy range of $0.15-12$ keV, with the sensitivity being better for the EPIC-pn than for the EPIC-MOS due to its larger effective area (Watson et al., 2001). The point spread functions[3] (PSFs) of the telescopes have similar sizes of $\sim 6''$ full width at half maximum (FWHM) and a half energy width (HEW) of $\sim 15''$. While the EPIC-MOS cameras have the better spectral resolution (~ 70 eV at 1 keV for EPIC-MOS compared to ~ 80 eV at 1 keV for EPIC-pn), the EPIC-pn camera has a much higher maximum timing resolution of 0.007 ms than the EPIC-MOS cameras with 1.75 ms (XMM-Newton Users Handbook, 2013). All three cameras possess calibration sources for on-board calibration. A filter wheel is attached in front of each camera with filters of three different thicknesses to prevent optical and UV radiation from reaching the X-ray detectors. The filter wheels also possess an open position and a closed position

[3] The point spread function (PSF) of an imaging system describes the shape of the focused image of an observed point source. A measure for the PSF is either the full width at half maximum (FWHM) of the intensity distribution, or the diameter of the area in which 50 % of its energy is contained (HEW).

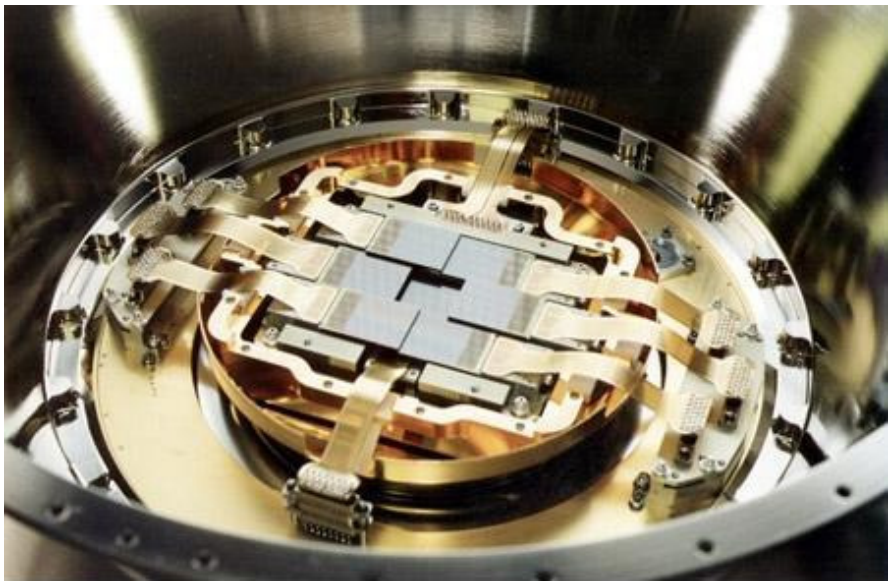

Figure 3.5: Image of one of the two EPIC-MOS detectors. The seven individual CCDs are visible in the center of the image. They are stepped with respect to each other to follow the focal plane curvature and to allow for an overlap of $\sim 0.3\,\mathrm{mm}$ to minimize the dead regions between adjacent CCDs. Credit: Image courtesy of Leicester University, University of Birmingham, CEA Service d'Astrophysique Saclay and ESA.

for calibration, background measurement, and for the protection of the detectors from damage in times of high soft proton background. A more detailed description of these cameras and of their similarities and differences is given in the following paragraphs.

EPIC-MOS Cameras

Two MOS (metal oxide semiconductor) cameras (EPIC-MOS1 and EPIC-MOS2) are part of the *XMM-Newton* EPIC instrument and detect X-rays in an energy range of $0.15 - 12\,\mathrm{keV}$[4]. They are situated in the focal points of those mirror modules which have the RGS grating stacks attached to them and therefore receive only 44 % of the reflected photons (XMM-Newton Users Handbook, 2013). Each EPIC-MOS detector consists of seven front-illuminated CCDs (see Fig. 3.5) with a size of $2.5\,\mathrm{cm} \times 2.5\,\mathrm{cm}$. Each CCD has 600×600 pixels with a pixel size of $40\,\mu\mathrm{m} \times 40\,\mu\mathrm{m}$, which corresponds to a FOV of $1\farcs1 \times 1\farcs1$ per pixel. To avoid that the gaps between single CCDs lie at the same position within the FOV, the EPIC-

[4] Scientifically useful energy range of the EPIC-MOS cameras: $0.2 - 10\,\mathrm{keV}$ (Turner et al., 2001).

MOS2 detector is rotated around its central CCD by an angle of 90° with respect to the EPIC-MOS1 detector[5].
For redundancy, each EPIC-MOS CCD has two readout nodes, each of which can be used to read out the whole CCD or half of it. Four different readout modes are available for the EPIC-MOS detectors:

- full frame mode: the whole detector is read out, with a time resolution of 2 600 ms;
- large window mode: 300×300 pixels of the central CCD are read out, with a time resolution of 900 ms;
- small window mode: only 100×100 pixels of the central CCD are read out, with a time resolution of 300 ms;
- timing mode: the information of only 100 pixel rows of the central CCD are read out quickly by loosing the spatial information within this row, with a time resolution of 1.75 ms.

The latter three modes affect only the central CCD of the EPIC-MOS detector, while the six peripheral CCDs are read out in the standard full frame mode. The window and timing modes are chosen only for the observation of bright sources which are either point sources or cover only a small fraction of the FOV, in order to avoid energy pile-up[6] and pattern pile-up[7].

The peripheral EPIC-MOS1 CCD6 was lost for scientific observations on March 09, 2005 most probably due to micrometeorite impact which scattered debris onto the focal plane. The same is presumed to have happened to the peripheral EPIC-MOS1 CCD3 on December 11, 2012. This led also to an increased noise level of EPIC-MOS1 CCD4. The remaining CCDs of EPIC-MOS1 remain fully operational for scientific studies (see XMM-Newton Users Handbook, 2013, for more information).

[5] The EPIC-pn detector is also rotated by an angle of 45° with respect to both EPIC-MOS detectors.

[6] Energy pile-up: If more than one photon hits the same pixel during the integration time, they are indistinguishable for the readout electronics. Consequently, they will be recorded as a single photon with the combined energy of the photons, which will lead to a distortion of the recorded spectrum and a too low measured photon flux. Pile-up occurs for bright sources with too high photon fluxes and can be avoided through shorter integration times.

[7] Pattern pile-up: Similar to energy pile-up, with the difference that in this case not the same but adjacent pixels are hit during the same integration time. This leads either to a rejection of the event due to an invalid resulting pattern, or to the false assumption that only one photon caused this pattern. Pattern pile-up has similar causes, effects, and remedies as energy pile-up.

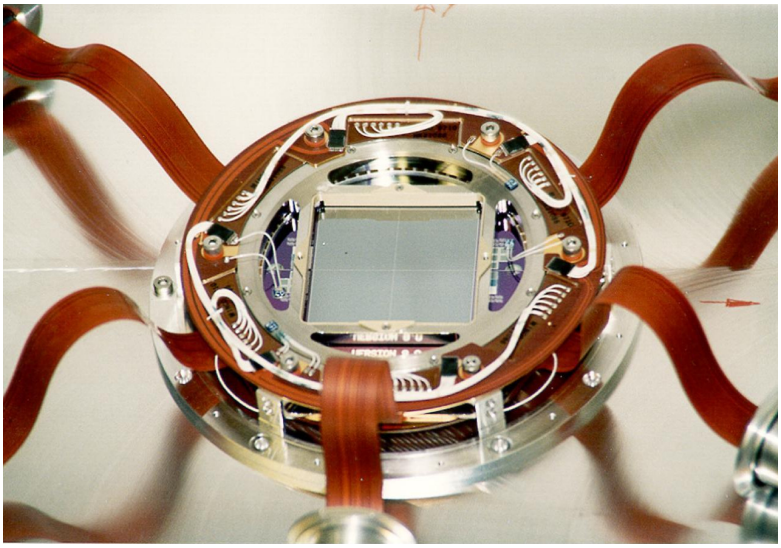

Figure 3.6: Image of the EPIC-pn detector of *XMM-Newton*. Visible is the connected 6 cm × 6 cm single silicon waver on which 12 CCDs are integrated, three of them in each quarter. Credit: Image courtesy of MPI-semiconductor laboratory, MPE; Astronomisches Institut Tübingen, Germany and ESA.

EPIC-pn Camera

The EPIC-pn camera has one pn-detector (see Fig. 3.6) which was developed under the leadership of the Max-Planck-Institute for Extraterrestrial Physics (MPE), Garching, Germany. Part of the readout electronics of the EPIC-pn detector was developed at the Institute for Astronomy and Astrophysics (IAAT) of the University of Tübingen.
The EPIC-pn detector is a fully depleted pn-CCD which is back-illuminated and operates in an energy range of 0.15 – 15 keV. The detector has a size of 6 cm × 6 cm and is a monolithic detector which has been created out of a single silicon waver hosting 12 integrated CCDs. Each CCD has a size of 1 cm × 3 cm and consists of 64 × 200 pixels with a size of 150 µm × 150 µm, corresponding to a field of view of $4\farcs1 \times 4\farcs1$ per pixel. A major difference to the EPIC-MOS cameras is that each pixel column of the EPIC-pn detector has its own readout node, resulting in 12 × 64 readout nodes, while each EPIC-MOS camera has 2 × 7 readout nodes. This enables a much faster readout of the EPIC-pn detector, which has even in full frame mode a very good time resolution of 73.34 ms. Having a ∼35 times better time resolution than the full frame mode of EPIC-MOS (XMM-Newton Users Handbook, 2013), the EPIC-pn detector is ideal for timing studies, while the EPIC-MOS detectors have the better spatial resolution due to their smaller pixel size.

Table 3.1: Overview of the properties of an *XMM-Newton* EPIC-MOS detector and the *XMM-Newton* EPIC-pn detector.

	EPIC-MOS	EPIC-pn
Energy range	0.15 – 12 keV	0.15 – 15 keV
FOV	30′	30′
Pixel size	40 µm	150 µm
PSF	14″(HEW)	15″(HEW)
Energy resolution	70 eV @ 1 keV	80 eV @ 1 keV
Max. time resolution	1.75 ms	0.007 ms
Illuminated from	front-side	back-side
Number of readout nodes	14	768

The EPIC-pn detector has six different readout modes:

- full frame mode: the whole detector is read out with a time resolution of 73.4 ms;
- extended full frame mode: similar to the previous mode, but has an extended integration time resulting in a time resolution of 199.1 ms, being ideal for the observation of extended sources;
- large window mode: only data from the inner half of each of the 64 pixel columns of each CCD is read out, while the outer half is used as a storage area, leading to a time resolution of 47.7 ms;
- small window mode: operates after the same principle as the large window mode, but with a much smaller window of 63×64 pixels in only one CCD, resulting in a time resolution of 5.7 ms;
- timing mode: the pixels in each pixel column of only one CCD are combined to macropixels with a size of 1×10 pixels which leads to a loss of the spatial resolution in one dimension, but improves the time resolution to 0.03 ms;
- burst mode: operates analogous to the timing mode, but with a macropixel consisting of 179 pixels, through which the spatial information of one dimension is completely lost, but the time resolution is further improved to 0.007 ms.

Depending on the readout mode, different percentages of so called 'out-of-time events' will be present in the data, ranging from 0.15 % in large window mode to 6.2 % in full frame mode, in disrespect of the two timing modes (Strüder et al., 2001). These out-of-time events occur when a photon hits the detector during the readout phase, in which the charges are shifted through the pixel column. When an event occurs during this phase, a false time stamp and position will be assigned to it (see Fig. 3.7). Since the EPIC-MOS detectors have much shorter transfer times than integration times, out-of-time events play a small role for data obtained

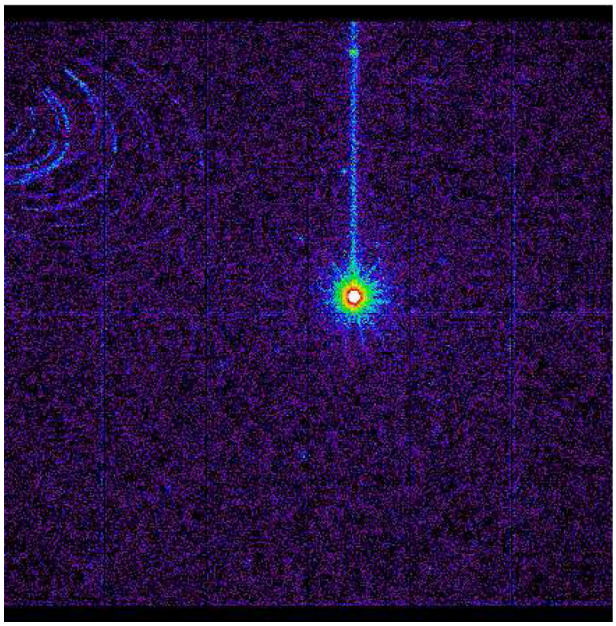

Figure 3.7: Example of out-of-time events in the reconstructed field of view of an EPIC-pn observation. The out-of-time events, which occur during the readout phase of the observation, are visible as streaks of enhanced emission originating from bright sources and running towards the readout nodes. In the upper left corner, stray light is visible as arc-like structures which are caused by a bright source lying just outside the FOV of the telescope. Credit: (XMM-Newton Users Handbook, 2013).

with the EPIC-MOS cameras. For the EPIC-pn detector, however, these out-of-time events make up a none-negligible fraction of the total number of events due to the considerably shorter integration times. These out-of-time events cannot be avoided and have to be accounted for statistically during data analysis.
A concluding summary of the properties of both the EPIC-MOS detectors and the EPIC-pn detector can be found in Table 3.1.

This chapter was aimed to provide an overview of the X-ray observatory *XMM-Newton*, whose data has been used for the spectral and morphological X-ray analyses which have been performed within the scope of this thesis. An introduction to the different science instruments on board the observatory has been given with a focus on the *XMM-Newton* EPIC instrument. In the following chapter, the different background components present in an X-ray observation and their subtraction or modeling during the analysis will be discussed as well as the data processing.

Chapter 4

Background Components and Data Processing of *XMM-Newton* Observations

Studying extended sources in X-rays provides many challenging tasks due to the often faint emission and the high level of both instrumental and astrophysical background present in the soft X-ray range. In addition, determining the local X-ray background is difficult, since the extended emission is often present in most of or in the entire FOV of an observation. In this chapter, the different background components of *XMM-Newton* EPIC observations are discussed and ways of reducing, eliminating, and estimating them during data processing or data analysis are presented. Further information about background handling can be found on the *XMM-Newton* background analysis web page[1] where also an overview[2] of the various background components is given. This chapter is based upon the information provided by these web pages, by Kuntz and Snowden (2008), and by the *XMM-Newton* ESAS cookbook (Snowden and Kuntz, 2011b).

The different background components of an *XMM-Newton* observation can be separated into three major categories: electronic background, photon background, and particle background. To handle these background components more efficiently, the *XMM-Newton* ESAS package[3] version 4.3 has been used within the scope of this thesis for the data processing of the X-ray data. The *XMM-Newton* ESAS package was developed by Snowden and Kuntz (Snowden and Kuntz, 2011b,a) and is part of the *XMM-Newton* Scientific Analysis System (SAS)[4]. It is a software package which has been developed to provide appropriate background subtraction

[1] `http://xmm2.esac.esa.int/external/xmm_sw_cal/background/`
[2] `http://www.star.le.ac.uk/~amr30/BG/BGTable.html`
[3] *XMM-Newton* ESAS: `http://xmm2.esac.esa.int/external/xmm_sw_cal/background/epic_esas.shtml`; `ftp://xmm.esac.esa.int/pub/xmm-esas/xmm-esas_4.3.pdf`
[4] SAS: `http://xmm.esa.int/sas/`

for the analysis of extended sources and diffuse emission, and for the creation of (mosaicked) images. It contains tasks for the removal of point sources, soft protons, and the quiescent particle background. By using these tasks and SAS tasks, it creates background subtracted spectra of user-defined regions and energy ranges of *XMM-Newton* EPIC observations. In addition, background-, exposure-, and vignetting-corrected images and mosaics can be produced for individual regions or for the whole FOV. The package also uses additional current calibration files (CCFs) which are not part of the standard CCFs and which contain filter wheel closed (FWC)[5], quiescent particle background, and soft proton calibration data. These additional CCFs are provided online[6]. While previous versions only included the handling of EPIC-MOS data, the *XMM-Newton* ESAS version 4.3 – used for the analyses of this thesis – is the first version which also includes tasks for the processing of data taken with the EPIC-pn camera.

4.1 Electronic Background

The electronic background of an *XMM-Newton* EPIC observation is created, for example, by the detectors and the readout electronics. Bad pixels, which can be either hot, dead, or flickering, can be handled by applying bad pixel maps, which are included in the *XMM-Newton* calibration files, available from the *XMM-Newton* calibration portal[7]. Readout noise is created due to statistical variations of the readout parameters like the number of photoelectrons or dark current. It is larger for quadruple, triple, and double events compared with single events, since it increases with the number of read-out pixels. Readout noise is mostly dominant at energies below $\sim 300\,\mathrm{eV}$ and is usually avoided by ignoring data points which lie below this energy threshold.
Another important component of the electronic background, which is irregularly observed in EPIC-MOS CCDs, are called anomalous states. These are states of an enhanced background level of individual EPIC-MOS CCDs. They manifest themselves as a plateau at energies $< 1\,\mathrm{keV}$ in the detected spectrum of an entire EPIC-MOS CCD (see Fig. 4.1). The origin of these states is unknown up to now, and the prevalent method of treating them is to exclude data from further analysis,

[5] Filter wheel closed observations: Observations which are performed with a closed photon entrance window of the detector. This is realized for *XMM-Newton* by an aluminum plate of 1 mm thickness which can be placed in front of the detector (Turner et al., 2001; Strüder et al., 2001). These observations are used for calibration and for the estimation of the electronic and quiescent particle background, since both X-ray photons and soft protons are blocked through the aluminum.

[6] *XMM-Newton* ESAS CCFs: `ftp://xmm.esac.esa.int/pub/ccf/constituents/extras/esas_caldb/`

[7] `http://xmm2.esac.esa.int/external/xmm_sw_cal/calib/`

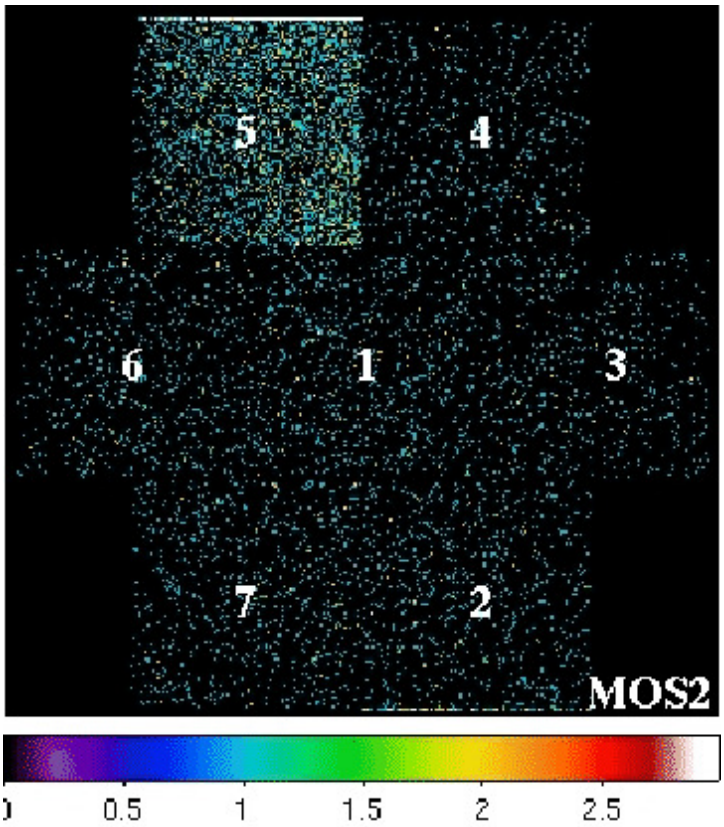

Figure 4.1: Event image of the EPIC-MOS2 detector in an energy range of 0.2 – 0.9 keV, taken from an observation during which an anomalous state occurred. EPIC-MOS CCD5 shows an enhanced background level in this energy range and can therefore be considered to be operating in an anomalous state. Credit: Snowden and Kuntz (2011b).

which originates from a CCD showing this anomaly during an observation. Since the identification of an anomalous state by eye is only possible for observations with long enough exposure times, a method was developed by Kuntz and Snowden (2008) and implemented into the *XMM-Newton* ESAS package which allows the systematic identification of most of these anomalous states, even for short exposure times. This method is based upon the observation that almost all anomalous states show a low hardness ratio and high count rates for the unexposed corners of the affected CCD. This method is implemented into the *XMM-Newton* ESAS task *mos_back*, which identifies affected CCDs. The call for all following *XMM-Newton* ESAS tasks provides the user with the possibility to deselect the particular CCDs and, therefore, to explicitly exclude them from the further analysis. This has also to be done with non-operating EPIC-MOS CCDs, of which the data cannot be used, e.g., due to a micrometeorite impact (see Sect. 3.1.3).

4.2 Particle Background

The particle background of *XMM-Newton* is created through particles present in the interstellar environment of the satellite. The major contributors to this background component are soft protons flares of the Sun and cosmic rays, which are discussed in this section.

4.2.1 Soft Proton Flares

Soft protons with energies of several 100 keV are emitted as flares from the Sun caused by magnetospheric reconnection events. These flares have a typical duration of minutes, while their frequency varies with the solar cycle. These soft protons can be funneled through the mirror shells of the telescopes of *XMM-Newton* onto its detectors. When they hit a detector and deposit energy, free electrons are created which are registered by the detector and thus mistaken as X-ray signals. Since these protons enter the telescope through the mirrors, they cannot hit the whole detector, but are limited to an area comparable to the FOV of the X-ray photons and are also vignetted. Since these soft proton flares are highly time-dependent, the largest part of them can be removed through light-curve screening. In the light curves, they can be recognized as a sudden increase in the count rate or as ripples in an otherwise flat light curve as expected in the observation of a non-variable source (see middle panel on the right side of Fig. 4.2). The flares can systematically be recognized by creating a count rate histogram as shown in the upper panels of Figure 4.2 which has been created with the *XMM-Newton* ESAS package for two observations which have been used for the analyses described in Chapter 5 and 6. For a constant source which is uncontaminated by soft protons, the count rate histogram can be described with a Gaussian, with its maximum lying at the nominal count rate of the observation (see upper left panel of Fig. 4.2). For an observation which is contaminated by flares, this Gaussian distribution is distorted and there is a tail towards higher count rates in the histogram (see upper right panel of Fig. 4.2). Data originating from times with count rates which deviate more than $\sim 2\,\sigma$ from the peak of the fitted Gaussian are believed to be created by flares and thus excluded from the further analysis. If the whole observation is heavily contaminated by flares, the data are often unusable for the study of diffuse emission. The light curve for the unexposed corners of an EPIC-MOS detector can be used to determine if the origin of the increased count rates are truly soft protons flares (see lower panels of Figure 4.2). This is the case if the flares are not seen in these corner light curves, since the soft protons are limited to the FOV of the detectors. If these light curves show the same increase in the count rate, they must be of different origin, e.g., from the

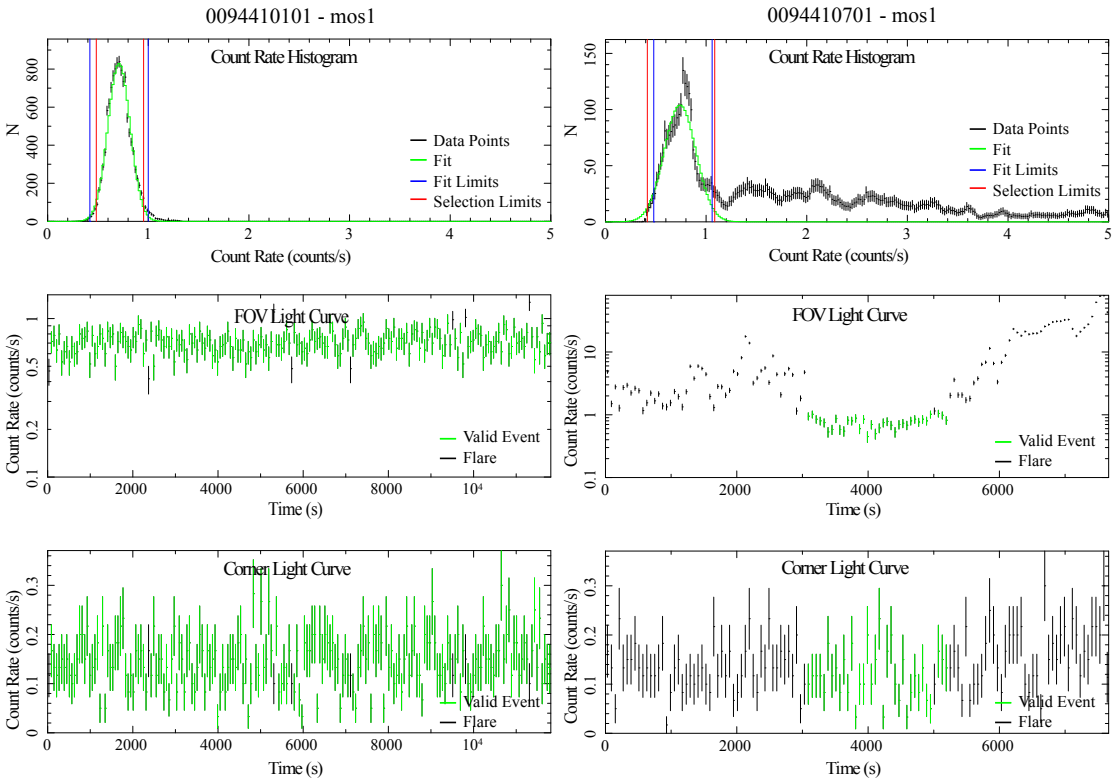

Figure 4.2: Output of the *XMM-Newton* SAS task *espfilt* for the EPIC-MOS1 detector for two observations used in the X-ray spectral analysis performed for this thesis. The left panel shows an observation (Obs.-ID: 0094410101) which is unaffected by soft proton flares, while the right panel shows a heavily contaminated observation (Obs.-ID: 0094410701). The upper plot of both panels show the count rate histogram for the whole FOV in the energy range of 2.5 – 8.5 keV. The green line shows the Gaussian which has been fitted to the data points lying between the blue lines. The red lines indicate the $\sim 2\,\sigma$ ranges of the fitted Gaussian. Data lying outside this range are dismissed as proton flares. The middle and bottom plots show the smoothed light curves of the FOV and of the unexposed corners of the detector, respectively. Both are created for the same energy range as the upper plots. Data points in the middle and bottom plots which are marked in black are assumed to be created by flares and are therefore excluded from the further analysis, while green data points mark useful events.

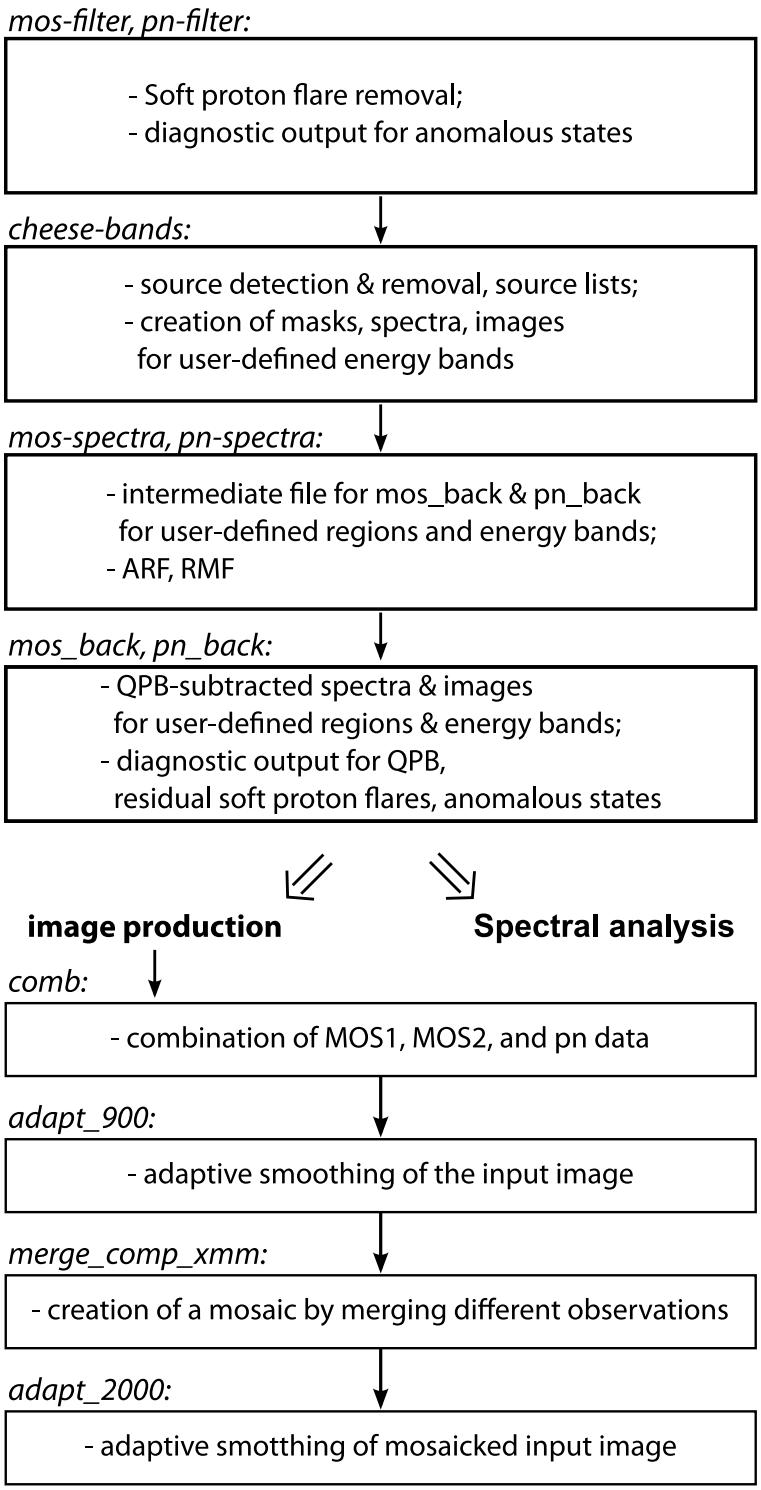

Figure 4.3: Overview of the basic *XMM-Newton* ESAS tasks which have been used for the processing of the *XMM-Newton* EPIC data.

quiescent particle background (see Sect. 4.2.2) or electronic noise (see Sect. 4.1).[8] Plots as shown in Figure 4.2 are provided by the *XMM-Newton* SAS task *espfilt*. This task is called by the *XMM-Newton* ESAS tasks *pn-/mos-filter*, which take care of the cleaning of the data and remove background events (see Fig. 4.3 for an overview of the most important *XMM-Newton* ESAS tasks).
However, residual soft proton flares often remain in the data, since they can also vary over longer time scales and can therefore be missed during light-curve screening (Kuntz and Snowden, 2008). These residual flares cannot be removed from the data, but have to be modeled during the spectral analysis (see Sect. 5.4).

4.2.2 Quiescent Particle Background

The quiescent particle background (QPB) is induced by cosmic rays[9] and originates either from the direct interaction of these high-energetic particles with the detector or from fluorescence lines. These lines are created when cosmic rays interact with the material of the satellite and excite a bound electron, which subsequently emits photons while de-exciting to its ground state. In the resulting spectrum of an observation which is affected by this background component, the quiescent particle background can be seen as a continuum with strong line emission. The energy, intensity, and distribution of the fluorescence lines measured by the detectors depend strongly on the material located in the immediate vicinity of the detectors. Therefore, the detected fluorescence lines have a strong spatial dependence which is different for each CCD (see Fig. 4.4). This strong spatial dependence should be considered when selecting a spectral extraction region in order to estimate the local background.
Since cosmic rays are able to penetrate the material of the satellite due to their high energies, the quiescent particle background is not limited to the field of view of a detector, but is distributed over the whole detector surface. Therefore, this background component can also be seen on the unexposed corners of the detectors and in observations with a closed filter wheel (FWC).
Apart from the strong spatial dependence, the quiescent particle background also shows a (slow) temporal variation, depending on the cosmic ray flux. This flux is lower in times of high solar activity, since the enhancement of the solar magnetic field and the subsequent extension of the magnetosphere deflect the charged cosmic rays more efficiently and therefore shield the satellite from their impact.

[8] This is only valid for the EPIC-MOS detectors, since the unexposed corners of the EPIC-pn detector will also show increased count rates due to out-of-time events (see Chapt. 3 for more information about out-of-time events).

[9] Cosmic rays: High-energetic particles of Galactic or extragalactic origin, which are mainly protons or the nuclei of fully ionized heavier particles, high-energetic photons, and electrons.

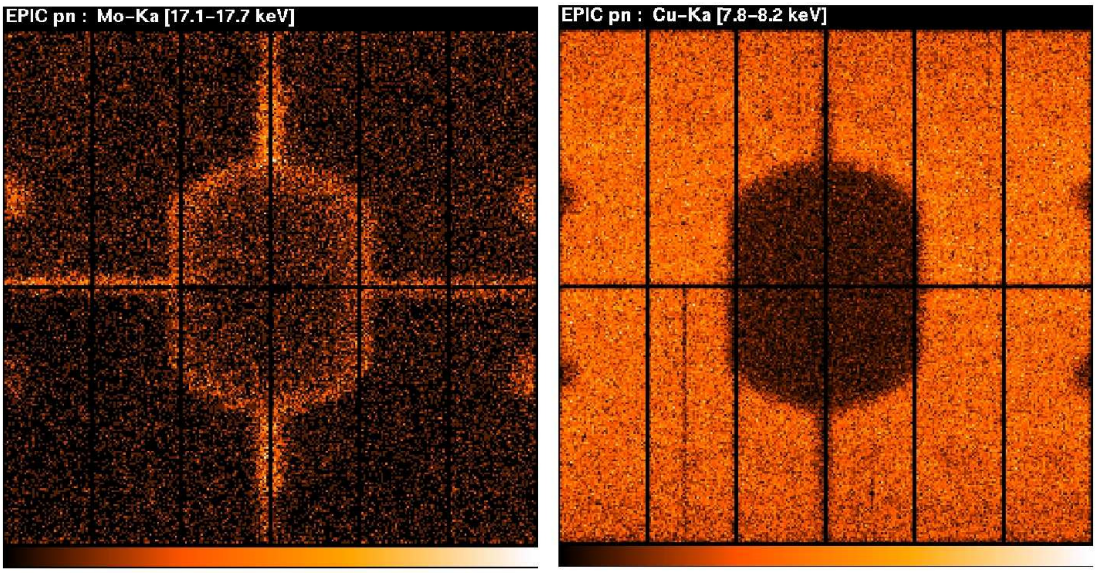

Figure 4.4: Background image showing the EPIC-pn detector in different energy bands. The strong spatial dependence of the detector background is clearly visible, which is caused by fluorescence lines within the material close to the detector. In this example, Mo (left panel) and Cu (right panel) lines are visible which are caused by the electronics board of the detector. Credit: XMM-Newton Users Handbook (2013).

The modeling of the quiescent particle background can be performed automatically by using the *XMM-Newton* ESAS tasks *pn_/mos_ back* (see Fig. 4.3). The procedure used by these tasks is described in the following paragraph and can also be found in Kuntz and Snowden (2008). All additional files needed for this procedure are included in the additional *XMM-Newton* ESAS CCFs.
As explained above, the QPB can be estimated by using the unexposed-corner data of the detectors. Since the statistics of these unexposed pixels is often very low, the spectra created out of these data have to be augmented in order to obtain a better statistics. This is done by searching a data base of all archived *XMM-Newton* observations for observations which show a similar shape of their unexposed corner spectra, i.e. a similar count rate in the energy range of $0.3-10\,\mathrm{keV}$ and a similar $(2.5-5\,\mathrm{keV})/(0.4-0.8)$ hardness ratio. The thus augmented spectra of the unexposed corners are used to scale the corner spectra of FWC data, in order to determine the correct level of QPB contamination. The thus determined scaling factor is then used to scale the FWC data of the desired detector region of interest, since the QPB shows a strong spatial dependance. To estimate the QPB for center CCDs which possess no unexposed corners, the results for the surrounding CCDs are used. The resulting particle background spectrum is then

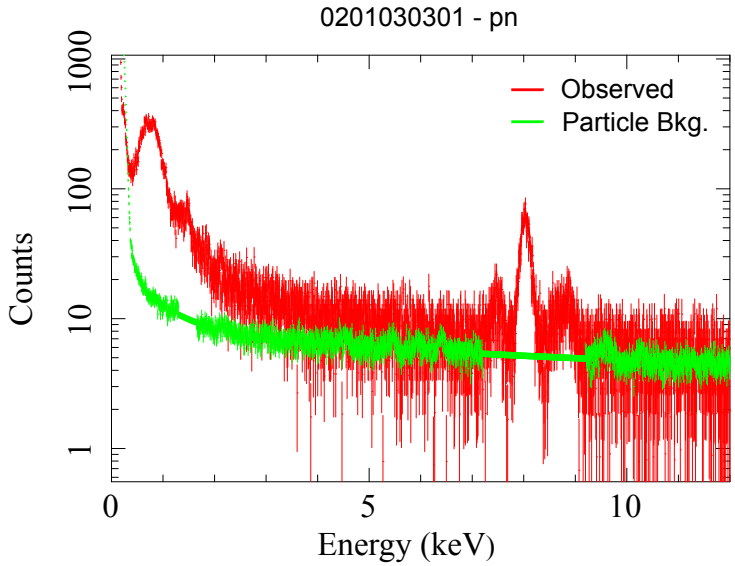

Figure 4.5: Output of the *XMM-Newton* ESAS task *pn_back* for the *XMM-Newton* EPIC observation with Obs.-ID 0201030301, which was used for the X-ray analysis performed within the scope of this thesis. The plot shows the observed spectrum (red) and the modeled spectrum of the quiescent particle background (green) as determined by *XMM-Newton* ESAS. The most prominent fluorescence lines are excluded from the background spectrum and have to be modeled during spectral analysis.

subtracted from the source spectrum (see Fig. 4.5) during the spectral analysis. The strong fluorescence lines visible in the particle background spectrum (Al Kα and Si Kα for the EPIC-MOS detectors, Al Kα and Cu lines for the EPIC-pn detector) are not subtracted from the source spectrum, since low gain variations which are part of the detector background would lead to considerable residuals in the spectral fits. Instead, these lines have to be included as Gaussians into the model of the source spectrum during the spectral analysis. More information about this procedure, which is automized in *XMM-Newton* ESAS, can be found for example in Snowden et al. (2008).

4.3 Photon Background

The third main background component are photons. The major part of these are X-ray photons, but also infrared, optical, and UV photons can be detected by the CCDs (XMM-Newton Users Handbook, 2013) and have to be blocked through filters which can be placed in front of the photon entrance window during

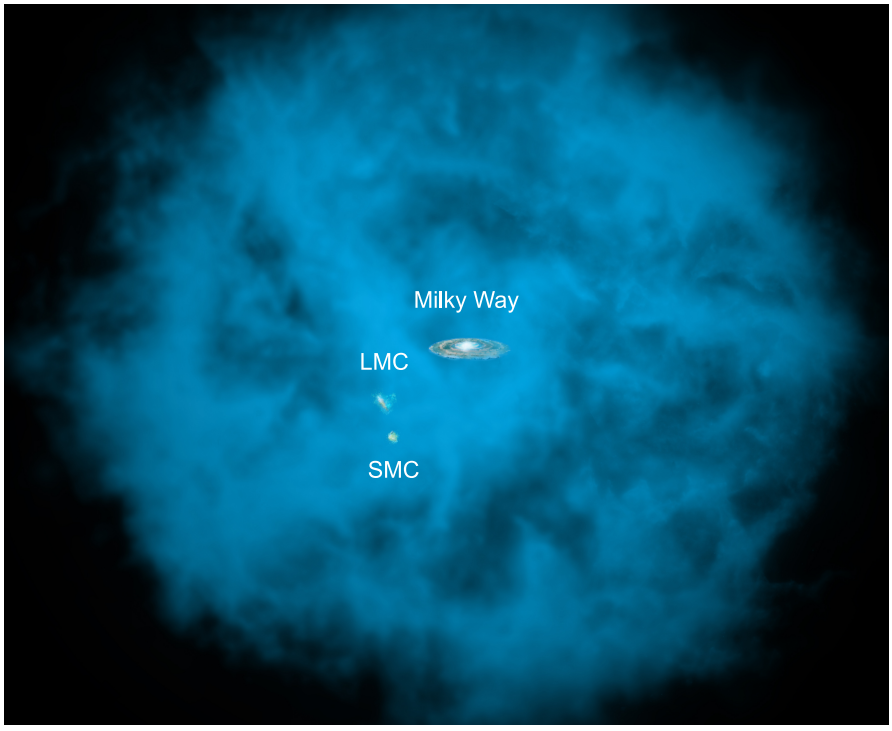

Figure 4.6: Artists impression of the Hot Galactic Halo around the Milky Way, which also encloses the Large and the Small Magellanic Cloud. Credit: NASA/CXC/M.Weiss; NASA/CXC/Ohio State/A.Gupta et al.

the observation. The major components of the X-ray background are caused by cosmic X-ray photons, solar wind charge exchange, point sources, and stray light. These components, which have a weak time- but a strong spatial dependence, are briefly introduced in this section.

4.3.1 Cosmic X-ray Background

The cosmic X-ray background (CXB) was first discovered by Giacconi et al. in the year 1962. It consists of photons with energies of $\sim 0.1 - 10\,\mathrm{keV}$ and shows a strong spatial variance depending on the observed region of the sky. It can roughly be separated into an extragalactic and a Galactic component.

The extragalactic component originates mainly from unresolved active galactic nuclei (Arnaud et al., 2011b). It is constant in time and can be described by a power law with a spectral index of $\alpha = 1.46$ (Chen et al., 1997), which has to be modeled for the spectral analysis.

The Galactic X-ray back- or foreground originates mainly from the Local Bubble and the Galactic Halo. The Local Bubble (Cox and Reynolds, 1987) is a region around the Sun which has a radius of $\sim 100-200\,\mathrm{pc}$ (Arnaud et al., 2011b) and is irregularly shaped. It is filled with hot gas which has temperatures of $\sim 10^6\,\mathrm{K}$, corresponding to $\sim 0.1\,\mathrm{keV}$, and emits thermal X-rays (e.g., Snowden et al., 1998). The Local Bubble is believed to have been created during the last $\sim 10^7\,\mathrm{yr}$ through multiple supernova explosions (e.g., Maíz-Apellániz, 2001) and stellar winds. Its soft X-ray emission creates an unabsorbed background component which has to be modeled in the spectrum.
The Hot Galactic Halo, which also contributes to the Galactic X-ray background, consists of a halo of hot gas around the Milky Way, which emits thermal X-rays. It has temperatures of some million Kelvin (e.g., Snowden et al., 1998) and a radius of $\sim 100\,\mathrm{kpc}$, therefore also enclosing the Large and the Small Magellanic Cloud (see Fig. 4.6). This hot halo is assumed to be created through Galactic fountains (see Sect. 2.4). These are fountains of hot gas which has been heated up through supernovae and stellar winds and which escape from the Galactic disk into the halo of the Galaxy. The emission of this Hot Galactic Halo can be described through a cooler halo emission at $0.1\,\mathrm{keV}$, and a hotter halo emission at $0.25-0.7\,\mathrm{keV}$, which have to be modeled in the spectrum.

4.3.2 Solar Wind Charge Exchange

Solar wind charge exchange (SWCX) is another source of soft X-ray background at $\lesssim 1\,\mathrm{keV}$ (e.g., Koutroumpa et al., 2009). It occurs when highly ionized particles from the solar wind interact with a particle, e.g., from the ISM and pick up an electron from a neutral atom. When this picked-up electron is in a highly excited state, it can emit X-rays while de-exciting. This leads to additional emission lines of, e.g., highly ionized C, O, Mg, Si, Fe, or Ni (Carter and Sembay, 2008). These lines are also observed in the emission of astrophysical plasma, and may therefore lead to a misinterpretation of the results of a spectral analysis. Observations which are contaminated by the emission of SWCX show enhanced emission lines of O VIII and Mg XI. In addition, they show a varying light curve in the energy range of $0.5-0.7\,\mathrm{keV}$ with a simultaneously quiet light curve in the range of $2-8\,\mathrm{keV}$ (Snowden and Kuntz, 2011b). Since this background component is variable on the time scale of some days, different observations of the same, time-independent source can be used to estimate the background and to fit its emission lines, although this may lead to a confusion with other, time-dependent background components.

4.3.3 Point Sources and Stray Light

Another background component encountered during the study of diffuse emission are point sources. These point sources can be removed during data processing using the *XMM-Newton* ESAS task *cheese-bands*. This task performs source detection and creates an editable source list as well as point source subtracted event images and exposure images for user-defined energy bands. This is done by combining the EPIC-MOS and EPIC-pn data and applying a flux threshold.
The final background component to be discussed in this chapter is stray light. Stray light originates from bright X-ray sources outside the field of view, but within 1.5° from the optical axes of the *XMM-Newton* telescopes (XMM-Newton Users Handbook, 2013). The emission of these sources which reaches the detectors is reflected only once from the mirrors of the Wolter-I telescopes – and not twice, as needed for focusing. To reduce stray light, an X-ray baffle is mounted in front of the mirrors of *XMM-Newton*. Thus, only a part of the FOV is contaminated by stray light, which appears as near-annular structures in the detector images (see Fig. 4.7 and XMM-Newton Users Handbook, 2013). This characteristic structure is a result of the interaction of the stray light with the supporting structure for the mirror shells (see Sect. 3.1).
If the spectrum of the stray-light producing source is known, its contribution to the contaminated observation can be estimated during the spectral analysis by adding a corresponding component to the model of the contaminated observation. Otherwise, heavily contaminated parts of the observation have to be excluded from further data analysis.

In this chapter, an overview of the various background components was given which have to be taken into account when studying diffuse soft X-ray emission with *XMM-Newton*. The contribution of the three major background components were discussed and ways were introduced of estimating, subtracting, or modeling these components during data processing or in the spectral analysis. These procedures were also applied to the X-ray data which were analyzed within the scope of this thesis to study the supergiant shell LMC-SGS 2 as well as the supernova remnant and the superbubble of DEM L299. These studies and their results are presented in the following chapters.

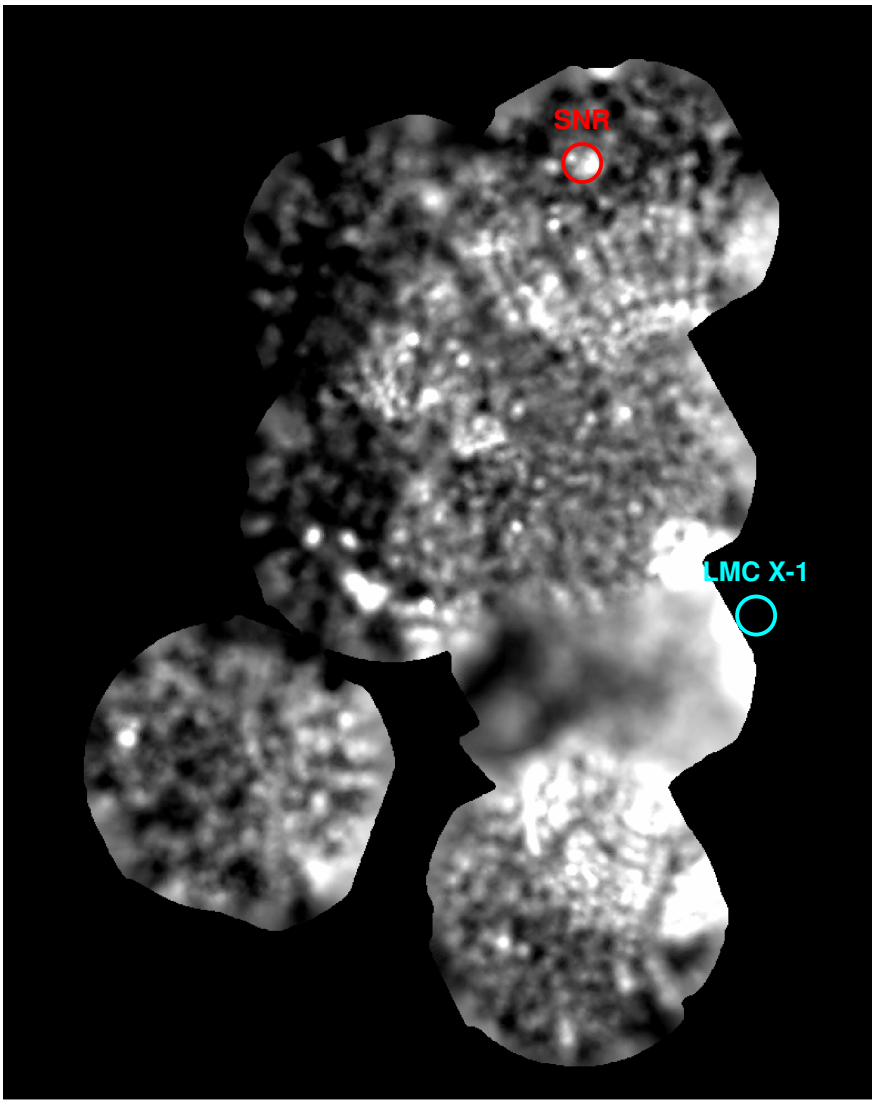

Figure 4.7: Mosaic image of all seven observations of the supergiant shell LMC-SGS 2 region used for the studies within this thesis (see Table 5.1) in the hard energy band (1.5 – 4.5 keV). Stray light, which is most probably originating from the X-ray binary LMC X-1 (marked in blue) is visible in almost all observations as near-annular structures. The position of the SNR B0543-68.9 (see Chapt. 6) is indicated by a red circle.

Chapter 5

Supergiant Shell LMC-SGS 2

The supergiant shell LMC-SGS 2 is a huge structure in the ISM which lies in the vicinity of the star-forming region 30 Doradus in the Large Magellanic Cloud (see Fig. 5.1). It has an enormous size of ~ 900 pc, which corresponds to $\sim 10\,\%$ of the size of its host galaxy. A morphological and X-ray spectral analysis of this supergiant shell (SGS) has been performed within the scope of this thesis. For these studies, X-ray data of *XMM-Newton* have been used, which show the entire supergiant shell in much more detail than shown in previous studies of data from the *Einstein* Observatory (Wang and Helfand, 1991) and *ROSAT* (Points et al., 2000).
In this chapter, the morphological and X-ray spectral analyses are presented which were performed within the scope of this thesis for the supergiant shell LMC-SGS 2. After an introduction about LMC-SGS 2 (Sect. 5.1), the *XMM-Newton* X-ray data are described which have been used for these studies (Sect. 5.2). The morphological studies are presented in Section 5.3, in which detailed X-ray images of LMC-SGS 2 are provided and compared with optical and radio 21 cm emission images of the supergiant shell. Section 5.4 introduces the model which has been used to perform the X-ray spectral analysis for all objects studied in the scope of this thesis, i.e. for the supergiant shell LMC-SGS 2 (Sect. 5.5), for SNR B0543-68.9, and for the DEM L299 superbubble (Sect. 6.4). The X-ray spectral analysis performed for LMC-SGS 2 is discussed in Section 5.5, and its results are used in Section 5.6 to determine further properties of the supergiant shell. Section 5.7 concludes this chapter with a summary and an outlook.

5.1 Introduction

Among the nine supergiant shells (SGSs) which have been identified in the LMC through Hα observations (see Goudis and Meaburn, 1978; Meaburn, 1980), supergiant shell LMC-SGS 2 is the brightest in X-rays (Wang and Helfand, 1991). It is

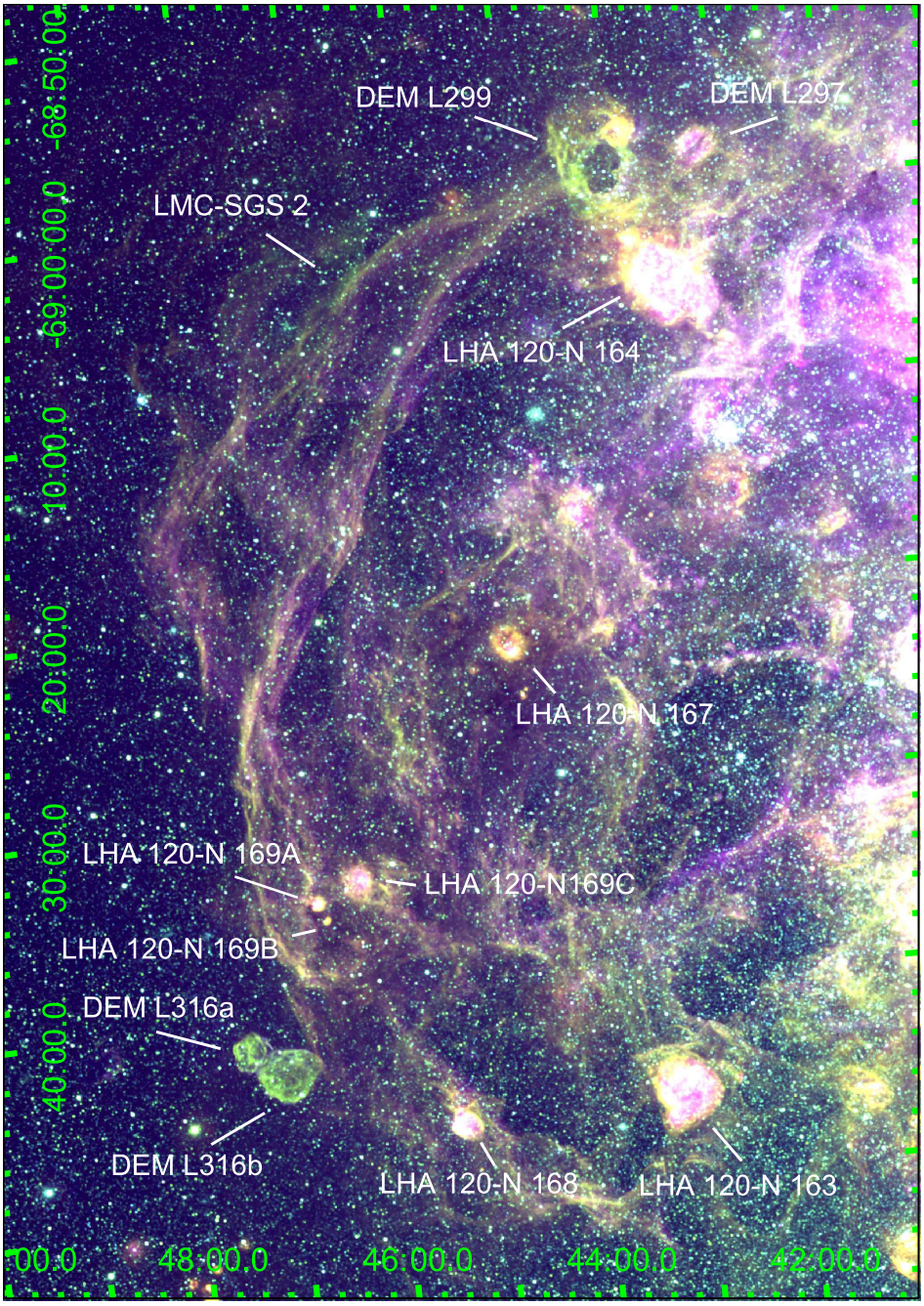

Figure 5.1: Optical image showing the LMC-SGS 2 region in the Large Magellanic Cloud. This region lies south-east of 30 Doradus, which is located just outside the plotted field of view. The image is a three-color image which has been created out of data of the Magellanic Cloud Emission Line Survey and shows Hα emission in red, [S II] emission in green, and [O III] emission in blue. It shows an area of $\sim 680\,\mathrm{kpc} \times 980\,\mathrm{kpc}$.

located east of 30 Doradus and is part of a region of the LMC which is observed to be very bright and to show a complex structure of hot and warm ISM. The H I gas associated with the supergiant shell LMC-SGS 2 is centered on RA 05:41:27, Dec -69:22.4 (J2000) and has a radius of 26′ (380 pc) as determined by Kim et al. (2003). It is located south-east of 30 Doradus with its center lying at RA 05:44, Dec -69:20 (J2000) (Book et al., 2008). It shows filaments of warm ISM visible in Hα, which reach an extent of ~ 900 pc (Goudis and Meaburn, 1978), and harbors hot ISM which is projected towards its interior (Wang and Helfand, 1991). In addition, a spur of hot ISM is observed which extends south from the optical shell, which has been suggested by Wang and Helfand (1991) to be indicative of a blowout of LMC-SGS 2, in which the hot gas escapes into the halo of the LMC. However, this could not be confirmed by Points et al. (1999), who found no supporting evidence in optical or radio wavelengths.
X-rays studies have been performed for LMC-SGS 2 using data of the *Einstein* Observatory (Wang and Helfand, 1991) and *ROSAT* (Points et al., 2000). Wang and Helfand (1991) determined its energy input through stellar winds and supernovae to be $\sim 3 \times 10^{53}$ erg, and obtained a temperature of 5×10^6 K ($k_\mathrm{B}T = 0.43$ keV) when assuming a column density of $\sim 3 \times 10^{21}\,\mathrm{cm}^{-2}$. They derived an age of $\sim 1.8 \times 10^7$ yr for LMC-SGS 2, while Book et al. (2008) obtained an age of 9×10^6 yr using H I data. *ROSAT* data of LMC-SGS 2 were analyzed by Points et al. (2000), who determined a temperature $k_\mathrm{B}T$ of $0.1-0.7$ keV for different regions of LMC-SGS 2 and of $0.1-0.5$ keV for the X-ray spur. Furthermore, they assumed a Galactic plus LMC column density of ~ 0.45 $(0.8-1.25) \times 10^{22}\,\mathrm{cm}^{-2}$ for LMC-SGS 2 and of ~ 0.42 $(0.07-1.35)$ $\times 10^{22}\,\mathrm{cm}^{-2}$ for the X-ray spur.
The morphology and kinematics of LMC-SGS 2 has been the subject of several analyses, including Wang and Helfand (1991), Points et al. (1999), Ambrocio-Cruz et al. (2004) and Book et al. (2008). Figure 5.1 shows LMC-SGS 2 in optical wavelengths. In this energy range, it shows a clear filamentary structure at its eastern border, while star formation regions are located at its western edge (Points et al., 1999). Points et al. (2000) remarked that regions interior of LMC-SGS 2 which show a low X-ray surface brightness have a large H I column density, suggesting that absorption might cause some of the variations in its X-ray brightness. This is supported by the fact that these variations are stronger in the softer X-ray bands, where absorption is more efficient. Caulet et al. (1982) found LMC-SGS 2 as an expanding shell with an expansion velocity of ~ 30 km/s within a local ISM, which has a heliocentric velocity of 245 km/s. In contrast, Points et al. (1999) and Ambrocio-Cruz et al. (2004) did not find the characteristic velocity distribution of a coherently expanding shell.[1] Instead, they concluded that two layers of H I

[1] The characteristic velocity distribution for an expanding shell is a single-component velocity profile at the border of the shell, and a two-component velocity profile within the shell, with the largest difference between these components near the center of the shell (Ambrocio-Cruz et al., 2004).

sheets seem to confine the hot gas, with only local expansion of smaller structures. Points et al. (1999) state that the hot gas seems to be heated by outflows from SNRs and star-forming regions within the interior of LMC-SGS 2, while the inner surface of the H I sheets is ionized by the UV radiation of massive stars located at the periphery of the supergiant shell. The studies of Points et al. (1999) and Ambrocio-Cruz et al. (2004) both yielded a heliocentric velocity of $\sim 250\,\mathrm{km/s}$ for the sheet observed as the front-side of LMC-SGS 2, and of $\sim 300\,\mathrm{km/s}$ for the sheet observed as its back-side. Also Book et al. (2008) concluded that LMC-SGS 2 is not a simply expanding shell, but possesses locally expanding substructures. In addition, they state that the whole complex seems to be part of a more extended, expanding H I structure. They also show that – besides optical data – 21 cm radio data is crucial for the identification of supergiant shells, since a shell will cease to emit Hα emission $\sim 12\,\mathrm{Myr}$ after the last OB associations within its periphery have disappeared. Thus, they concluded that Hα emission is not sufficient for the unambiguous identification of a supergiant shell. In the following sections, the morphological and X-ray spectral analysis of LMC-SGS 2 will be discussed which has been performed using X-ray, optical, and radio data.

5.2 X-ray Data

For the analysis of the supergiant shell LMC-SGS 2, we have used the data of ten *XMM-Newton* EPIC observations, listed in Tables 5.1 and 5.2. Four of these observations (Obs. 1 – 4) cover LMC-SGS 2. Among these, Observation 1 also covers DEM L299 and was used for the studies of SNR B0543-68.9 and the DEM L299 superbubble as described in Chapter 6. Observations 5 and 6 cover the X-ray spur extending south of LMC-SGS 2, while Observation 7 shows the region south-east of LMC-SGS 2 which has been chosen for comparison due to its proximity to the supergiant shell. The remaining three pointings (Obs. 8 – 10) are observations of the South Ecliptic Pole (SEP)[2], which have been used for background estimation (see Sect. 5.4). An overview of the relative positions of these observations is provided in Figure 5.2. More information about the observations can be found in Tables 5.1 and 5.2.
Each of the ten observations comprises data from all three *XMM-Newton* EPIC detectors. For eight of these observations, at least one EPIC-MOS CCD was identified during data analysis to be operating in an anomalous state (see Sect. 4.1). The data of affected CCDs were therefore excluded from further analysis. A list of the affected CCDs during the respective observations is given in Table 5.3. In addition, Observation 7 is lacking the data from EPIC-MOS1 CCD6 which was

[2] SEP – **S**outh **E**cliptic **P**ole: The SEP is the southern of the two poles which are defined by the ecliptic plane, on which the Earth travels around the Sun.

Table 5.1: Overview of the ten *XMM-Newton* EPIC observations which have been used to perform the morphological and spectral analysis of LMC-SGS 2 in X-rays. Observation 1 – 4 of this list cover LMC-SGS 2 as observed in optical wavelengths (cf. Fig. 5.2). Observations 5 and 6 cover the X-ray spur, while Observation 7 shows a region east of LMC-SGS 2, which was tested for its suitability for local background estimation. Observation 8 – 10 are targeted on the South Ecliptic Pole (SEP) and have been used for background estimation during the X-ray spectral analysis.

	Observed Reg.	Obs.-ID	Target		Obs.-Date
			RA (J2000)	Dec (J2000)	yyyy-mm-dd
1)	LMC-SGS 2	0094410101	05 42 36.0	-69 05 00.0	2001-10-19
2)	LMC-SGS 2	0201030201	05 46 36.0	-69 12 00.0	2004-01-05
3)	LMC-SGS 2	0201030101	05 46 36.0	-69 35 00.0	2004-01-05
4)	LMC-SGS 2	0094410201	05 43 00.0	-69 30 00.0	2001-10-19/20
5)	X-ray spur	0094410701	05 43 00.0	-69 50 00.0	2001-10-20
6)	X-ray spur	0201030301	05 43 00.0	-70 15 00.0	2004-01-13
7)	Local Bkg.	0402000201	05 49 47.3	-69 59 48.0	2006-08-29
8)	SEP	0162160101	06 00 00.0	-66 33 38.0	2003-11-24
9)	SEP	0162160301	06 00 00.0	-66 33 38.0	2003-12-05
10)	SEP	0162160501	06 00 00.0	-66 33 38.0	2003-12-14

Table 5.2: Continuation of Table 5.1. The listed counts refer to the number of counts after data processing.

	PI	Eff. Obs. Time			Exposure			Counts		
		MOS1 [ks]	MOS2 [ks]	PN [ks]	MOS1 [ks]	MOS2 [ks]	PN [ks]	MOS1 [$\times 10^3$]	MOS2 [$\times 10^3$]	PN [$\times 10^3$]
1)	Y.-H. Chu	11.3	11.4	8.9	11.8	11.8	9.2	$37.3_{\pm 0.2}$	$38.5_{\pm 0.2}$	$76.6_{\pm 0.3}$
2)	Y.-H. Chu	11.5	11.3	7.9	11.7	11.7	8.3	$26.4_{\pm 0.2}$	$28.6_{\pm 0.2}$	$43.5_{\pm 0.3}$
3)	Y.-H. Chu	10.8	11.0	7.4	11.3	11.3	7.9	$25.1_{\pm 0.2}$	$28.0_{\pm 0.2}$	$40.5_{\pm 0.3}$
4)	Y.-H. Chu	11.3	11.4	8.9	11.8	11.8	9.2	$39.3_{\pm 0.2}$	$40.7_{\pm 0.3}$	$86.1_{\pm 0.3}$
5)	Y.-H. Chu	2.1	1.9	1.5	5.3	5.4	2.6	$7.9_{\pm 0.1}$	$7.2_{\pm 0.1}$	$15.9_{\pm 0.2}$
6)	Y.-H. Chu	10.7	11.0	7.9	11.7	11.7	8.3	$35.3_{\pm 0.2}$	$35.0_{\pm 0.2}$	$70.1_{\pm 0.3}$
7)	F. Haberl	8.5	8.3	2.6	15.3	15.2	10.2	$20.3_{\pm 0.2}$	$23.2_{\pm 0.2}$	$15.8_{\pm 0.2}$
8)	B. Altieri	12.0	12.4	9.8	13.2	13.2	11.5	$18.9_{\pm 0.2}$	$20.0_{\pm 0.2}$	$39.4_{\pm 0.2}$
9)	B. Altieri	8.6	8.6	8.0	11.1	11.1	9.4	$14.7_{\pm 0.2}$	$14.7_{\pm 0.2}$	$31.6_{\pm 0.2}$
10)	B. Altieri	9.5	9.3	7.8	10.4	10.5	9.0	$15.9_{\pm 0.2}$	$15.4_{\pm 0.2}$	$29.8_{\pm 0.2}$

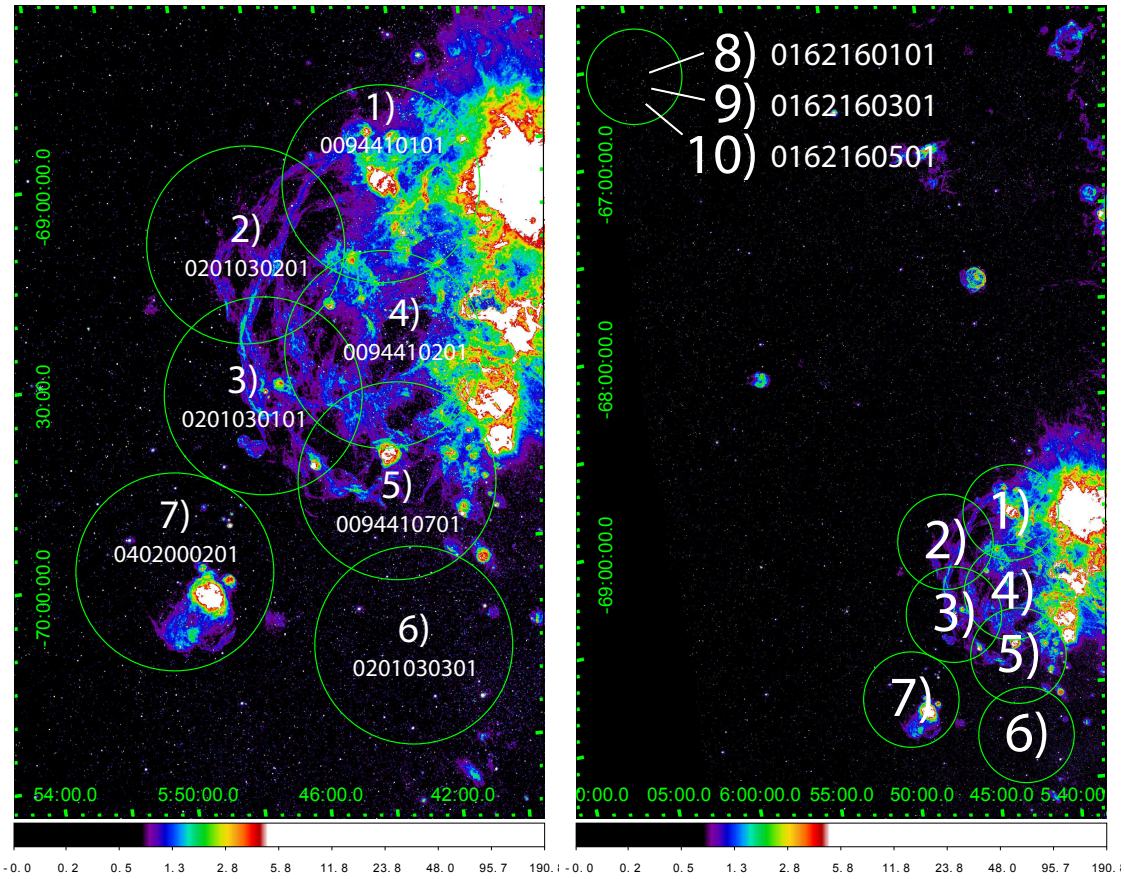

Figure 5.2: Positions of the ten *XMM-Newton* EPIC observations used for the studies of LMC-SGS 2 overlaid onto an optical image showing this region in Hα emission, created out of MCELS data. Each pointing is labeled with its observation-ID as listed in Table 5.1.

Table 5.3: List of EPIC-MOS CCDs which were found to have been operating in an anomalous state at the time of the observation. For the respective observations, the data of these CCDs have not been used for further data analysis.

	Observation	CCD operating in an anomalous state
1)	0094410101	EPIC-MOS1 CCD5
2)	0201030201	EPIC-MOS2 CCD5
3)	0201030101	EPIC-MOS2 CCD5
4)	0094410201	EPIC-MOS1 CCD4; EPIC-MOS1 CCD5
5)	0094410701	EPIC-MOS1 CCD5
6)	0201030301	EPIC-MOS1 CCD4; EPIC-MOS2 CCD5
7)	0402000201	EPIC-MOS2 CCD5
8)	0162160101	–
9)	0162160301	EPIC-MOS1 CCD4
10)	0162160501	–

lost for scientific observations in the year 2005 due to the impact of a micrometeorite (see Sect. 3.1.3).
The observations were performed between the years 2001 and 2006, with the observations of LMC-SGS 2 and of the X-ray spur (Obs. 1 – 6) taken within a time span of 2.5 yr. They were taken in (extended) full frame mode with an average exposure time of 11 ks. This resulted in an average effective exposure time of 9 ks after data processing, and an average number of count of $(27\,000^{+1\,200}_{-1\,200})$ counts per detector and observation.

The data processing has been performed with the help of the *XMM-Newton* ESAS package version 4.3 and the *XMM-Newton* SAS package 11.0.0. Detailed information about background handling and data processing can be found in Chapter 4. During data processing, soft proton flares were filtered, the quiescent particle background was subtracted, and point sources were removed from the observational data. The point-source detection has been performed using a flux threshold of $10^{-14}\,\mathrm{erg\,cm^{-2}\,s^{-2}}$, and detected point sources were excluded down to a surface brightness of 50 % of the surrounding background. After the execution of this *XMM-Newton* ESAS task, the point-source list was manually checked and revised where needed.

Basically all of the seven observations of the LMC-SGS 2 region used for the studies within this thesis show stray light (see Sect. 4.3.3) in the hard energy band of 1.5 – 4.5 keV. This stray light seems to originate from the high-mass X-ray binary LMC X-1 which is projected south-west of supergiant shell LMC-SGS 2 (see Fig. 4.7). Observation 1 (containing the north-western part of supergiant shell LMC-SGS 2) and Observation 6 (containing the X-ray spur in the south)

show the most obvious stray-light contamination. Nevertheless, DEM L299 lies within the north-eastern, stray-light free half of the FOV of Observation 1 and is therefore not contaminated. The stray-light contamination of LMC-SGS 2 seems limited to the hard energy band, which is not in the main focus of the studies performed within the scope of this thesis. Thus, stray-light contamination was not taken into further account during this analysis.

5.3 Morphological Studies

We used processed *XMM-Newton* EPIC data sets of the seven observations covering the LMC-SGS 2 region to create the X-ray mosaic shown in Figure 5.3. It is a three-color image which shows in red the soft energy band (0.3 – 0.8 keV), in green the medium energy band (0.8 – 1.5 keV), and in blue the hard energy band (1.5 – 4.5 keV). Diffuse X-ray emission is visible in this mosaic at the projected position of the supergiant shell LMC-SGS 2 (Obs. 1 – 4) and of the X-ray spur south to it (Obs. 5 and 6). Thus, this emission observed in Obs. 1 – 4 seems to originate from the hot gas inside the supergiant shell. The mosaic shows the entire supergiant shell LMC-SGS 2 in much more detail than previous studies did. Its eastern part is clearly confined (see Obs. 2 and 3), while the western side of LMC-SGS 2 shows less definite structures, but a brighter and more extended X-ray emission (see Obs. 1 and 4). Figure 5.4 shows the same observations in the soft, medium, hard, and broad (0.3 – 8 keV) energy band. It becomes obvious from this figure that the major part of the LMC-SGS 2 X-ray emission is present in the soft and medium energy band (Figs. 5.4a and 5.4b), while the hard energy band mainly shows stray light (Fig. 5.4c), most likely originating form LMC X-1. In Observations 5 and 6, the X-ray spur is clearly visible.
Since Observation 5 was heavily contaminated by soft proton flares, it has a much lower effective observation time after data processing than the other data sets and therefore has a low statistics. Observation 7, which is pointed south-east of LMC-SGS 2, shows much less diffuse X-ray emission than the supergiant shell in the soft and medium energy band and might therefore be used for local background estimation of LMC-SGS 2 (see Sect. 5.5). Nevertheless, the strong spatial dependance of diffuse X-ray emission in this region and the vast extent of the supergiant shell of 900 pc leaves a high uncertainty in such a background estimation.

At the northern rim of the supergiant shell LMC-SGS 2 (in Obs. 1), DEM L299 can be recognized as an X-ray bright region in the soft and medium energy range, which is discussed and analyzed in Chapter 6. Figures 5.5 – 5.7 show a comparison of the X-ray image of LMC-SGS 2 with its appearance in optical and radio energy bands. For this comparison, 21 cm H I radio data of the Magellanic Cloud Survey

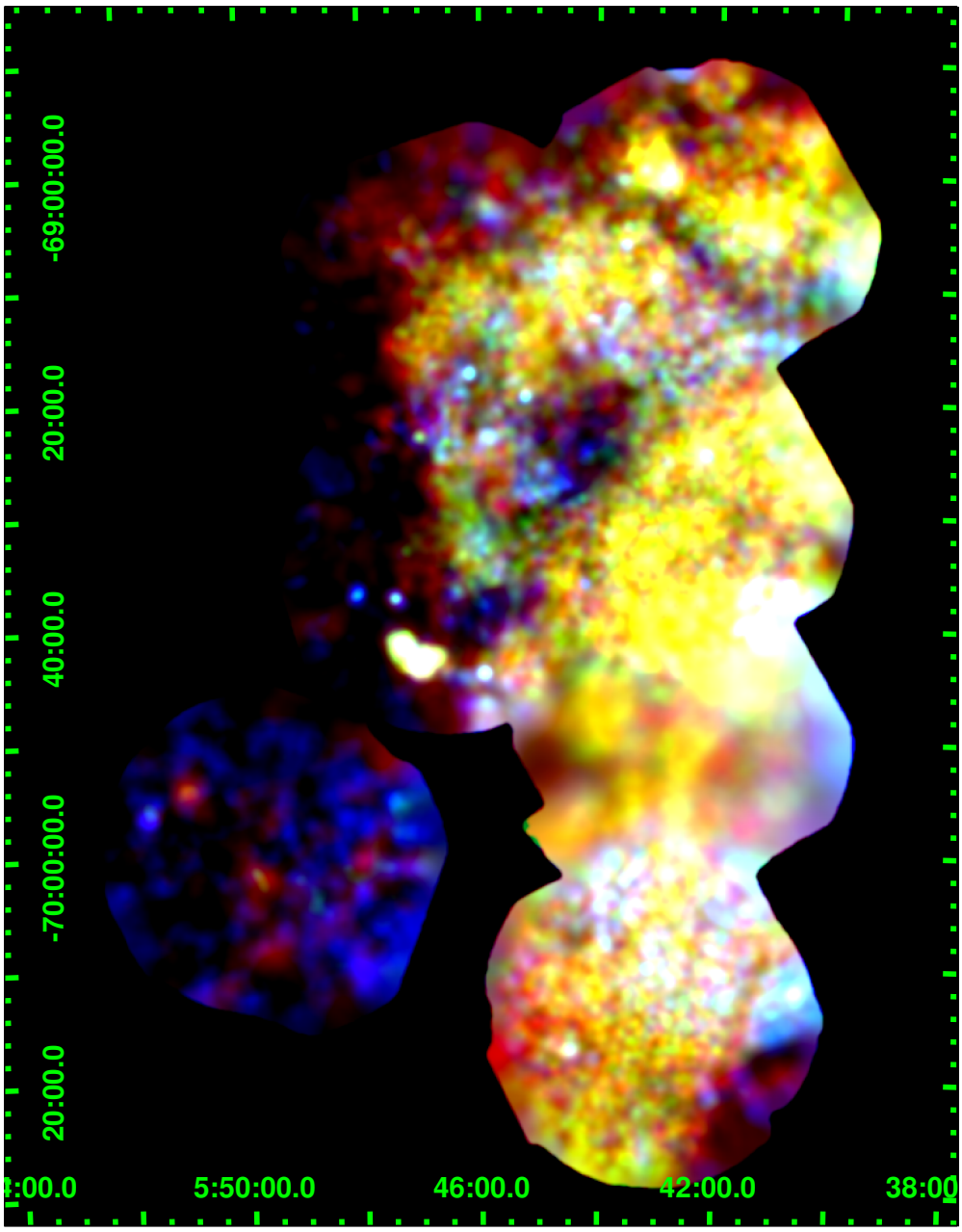

Figure 5.3: X-ray mosaic created out of the seven *XMM-Newton* observations showing the supergiant shell LMC-SGS 2. This three-color image shows in red the soft (0.3 – 0.8 keV), in green the medium (0.8 – 1.5 keV), and in blue the hard (1.5 – 4.5 keV) X-ray energy band.

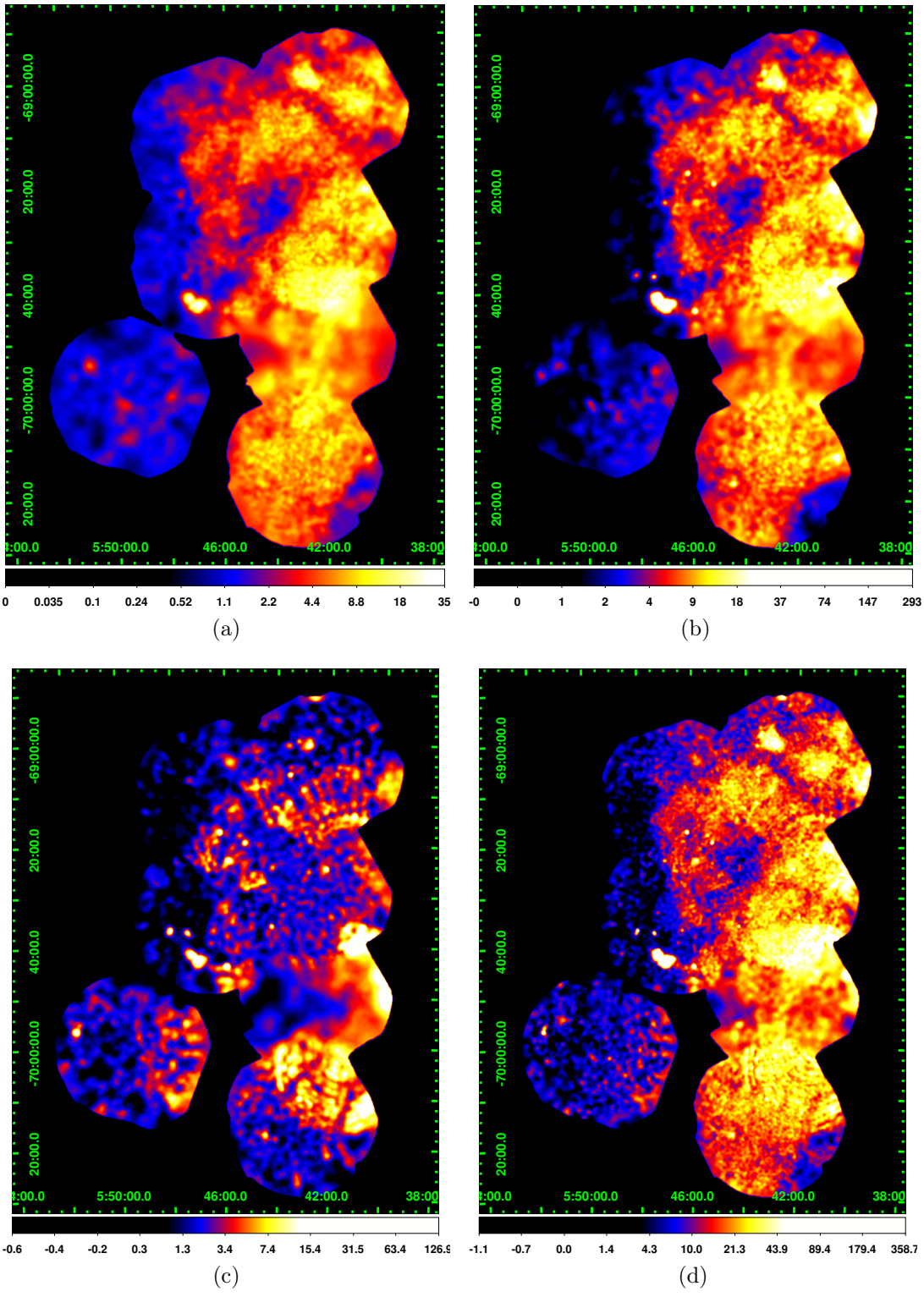

Figure 5.4: X-ray images showing the supergiant shell LMC-SGS 2 in an energy range of (a) 0.3 – 0.8 keV, (b) 0.8 – 1.5 keV, (c) 1.5 – 4.5 keV, and (d) 0.3 – 8.0 keV.

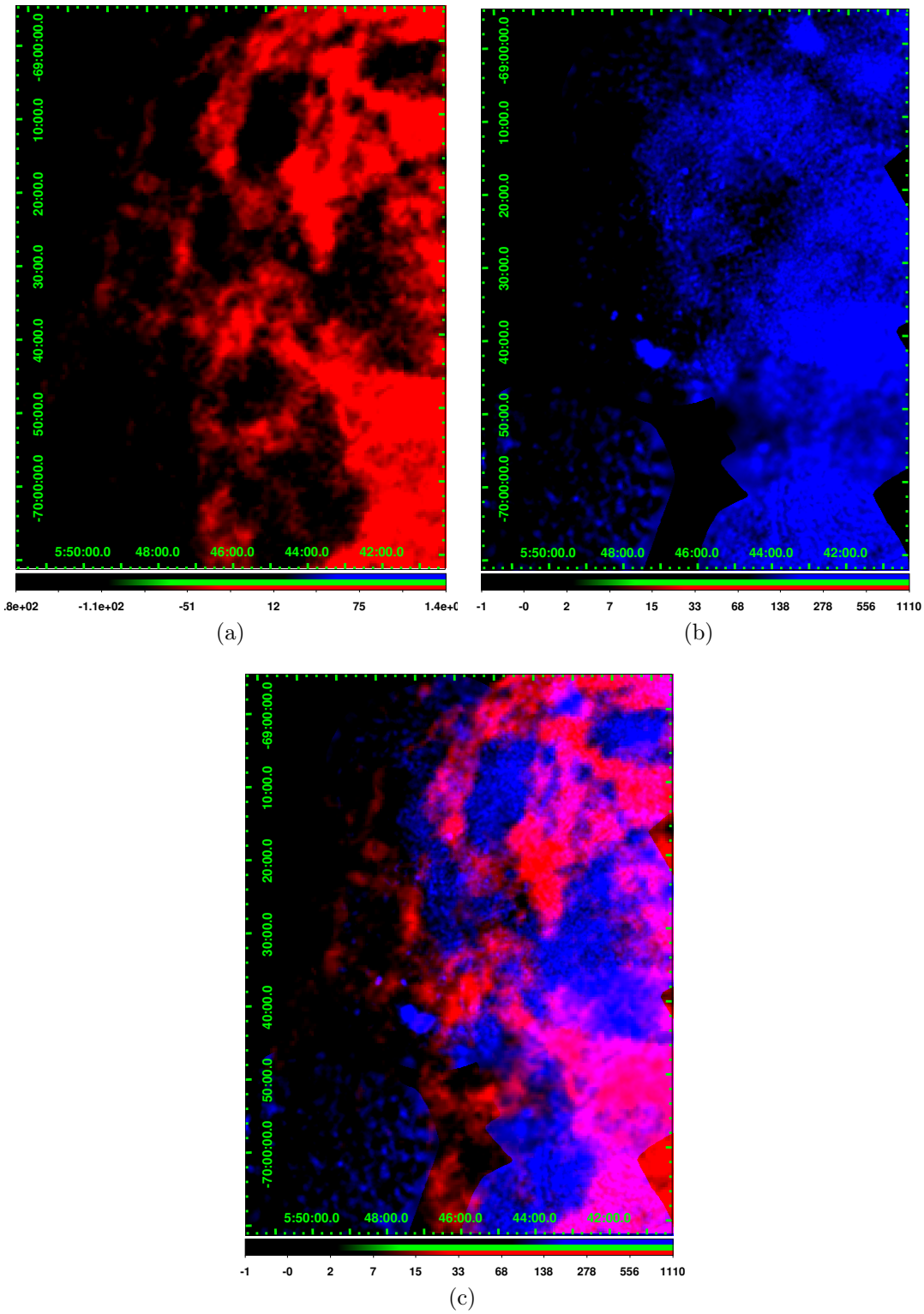

Figure 5.5: Comparison between (a) the radio and (b) the X-ray morphology of LMC-SGS 2, using radio 21 cm MCS data and the *XMM-Newton* broadband X-ray image of Figure 5.4d, respectively. (c): Overlay of (a) and (b).

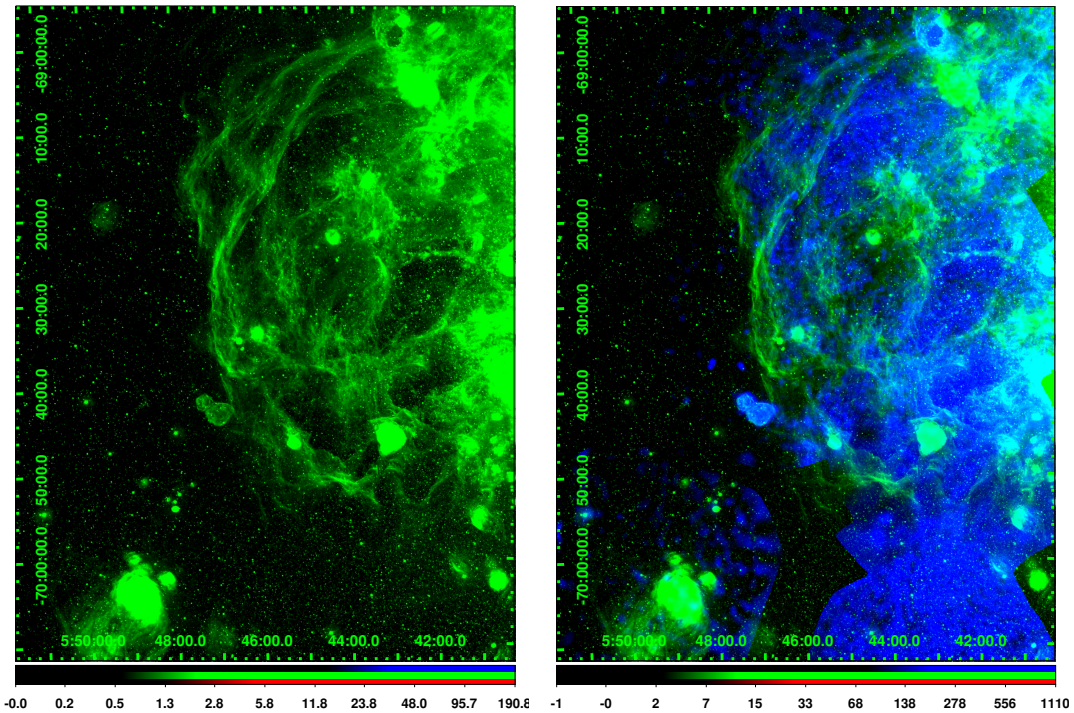

(a) (b)

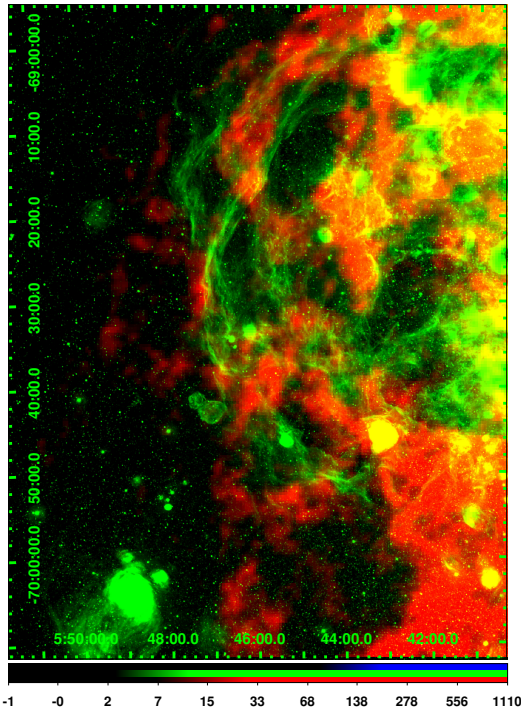

(c)

Figure 5.6: Same as Figure 5.5, but for optical and X-ray data. The optical data are the same MCELS Hα data as used in Figure 5.2.

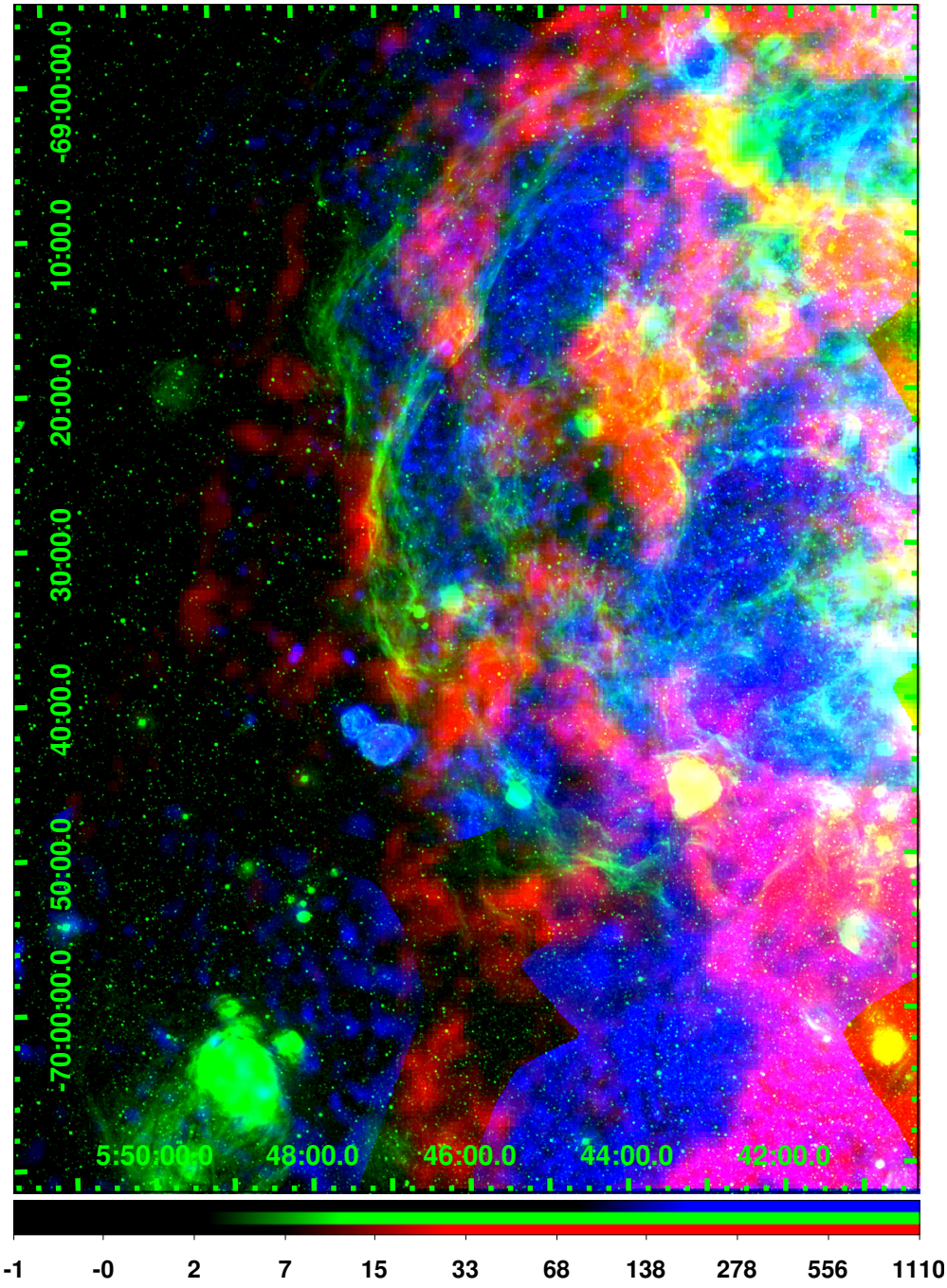

Figure 5.7: Three-color image showing the supergiant shell LMC-SGS 2 in radio (red), optical (green), and X-ray (blue) wavelengths. For the creation of this image, the same data as in Figures 5.5a, 5.6a, and 5.5b have been used.

(MCS; Kim et al., 1998, 2003) and Hα emission line data of the Magellanic Cloud Emission Line Survey (MCELS; e.g. Smith et al., 2000) have been used. The radio image of LMC-SGS 2 (Fig. 5.5a), which traces the position of neutral hydrogen, shows areas of bright emission and large voids. When comparing the broadband X-ray image (Fig. 5.4d) of LMC-SGS 2 with this radio image, as done in Figure 5.5c, it becomes obvious that the large patches of bright X-ray emission coincide with the voids visible at radio wavelengths. This suggests that the H I shells are filled with hot gas, which generates the diffuse X-ray emission. In addition, the area of low X-ray surface brightness projected towards the center of LMC-SGS 2 (see Sect. 5.1) coincides with the projection of a bright area of 21 cm emission, as previously reported by Points et al. (2000). In Figure 5.7, the radio and X-ray image is compared to the optical image of LMC-SGS 2 (Fig. 5.6a). In the overlay of the optical and X-ray data (Fig. 5.6b), the X-ray emission appears confined by the Hα filaments at the eastern and northern rim of LMC-SGS 2 in projection. Comparing the Hα image with the radio image of LMC-SGS 2 (see Fig. 5.6c), the Hα filaments are clearly confined in projection by the radio shells. The complete three-color image of LMC-SGS 2 is shown in Figure 5.7, in which the 21 cm radio emission is plotted in red, the optical Hα emission in green, and the X-ray emission in blue. This multi-frequency appearance of LMC-SGS 2 is the expected structure for an area of expanding hot gas, which is sweeping up a shell of warm and cold ISM.

5.4 Model used for Spectral Fitting

The X-ray *XMM-Newton* EPIC data which were used to perform the morphological study were also used to perform an X-ray spectral analysis of LMC-SGS 2. In this section, the model is described which has been used for the X-ray spectral analysis of supergiant shell LMC-SGS 2 (Sect. 5.5) and DEM L299 (Sect. 6.4). The X-ray spectral fitting package Xspec[3] version 12.7.1 (Arnaud, 1996) has been used to perform the spectral analyses.

The model which has been used within this analysis is given in Figure 5.8. It is based upon the one given by Snowden and Kuntz (2011b) for the study of extended X-ray emission observed with *XMM-Newton*. In the model, the SOURCE component represents the examined source emission, for which several Xspec model components have been tried: the *apec* model (Smith et al., 2001), the *vnei* model

[3] Xspec is an interactive program written for X-ray spectral fitting. It is detector-independent and can therefore be used to analyze data of any spectral X-ray telescope, like for example *XMM-Newton* or *Chandra* (Arnaud et al., 2011a). Web page: `http://heasarc.nasa.gov/xanadu/xspec/`

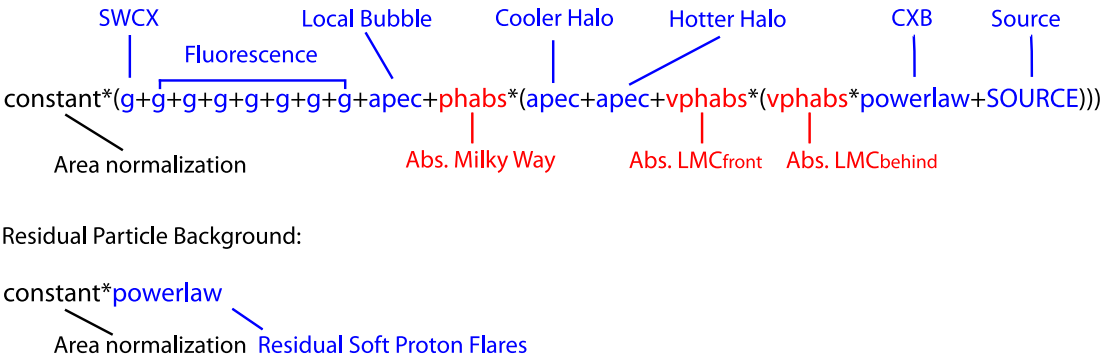

Figure 5.8: Illustration of the model used for the X-ray fits of supergiant shell LMC-SGS 2, SNR B0543-68.9, and the DEM L299 superbubble. Emission components are shown in blue, while absorption components are shown in red.

(Borkowski, 2000), and the *vpshock* model (Borkowski, 2000). The *apec* model describes the emission of a collisionally ionized gas, consisting of thermal bremsstrahlung and line emission, while assuming collisional ionization equilibrium (CIE, see Sect. 2.5.2). In contrast, the models *vnei* and *vpshock* describe a shocked gas while considering collisional non-equilibrium ionization (NEI) effects. *vnei* is a single ionization-timescale model, which assumes a delta function for the timescale distribution. In contrast, *vpshock* assumes a plane-parallel shock and determines a lower and upper limit for the ionization timescale (Borkowski et al., 2001). In all source components, elemental abundances were set to half of the solar values, representing typical LMC abundances (Russell and Dopita, 1992). The abundances could not be fitted freely during the spectral analysis, since the low statistics of the observations did not allow for a more precise determination during the fits. All other parameters of the source component were fitted freely to the LMC-SGS 2 (or DEM L299) data. In the model for the simultaneously fitted SEP data, which was used for background estimation (see below), the normalization of this source component was set to zero.
Besides this source component (SOURCE), the model consists of several absorption components (*phabs, vphabs*), fore- and background emission components (*apec, powerlaw*), Gaussian lines (*Gaussian (g)*), and a constant (*constant*). These components account for different types of background emission and their motivation and parameters will be discussed in more detail in the following paragraphs.

Foreground emission originating from the Local Bubble (see Sect. 4.3.1) is represented in the model by an unabsorbed thermal component (Xspec model: *apec*) with a fixed temperature of $k_{\mathrm{B}}T = 0.1\,\mathrm{keV}$. The emission of the cooler and hotter Galactic Halo (see Sect. 4.3.1) is included into the model as two separate thermal components, which are absorbed by the Milky Way (Xspec models: $phabs \times (apec \times apec)$), with temperatures fixed at 0.1 keV and 0.5 keV, respec-

tively. The Milky Way absorption has been fixed to $N_{\mathrm{H,MW}} = 0.06 \times 10^{22}\,\mathrm{cm}^{-2}$, according to Dickey and Lockman (1990).
To account for the emission of the unresolved, extragalactic cosmic X-ray background (see Sect. 4.3.1), the model includes a power law component, which is absorbed by the Milky Way and by the LMC (Xspec models:*phabs* × *vphabs* × *vphabs* × *powerlaw*). In this model, the LMC absorption is separated into two components: one to account for the absorption through material which lies in the line of sight in front of the source when observed from the Milky Way (labeled in Fig. 5.8 as *Abs.* LMC_{front}), and one representing absorption of the background radiation through material which lies behind the source (labeled as *Abs.* LMC_{behind}). The spectral index of the power law was fixed at a value of $\alpha = 1.46$ (Chen et al., 1997). Like for the source component, all chemical abundances of the LMC absorption components were fixed at half of the value for solar abundances, as generally assumed for the LMC.
Instrumental fluorescence lines, which are caused by the quiescence particle background (see Sect. 4.2.2), are modeled by six Gaussians (Xspec model: *Gaussian*) with zero width and at an energy of 1.49 keV (Al Kα) and 1.75 keV (Si Kα) for the EPIC-MOS detectors, and of 1.49 keV (Al Kα), 7.49 keV, 7.11 keV, 8.04 keV, 8.89 keV, and 8.62 keV (Cu Kα lines) for the EPIC-pn detector.
Since Koutroumpa et al. (2009) found evidence for contamination by solar wind charge exchange (SWCX) in the data of the SEP observations, different typical SWCX emission lines (see Sect. 4.3.2) were tested as model components for the spectra of the LMC-SGS 2 and DEM L299 during the spectral X-ray analysis. Only the O VIII line at 0.65 keV was found to make an obvious improvement in the residuals of the fit. Therefore, this line was added to the model as a Gaussian (Xspec model: *Gaussian*) with zero width and a frozen energy of 0.65 keV.
Residual soft proton flares (see Sect. 4.2.1) can be fitted through an unfolded (broken) power law (Xspec model: *powerlaw*). This power law must not be folded with the ancillary response file (ARF)[4]. A diagonal unitary redistribution matrix file (RMF)[5] has to be used, which is provided in the CCF data of *XMM-Newton*

[4] ARF – ancillary response file: The ARF connects the number of photons which are registered by the detector, with the number of photons that enter the instrument through the mirror module. It is calculated by multiplying the effective area with the quantum efficiency of the instrument. The effective area is a combination of the area of the telescope, of the filter, and of the detector as 'seen' by photons. It has a different size depending on the energy of the incoming photons due to their energy dependent cross section. The quantum efficiency describes the number of photons which are registered by a detector relative to the number of photons which hit the detector. Like the effective area, the quantum efficiency is energy dependent.

[5] RMF – redistribution matrix file: While the ARF is used to determine the number of photons which are registered by the detector, the RMF converts the energy of each registered photon into a value for the pulse height of the signal which is obtained when reading out the detector. This conversion also considers the finite energy resolution of the detector. Thus,

ESAS (see Chapt. 4). Six separate models (see second line of Fig. 5.8) were added to the Xspec model – one for each detector of the source observation and of the simultaneously fitted combined SEP observations (see below). The spectrum of the residual protons can usually be fitted using a power law index of 0.2 – 1.3 (Snowden and Kuntz, 2011b).
Both the main model and the six separate models are multiplied by a constant (Xspec model: *constant*). This constant accounts for the different effective sizes of the spectral extraction regions for each detector and for each observation, in particular between the SEP and LMC-SGS 2 extraction regions (see Sect. 6.4 for more information). Even if the spectral extraction regions would be defined similarly for all observations and detectors, their size usually differs, for example due to excluded CCDs, bad pixels, or hot columns.

To estimate the cosmic X-ray background of LMC-SGS 2 and DEM L299, the three combined SEP observations were fitted simultaneously to the LMC data. The SEP observations can be considered to be representative for the X-ray background of the supergiant shell LMC-SGS 2 and DEM L299, since the SEP is projected close to both objects (with an apparent separation of $\sim 190'$ between the SEP and the center of the supergiant shell LMC-SGS 2). Furthermore, the field of view of the SEP observations is relatively empty, and they have a sufficiently long, combined effective exposure time of ~ 30 ks. This method of background estimation was favored over a local background estimation from a region within the same observation, since a local background extraction region would unavoidably be contaminated by the X-ray emitting hot gas which is present in almost the entire field of view of the Observations 1 – 6, while Observation 7 was found to have too low statistics for background estimation (see Sect. 5.5). The appropriateness of the performed background estimation through the combined SEP observations compared with a local background estimation has been tested for DEM L299 and is described in Section 6.4. The tests confirmed the validity of the estimates via the SEP observations.
The three SEP observations were combined with the help of the ftool[6] (Blackburn, 1995) task *mathpha*. This function was used to sum up the spectra and the exposure times of the individual SEP observations. For area correction, the backscale keyword in the header of the resulting FITS[7]-file has been set to the mean value

the comparison of a spectral model with observations data is only reasonable after folding the model with the ARF and the RMF.

[6] ftool: Ftool is a general package of software for the manipulation of FITS files. It is available at `http://heasarc.gsfc.nasa.gov/ftools/`.

[7] FITS – Flexible Image Transport System: FITS is a format for images which has been developed to handle multidimensional arrays and 2-dimensional tables. Therefore, it is ideal for storing spectra, images, and data cubes. Thus, it is widely spread in astronomy, for which it has originally been established. The format has been developed in the late 1970's and was first standardized in 1981. It consists of one or more cooperated header plus data units,

of the backscale variable of the three individual SEP observations.

The normalizations of the model components representing the cosmic X-ray background were fitted freely and linked between all detectors. The other parameters of these components were frozen. The normalizations of the Gaussians were unlinked for all detectors and observations. During the fitting procedure, the positions of the lines were first frozen at their respective energies. After the other components were reasonably fitted, the energies of the Gaussians were fitted freely and then frozen again. Gaussians which could not be fitted due to the low statistics of the observations were set to a normalization of zero and frozen.
The power law index of the models representing residual soft proton flares should not be linked between EPIC-pn and EPIC-MOS data due to their different response to them, and none of the normalizations should be linked (Snowden and Kuntz, 2011b). Since the statistics of the observations used for the studies within this thesis did not allow a free fitting of their power law indices, they were frozen at 1 and only their unlinked normalizations were fitted.
Before fitting, all spectra were binned to a minimum of 50 counts per channel. The fits were performed in an energy range of $0.3-10\,\mathrm{keV}$ and $0.4-10\,\mathrm{keV}$, depending on the level of detector noise in the energy range $<0.4\,\mathrm{keV}$. The specific fitting procedures used for the analysis of the supergiant shell LMC-SGS 2 and of DEM L299 are described in the Sections 5.5 and 6.4, respectively.

As a first test of the established model, it was used to fit the supernova remnant DEM L316a, which is one of the two supernova remnants in DEM L316 visible in Observation 3 (see Fig. 5.1). The fitting results were compared with the ones obtained by Williams and Chu (2005), who used the same *XMM-Newton* data together with additional *Chandra* data to study DEM L316a. Since both results were in good agreement, major flaws in the established model could be excluded. In the following section, the results of the thus performed X-ray spectral analysis of the supergiant shell LMC-SGS 2 are given.

5.5 X-ray Spectral Analysis

An X-ray spectral analysis of LMC-SGS 2 was performed using the data of the seven *XMM-Newton* EPIC observations of the LMC-SGS 2 region (see Table 5.1). As spectral extraction regions, the entire field of view of each individual observation was taken, and a spectral analysis has been performed individually for each of these observations. In addition, one smaller spectral extraction region has been defined for each pointing, which was taken as a cross-check for the fitting results

in which – besides the data itself – a lot of additional information about the data and the observation can be stored.

of the entire FOV (see below). For the spectral fits, the model described in Section 5.4 has been used. To model the emission of LMC-SGS 2, the Xspec models *apec*, *vpshock*, and *vnei* were tested separately as source component (see Sect. 5.4). Their temperature was fitted freely, while different temperatures were tried as a starting point of the fits. The LMC-SGS 2 data of each pointing were fitted simultaneously with the combined SEP data. Since the combined SEP observations have much higher statistics than the individual LMC-SGS 2 observations, the SEP data dominate in the calculation of the reduced χ^2. Hence, as a next step, the back- and foreground components of the LMC-SGS 2 spectra were frozen at the values determined during the simultaneous fits, and the SEP data were removed. Thus, the source component of the LMC-SGS 2 model was fitted again to the LMC-SGS 2 data alone – without the SEP data, but with the previously determined, frozen background components – in order to obtain a more meaningful reduced χ^2. (The same fitting method was applied to the DEM L299 spectra; see Sect. 6.4.)
For Observation 7, which was initially intended as a test for the local background, no conclusive fitting results could be achieved, due to the low statistics of this observation. Therefore, this observation was not suitable for an additional, local background estimation.

As spectral extraction regions of each observation, the entire FOV of the respective observation was chosen for each pointing, since the major part of the emission present in these observations seems to originate from LMC-SGS 2 and the X-ray spur (see Fig. 5.9a). This estimation is not valid for Observations 1 and 3, which show bright X-ray emission originating from DEM L299 (i.e. from the DEM L299 superbubble and from SNR B0543-68.9) and DEM L316, respectively (see Figs. 5.1 and 5.4). Hence, the contribution of this emission to the LMC-SGS 2 emission was accounted for by adding an additional component to the model of these observations with the best-fit parameters of DEM L299 and DEM L316. The best-fit parameters for DEM L299 were taken from the X-ray spectral analysis performed for the DEM L299 superbubble and for SNR B0543-68.9 within the scope of this thesis (see Chapt. 6), and those for DEM L316 from Williams and Chu (2005). Since these additional components improved slightly the reduced χ^2 of these fits, the fitting results obtained with this additional model component were used when determining the parameters of LMC-SGS 2.
To test the validity of the assumption that the FOV emission is dominated by the LMC-SGS 2 emission, smaller spectral extraction regions were defined, which possess lower statistics but do not go beyond the border of LMC-SGS 2 or the X-ray spur, as defined by the X-ray emission (see Fig. 5.9b). The selection criteria for these smaller extraction regions comprised a coverage of LMC-SGS 2 or the X-ray spur as defined in X-rays, as little stray light contamination through LMC X-1 as possible (quantified through the X-ray images of Fig. 5.4), and the availability of

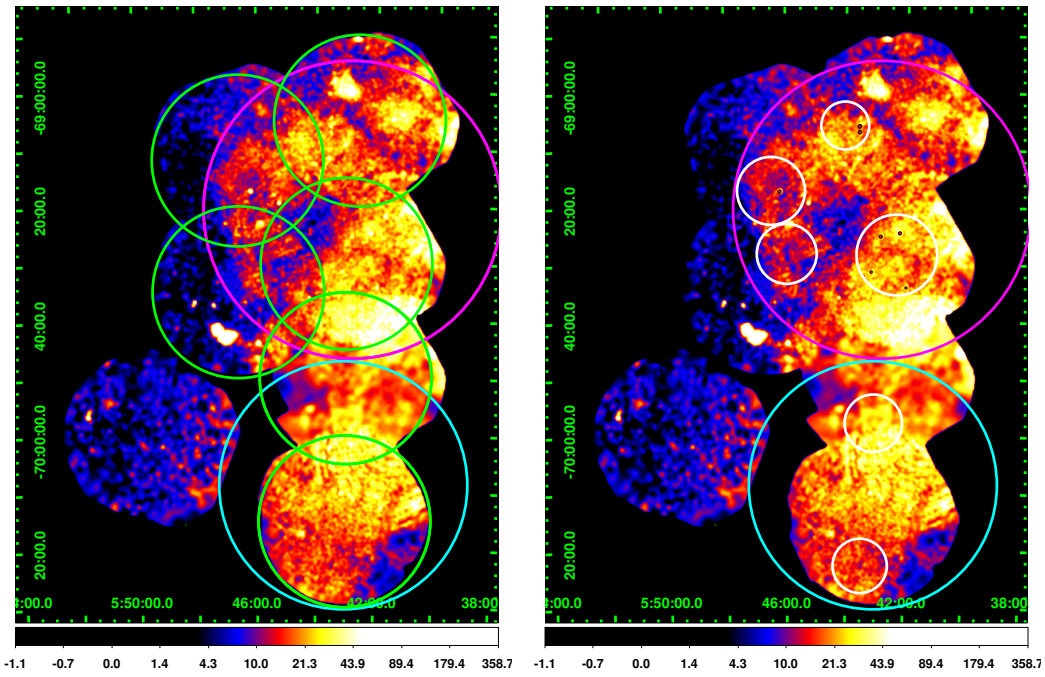

Figure 5.9: Broadband X-ray image of Figure 5.4d showing the spectral extraction regions of LMC-SGS 2 and the X-ray spur. In (a), the spectral extraction regions are defined as the FOV of each observation (marked in green), while (b) shows the smaller extraction regions (marked in white), with the additionally removed point sources marked with small, black circles. In both images, the magenta circle indicates the position of the sphere which has been used to determine the intersecting volume of the cylinder as defined by the spectral extraction regions and the approximate volume of the supergiant shell. The blue circle indicates the same for the X-ray spur.

data of all three *XMM-Newton* EPIC detectors for this region.[8] For Observation 1, an area had to be selected for which no EPIC-MOS1 data were available, due to a too large stray light contamination of the other parts of the FOV which cover the LMC-SGS 2 emission. Thus, the spectra of this region possess a lower statistics than that of the other regions. For the smaller extraction regions, seven additional point sources have been excluded, which were not detected during point-source screening: two point sources in Observation 1, one point source in Observation 2, and four point sources in Observation 4 (see Fig. 5.9b). These point sources were not detected during data processing and are not excluded in the spectra of the entire FOV.

[8] For all observations, data of at least one EPIC-MOS detector had to be excluded from the analysis due to anomalous state activity (see Sect. 4.1).

Table 5.4: Best-fit parameters obtained for the *XMM-Newton* EPIC observations of LMC-SGS 2 (Obs. 1 – 4) and the X-ray spur (Obs. 5 and 6) for the entire FOV of each observation (see Fig. 5.9a). In addition, the average values of the fitting results are listed for LMC-SGS 2 and the X-ray spur. Listed is the temperature $k_{\mathrm{B}}T$, the ionization timescale τ, the normalization *norm* (also referred to as K), the column density $N_{\mathrm{H,LMC}}$ of hydrogen within the LMC, and the reduced χ^2 of the fits with (first value) and without (second value, in parenthesis) the influence of the SEP observations on the reduced χ^2. For Observation 1 and 3, those fitting results are listed for which the additional sources of emission within the FOV have been modeled. For all observations, these best-fit parameters were obtained with the *vpshock* model. Uncertainties are upper and lower 90 % confidence ranges.

Obs.-ID	$k_{\mathrm{B}}T$ [keV]	τ [10^{11} s cm^{-3}]	*norm* [10^{-2} cm^{-5}]	$N_{\mathrm{H,LMC}}$ [10^{22} cm^{-2}]	Red. χ^2
1) 0094410101	0.63 (0.60 – 0.66)	2.2 (2.1 – 2.7)	1.1 (1.0 – 1.2)	0.42 (0.38 – 0.45)	1.1 (1.5)
2) 0201030201	0.52 (0.49 – 0.54)	4.9 (4.1 – 5.7)	0.85 (0.75 – 1.0)	0.45 (0.39 – 0.52)	1.1 (1.6)
3) 0201030101	0.62 (0.60 – 0.65)	2.3 (1.9 – 3.0)	0.69 (0.61 – 0.79)	0.60 (0.53 – 0.61)	1.2 (1.6)
4) 0094410201	0.61 (0.60 – 0.62)	2.9 (2.7 – 3.2)	1.2 (1.1 – 1.3)	0.26 (0.25 – 0.29)	1.3 (1.9)
LMC-SGS 2	0.60 (0.58 – 0.62)	3.1 (2.8 – 3.5)	0.96 (0.91 – 1.02)	0.43 (0.40 – 0.46)	1.2 (1.7)
5) 0094410701	0.58 (0.54 – 0.59)	4.1 (3.3 – 5.2)	1.1 (0.9 – 1.3)	0.14 (0.08 – 0.22)	1.1 (2.0)
6) 0201030301	0.47 (0.45 – 0.49)	5.1 (4.6 – 5.6)	1.6 (1.4 – 1.8)	0.38 (0.34 – 0.42)	1.3 (1.8)
X-ray spur	0.53 (0.50 – 0.55)	4.6 (4.1 – 5.3)	1.4 (1.2 – 1.6)	0.26 (0.22 – 0.30)	1.2 (1.9)

Table 5.5: Same as Table 5.4, but for the fitting results of the smaller spectral extraction regions as indicated in Figure 5.9b.

Obs.-ID	$k_{\mathrm{B}}T$ [keV]	τ [10^{11} s cm^{-3}]	*norm* [10^{-2} cm^{-5}]	$N_{\mathrm{H,LMC}}$ [10^{22} cm^{-2}]	Red. χ^2
1) 0094410101	0.56 (0.48 – 0.62)	3.6 (2.3 – 5.3)	0.13 (0.10 – 0.18)	0.33 (0.21 – 0.48)	0.9 (1.2)
2) 0201030201	0.51 (0.47 – 0.54)	6.4 (4.8 – 8.9)	0.24 (0.20 – 0.32)	0.50 (0.47 – 0.54)	1.0 (1.6)
3) 0201030101	0.59 (0.47 – 0.64)	5.3 (1.6 – 8.6)	0.17 (0.16 – 0.36)	0.57 (0.52 – 0.91)	0.9 (1.6)
4) 0094410201	0.62 (0.60 – 0.64)	3.2 (2.6 – 3.8)	0.33 (0.31 – 0.36)	0.25 (0.20 – 0.29)	0.9 (1.2)
LMC-SGS 2	0.57 (0.54 – 0.63)	4.6 (3.5 – 5.8)	0.22 (0.20 – 0.28)	0.41 (0.37 – 0.51)	1.0 (1.5)
5) 0094410701	0.63 (0.55 – 0.73)	2.6 (1.2 – 4.6)	0.12 (0.10 – 0.17)	0.14 (0.01 – 0.31)	0.9 (1.4)
6) 0201030301	0.42 (0.31 – 0.47)	9.8 (> 6.9)	0.25 (0.19 – 0.54)	0.41 (0.33 – 0.56)	0.9 (1.4)
X-ray spur	0.53 (0.46 – 0.59)	6.2 (> 4.5)	0.19 (0.15 – 0.34)	0.28 (0.20 – 0.40)	0.9 (1.4)

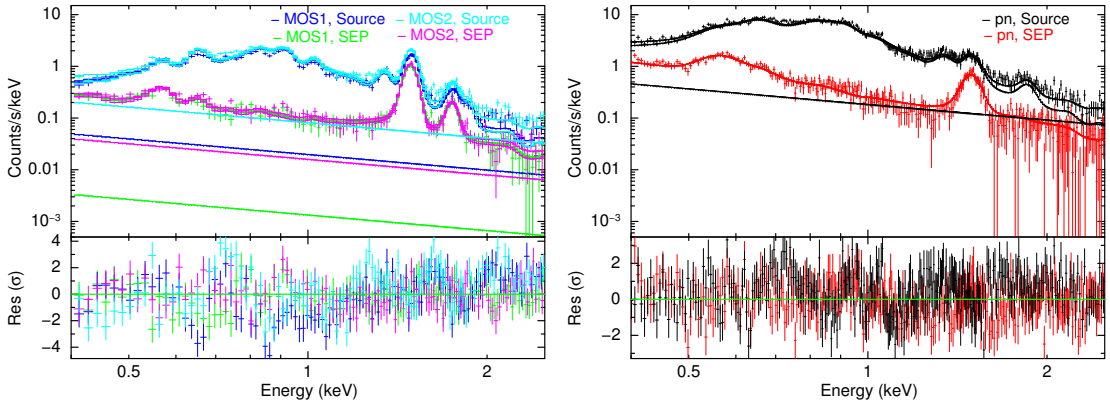

(a) (b)

Figure 5.10: Source and SEP data points and fitted model for the entire FOV of Observation 1 with Obs.-ID 0094410101, for (a) the EPIC-MOS1 and EPIC-MOS2 detectors, and (b) the EPIC-pn detector. For these fits, the *vpshock* model has been used as the source component. The spectrum is plotted in an energy range of 0.4 – 2.5 keV, and the residuals are shown in the lower part of the plot. The modelled residual soft proton component is visible as a straight line. Crosses indicate data points, while the solid lines are the fitted model with (upper line) and without (lower line) the contribution of the residual soft proton component to the model.

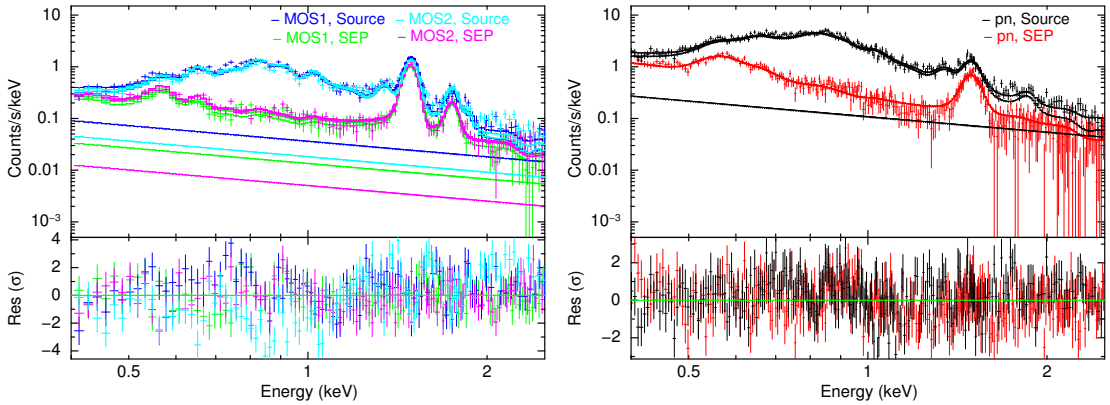

(a) (b)

Figure 5.11: Same as Figure 5.10, but for Obs. 2 with Obs.-ID 0201030201.

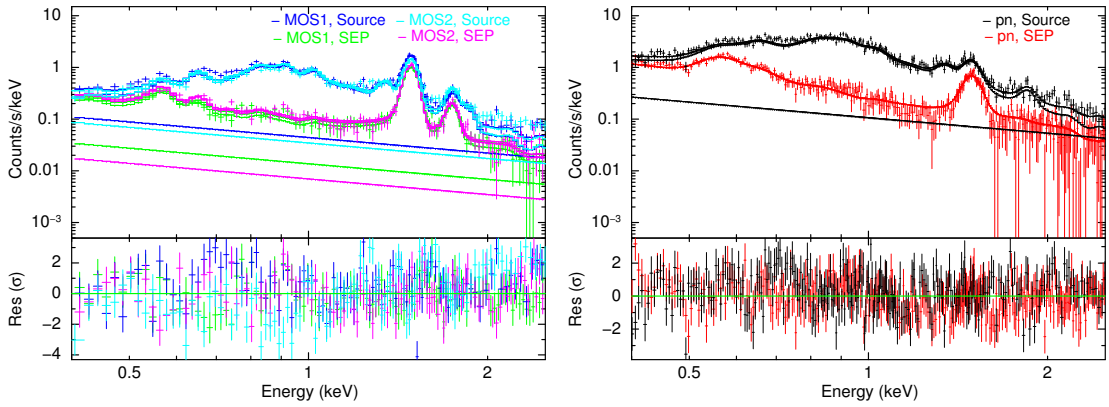

(a) (b)

Figure 5.12: Same as Figure 5.10, but for Obs. 3 with Obs.-ID 0201030101.

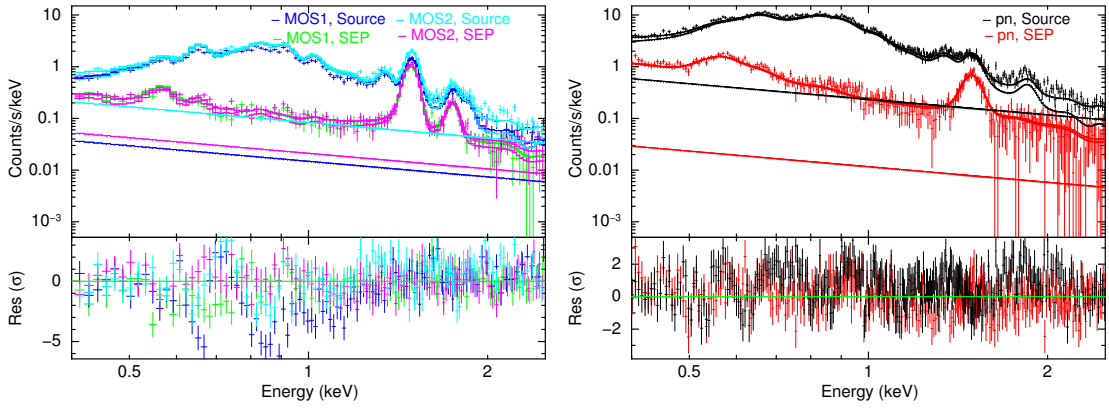

(a) (b)

Figure 5.13: Same as Figure 5.10, but for Obs. 4 with Obs.-ID 0094410201.

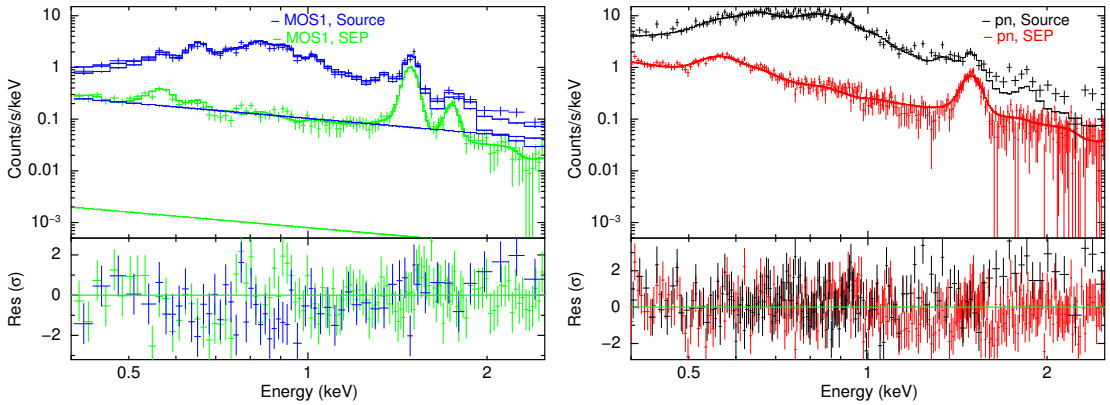

(a) (b)

Figure 5.14: Same as Figure 5.10, but for Obs. 5 with Obs.-ID 0094410701.

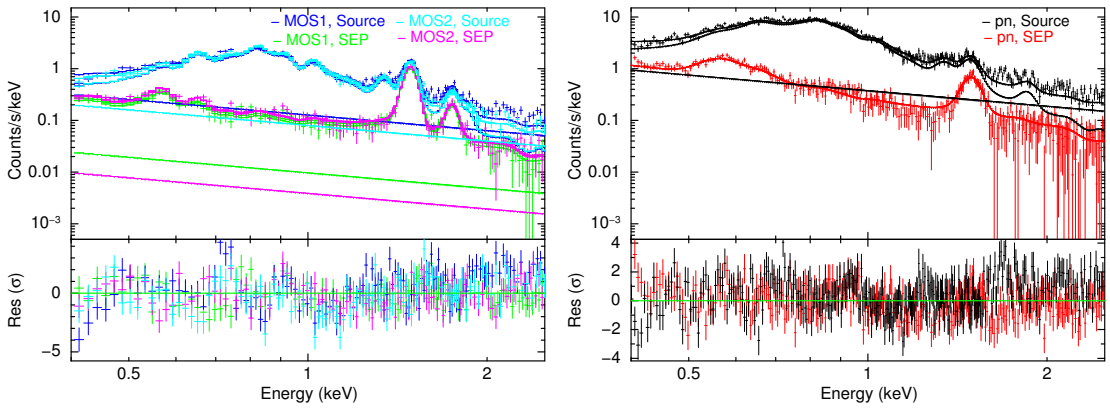

(a) (b)

Figure 5.15: Same as Figure 5.10, but for Obs. 6 with Obs.-ID 0201030301.

For the observations of the supergiant shell and of the X-ray spur, the best reduced χ^2 was obtained with the *vpshock* model. The resulting best-fit parameters for the FOV extraction regions and for the smaller extraction regions are listed in Table 5.4 and 5.5. The spectral fits of the entire FOV of the individual observations and the respective smaller extraction region resulted in similar best-fit temperatures with overlapping confidence intervalls. Thus, temperatures obtained from the FOV of each observation were confirmed by the fitting results of the smaller regions. The results of both types of extraction regions will be considered in Section 5.6 when determining further properties of LMC-SGS 2 and the X-ray spur. The fitted spectra extracted from the entire FOV of the individual pointings are plotted in Figure 5.10 – 5.15. The four individual LMC-SGS 2 observations resulted to have an average temperature of $(0.60^{+0.02}_{-0.02})$ keV, i.e. $(7.0^{+0.3}_{-0.3}) \times 10^6$ K, (for the smaller extraction regions: $(0.57^{+0.06}_{-0.03})$ keV, i.e. $(6.7^{+0.7}_{-0.4}) \times 10^6$ K) and an average column density of $(0.43^{+0.03}_{-0.03}) \times 10^{22}\,\mathrm{cm}^{-2}$ (for the smaller extraction regions: $(0.41^{+0.10}_{-0.04}) \times 10^{22}\,\mathrm{cm}^{-2}$). The average ionization timescale was determined to be $(3.1^{+0.3}_{-0.4}) \times 10^{11}\,\mathrm{s\,cm}^{-3}$ (for the smaller extraction regions: $(4.6^{+1.2}_{-1.1}) \times 10^{11}\,\mathrm{s\,cm}^{-3}$), indicating that the gas has not yet re-established collisional ionization equilibrium. For the X-ray spur, the best-fit results were also obtained with the *vpshock* model. For this region, an average temperature of $(0.53^{+0.02}_{-0.03})$ keV, i.e. $(6.2^{+0.3}_{-0.4}) \times 10^6$ K, (for the smaller extraction regions: $(0.53^{+0.06}_{-0.07})$ keV, i.e. $(6.2^{+0.7}_{-0.9}) \times 10^6$ K) was determined, which is lower than for LMC-SGS 2. Also, the column density of $(0.26^{+0.04}_{-0.04}) \times 10^{22}\,\mathrm{cm}^{-2}$ (for the smaller extraction regions: $(0.28^{+0.12}_{-0.08}) \times 10^{22}\,\mathrm{cm}^{-2}$) is slightly lower than that for the supergiant shell. The ionization timescale was found to be $(4.6^{+0.7}_{-0.5}) \times 10^{11}\,\mathrm{s\,cm}^{-3}$ (for the smaller extraction regions: $6.2\,(>4.5) \times 10^{11}\,\mathrm{s\,cm}^{-3}$), indicating collisional non-equilibrium ionization. The determined temperature for LMC-SGS 2 is higher but comparable with the 0.43 keV as determined by Wang and Helfand (1991) using data from the *Einstein* observatory and assuming a column density of $\sim 0.3 \times 10^{22}\,\mathrm{cm}^{-2}$. This assumed column density is comparable to the one determined during the spectral analysis performed within the scope of this thesis. Considering the different column densities, the resulting temperatures seem to be in good agreement. Points et al. (2000) used the *ROSAT* data to study individual regions of LMC-SGS 2, for which they determined a temperature range of 0.1 –0.7 keV for the supergiant shell and 0.1 – 0.5 keV for the X-ray spur, which is in good agreement with the results of the analysis performed within the scope of this thesis. The same holds for the column density, for which Points et al. (2000) assumed values of $\sim 0.45\ (0.8 - 1.25)\ \times 10^{22}\,\mathrm{cm}^{-2}$ for LMC-SGS 2 and $\sim 0.42\ (0.07 - 1.35)\ \times 10^{22}\,\mathrm{cm}^{-2}$ for the X-ray spur (see Sect. 5.1).
The resulting column density towards the X-ray spur is much lower than the one determined towards LMC-SGS 2. Furthermore, the column density determined for Observations 2 and 3 are higher than those resulting for Observation 1 and 4, which is valid in particular for the fitting results of the smaller extraction regions listed in Table 5.5. This is in agreement with the X-ray morphology of

LMC-SGS 2 in the soft and medium energy band, in which the eastern part of the supergiant shell shows fainter X-ray emission than its western part (cf. Fig. 5.4), corresponding to a higher absorption.

5.6 Discussion

In this section, the fitted parameters of LMC-SGS 2 and the X-ray spur as described in Section 5.5 are used to calculate further properties of both objects. For these calculations, the ideal gas equations are used. A more detailed description of the used formulae can be found in Section 6.5.2, in which similar calculations have been performed for the DEM L299 superbubble.
The calculations have been performed individually for the average spectral results of the FOV and of the smaller extraction regions. The differences of the results of the spectral analysis for the different types of extraction regions had only a minor influence on the results of the properties determined in this section, with a difference of less than $\sim$ 5 % for LMC-SGS 2 and less than $\sim$ 8 % for the X-ray spur, and with the results for both extraction regions lying within the confidence ranges of each other for each observations, respectively.

The total hydrogen number density $n_{\mathrm{H,SGS}}$ of the hot gas inside LMC-SGS 2 was determined by using the fitted normalization K of the *vpshock* model, which provided the best fitting results for all pointings. For each of the four observations which cover LMC-SGS 2 (Obs. 1 – 4), a total hydrogen number density was determined using the equation

$$n_{\mathrm{H}} = \left(\frac{4\pi K D^2}{1.2 \times 10^{-14} V_{\mathrm{int}}\, \phi} \right)^{1/2} , \tag{5.1}$$

with D being the distance to the LMC and V_{int} being the volume resulting from the spectral extraction. For the calculation done for the entire FOV of each observation, this volume was defined as the intersection between a cylinder with a radius of $R_{\mathrm{c}} = 15'$ (as defined by the FOV of the individual observations) and a sphere with a radius $R_{\mathrm{S}} = 26'$ (as given by Kim et al. (2003) for LMC-SGS 2 as defined in H I), as shown in Figure 5.9a. The intersecting volume of both geometric shapes were determined according to Lamarche and Leroy (1990). This resulted in intersecting volumes of $2.08 \times 10^{63}\,\mathrm{cm}^3$, $1.31 \times 10^{63}\,\mathrm{cm}^3$, $9.95 \times 10^{62}\,\mathrm{cm}^3$, and $2.73 \times 10^{63}\,\mathrm{cm}^3$ for Observations 1 – 4. For the smaller extraction regions, the intersection of the respective cylinder defined by each extraction region and the sphere with a radius of $R_{\mathrm{S}} = 26'$ was taken (see Fig. 5.9b). This resulted in volumes of $3.67 \times 10^{62}\,\mathrm{cm}^3$, $3.22 \times 10^{62}\,\mathrm{cm}^3$, $2.75 \times 10^{62}\,\mathrm{cm}^3$, and $6.86 \times 10^{62}\,\mathrm{cm}^3$ for Observations 1 – 4. The filling factor ϕ for the hot gas inside the supergiant

shell was assumed to be equal to one. Averaging over the individual results for $n_{\rm H,SGS}$ obtained for each of the four observations, a mean total hydrogen number density $< n_{\rm H,SGS} >$ of $(0.012^{+0.001}_{-0.001})\,\phi^{-0.5}\,{\rm cm}^{-3}$ was obtained for LMC-SGS 2 as determined for the FOVs, and of $(0.012^{+0.002}_{-0.001})\,\phi^{-0.5}\,{\rm cm}^{-3}$ as determined for the smaller extraction regions. This average value for LMC-SGS 2 has been used to calculate the thermal pressure of the hot gas inside the supergiant shell by using the ideal gas equation, resulting in

$$p_{\rm SGS,i}/k_{\rm B} = 2.31 \; < n_{\rm H,SGS} > < T_{\rm X,SGS} > = (1.9^{+0.2}_{-0.2}) \; \times \; 10^5\,\phi^{-0.5}\,{\rm cm}^{-3}\,{\rm K}\,, \quad (5.2)$$

with $< T_{\rm X,SGS} >$ being the average fitted X-ray temperature of $(0.60^{+0.02}_{-0.02})\,{\rm keV}$ for LMC-SGS 2 as determined for the FOV (see Table 5.4).[9] For the smaller extraction regions, the average temperature of $(0.57^{+0.06}_{-0.03})\,{\rm keV}$ lead to a thermal pressure of $(1.8^{+0.4}_{-0.2}) \; \times \; 10^5\,\phi^{-0.5}\,{\rm cm}^{-3}\,{\rm K}$. The resulting thermal pressure is in agreement with the pressure of $\sim 10^5 - 10^6\,{\rm cm}^{-3}\,{\rm K}$ as expected for star-forming regions (Malhotra et al., 2001) and conforms to the value of $\sim 10^5\,{\rm cm}^{-3}\,{\rm K}$ as estimated by Oey and García-Segura (2004) for the LMC. The resulting pressure is higher than determined for example for another LMC supergiant shell (LMC-SGS 4: $p_{\rm SGS,i}/k_{\rm B} = 2 \times 10^4\,{\rm cm}^{-3}\,{\rm K}$, Bomans et al., 1994) using *ROSAT* data, but comparable values and higher values have also been obtained for LMC superbubbles (e.g. for LHA-N 158: $p_{\rm SB,i}/k_{\rm B} = (1.1^{+0.3}_{-0.3}) \; \times \; 10^6\,\phi^{-0.5}\,{\rm cm}^{-3}\,{\rm K}$, Sasaki et al., 2011). Despite of the high interior pressure of the supergiant shell, it can survive in the LMC due to the galaxy's large interstellar pressure, which counteracts the shell growth (Oey and García-Segura, 2004). A large interstellar pressure, which is larger than the midplane pressure estimated for the Milky Way ($3 \times 10^4\,{\rm cm}^{-3}\,{\rm K}$, see e.g. Oey and García-Segura, 2004), is typical for star-forming galaxies, since the turbulent pressure, cosmic-ray pressure, and magnetic pressure increase with the star-formation rate (e.g. Oey and García-Segura, 2004). In addition, the expansion of the bubble leads to a compression of the ambient magnetic field, which counteracts the expansion as a self-induced impedance (Slavin and Cox, 1992).
The thermal energy content of the hot gas inside the supergiant shell can be determined by using the ideal gas equations through the following relation:

$$E_{\rm th,SGS} = (3/2)\,p_{\rm SGS,i} V_{\rm SGS}\,\phi = (1.1^{+0.2}_{-0.3}) \; \times \; 10^{53}\,\phi^{0.5}\,{\rm erg}\,, \quad (5.3)$$

with $V_{\rm SGS} = (2.88^{+0.26}_{-0.57}) \times 10^{63}\,{\rm cm}^3$ being the volume of LMC-SGS 2 as defined by the X-ray emission (see Fig. 5.16). This volume has been approximated by an ellipsoid with radii of $a = 18\farcm5^{+0\farcm6}_{-2\farcm1} = c$ (i.e. $(\sim 269^{+12}_{-32})\,{\rm pc}$) and $b = 22\farcm2^{+1\farcm2}_{-2\farcm0}$ (i.e. $(\sim 323^{+20}_{-32})\,{\rm pc}$), as indicated in Figure 5.16. For the smaller extraction regions, a thermal energy content of $(1.1^{+0.3}_{-0.3}) \; \times \; 10^{53}\,\phi^{0.5}\,{\rm erg}$ has been obtained.

[9] Unless otherwise stated, the given values are the results as obtained from the data of the entire FOV, while the results from the smaller spectral extraction regions are given in brackets.

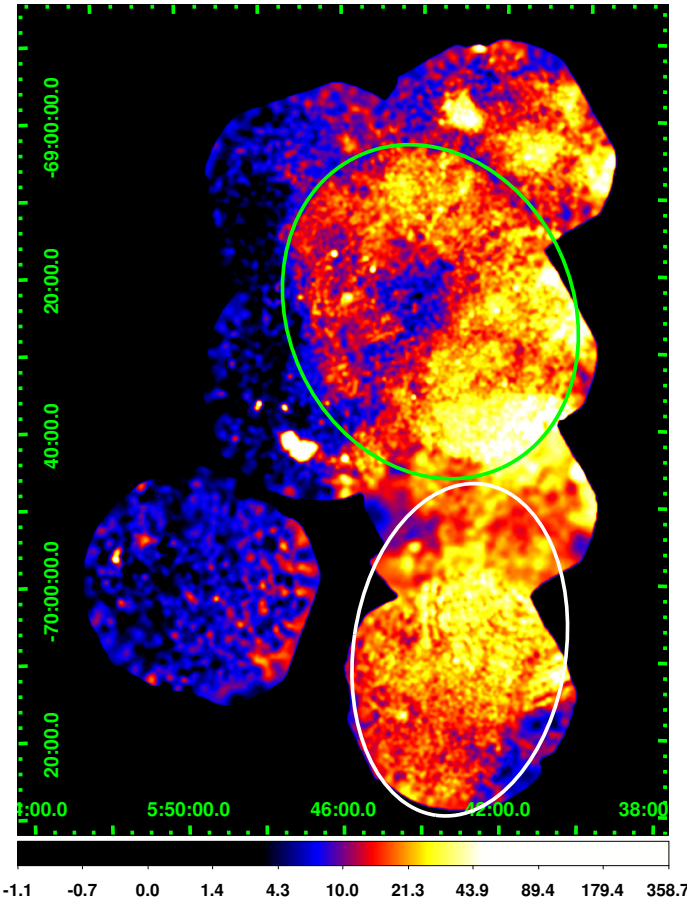

Figure 5.16: Broadband X-ray image of Figure 5.4d, in which the areas are indicated which show diffuse X-ray emission projected towards LMC-SGS 2 (marked in green) and towards the X-ray spur (marked in white). These ellipses have been used to estimate the volume of the X-ray emitting region of LMC-SGS 2 and the X-ray spur.

As expected, the calculated thermal energy content of the hot gas is lower than the energy input of $\sim 3 \times 10^{53}$ erg through stellar winds and supernovae which has been determined by Wang and Helfand (1991) using data of the *Einstein* Observatory. The thermal energy of the hot gas is required to be lower than the total energy input, since part of the energy can be found as kinetic energy of the warm and cold shell of the supergiant shell.
The mass of the hot gas inside LMC-SGS 2 has been calculated by applying the equation

$$M_{\mathrm{SGS,i}} = 2.31 \; < n_{\mathrm{H,SGS}} > \mu \, m_{\mathrm{H}} V_{\mathrm{SGS}} \, \phi = (4.1^{+0.1}_{-1.0}) \times 10^4 \, \phi^{0.5} \, M_{\odot} \, , \qquad (5.4)$$

with $\mu = 0.61$ being the molecular weight of a fully ionized gas and m_{H} being the hydrogen mass. For the smaller extraction regions, a mass of $(4.1^{+0.9}_{-1.0}) \times 10^4 \, \phi^{0.5} \, M_{\odot}$

has been determined. The mass and the thermal energy content of the hot gas have a strong dependance on the volume assumed for the X-ray emitting region. Thus, an increase of the volume by a factor of two leads to an increase of the mass and energy content of about the same factor. This should be kept in mind when considering these values.

The same calculations have been performed for the X-ray spur which extends south of LMC-SGS 2. For the calculations performed with the fitting results for the entire FOV of each observation, the volume $V_{\mathrm{int,XS}}$ has been assumed to be equal to the intersecting volume of a cylinder with a radius of $15'$ (corresponding to the FOV of each individual observation) and a sphere with a radius ~ 200 pc (as assumed by Points et al. (2000) for half the width and depth of the X-ray spur), as can be seen in Figure 5.9a. This intersecting volume has been determined according to Lamarche and Leroy (1990) and resulted to be $1.002 \times 10^{63}\,\mathrm{cm}^3$ and $2.222 \times 10^{63}\,\mathrm{cm}^3$ for Observations 5 and 6. (For the intersection of the sphere with the cylinders as defined by the smaller extraction regions, a volume of $2.619 \times 10^{62}\,\mathrm{cm}^3$ and $2.020 \times 10^{62}\,\mathrm{cm}^3$ has been determined for Observations 5 and 6; see Fig. 5.9b.) This led to a mean total hydrogen number density of $< n_{\mathrm{H,SGS,XS}} > = (0.015^{+0.002}_{-0.002})\,\phi^{-0.5}\,\mathrm{cm}^{-3}$. (For the smaller extraction regions, a value of $(0.014^{+0.06}_{-0.002})\,\phi^{-0.5}\,\mathrm{cm}^{-3}$ has been obtained.) The volume of the X-ray emitting region required for the determination of the thermal energy content and the mass of the hot gas has been defined according to the X-ray images as an ellipse with radii of $a = 21\farcm66^{+0\farcm2}_{-0\farcm8}$ (i.e. $(\sim 314.8^{+9.0}_{-14.8})$ pc) and $b = 13\farcm76^{+1\farcm91}_{-2\farcm32} = c$ (i.e. $(\sim 199.9^{+28.4}_{-34.2})$ pc), resulting in a volume of $(1.548^{+0.315}_{-0.382}) \times 10^{63}\,\mathrm{cm}^3$ (see Fig. 5.16). For the hot gas,

- a pressure of $p_{\mathrm{SGS,XS,i}}/k_{\mathrm{B}} = (2.1^{+0.4}_{-0.4}) \times 10^5 \phi^{-0.5}\,\mathrm{cm}^{-3}\,\mathrm{K}$,
  (for the smaller extraction regions: $(< 2.0^{+0.4}) \times 10^5 \phi^{-0.5}\,\mathrm{cm}^{-3}\,\mathrm{K}$)
- a thermal energy content of $E_{\mathrm{th,SGS,XS}} = (0.67^{+0.19}_{-0.21}) \times 10^{53}\,\phi^{0.5}\,\mathrm{erg}$
  (for the smaller extraction regions: $(< 0.64^{+0.19}) \times 10^{53}\,\phi^{0.5}\,\mathrm{erg}$), and
- a mass of $M_{\mathrm{SGS,XS,i}} = (2.8^{+0.8}_{-0.9}) \times 10^4\,\phi^{0.5}\,M_\odot$
  (for the smaller extraction regions: $(< 2.6^{+0.7}) \times 10^4\,\phi^{0.5}\,M_\odot$)

were calculated. Again, the mass and the energy content depend strongly on the assumed volume of the X-ray emitting region. Furthermore, it has to be considered that Observation 5 does not only have a lower statistics than the other observations (see Table 5.2), but that it includes emission of both the X-ray spur and of LMC-SGS 2. Thus, for the X-ray spur, the results of the smaller extraction regions should be favored instead of the entire FOV, although they possess the lower statistics.

The values obtained for the X-ray spur can be used to determine an estimation of the parameters for LMC-SGS 2 plus the X-ray spur, for the case that both areas should be physically connected. Adding both results,

- a the thermal energy content of $E_{\mathrm{th,SGS}} = (1.8^{+0.3}_{-0.4}) \times 10^{53}\,\phi^{0.5}\,\mathrm{erg}$
  (for the smaller extraction regions: $(< 1.7^{+0.4}) \times 10^{53}\,\phi^{0.5}\,\mathrm{erg}$), and
- a mass of $M_{\mathrm{SGS,i}} = (6.9^{+0.9}_{-1.4}) \times 10^{4}\,\phi^{0.5}\,M_{\odot}$
  (for the smaller extraction regions: $(< 6.7^{+1.2}) \times 10^{4}\,\phi^{0.5}\,M_{\odot}$)

were obtained for the hot gas.

All determined parameters are consistent with the concept of a supergiant shell. In order to get better constraints on the parameters, more detailed spectral extraction regions are required, as well as longer observation times. This would also allow for a more detailed analysis of the spatial dependance of the different parameters, which requires longer observation times, since the current X-ray data possess too low statistics for the definition of small spectral extraction regions.

5.7 Summary and Outlook

In this chapter, the morphological and X-ray spectral analysis of LMC-SGS 2 and the X-ray spur were presented. After an introduction to the used data sets of *XMM-Newton* and to the model used for the spectral fits, the morphological studies performed in X-ray, optical, and radio wavelengths were presented. For these studies, X-ray images of the LMC-SGS 2 region were created which show the supergiant shell in more detail than previous studies did. This allows a more precise confinement of the supergiant shell, enabling a better characterization of its properties.

In the X-ray spectral analysis, basic properties of LMC-SGS 2 and the X-ray spur could be determined for two kinds of spectral extraction regions. For both LMC-SGS 2 and the X-ray spur, the best fitting results were achieved with the *vpshock* model.

For LMC-SGS 2, the obtained average best-fit values for the FOVs are

- a temperature of $k_{\mathrm{B}}T_{\mathrm{X,SGS}} = (0.60^{+0.02}_{-0.02})\,\mathrm{keV}$
  (for the smaller extraction regions: $(0.57^{+0.06}_{-0.03})\,\mathrm{keV}$),
- an ionization timescale of $\tau_{\mathrm{SGS}} = (3.1^{+0.3}_{-0.4}) \times 10^{11}\,\mathrm{s\,cm^{-3}}$
  (for the smaller extraction regions: $(4.6^{+1.2}_{-1.1}) \times 10^{11}\,\mathrm{s\,cm^{-3}}$), and
- a column density within the LMC of $N_{\mathrm{H,LMC,SGS}} = (0.43^{+0.03}_{-0.03}) \times 10^{22}\,\mathrm{cm^{-2}}$
  (for the smaller extraction regions: $(0.41^{+0.10}_{-0.04}) \times 10^{22}\,\mathrm{cm^{-2}}$).

The X-ray spur was found to have

- a temperature of $k_{\mathrm{B}}T_{\mathrm{X,SGS,XS}} = (0.53^{+0.02}_{-0.03})\,\mathrm{keV}$
  (for the smaller extraction regions: $(0.53^{+0.06}_{-0.07})\,\mathrm{keV}$),
- an ionization timescale of $\tau_{\mathrm{SGS,XS}} = (4.6^{+0.7}_{-0.5}) \times 10^{11}\,\mathrm{s\,cm^{-3}}$
  (for the smaller extraction regions: $6.2\,(>\,4.5) \times 10^{11}\,\mathrm{s\,cm^{-3}}$), and
- a column density of $N_{\mathrm{H,LMC,SGS,XS}} = (0.26^{+0.04}_{-0.04}) \times 10^{22}\,\mathrm{cm^{-2}}$
  (for the smaller extraction regions: $(0.28^{+0.12}_{-0.08}) \times 10^{22}\,\mathrm{cm^{-2}}$).

The obtained temperatures and the densities are consistent with values reported in previous studies by Wang and Helfand (1991) and Points et al. (2000). Furthermore, the column densities are coherent with the results of the morphological studies. The ideal gas equations were used to calculate further properties of LMC-SGS 2 and the X-ray spur out of the parameters obtained during the spectral analysis. A summary of these determined properties is provided in Table 5.6. By comparison with the smaller extraction regions, it was shown that the spectral extracted from the entire FOV of each observation are representative for the emission of LMC-SGS 2 and the X-ray spur. When considering these results, it should be kept in mind that the thermal energy content and the mass of the hot gas depend strongly on the volume assumed for the X-ray emitting gas.

To obtain more precise values for the parameters of LMC-SGS 2 and the X-ray spur, a spectral analysis of smaller regions is necessary, which follow the morphology of the X-ray emission more accurately. Since the current *XMM-Newton* data possess too low statistics for the definition of small spectral extraction regions, further X-ray observations are required to perform a detailed morphological and spectral spatial analysis of LMC-SGS 2, in which the spatial dependance of these parameters can be examined. An estimation of the stray light contamination of these pointings by LMC X-1 will allow to determine the properties of the gas more accurately. A population study of the LMC-SGS 2 region would enable the creation of an energy budget for the supergiant shell. This could be used to test if the growth-rate discrepancy (see Sect. 2.4.1) observed for superbubbles also applies for LMC-SGS 2. Furthermore, the luminosity of LMC-SGS 2 can be determined out of the X-ray data. In order to obtain a good estimate for the luminosity, the contribution of low- and high-mass stars to the diffuse X-ray emission of this region has to be determined. Additional X-ray observations of the X-ray spur – in particular of the region covered by Observation 5 which was heavily contaminated by solar flares – will allow for a more complete mass and energy determination for LMC-SGS 2 and the X-ray spur. In addition, the stellar contribution to the diffuse emission of LMC-SGS 2 and in particular of the X-ray spur has to be investigated by performing a population study and determining the number of low- and high-mass stars within this region.

All these studies are complicated by the vast extent ($\sim 900\,\mathrm{pc}$) of the supergiant shell. These tasks are easier to accomplish for superbubbles, which follow the same physical principles as supergiant shells, but have much smaller sizes of $\sim 100\,\mathrm{pc}$. The studies performed within the scope of this thesis for the DEM L299 superbubble are discussed in the following chapter, together with the analysis of the supernova remnant SNR B0543-68.9.

Table 5.6: Summary of the calculated properties of supergiant shell LMC-SGS 2, the X-ray spur, and the combined values for the supergiant shell plus X-ray spur. Given are the results for the FOV of the observations and for the smaller extraction regions (s.e.r.).

Object	Parameter	Value	Unit
Supergiant Shell LMC-SGS 2; FOV	Pressure/k_B	$1.9^{+0.2}_{-0.2}$	$\times 10^5 \phi^{-0.5}\,\mathrm{cm^{-3}\,K}$
	Thermal energy content	$1.1^{+0.2}_{-0.3}$	$\times 10^{53} \phi^{0.5}\,\mathrm{erg}$
	Mass of the hot gas inside the superbubble	$4.1^{+0.1}_{-1.0}$	$\times 10^4\, \phi^{0.5}\,\mathrm{M_\odot}$
Supergiant Shell LMC-SGS 2; s.e.r.	Pressure/k_B	$1.8^{+0.4}_{-0.2}$	$\times 10^5 \phi^{-0.5}\,\mathrm{cm^{-3}\,K}$
	Thermal energy content	$1.1^{+0.3}_{-0.3}$	$\times 10^{53} \phi^{0.5}\,\mathrm{erg}$
	Mass of the hot gas inside the superbubble	$4.1^{+0.9}_{-1.0}$	$\times 10^4\, \phi^{0.5}\,\mathrm{M_\odot}$
X-ray spur; FOV	Pressure/k_B	$2.1^{+0.4}_{-0.4}$	$\times 10^5 \phi^{-0.5}\,\mathrm{cm^{-3}\,K}$
	Thermal energy content	$0.67^{+0.19}_{-0.21}$	$\times 10^{53}\, \phi^{0.5}\,\mathrm{erg}$
	Mass of hot gas	$2.8^{+0.8}_{-0.9}$	$\times 10^4\, \phi^{0.5}\,\mathrm{M_\odot}$
X-ray spur; s.e.r.	Pressure/k_B	$< 2.0^{+0.4}$	$\times 10^5 \phi^{-0.5}\,\mathrm{cm^{-3}\,K}$
	Thermal energy content	$< 0.64^{+0.19}$	$\times 10^{53}\, \phi^{0.5}\,\mathrm{erg}$
	Mass of hot gas	$< 2.6^{+0.7}$	$\times 10^4\, \phi^{0.5}\,\mathrm{M_\odot}$
Combined LMC-SGS 2 & X-ray spur; FOV	Thermal energy content	$1.8^{+0.3}_{-0.4}$	$\times 10^{53} \phi^{0.5}\,\mathrm{erg}$
	Mass of hot gas	$6.9^{+0.9}_{-1.4}$	$\times 10^4\, \phi^{0.5}\,\mathrm{M_\odot}$
Combined LMC-SGS 2 & X-ray spur; s.e.r.	Thermal energy content	$< 1.7^{+0.4}$	$\times 10^{53} \phi^{0.5}\,\mathrm{erg}$
	Mass of hot gas	$< 6.7^{+1.2}$	$\times 10^4\, \phi^{0.5}\,\mathrm{M_\odot}$

Chapter 6

DEM L299: Supernova Remnant and Superbubble

The H II region DEM L299 is a complex area of interstellar medium, which is located in the eastern part of the Large Magellanic Cloud and harbors the supernova remnant SNR B0543-68.9. It can be found east of the famous and large star-formation region 30 Doradus, and lies at the northern rim of the supergiant shell LMC-SGS 2. In the course of this dissertation, the morphology of DEM L299 has been studied at optical, radio, and X-ray wavelengths and a spectral analysis has been performed in the X-ray band. In optical light, emission line studies reveal the distribution and composition of the ionized and therefore warm gas of DEM L299. At radio frequencies, 21 cm H I data show the distribution of the neutral hydrogen of this region, and radio-continuum data provide information whether the radiation is of thermal or non-thermal origin. By using X-rays, the hot interstellar medium can be observed. These studies revealed a more complex structure of DEM L299 as expected on first glance, giving strong evidence for DEM L299 to be a superposition of the supernova remnant SNR B0543-68.9 with a superbubble.
In this chapter, the analyses of DEM L299 which have been performed within the scope of this thesis are described and the results of these studies are given. After an introduction to the DEM L299 region (see Sect. 6.1), the X-ray, optical, and radio data are presented (see Sect. 6.2). Section 6.3 discusses the morphological studies in these energy bands, followed by a description of the X-ray spectral analysis in Section 6.4. The results of these studies are used to calculate further properties of SNR B0543-68.9, the superbubble, and the blowout of the superbubble which is indicated by the optical images (see Sect. 6.5). The effects of non-equilibrium ionization on the resulting values are discussed and the contribution of stars to the X-ray luminosity of DEM L299 is determined. Finally, the energy and mass input to the superbubble through stellar winds and supernovae is calculated, before the chapter is concluded with a summary (Sect. 6.6). The analyses of the DEM L299 region and their results are published in Warth et al. (2014).

6.1 Introduction to DEM L299

DEM L299 is an H II region which has first been listed in the Hα catalog of Henize (1956) as the emission nebula LHA 120-N 165. In optical light, this H II region has a shell-like structure with a shell diameter of $\sim 5\farcm8 \times 4'$, corresponding to $\sim 84\,\mathrm{pc} \times 58\,\mathrm{pc}$ assuming an LMC distance of 50 kpc (Pietrzyński et al., 2013), and a central cavity of $1\farcm8 \times 2\farcm3$ ($26\,\mathrm{pc} \times 33\,\mathrm{pc}$), as determined by Desai et al. (2010). DEM L299 has been observed by the *Einstein Observatory* (Long et al., 1981; Wang et al., 1991) and by *ROSAT* (Haberl and Pietsch, 1999). While its X-ray size of $4\farcm3$ (62 pc) approximately corresponds to its optical size, it has a much smaller radio extent of $3'$ (44 pc) as determined by Berkhuijsen (1986). Within DEM L299 lies the supernova remnant SNR B0543-68.9, which has been classified as an SNR candidate in the Hα catalog of Davies et al. (1976) and has been optically confirmed by Mathewson et al. (1983).
The area around DEM L299 as observed in optical wavelengths is shown in Figure 6.1. Another, smaller H II region is projected at the north-western rim of DEM L299 with a diameter of $\sim 1'$. This H II region contains a young stellar object as well as an OB-star and is located exterior to the boundary of SNR B0543-68.9 (Desai et al., 2010). South of DEM L299 lies the H II region LHA 120-N 164, and in the west DEM L297 is situated. The H II region DEM L299 itself has previously not been studied very thoroughly due to its proximity to 30 Doradus and the busy field of view which makes it hard to observe, considering the given light-contamination and confusion with back- and foreground interstellar medium (cf. Fig. 6.1). The studies of DEM L299 performed in the course of this dissertation are the subject of this chapter and will be discussed in the following sections.

6.2 X-ray, Optical, and Radio Data

For the multi-wavelength study, data of X-ray, optical and radio wavelengths were used. These data and their reduction are discussed in this section.

For the X-ray analysis, data of the European Photon Imaging Camera of the satellite *XMM-Newton* were used (see Chapt. 3 for more information about *XMM-Newton*). For this study, the archived *XMM-Newton* observation 0094410101 was used, which will be hereafter referred to as the DEM L299 observation. This is one of the six observations used to investigate the supergiant shell LMC-SGS 2 as described in Chapter 5 and is roughly centered on the H II region LHA 120-N 164 which lies south of DEM L299 (cf. Fig. 6.1). This observation was taken in 2001 in full-frame mode with the medium filter and has an original duration

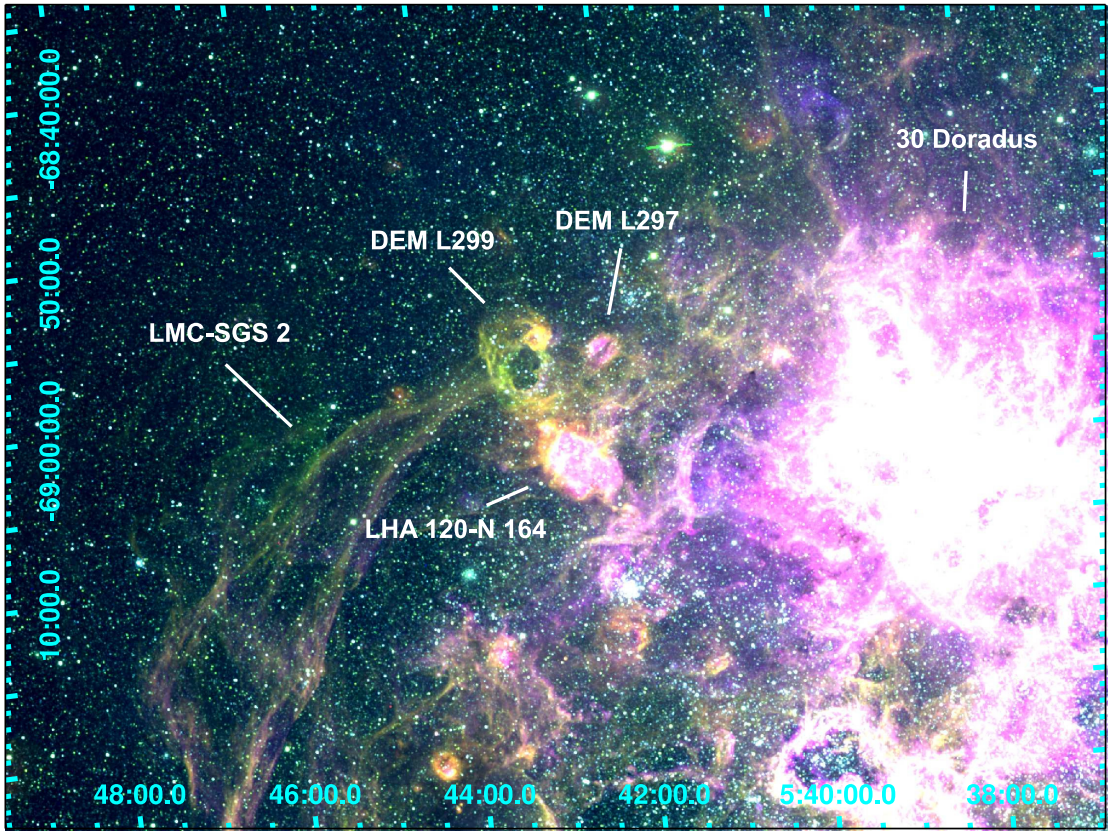

Figure 6.1: Three-color image of the vicinity of DEM L299 as observed in optical wavelengths. Hα emission is plotted in red, [S II] emission in green, and [O III] emission in blue. DEM L299 is visible at the center of the image as a shell-like structure, with the H II regions LHA 120-N 164 and DEM L297 lying south and west of it. The image is dominated by the bright star-forming region 30 Doradus in the west, and the northern half of the supergiant shell LMC-SGS 2 can be seen as a filamentary structure in the south-east. The image has been created out of MCELS data and shows an area of the sky of $\sim 67' \times 50'$ ($\sim 974\,\mathrm{pc} \times 727\,\mathrm{pc}$) with east towards the left side of the image and north upwards.

Table 6.1: Table showing the specifications of the *XMM-Newton* observations used for the X-ray analysis. Given are the soft proton flare filtered, effective observation times for the DEM L299 and the three SEP observations.

Observed Region	Obs.-ID	Filter	Eff. Obs. Time			P.I.*	Obs. Date
			MOS1 [ks]	MOS2 [ks]	pn [ks]		
DEM L299	0094410101	Medium	11.3	11.4	8.9	Y.-H. Chu	2001
SEP	0162160101	Thin1	12.0	12.4	9.8	B. Altieri	2003
SEP	0162160301	Thin1	8.6	8.6	8.0	B. Altieri	2003
SEP	0162160501	Thin1	9.5	9.3	7.8	B. Altieri	2003

* P.I.: principal investigator.

of 12 ks. After data processing, an effective observation time of 11 ks for the EPIC-MOS1 and EPIC-MOS2 detectors and 9 ks for the EPIC-pn detector were obtained (for more information about the observation and about the data processing, see Sect. 5.2 and Chapt. 4). Analog to the studies of supergiant shell LMC-SGS 2 (see Chapt. 5), the three combined observations of the South Ecliptic Pole (SEP) were used for background estimation, with an effective observation time of 30 ks for the EPIC-MOS1 and EPIC-MOS2 detectors and 26 ks for the EPIC-pn detector. More information about these four observations can also be found in Section 5.2 and in Table 6.1. The processing of these data was performed as described in Chapter 4 with the help of the *XMM-Newton* ESAS package. During the processing, the quiescent particle background, soft proton flares, and point sources were identified and subtracted. EPIC-MOS1 CCD5 of the DEM L299 observation has been found to be operating in an anomalous state and its data were therefore excluded from the analysis. The same is true for EPIC-MOS1 CCD4 of the SEP observation with Observation-ID 0162160301.

For the optical studies of DEM L299, data of the Magellanic Cloud Emission Line Survey (MCELS)[1] have been used (e.g. Smith et al., 2000). This survey is supported by the Cerro Tololo Inter-American Observatory (CTIO)[2] and the University of Michigan (UM). It covers most of the ionized interstellar medium of the Large and the Small Magellanic Cloud in three optical emission lines: the Hα line at 6563 Å, which is the transition line from the state of principle quantum number $n = 2$ to the $n = 3$ state of neutral hydrogen, and the two forbidden lines [S II] and [O III] at 6724 Å and 5007 Å. In addition, two continuum bands have been used in the survey for the subtraction of the stellar continuum. The data

[1] Magellanic Cloud Emission Line Survey (MCELS) homepage: `http://www.ctio.noao.edu/mcels/`

[2] For more information about the CTIO, see `http://www.ctio.noao.edu/noao/`

have been taken with the UM/CTIO Curtis Schmidt telescope, which is situated at CTIO in Chile to where it was moved in 1966 due to better observation conditions, after it had been installed in Michigan at the Portage Lake Observatory in 1950. This telescope is a 0.6-meter aperture f/3.5 Schmidt telescope and is dedicated to study artificial space debris. It has a SITE 2048×2048 CCD camera with a resolution of $2\farcs3$/pixel and an FOV of $1.35° \times 1.35°$ per image.
The MCELS data used in this analysis were reduced by Sean D. Points from the Cerro Tololo Inter-American Observatory, Chile. The data were sky-subtracted, flux-calibrated, and continuum subtracted. The images created out of these data are exposure time normalized to one second and smoothed.

In addition to these MCELS optical emission line data, radio-continuum data and H I 21 cm emission line data were used to study DEM L299 at radio wavelengths. For the radio-continuum studies, data of the Molonglo Synthesis Telescope (MOST) and the Australia Telescope Compact Array (ATCA) were used. MOST is a radio telescope observing at 843 MHz operated by the School of Physics of the University of Sydney and is located near the Molonglo River close to Canberra, Australia (see Fig. 6.2a). It consists of two cylindrical paraboloids and has a total size of $1.5\,\mathrm{km} \times 12\,\mathrm{m}$ (see MOST homepage[3]). The telescope is east-west aligned and can be rotated around its longer axis. MOST performed for example the Sydney University Molonglo Sky Survey (SUMSS) of the Southern Hemisphere. ATCA is an Australian telescope array which consists of five movable and one fixed 22-meter antennas (see Fig. 6.2b). The dishes can be moved in configurations with baselines between 75 m and 6 km. Thus, wavelengths between 0.3 cm and 20 cm can be observed (see ATCA Users Guide, 2010). It is located at the Narrabri Observatory and is part of the Australia Telescope National Facility (ATNF)[4]. The MOST and ATCA data of DEM L299 which were used within this thesis were processed by Luke M. Bozzetto and Miroslav D. Filipović from the University of Western Sydney, Australia. They used unpublished images as described by Mills et al. (1984) for 36 cm flux density measurements and images from Hughes et al. (2007) for 20 cm measurements. Furthermore, they combined the ATCA observations with mosaic observations from project C918 (Dickel et al., 2005). More about this radio-continuum data and the data reduction can be found for example in Warth et al. (2014).

[3] MOST homepage: `http://www.physics.usyd.edu.au/sifa/Main/MOST`

[4] ATNF – **A**ustralia **T**elescope **N**ational **F**acility: The ATNF is operated by Australia's national science agency CSIRO, the Commonwealth Scientific and Industrial Research Organisation. ATNF is a facility which is supporting Australia's research in radio astronomy. The four Australian radio observatories which are part of the ATNF – among them the ATCA and Parkes telescopes – can be used together for Very Long Baseline Interferometry which yields highly resolved radio data.

(a)

(b)

(c)

Figure 6.2: Three Australian radio telescopes. (a): The MOST radio telescope consists of two cylindrical paraboloids with a total size of 1.5 km × 12 m. It is situated near Canberra, Australia. Credit: George Warr (MOST homepage, `http://www.physics.usyd.edu.au/sifa/Main/MOST`) (b): Image of the ATCA radio observatory located near Narrabri, Australia. Shown are five of the six 22 m antennas, with the sixth being located 3 km further west. Credit: ATCA Users Guide (2010). (c): Image of the 64 m Parkes radio telescope situated near Parkes, Australia. Credit: Parkes homepage: `http://www.csiro.au/Portals/Education/Programs/Parkes-Radio-Telescope.aspx`.

To perform the H I 21 cm radio analysis, data of the Magellanic Cloud Survey (MCS; Kim et al., 1998, 2003) were used which can be retrieved from the project's web page[5]. The MCS is an H I survey of the LMC which combines ATCA and Parkes multi-beam receiver data. The Parkes radio telescope, lying close to the same-named town in Australia, is a movable 64-meter dish telescope which has been operating since 1961 (Fig. 6.2c). It is part of the ATNF and has also been used e.g. for the communication with space missions like the Apollo missions and the Mars rover. The Parkes multi-beam receiver is a 13-beam cooled 21 cm receiver system mounted at the prime focus of the dish. More about this receiver can be found in Staveley-Smith et al. (1996).
For the MCS, the ATCA data provide information about the small-scale structure of the ISM below $20'$, while the Parkes data give new insights into the large-scale structure of the LMC above $1°$. The merged data set, which can be downloaded from the MCS web page[6], has a velocity resolution of 1.649 km/s and is sensitive to structures with a size of ≥ 15 pc.

6.3 Morphological Studies

This section presents the studies which have been performed within the scope of this thesis in X-ray, optical and radio energy bands to understand the morphology of DEM L299. Within these studies, DEM L299 has been found to be a superposition of the supernova remnant SNR B0543-68.9 and a superbubble. Different properties of the SNR were used to determine its exact position and extend. While the superbubble was identified using the optical data, H I 21 cm data were used to investigate the position of both objects with respect to each other.

6.3.1 X-ray Images

To study the morphology of DEM L299 in X-rays, images were created using *XMM-Newton* EPIC data of observation 0094410101. The processing of these data is described in Chapter 4. After data processing, the *XMM-Newton* ESAS tasks *comb* and *adapt_900* were used to create images which are adaptively smoothed, point source subtracted, vignetting- and exposure-corrected, quiescent particle background subtracted, and soft proton filtered (see Sect. 6.2). For these images, the combined EPIC-MOS1, EPIC-MOS2, and EPIC-pn data were rebinned with a factor of two, and adaptively smoothed with a smoothing counts value of 50.

[5] MCS homepage: `http://www.atnf.csiro.au/research/lmc_h1/index.html`
[6] Query form for the online retrieval of MCS data: `http://www.atnf.csiro.au/research/HI/mc/queryForm.html`

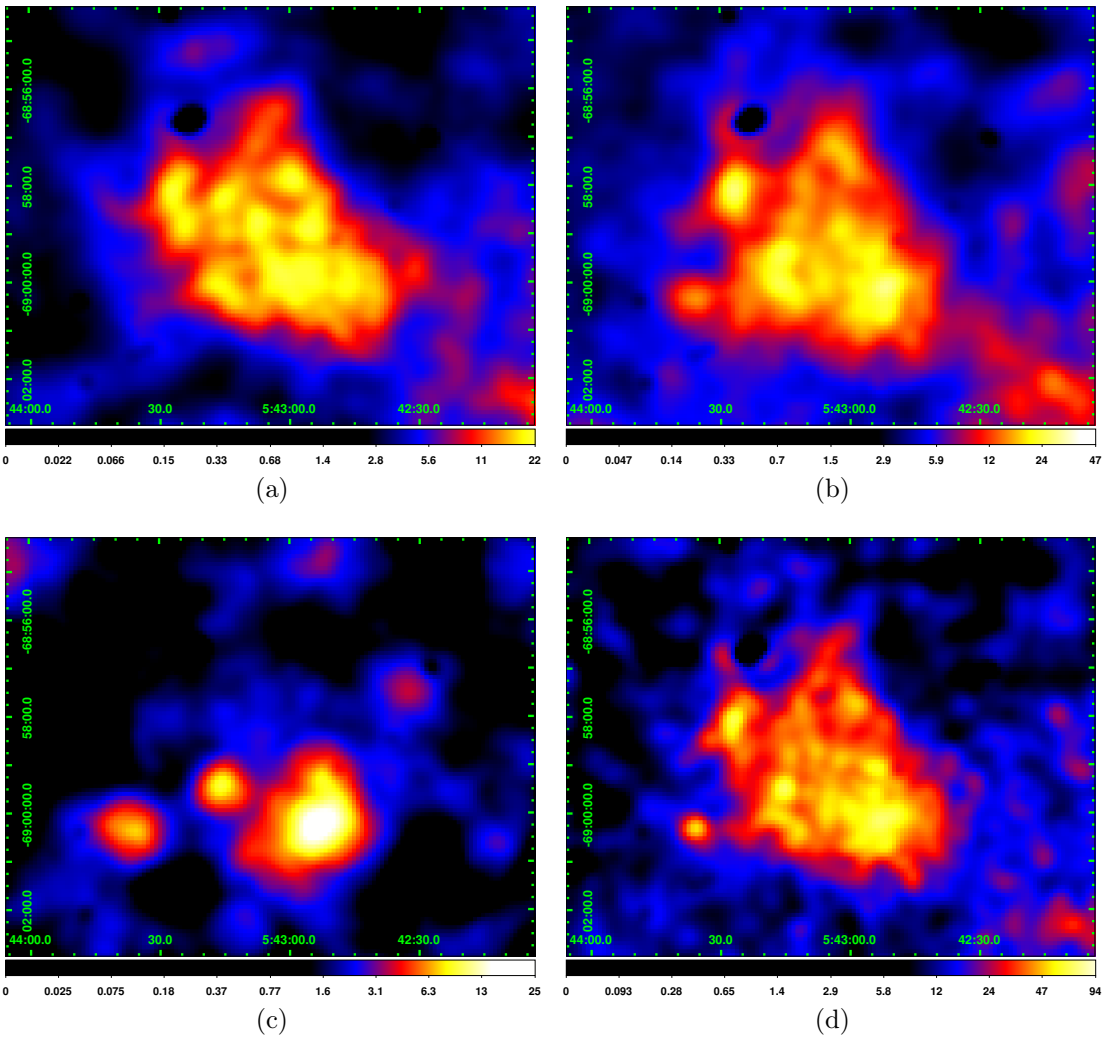

Figure 6.3: Intensity-scaled *XMM-Newton* X-ray images showing DEM L299 in energy ranges of (a) 0.3 – 0.8 keV (soft band), (b) 0.8 – 1.5 keV (medium band), (c) 1.5 – 4.5 keV (hard band), and (d) 0.3 – 8.0 keV (broad band). The images show an area of the sky of $\sim 158\,\mathrm{pc} \times 125\,\mathrm{pc}$ ($10\farcm9 \times 8\farcm6$) and have been smoothed adaptively and additionally by a Gaussian with a kernel radius of three pixels. Scales are in units of counts/s/deg^2.

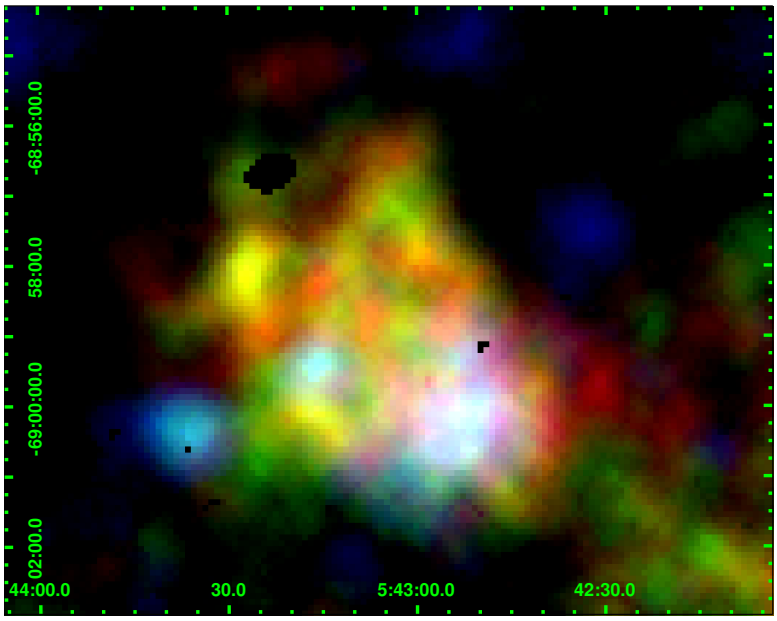

Figure 6.4: Three-color X-ray image of DEM L299 in which the soft energy band (0.3 – 0.8 keV) is plotted in red, the medium band (0.8 – 1.5 keV) in green, and the hard band (1.5 – 4.5 keV) in blue. The image shows the same area of the sky as Figure 6.3 and the same smoothing parameters and scale units were used. Areas appearing in white color show an enhanced X-ray emission in all three energy bands.

For a better presentation, these images were then smoothed again with a Gaussian using a smoothing kernel radius of three pixels.
The resulting images are shown in Figure 6.3 in four different energy bands. These images are intensity-scaled zoom-ins onto the FOV of the DEM L299 observation in the energy bands of

- 0.3 – 0.8 keV (soft band),
- 0.8 – 1.5 keV (medium band),
- 1.5 – 4.5 keV (hard band), and
- 0.3 – 8.0 keV (broad band).

The images show an area of the sky of $10\farcm9 \times 8\farcm6$ which corresponds to a size of $\sim 158\,\mathrm{pc} \times 125\,\mathrm{pc}$, assuming an LMC distance of 50 kpc. At the center of each image, DEM L299 can easily be recognized as a region of enhanced diffuse X-ray emission. A point source has been subtracted at the northern rim of DEM L299, which corresponds to the position of the stellar X-ray source [SHP2000] LMC 347 (Sasaki et al., 2000). In all four energy bands, the diffuse X-ray emission is brightest at the south-western part of DEM L299. This can also be seen in the three-color image of Figure 6.4, which is a Red-Green-Blue (RGB) image that shows the soft

energy band in red, the medium band in green, and the hard band in blue. In these images, the area containing the brightest X-ray emission appears in white color, indicating that it is bright in all three energy bands. The fact that the intensity of the emission decreases in all energy bands around this area of enhanced emission – and not only in the soft energy band – indicates that a true decrease of diffuse X-ray emission is observed. In contrast, an only apparent decrease caused by absorption would be observable only in the softer X-ray energy bands. In the hard band, the enhanced emission is almost entirely restricted to this area, while in the other three X-ray bands, the emission occupies a much larger area and has a similar appearance in these bands.

6.3.2 Optical Images

For the studies of DEM L299 in optical wavelengths, optical images were created out of the MCELS emission line data which were reduced by Sean D. Points from the Cerro Tololo Inter-American Observatory, Chile. For the data reduction, he performed a continuum subtraction, flux calibration, sky subtraction, and smoothed the images. The resulting Hα, [S II], and [O III] images are shown in Figure 6.5.

All three images show a very similar appearance of DEM L299 which is characterized by a shell-like structure with a diameter of $4'$ (58 pc) and a central cavity with a diameter of $\sim 2'$ (~ 29 pc). In [O III], this shell has a break at its north-western rim, while the [S II] and Hα images show a blurred structure at the position of this break in the [O III] emission, which suggests a blowout from the shell-like structure at this position. The blowout is also indicated by an enhancement in the soft and medium X-ray emission at this position (Fig. 6.3), although the statistics of the *XMM-Newton* X-ray observation of DEM L299 is too low to obtain a clear distinction of the blowout from the X-ray background. South-west of this shell lies a region of enhanced Hα and [S II] emission which cannot be found in the [O III] image. Apart from DEM L299, the northern rim of the supergiant shell LMC-SGS 2 and LHA 120-N 164 are visible in the east as a filament and in the south as a region of bright emission, respectively, and also DEM L297 and the YSO are easily identified (see Fig. 6.1 for the relative positions of these objects).

To determine the exact position of the supernova remnant SNR B0543-68.9, the [S II]/Hα flux ratio can be used, since the relative flux of these two lines provides information about the ionization mechanism that produced these ionization states (see Sect. 2.5.3): a high ratio indicates shock-ionization, while a low ratio points to photo-ionization. To investigate this, the flux-ratio image of DEM L299 was created (Fig. 6.6). A circular structure with an enhanced flux ratio and a radius

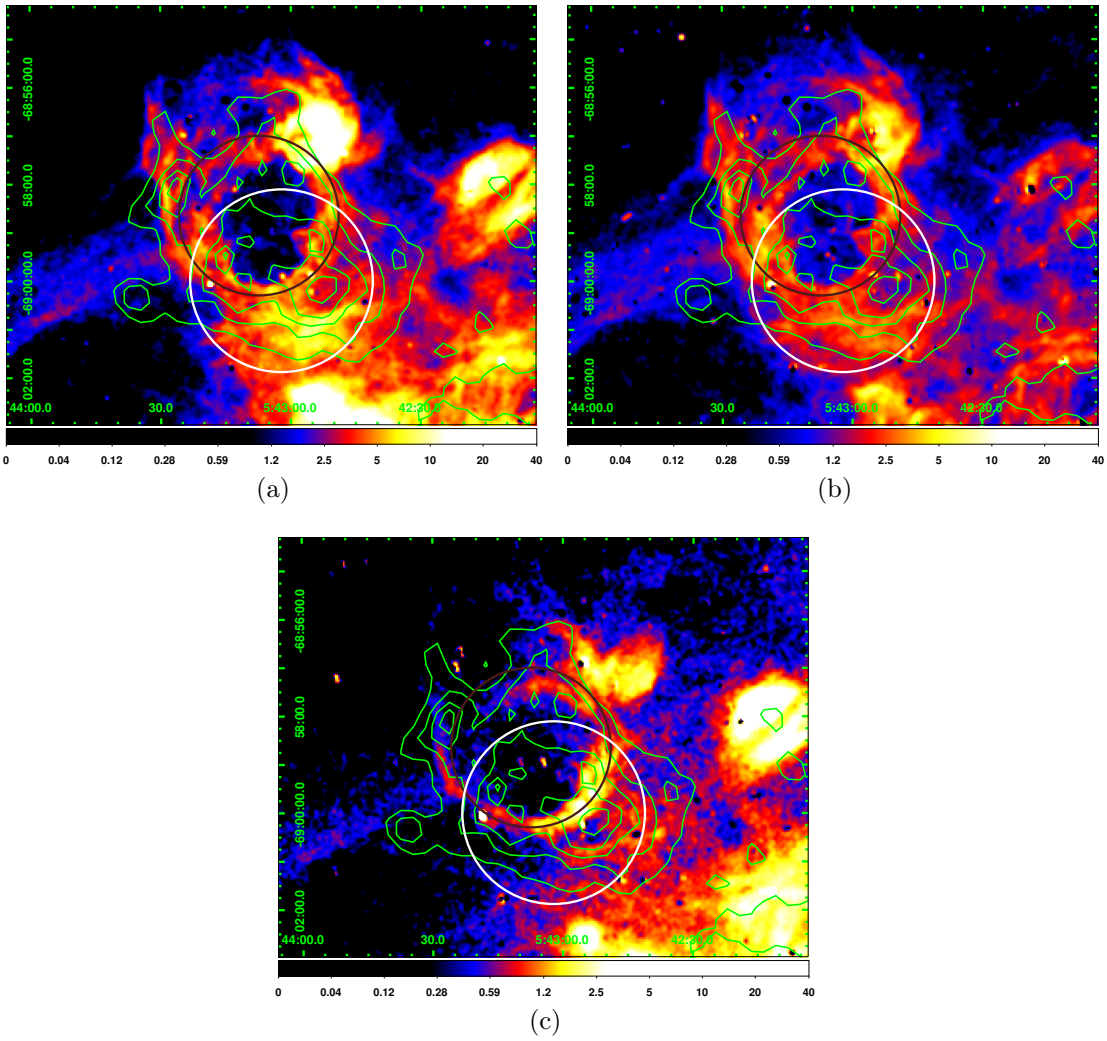

Figure 6.5: Intensity-scaled, continuum-subtracted, flux-calibrated, sky-subtracted, and smoothed optical images created out of MCELS data, showing DEM L299 in (a) Hα, (b) [S II], and (c) [O III]. The white circle marks the position of SNR B0543-68.9 as determined through the [S II]/Hα flux ratio (see Fig. 6.6), while the black circle indicates the position of the Hα cavity. Overlaid onto these images are the contours of the broadband X-ray image shown in Figure 6.3 with contour levels at 18, 28.5, 39, 49.5, and 60 counts/s/deg^2. Scales are in units of erg/cm^2/s, and the shown area of the sky is the same as in Figure 6.3. The data were reduced by Sean D. Points, Cerro Tololo Inter-American Observatory, Chile.

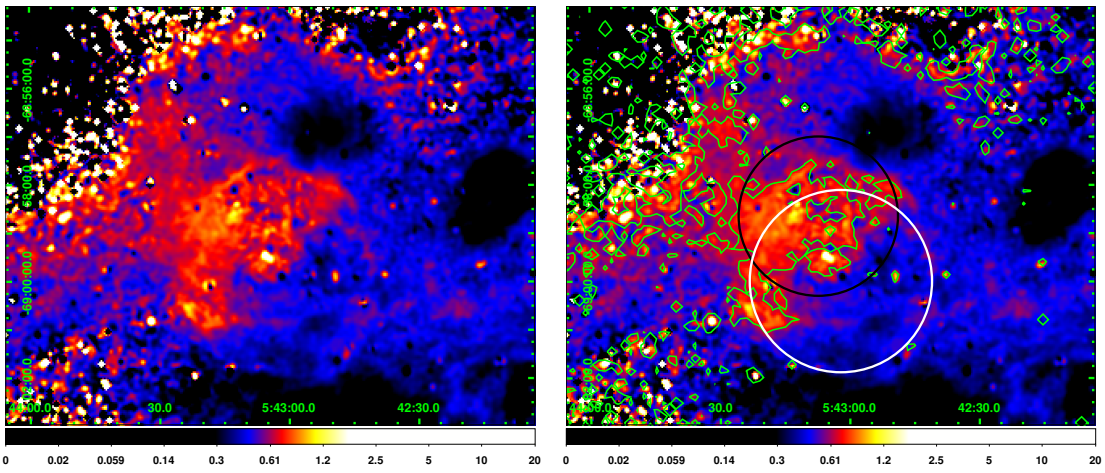

(a) (b)

Figure 6.6: [S II]/Hα flux-ratio image of DEM L299, created out of the [S II] and Hα images of Figure 6.5, showing the same are of the sky as Figure 6.3. (a): A circular structure with an enhanced flux ratio is clearly visible in the center of the image, being indicative for an SNR. (b): Same as (a), but with contour levels at 0.46 and 0.67. The position of this circular structure is marked with a white circle, while the black circle indicates the position of the Hα cavity as defined in Figure 6.5. Apart from DEM L299, LHA 120-N 164 is visible in the south, DEM L297 in the west, and the YSO and the OB-star in the north-west, each with a low [S II]/Hα flux ratio, which indicates photo-ionization and is therefore consistent with their nature.

of $\sim 2'$ (~ 30 pc) is clearly visible in the middle of the image, with its center lying at RA 05:43:02.2, Dec -69:00:00.0 (J2000). The north-eastern half of this structure has a flux ratio of $\gtrsim 0.67$, which is a strong indication for the shock-ionized shell of an SNR lying in an H II region (Fesen et al., 1985). Therefore, this spherical structure should indicate the position of SNR B0543-68.9. When comparing its position with the position of the Hα cavity as indicated in Figures 6.5 and 6.6, it becomes evident that the positions of these two structures do not conform to each other, but that the center of the Hα cavity lies $\sim 1\farcm4$ (~ 20 pc) more to the north and $\sim 0\farcm5$ (~ 7 pc) more to the east of the shock-ionized circular structure. Furthermore, no shell-like structure is visible around the Hα cavity in the flux-ratio image. This is a strong indication that these two structures represent two distinct objects which are observed in superposition: SNR B0543-68.9, as defined by the [S II]/Hα flux ratio, and a superbubble, as defined by the clearly visible shell in Hα, [S II], and [O III] emission. Both the area of brightest X-ray emission of DEM L299 and the region south-west of the Hα cavity which is bright in Hα and [S II], but not in [O III], lie outside of the superbubble, but inside the borders of

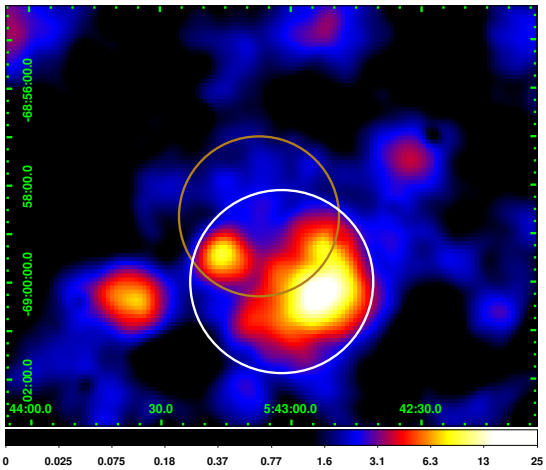

Figure 6.7: *XMM-Newton* EPIC image of DEM L299 in the hard X-ray energy band of 1.5 – 4.5 keV. The position of the SNR as determined through the [S II]/Hα flux ratio is marked with a white circle, while the brown circle indicates the position of the Hα cavity. The brightest region of hard X-ray emission is projected within the borders of the SNR. Smoothing parameters, scale parameters, and the area of the sky are the same as in Figure 6.3.

the SNR. They are located in the south-western part of the SNR which has a low [S II]/Hα flux ratio, while the higher flux ratio roughly corresponds to that area of the SNR which overlaps with the superbubble in projection. When comparing the hard X-ray image with the [S II]/Hα flux-ratio image (see Fig. 6.7), it becomes evident that the projection of the hard emission is almost entirely restricted to the position of the SNR.

6.3.3 Radio-Continuum Images

To study DEM L299 in radio wavelengths, Luke M. Bozzetto and Miroslav D. Filipović from the University of Western Sydney, Australia, processed and reduced the radio-continuum data which were used to create the images shown in Figure 6.8. These images show the region in wavelengths of 20 cm and 36 cm, with overlaid Hα contours and marked positions of SNR B0543-68.9 and the superbubble. At the position of these objects, a clear enhancement of the radio-continuum emission can be seen. In both images, the emission shows the same basic features: a shell-like structure and a tendency of the emission to follow rather the distribution of the Hα emission than the distribution of the X-ray emission. Compared to the distribution of the 36 cm emission, the 20 cm emission shows a much more obvious correspondence of the radio emission with the Hα emission, which is probably due to its lower background emission. Furthermore, the same surrounding

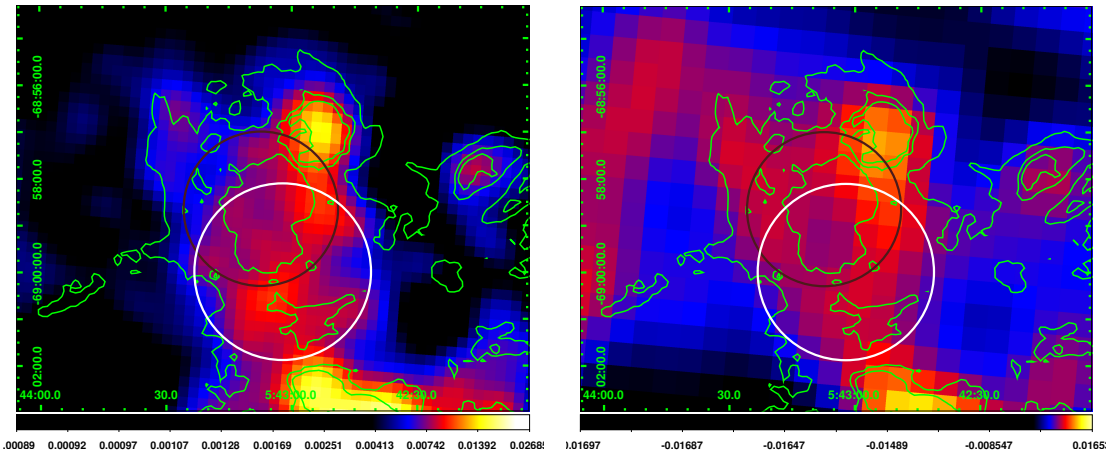

(a) (b)

Figure 6.8: Radio 20 cm (a) and 36 cm (b) images of DEM L299 created out of ATCA and MOST data. The position of SNR B0543-68.9 and of the superbubble is marked with a white and a black circle, respectively. Hα contours taken from Figure 6.5a are overlaid onto these images with contour levels at 2, 6, and 10 erg/cm^2/s. A clear correspondance between the Hα emission and the radio emission can be seen in the 20 cm image and is also indicated in the 36 cm image. Both images have been smoothed by a Gaussian using a kernel radius of two pixels and show the same area of the sky as Figure 6.3. Scale units are in Jy/beam. Credit: data processed and reduced by L. M. Bozzetto and M. D. Filipović from the University of Western Sydney, Australia.

features can be seen in these radio bands as in the optical emission lines: LHA 120-N 164, DEM L297, and the young stellar object with the OB-star.
In order to estimate whether this radio-continuum emission is created through synchrotron radiation which would indicate an SNR, or through thermal emission as can be originating from an H II region, Luke M. Bozzetto and Miroslav D. Filipović created the spectral index map of DEM L299 shown in Figure 6.9. The index map has been created using the 20 cm and 36 cm data (Fig. 6.8). The position of the SNR and of the superbubble is marked with the red and the black circle, respectively. A clear distinction between DEM L299 and the H II region LHA 120-N 164 south-west of it can be obtained through their different spectral indices: the region around DEM L299 has a spectral index between -1 and 0, which is typical for an SNR, while LHA 120-N 164 shows typical values for an H II region, with spectral indices ranging from 0 and $+2$. This indicates that the radio emission at the position of SNR B0543-68.9 is indeed synchrotron emission, which is likely to originate from the remnant. The rather flat spectral index matches the rather mature age of SNR B0543-68.9 as determined during the X-ray spectral analysis, presented in Section 6.4.

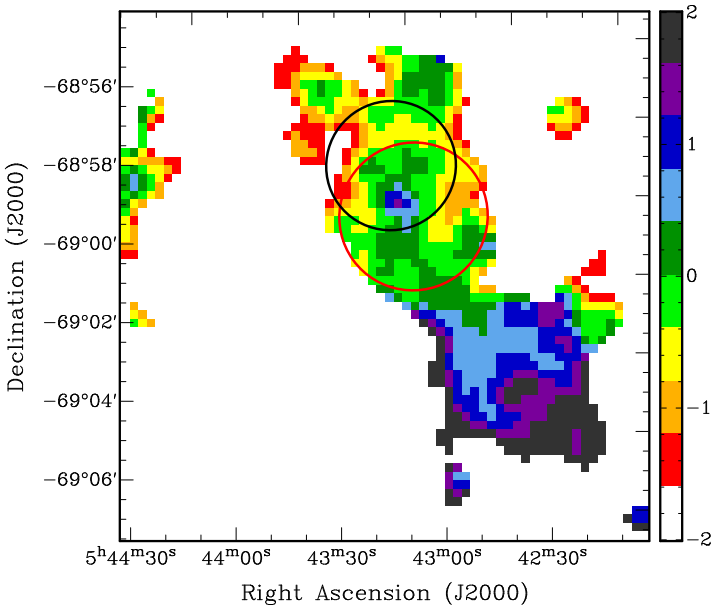

Figure 6.9: Spectral index map of the region around DEM L299 which was created out of the 20 cm and 36 cm radio images shown in Figure 6.8. The position of SNR B0543-68.9 and of the superbubble is marked with a red circle (corresponding to the white circle shown in the previous figures) and a black circle, respectively. South-west of both objects, the H II region LHA 120-N 164 can easily be distinguished from DEM L299 due to its lower spectral index. Credit: L. M. Bozzetto and M. D. Filipović, University of Western Sydney, Australia; Warth et al. (2014); modified.

6.3.4 H I 21 cm Radio Images

A morphological study of the distribution of the neutral hydrogen of DEM L299 was performed via the 21 cm radio data. Through the redshift and blueshift of this line, information is obtained about the position of the neutral hydrogen within the LMC. Since the LMC and the Milky Way are moving with respect to each other, every region in the LMC has a certain velocity relative to the Earth. This relative velocity can be observed through a shift of the 21 cm line. Although an unknown proper motion of the observed objects will cause a misinterpretation of their position, the thus obtained over-all picture of the LMC is a good approximation. Therefore, observing the 21 cm line yields 3-D information about the position of the gas. With this method, a data cube is obtained which shows in two dimensions the intensity-scaled RA-Dec position and in the third dimension the intensity-scaled heliocentric velocity of the neutral hydrogen.

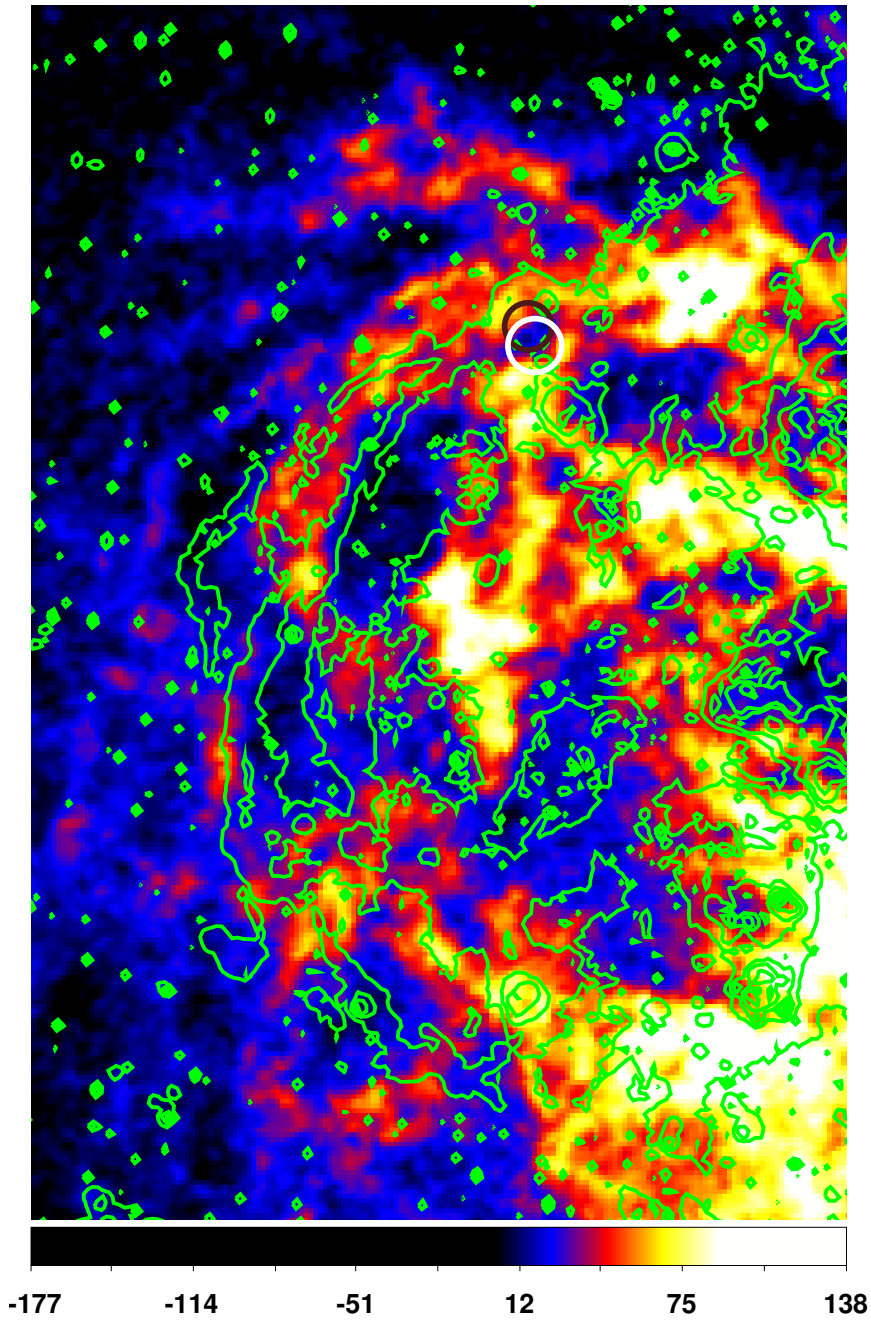

Figure 6.10: Combined ATCA and Parkes H I 21 cm radio data of the Magellanic Cloud Survey showing an area with a size of $57' \times 85'$ ($\sim 828\,\mathrm{pc} \times 1235\,\mathrm{pc}$) around DEM L299 at a heliocentric velocity of $\sim 264\,\mathrm{km/s}$. Hα contours of the MCELS data are overlaid, with contour levels at ~ 0.3, 96, and 191 erg/cm^2/s and with a contour smoothness of two. supergiant shell LMC-SGS 2 is visible as a shell-like structure consisting of filaments in both the radio and the optical data. The position of SNR B0543-68.9 and of the superbubble is marked in white and black, respectively. Scales are in Kelvin, representing the brightness temperature.

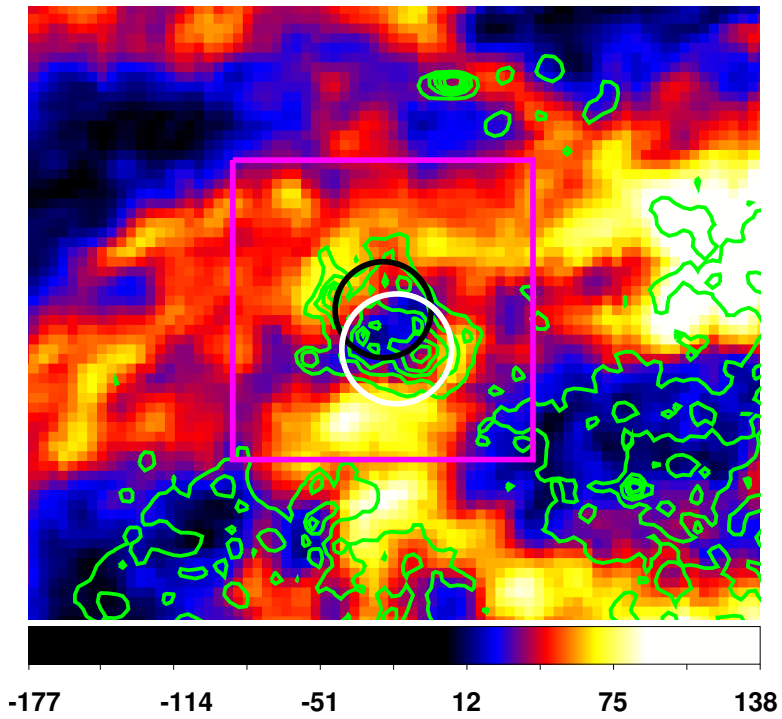

Figure 6.11: Zoom-in of Figure 6.10 onto DEM L299, with overlaid X-ray contours of the broadband *XMM-Newton* observation. The image shows an area of the sky of $\sim 25' \times 21'$ ($\sim 363\,\mathrm{pc} \times 305\,\mathrm{pc}$), with the position of SNR B0543-68.9 and of the superbubble marked with a white and a black circle, respectively. The H I emission indicates a shell-like structure around both objects. The magenta box marks the area which has been used to create the channel maps of Figure 6.12 and the position-velocity plots of Figure 6.13.

The aim of this study was to proof if a common shell of neutral hydrogen can be identified around SNR B0543-68.9 and the superbubble, which would be a strong evidence that both objects lie close together, indicating that they might have the same population of stars as their common origin. A shell of neutral hydrogen is expected to be found around superbubbles and older SNRs, since the expanding hot gas sweeps up the surrounding cold ISM.
To perform this study, 21 cm radio data of the Magellanic Cloud Survey (MCS) (Kim et al., 1998, 2003) have been used. Figure 6.10 shows this MCS H I 21 cm data of a large area of the sky around DEM L299 – including the supergiant shell LMC-SGS 2 – with a size of $0.7\,\mathrm{kpc} \times 1\,\mathrm{kpc}$ and at a heliocentric velocity of $\sim 264\,\mathrm{km/s}$. The position of SNR B0543-68.9 and of the superbubble is marked with a white and a black circle, respectively, and Hα contours are overlaid onto the image. Lying south-east of DEM L299, the supergiant shell LMC-SGS 2 can be recognized as a shell-like structure consisting of filaments. A zoom-in onto

DEM L299 is shown in Figure 6.11, with overlaid X-ray contours of the FOV of the broadband *XMM-Newton* observation and with the marked positions of the SNR and the superbubble. The bright X-ray regions south-east and south-west of DEM L299 coincide with the regions with low radio emission, in consistency with the assumption that these H I shells of cold ISM are filled with hot ISM, visible in X-rays. In Figure 6.11, the magenta square, which has a size of $10\farcm3 \times 10\farcm3$ ($150\,\mathrm{pc} \times 150\,\mathrm{pc}$), marks the area which has been used to further investigate the 3-D distribution of the neutral hydrogen around DEM L299. For this purpose, channel maps (Fig. 6.12) and position-velocity plots (Fig. 6.13) were created for this area. The channel maps in Figure 6.12 show the RA-Dec position of the neutral hydrogen gas in the DEM L299 region at different velocities. To create the channel maps, velocity slices were cut from the data cube at heliocentric velocities between $\sim 233\,\mathrm{km/s}$ and $\sim 327\,\mathrm{km/s}$ in steps of the resolution limit of $1.649\,\mathrm{km/s}$. To obtain better statistics, three velocity slices were combined to form one plot, resulting in the 20 plots show in Figure 6.12 with velocity steps of $\sim 4.95\,\mathrm{km/s}$ between the separate plots. At heliocentric velocities of $302-312\,\mathrm{km/s}$, the northern rim of the supergiant shell LMC-SGS 2 can be seen as an enhancement of the emission in the south-east. In these plots, the position of SNR B0543-68.9 and of the superbubble is marked with a white and a brown circle, respectively. A shell-like structure is visible at heliocentric velocities of $258-277\,\mathrm{km/s}$ (plots in second row of Fig. 6.12), which can most easily be recognized in the plots with heliocentric velocities of $263\,\mathrm{km/s}$ and $268\,\mathrm{km/s}$. This structure suggests the existence of a shell of neutral hydrogen surrounding both SNR B0543-68.9 and the superbubble, indicating that both objects lie close to each other. However, these plots represent no final proof for this, since the proper motion of the gas leads to projection effect in the channel maps.

Position-velocity plots were created to further investigate the distribution of the neutral hydrogen. If one considers the channel maps of Figure 6.12 to show the 'front side' of the 21 cm data cube, then the position-velocity plots of Figure 6.13 show the data cube from the other sides: Figure 6.13a shows the data cube 'from top', and the plots of Figure 6.13b show it 'sideways'. This means that the plots of Figure 6.13a show different slices of the data cube, with each slice showing the intensity of the H I emission as a function of the RA-position (on the abscissa) and the velocity (on the ordinate). The different plots show this for different Dec-positions. The RA- and Dec-positions are taken from the magenta box in Figure 6.11. Thus, the first plot of Figure 6.13a shows the combined lowest two pixel rows of the magenta box (i.e. from east to west) over a velocity range from $251-322\,\mathrm{km/s}$. The second plot shows the combined third and forth pixel row of the magenta box over the same velocity range, and so on. The pixel rows were combined to obtain better statistics. This velocity intervall was chosen since Points et al. (1999) determined the velocity of the borders of the supergiant shell

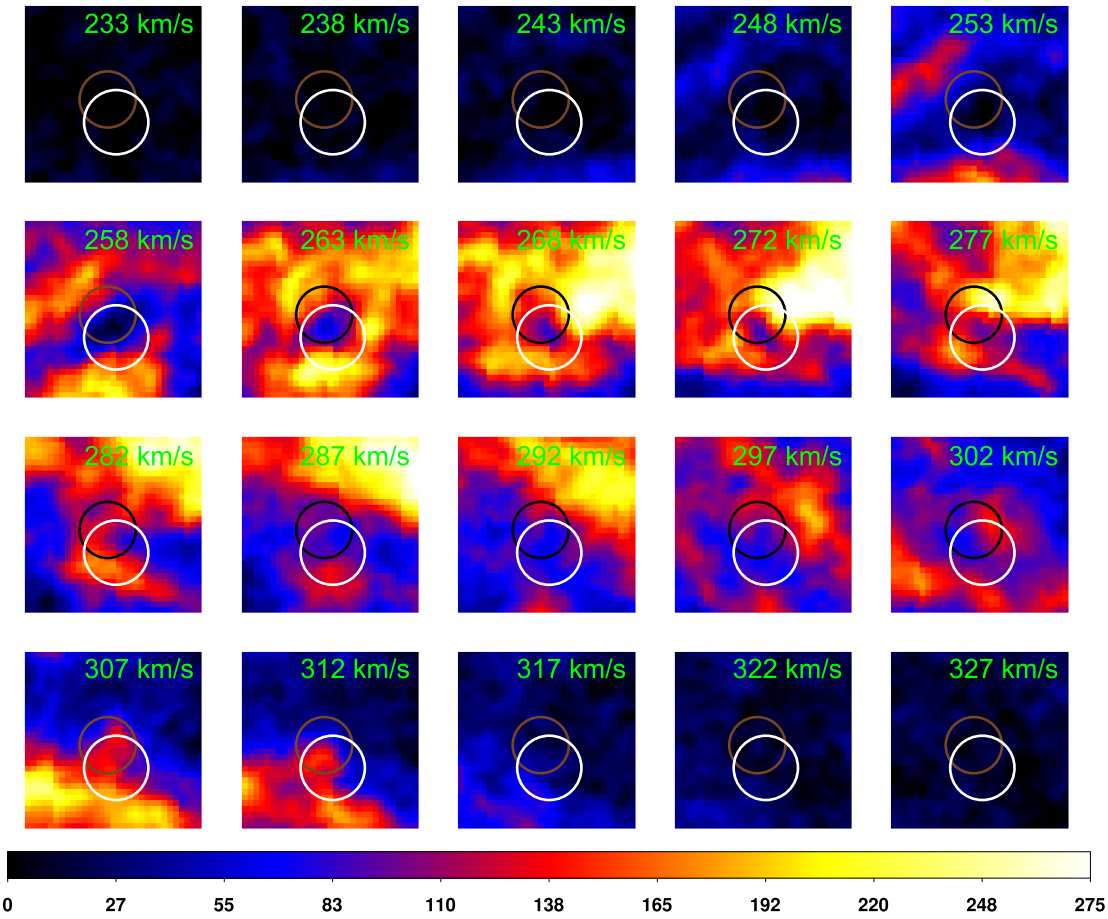

Figure 6.12: Channel maps showing DEM L299 in the 21 cm emission line of neutral hydrogen at different velocity slices between 233 – 327 km/s in steps of ∼ 5 km/s. The position of SNR B0543-68.9 and of the superbubble is marked with a white circle and a dark circle, respectively. Each image shows an area of the sky of $10\farcm3 \times 10\farcm3$ (150 pc × 150 pc) as indicated by the magenta box in Figure 6.11. Scales are in Kelvin, representing the brightness temperature.

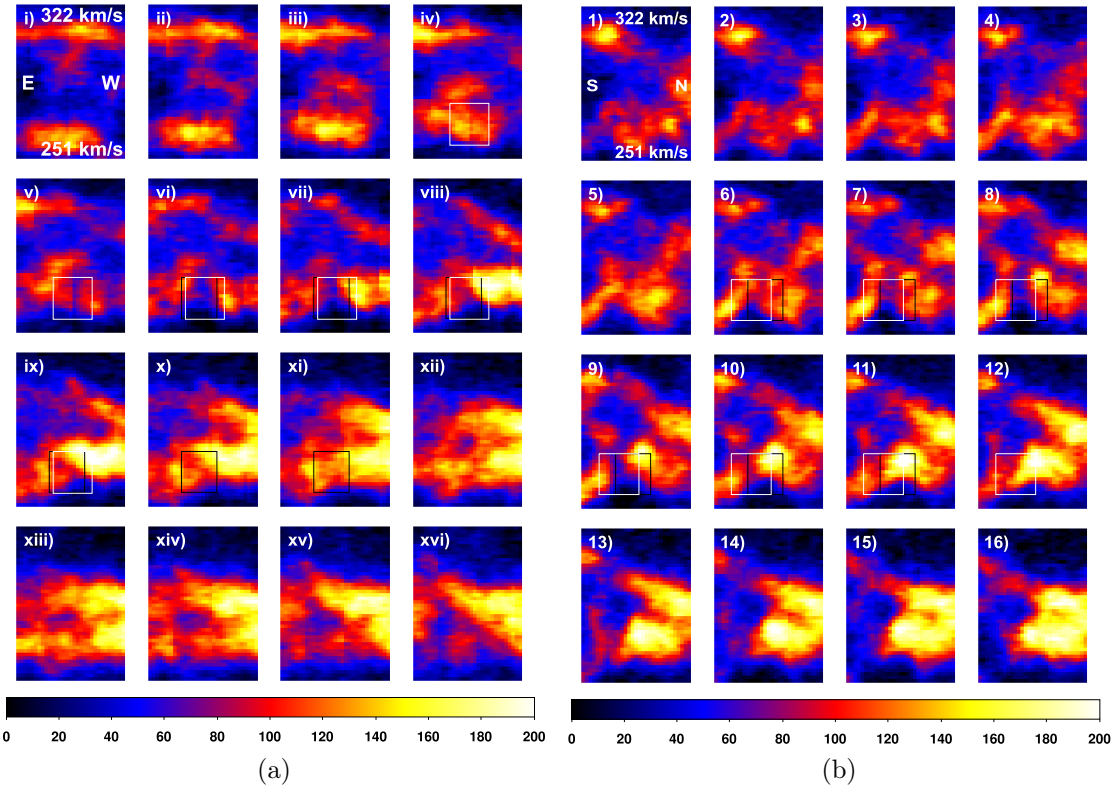

Figure 6.13: Position-velocity plots of DEM L299. (a): Position-velocity plots showing the intensity of the 21 cm emission line of neutral hydrogen for DEM L299, with the heliocentric velocity (ordinate) of the neutral hydrogen plotted against its RA-position (abscissa). The different plots show this for different Dec-positions. The RA- and Dec-positions are taken from the magenta box in Figure 6.11. The first plot shows the two combined most southern pixel rows of the magenta box. The next plot (to the right) has been created using the third and forth pixel row of the magenta box, and so on. East is left and west is right in the resulting position-velocity plots. The width of the white and black rectangle indicates the position of SNR B0543-68.9 and of the superbubble, respectively, and its height marks velocity range (258 – 277 km/s), in which a shell-like structure was found in the channel maps of Figure 6.12. Scales are in Kelvin. (b): Same as (a), but for the heliocentric velocity plotted against the Dec-position of the gas. The different plots show different RA-positions. The first plot shows the two combined most eastern pixel columns of the magenta box, the next plot the third and fourth column, and so on. South is left and north is right in the resulting position-velocity plots.

LMC-SGS 2 to be 250 km/s and 300 km/s, respectively, and in the H I catalog of Kim et al. (2007), a velocity of $\sim$280 km/s is given for the large H I cloud which is projected towards DEM L299. The plots in Figure 6.13b were created following the same procedure, but – instead of pixel rows – the pixel columns of the magenta box are plotted against the velocity. The different plots of Figure 6.13b show this for different RA-positions. Thus, the first plot shows the first two pixel columns (from left to right) of the magenta box (i.e. from south to north) in the same velocity range, the second plot shows the third and fourth pixel column, and so forth. In the plots, the position of SNR B0543-68.9 and of the superbubble is marked with the white and the black square, respectively. The extent of these squares in the velocity-ordinate has been determined through the existence of a hydrogen shell at the respective velocity slices of Figure 6.12. At the thus marked positions, a shell-like structure can be assumed, although the data are highly ambiguous. In the south-north plots (Fig. 6.13b), this shell can be recognized more clearly, and also the YSO is visible as a bright region of radio emission.
In the channel maps as well as in the position-velocity plots of DEM L299, a shell-like structure with an enhanced H I 21 cm radio emission could be recognized, indicating a common shell around both SNR B0543-68.9 and the superbubble. The existence of a common shell of neutral hydrogen would represent a strong evidence that both objects lie close together, indicating a common origin. Since in particular the position-velocity plots are not unambiguous and since projection effects always have to be taken into account, the observed common H I shell as indicated by the 21 cm data should not be considered as a proof, but as an indication that both objects lie close to each other.

In the morphological studies performed with optical, X-ray, radio-continuum, and radio 21 cm data, strong indication was found that the H II region DEM L299 consists of the superposition of the supernova remnant SNR B0543-68.9 and a superbubble. The position of the SNR is defined through the [S II]/Hα flux ratio and the position of the superbubble through the Hα, [S II], and [O III] cavity. For the remnant, all three indicators for an SNR could be confirmed: diffuse X-ray emission, an enhanced [S II]/Hα flux ratio, and synchrotron radio emission. As indicators for the superbubble, an optical shell with a central cavity was found, as well as diffuse X-ray emission. A comparison of the emission at different wavelengths showed that the SNR-only region shows much more emission in optical and hard X-rays than the overlap region between SNR B0543-68.9 and the superbubble, while no absorption effects could be detected in X-rays, which indicates an actual change in the strength of the emission. The radio-continuum data suggest a rather mature remnant, which agrees with the age of SNR B0543-68.9 as determined in the X-ray spectral analysis (see Sect. 6.4). In the 21 cm radio data, a shell-like structure could be recognized surrounding both objects, which suggests that they lie close to each other, indicating that they might have

a common population of stars as their origin and are not just by chance projected towards the same area of the sky.

6.4 X-ray Spectral Analysis

An X-ray spectral analysis of DEM L299 has been performed within the scope of this thesis, using data of the European Photon Imaging Camera of the *XMM-Newton* satellite. For the examination of DEM L299, four different extraction regions for the spectral analysis were defined, which can be seen in Figure 6.14:

a) an SNR region as defined by the [S II]/Hα flux-ratio image (marked in white);

b) a superbubble-only region, which contains only that part of the superbubble as defined through the Hα image which is not projected in superposition with the remnant (marked in brown);

c) a blowout region as indicated in the optical as well as in the soft and medium X-ray images (marked in green); and

d) a local background region of an as much as possible empty region within the same DEM L299 observation (marked in magenta).

The processing of the X-ray data and the model used for the fitting of the data is described in Chapter 4 and in Section 5.4. For all spectral extraction regions, the same procedure and model has been used, with exception of the SNR region, for which an additional thermal component was added to the model to account for superbubble contamination, as discussed below. As described in Section 5.4, the SEP observations were fitted simultaneously to the DEM L299 data for the estimation of the X-ray background of DEM L299. Each of the four spectral extraction regions *a)*–*d)* has a much smaller size than the FOV which has been used as an extraction region for the combined SEP observations. To account for these different sizes of the extraction regions of the DEM L299 spectra and the simultaneously fitted SEP spectra, each SEP model – the main model and the six residual soft proton models (see Sect. 5.4) – was multiplied by a constant which was determined through the ratio of these areas: constant $= \frac{\text{SEP area}}{\text{DEM L299 area}}$.[7] This normalization is necessary since Xspec does not include an area normalization of the data, but plots it in counts/s/keV. The model for the SEP spectrum is multiplied with this constant. (Alternatively, the *data* of the SEP observations – i.e. the flux – could be divided by this constant.) The area normalization was done in order to be able to fit simultaneously one common model to both observations,

[7] For the DEM L299 model, this constant is set to one.

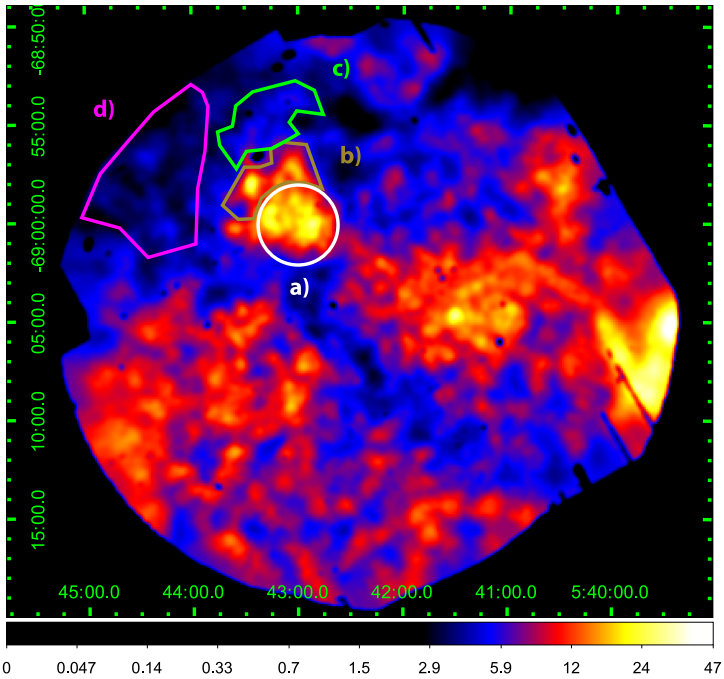

Figure 6.14: Intensity-scaled X-ray image showing the FOV of the *XMM-Newton* observation of DEM L299 in an energy range of 0.8 – 1.5 keV. The different spectral extraction regions used for fitting during the X-ray spectral analysis of DEM L299 are marked in white for the SNR region (labeled as region *a*), in brown for the superbubble-only region (region *b*), in green for the blowout region (region *c*), and in magenta for the local background region (region *d*). The image has been smoothed by a Gaussian using a kernel radius of three pixels. Scales are in units of counts/s/deg^2.

with linked normalizations for the X-ray background components.

As a test for the appropriateness of this background estimation via the SEP observations, the local background of the DEM L299 observation was extracted from an as much as possible empty field within the same *XMM-Newton* pointing. For the extraction region of the local background, an area was chosen which is located east of DEM L299 (see Fig. 6.14). The spectrum of this local background region was fitted simultaneously to the SEP spectrum, using the same model as described in Section 5.4, with the normalization of the source component – which is not present in this background observation – set to zero. Both spectra were in good agreement, apart from a small thermal excess in the local background spectrum which could be fitted with an additional thermal component. For this additional component, Xspec's thermal plasma model *apec*, the shock-ionized NEI plasma model *vpshock*, and the collision-ionized NEI plasma model *vnei* were tested (see Sect. 5.4 for more information about these models). Due to the high uncertain-

Table 6.2: Best-fit parameters for the SNR region, the polygonal region (i.e. the superbubble-only region), the blowout region, and the local background region. Listed for each region are the temperature $k_{\mathrm{B}}T$, the ionization timescale τ, the normalization *norm* (also referred to as K), the column density $N_{\mathrm{H,LMC}}$ of hydrogen within the LMC, and the reduced χ^2 of the fits. For all fitting regions, these parameters were obtained with the *vpshock* model. Uncertainties are upper and lower 90 % confidence ranges. The listed reduced χ^2 are those fitted without the SEP data.

		SNR	Polygon	Blowout	Local Bkg.
$k_{\mathrm{B}}T$	[keV]	0.64 (0.44 – 1.37)	0.74 (0.44 – 1.1)	0.62 (0.2 – 1.0)	0.69 (0.6 – 0.9)
τ	$[10^{10}\,\mathrm{s\,cm^{-3}}]$	2.1 (1.5 – 3.4)	8.5 (2.6 – 28)	37 (2.5 – 150)	46 (14 – 110)
norm	$[10^{-4}\,\mathrm{cm^{-5}}]$	8.3 (1.8 – 17.3)	1.7 (1.2 – 7.5)	1.2 (0.5 – 63.1)	1.2 (0.9 – 1.6)
$N_{\mathrm{H,LMC}}$	$[10^{22}\,\mathrm{cm^{-2}}]$	0.66 (0.59 – 0.77)	0.30 (0.07 – 0.66)	0.27 (0 – 1.2)	0.07 (<0.3)
Red. χ^2		1.2	0.8	0.9	1.3

ties which resulted from the large number of model components, a series of fits was performed, in which 20 different temperatures between 0.1 keV and 7.0 keV were used as starting points for the energy parameter of the source component. Although set to different starting points, this energy parameter was fitted freely. The best reduced χ^2 of 1.3 was obtained with the *vpshock* and the *vnei* model. Since the *vnei* model resulted in a high column density of $1.1 \times 10^{22}\,\mathrm{cm^{-2}}$, which is not confirmed by the optical and radio observations, the *vpshock* model was considered to be the most appropriate model in this case. It shows a low column density of $0.07 \times 10^{22}\,\mathrm{cm^{-2}}$, which corresponds to the low emissivity of this extraction region in the optical and radio observations. The best-fit results for the *vpshock* model for this local background region are listed in Table 6.2. The inclusion of the thermal component increased the goodness of the fit considerably (from 2.1 to 1.3 without the SEP observations, see below). Most likely, this component is caused by the hot gas which is present in the entire FOV of the observation and probably in the entire supergiant shell LMC-SGS 2 region. However, the statistics of this local background spectrum are much too low (~ 0.06 counts/s) to be fitted simultaneously to the DEM L299 spectra, which already have low statistics as well (SNR: ~ 0.19 counts/s, superbubble: ~ 0.08 counts/s, blowout: ~ 0.04 counts/s). Nevertheless, this additional thermal component was taken into account when estimating the luminosities of the different DEM L299 regions.

The spectral analyses of the SNR, the superbubble, and the blowout extraction region were performed with the same model as described in Section 5.4. Since the SNR and the superbubble are strongly overlapping, a contamination of the SNR spectrum through the superbubble emission has to be assumed and vice versa. To account for this, a superbubble-only region was defined (see region *b)* in

Fig. 6.14, marked in brown), which contains only those parts of the superbubble which are not overlapping with the SNR as defined by the [S II]/Hα flux-ratio image. After fitting the data which were extracted from this superbubble-only region, the resulting parameters were added to the model of the SNR spectrum as an additional model component and frozen. The normalization of this additional component was adjusted to account for the different sizes of the superbubble-only region and the overlapping region of SNR B0543-68.9 and the superbubble. To do so, the normalization of this additional component has been multiplied by the ratio of the overlap of the SNR fitting region with the superbubble as defined through the Hα image and the size of the polygonal superbubble-only region.
For the source component of the SNR, superbubble, and blowout, the same models were tested as for the local background (*apec*, *vpshock*, *vnei*) and the same fitting procedure of testing a series of 20 different energies was used. This series resulted in several sets of favored fitting results, which were compared for their reduced χ^2 and in the ability to determine their 90 % uncertainty limits. For all three regions, the *vpshock* model provided the best fitting results, although in some cases the *vnei* model yielded an only slightly worse reduced χ^2. However, for the further discussion of these regions, the results obtained with the *vpshock* model were used, since the resulting parameters were very similar. As already done for the fits of the supergiant shell LMC-SGS 2, the spectra of the DEM L299 regions were first fitted simultaneously to the SEP spectra. Then, all background parameters of the DEM L299 model were frozen at the values determined through these simultaneous fits, the SEP data were removed, and the source component of the DEM L299 spectra was fitted again. Through this, a more meaningful reduced χ^2 was obtained, since with this method, the goodness of the fit is no longer dominated by the SEP data and the change in the fitting results of the source region is negligible. The fitting results for all regions are shown in Table 6.2 and the fitted spectra of the SNR region are plotted in Figures 6.15 and 6.16.

As a best-fit result for the superbubble, a temperature of $k_\mathrm{B}T_\mathrm{X,SB} = (0.74^{+0.36}_{-0.30})\,\mathrm{keV}$ and a hydrogen column density within the Large Magellanic Cloud of $N_\mathrm{H,LMC,SB} = (0.30^{+0.36}_{-0.23}) \times 10^{22}\,\mathrm{cm}^{-2}$ were obtained. Uncertainties of the fitted parameters are 90 % confidence ranges throughout this thesis, unless otherwise stated. Adopting this temperature $k_\mathrm{B}T_\mathrm{X,SB}$, the normalization timescale, and the area-corrected normalization for the additional component in the SNR model, a temperature for SNR B0543-68.9 of $k_\mathrm{B}T_\mathrm{X,SNR} = (0.64^{+0.73}_{-0.20})\,\mathrm{keV}$ and an ionization timescale of $\tau_\mathrm{SNR} = (2.1^{+1.3}_{-0.6}) \times 10^{10}\,\mathrm{s\,cm}^{-3}$ were achieved. For the blowout, comparable values as for the superbubble were obtained, being consistent with a blowout, although the temperature of a blowout is expected to be lower than that of the superbubble due to the cooling of the gas through its expansion. Since the large uncertainties prevent a better constraint of the temperature, the data do not allow to decide which temperature is higher. For the blowout, a temperature

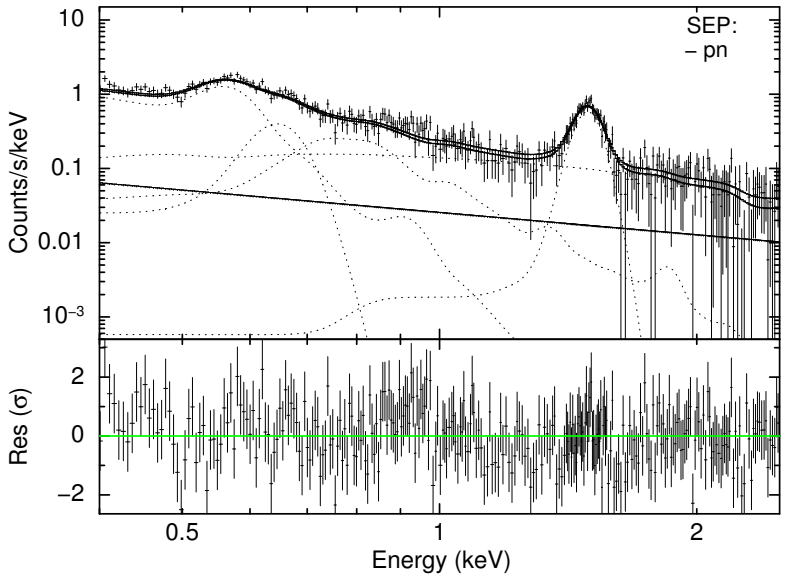

Figure 6.15: Fitted *XMM-Newton* EPIC-pn spectrum of the combined SEP observations which were simultaneously fitted to the DEM L299 spectrum for background estimation (see Fig. 6.16). The spectrum is plotted in an energy range of 0.4 – 2.5 keV with additive model components (dotted lines) and residuals (lower part of plot). The modeled residual soft proton component is visible as a straight line. Crosses indicate data points, while the solid lines represent the fitted model with (upper line) and without (lower line) the contribution of the residual soft proton component to the model.

of $k_{\mathrm{B}}T_{\mathrm{X,BL}} = (0.62^{+0.38}_{-0.42})\,\mathrm{keV}$ and a column density of the LMC of $N_{\mathrm{H,LMC,BL}} = (0.27^{+0.93}_{-0.27}) \times 10^{22}\,\mathrm{cm}^{-2}$ were obtained.

The luminosity was obtained for all four extraction regions *a) – d)* (see Fig. 6.14) in the energy range of 0.5 – 8 keV by determining their flux using the Xspec function *flux* and multiplying it with the area $4\pi D^2_{\mathrm{LMC}}$, with D_{LMC} being the distance to the LMC. The X-ray fluxes were calculated by setting all back- and foreground parameters as well as the absorption of the LMC and the Milky Way to zero. Since the resulting luminosities determined with and without the SEP data (as described above) deviate less than 1 % from each other, only the luminosities determined without the SEP data are listed in Table 6.3. This table gives the absorbed and unabsorbed luminosities of the fitting regions, with and without subtraction of the local background contribution. Before subtracting the luminosity of the local background from the SNR, blowout, and superbubble-only region, it was scaled to the respective size of the other region (row three of Table 6.3 gives the size of the extraction region in percent compared to the size of the extraction region of the local background). Since the accuracy of the local background fit

remains uncertain due to the low statistics of the pointing, the local background subtracted values should be considered as tentative. However, since the contribution of the local background emission to the unabsorbed luminosities of the source regions is small, the local background subtracted, unabsorbed luminosities will be used for further calculations. Since the spectral extraction region of the SNR is a superposition of the SNR and the superbubble, several luminosities are listed in Table 6.3 for this extraction region: the total luminosity of this region, the luminosity due to the SNR contribution to this region, and the luminosity due to the superbubble contribution. The latter two contributions were determined by putting the other thermal model component to zero, respectively, when calculating the flux. Since the uncertainty of the luminosity is proportional to the uncertainty of the normalization of the *vpshock* model component, the percentual uncertainty of the normalization was determined and used to estimate the uncertainty of the luminosity. For the superbubble, the local background subtracted unabsorbed luminosity was determined to be $(3.4^{+7.8}_{-1.2}) \times 10^{35}\,\mathrm{erg\,s^{-1}}$, which is the sum of the values of the polygonal superbubble-only extraction region and of the superbubble contribution to the luminosity of the SNR extraction region. The local background subtracted, unabsorbed luminosity of the blowout was calculated to be $(5.6^{+286.5}_{-3.3}) \times 10^{34}\,\mathrm{erg\,s^{-1}}$. The SNR contribution to the luminosity of the SNR extraction region was used to determine a local background subtracted, unabsorbed luminosity of $(1.5^{+1.6}_{-1.2}) \times 10^{36}\,\mathrm{erg\,s^{-1}}$ for the SNR.

In this section, the X-ray spectral analysis was described which was performed for the DEM L299 region using *XMM-Newton* data, and its results were presented. For background estimation, three combined observations of the South Ecliptic Pole were used, which were fitted simultaneously to the DEM L299 data. As a test for this background estimation, data were extracted from an as much as possible empty region next to DEM L299 within the same *XMM-Newton* observation and were fitted simultaneously to the SEP data. The fits showed a good agreement, although a small thermal component was still present in the local background. This thermal component was considered when determining the luminosities of the examined objects. For SNR B0543-68.9, a temperature of $k_\mathrm{B}T_\mathrm{X,SNR} = (0.64^{+0.73}_{-0.20})\,\mathrm{keV}$ was determined and an ionization timescale of $\tau_\mathrm{SNR} = (2.1^{+1.3}_{-0.6}) \times 10^{10}\,\mathrm{s\,cm^{-3}}$. The superbubble resulted to have a column density within the LMC of $N_\mathrm{H,LMC,SB} = (0.30^{+0.36}_{-0.23}) \times 10^{22}\,\mathrm{cm^{-2}}$ and a temperature of $k_\mathrm{B}T_\mathrm{X,SB} = (0.74^{+0.36}_{-0.30})\,\mathrm{keV}$. The values obtained for the blowout region are reasonable when compared to the values of the superbubble region, with a temperature of $k_\mathrm{B}T_\mathrm{X,BL} = (0.62^{+0.38}_{-0.42})\,\mathrm{keV}$ and a column density of $N_\mathrm{H,LMC,BL} = (0.27^{+0.93}_{-0.27}) \times 10^{22}\,\mathrm{cm^{-2}}$. For the calculation of the luminosities, the different contributions of the SNR and the superbubble to the total luminosity of the SNR extraction region were taken into account – a consequence of the superposition of both objects. A local background subtracted, unabsorbed luminosity of $(1.5^{+1.6}_{-1.2}) \times 10^{36}\,\mathrm{erg\,s^{-1}}$ was determined for SNR B0543-

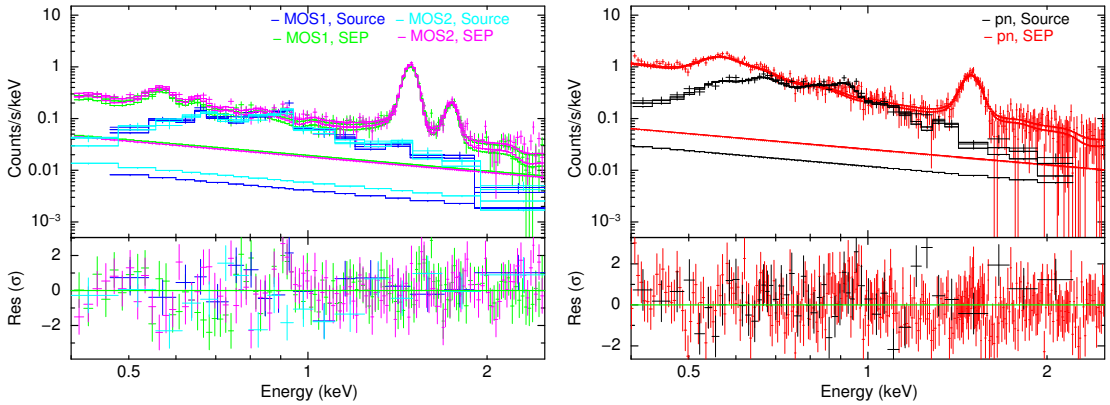

(a) (b)

Figure 6.16: Source and SEP data points and fitted model for (a): the EPIC-MOS1 and EPIC-MOS2 detectors, and (b): for the EPIC-pn detector. These source and background spectra were used for the fits of the SNR region with the *vpshock* model as source component. The parameters of the plots are the same as those in Figure 6.15, unless otherwise stated.

Table 6.3: Luminosities in the energy range of 0.5 – 8 keV calculated for the extraction region of the SNR, the polygonal region (i.e. part of the superbubble), the blowout, and the local background. Given are the absorbed and unabsorbed luminosities with and without local background subtraction. The third row gives the percentual size of the extraction region with respect to the size of the local background region. This percentage was used to determine the background subtracted luminosities. Uncertainties are upper and lower 90 % confidence ranges.

Fitting region		SNR		
		Total	SNR	SB
Absorbed L_x	[10^{35} erg/s]	1.5 (0.3 – 3.1)	1.3 (0.2 – 2.7)	0.2 (0.04 – 0.5)
Unabsorbed L_x	[10^{35} erg/s]	16.0 (3.4 – 33.3)	14.7 (3.1 – 30.6)	1.3 (0.2 – 2.7)
Size cp. to local Bkg.	[%]	34.0	24.8	14.2
Local Bkg. subtracted L_x	[10^{35} erg/s]	1.3 (0.2 – 2.7)	1.2 (0.2 – 2.5)	0.1 (0.02 – 0.3)
Unabs. local Bkg. subtr. L_x	[10^{35} erg/s]	15.7 (3.4 – 32.7)	14.5 (3.1 – 30.2)	1.2 (0.2 – 2.5)

Fitting region		Polygon	Blowout	Local Bkg.
Absorbed L_x	[10^{35} erg/s]	0.8 (0.77 – 3.5)	0.3 (0.1 – 17.9)	0.5 (0.3 – 0.7)
Unabsorbed L_x	[10^{35} erg/s]	2.4 (1.8 – 10.7)	0.8 (0.3 – 43.4)	0.8 (0.5 – 1.0)
Size cp. to local Bkg.	[%]	26.2	35.5	100.0
Local Bkg. subtracted L_x	[10^{35} erg/s]	0.7 (0.5 – 2.3)	0.2 (0.06 – 8.6)	0
Unabs. local Bkg. subtr. L_x	[10^{35} erg/s]	2.2 (1.6 – 9.8)	0.6 (0.2 – 29.2)	0

68.9, and of $(3.4^{+7.8}_{-1.2}) \times 10^{35}\,\mathrm{erg\,s^{-1}}$ and $(5.6^{+286.5}_{-3.3}) \times 10^{34}\,\mathrm{erg\,s^{-1}}$ for the superbubble and its blowout. These results will be used in the following section to calculate further properties of the objects.

6.5 Discussion

In this section, the calculation of further properties of SNR B0543-68.9, the superbubble, and the blowout will be discussed. Special attention is paid to the contribution of stars to the diffuse X-ray luminosity of the DEM L299 region and to the energy and mass input of the superbubble. The calculations performed in this section follow the same approach as the ones presented in Sasaki et al. (2004) and Bozzetto et al. (2014).

6.5.1 Supernova Remnant SNR B0543-68.9

To determine further properties of SNR B0543-68.9, the Sedov-Talyor-von Neumann self-similar solution (in short: Sedov solution or Sedov model) is used, which is valid for SNRs in their adiabatic phase (Sedov, 1959; Taylor, 1950; von Neumann, 1947). Before the calculations are presented, a short description of the Sedov solution, of the concept of collisional ionization equilibrium (CIE), and of temperature equilibration are given, including ways to test for CIE and temperature equilibration. A more detailed introduction concerning these topics can be found in Section 2.5.2.

The adiabatic phase of an SNR is defined as the phase in which only a small fraction of the remnant's energy is radiated away and a reverse shock is formed due to the swept-up ISM. In this phase, the SNR can be described through the Sedov solution (see Sect. 2.5.2 for an overview of this solution). SNR B0543-68.9 can be assumed to be in a late adiabatic phase, since it has a large diameter of $\sim 60\,\mathrm{pc}$ and due to the fact that good fitting results were obtained with the *vpshock* model when assuming LMC abundances, indicating that the SNR is dominated by the emission of shocked ISM and not by the emission of its ejecta. In the Sedov model, the evolution of a remnant depends only on the initial energy E_0 of the explosion and on the density n_0 of the ambient gas at the time of the explosion. Assumptions for this model are a homogenous ambient medium, a spherical symmetric point explosion, and a monatomic ideal gas. The Rankine-Hugoniot jump conditions (Rankine, 1870; Hugoniot, 1887, 1889) are used, which describe the relationship between the properties of the gas in front of the shock front and directly behind the shock front. For an ideal gas, for example, the relationship between the density of the gas in front of the shock (ρ_0) and directly behind the shock (ρ_1) is $\rho_1 = 4\rho_0$.

In the Sedov phase, the hot, X-ray emitting gas has its highest density close to the shell due to shocked ISM, and decreases towards the center of the SNR. The Sedov model has been used to calculate further properties of SNR B0543-68.9 (see below).

As the fits indicate an incompletely re-established collisional ionization equilibrium (CIE) for the SNR B0543-68.9, the degree of collisional non-equilibrium ionization (NEI) are discussed in this section as well as the effects of a not re-established temperature equilibration onto the calculated properties of the SNR.
A way to estimate how well CIE has been re-established is given by Smith and Hughes (2010). They provide a plot which shows the characteristic maximum ionization timescale for different elements of a plasma as a function of temperature (see Smith and Hughes, 2010, Fig. 1). Their plot can be used to estimate the degree of CIE using the fitted values for the X-ray temperature and the ionization timescale. Comparing the fitted X-ray temperature $T_{\mathrm{X,SNR}}$ and the ionization timescale τ_{SNR} for SNR B0543-68.9 with their plot, it was found that the ionization timescale of carbon has already been reached, and within the uncertainties of $T_{\mathrm{X,SNR}}$ and τ_{SNR}, the same is true for nitrogen, oxygen and neon, while the heavier elements Mg, Al, Si, S, Ar, Ca, Fe, and Ni are still in NEI. Thus, according to the method of Smith and Hughes (2010), only carbon should be near collisional ionization equilibrium, while most of the heavier elements are still in NEI. These results are in agreement with the value obtained for the ionization timescale ($\tau_{\mathrm{SNR}} = (2.1^{+1.3}_{-0.6}) \times 10^{10}\,\mathrm{s\,cm^{-3}}$) as determined during the X-ray spectral analysis (see Sect. 6.4) indicating NEI, since Smith and Hughes (2010) give an estimate for τ of some $10^{12}\,\mathrm{s\,cm^{-3}}$ for a fully re-established CIE. A further indication for NEI is the better fit result for the NEI model *vpshock* than for the CIE model *apec* (see Sect. 6.4).

A method introduced by Itoh (1978) was used to estimate how well temperature equilibration has been re-established again and to calculate its effect on the properties of the SNR as determined through the Sedov solution. In this method, the intersection point $f_{\mathrm{T}} := < T_{\mathrm{e}} > / T_{\mathrm{S}} \approx T_{\mathrm{X,SNR}}/T_{\mathrm{S}}$ between the curve for Coulomb equilibration and the curve defined by $T_{\mathrm{X,SNR}}/T_{\mathrm{S}} = 0.043 T_{\mathrm{X,SNR}}(R_{\mathrm{SNR}} n_0)^{-1/2} \nu^{7/5}$ is used to estimate the degree of temperature equilibration, with the average electron temperature $< T_{\mathrm{e}} >$, the shock temperature T_{S}, the X-ray temperature $T_{\mathrm{X,SNR}}$, the SNR radius R_{SNR}, the pre-shock number density of nuclei n_0, and the reduced time variable ν (see Sect. 2.5.2 for more information about this method). A value of $f_{\mathrm{T}} = 1$ indicates a fully re-established temperature equilibration with $< T_{\mathrm{e}} > = T_{\mathrm{S}}$, while smaller values imply an incomplete equilibration. This method was applied to SNR B0543-68.9 within the scope of this thesis. For this, the X-ray temperature $k_{\mathrm{B}} T_{\mathrm{X,SNR}} = (0.64^{+0.73}_{-0.20})\,\mathrm{keV}$ was used, as determined in Section 6.4. Furthermore, the [S II]/Hα flux-ratio image (Fig. 6.6) was used

to obtain the radius of $R_{\rm SNR} = 113''^{+16''}_{-8''} = (27.4^{+4.1}_{-2.2})\,{\rm pc}$ for SNR B0543-68.9, assuming a distance of 50 kpc to the LMC. The fitted normalization of the *vpshock* model can be used to determine the emission measure and, out of this, the pre-shock number density of hydrogen $n_{\rm H,0}$ (see below for the detailed calculations). By using this value and assuming cosmic abundances, a pre-shock number density of nuclei of $n_0 \approx 1.1 n_{\rm H0} = 0.069(^{+0.041}_{-0.030})\,{\rm cm}^{-3}$ is found for the ambient gas at the time of the explosion. With these parameters, a value of $f_{\rm T} = T_{\rm X,SNR}/T_{\rm S} = 0.37^{+0.59}_{-0.35}$ was obtained, which indicates that temperature equilibration has not yet been re-established. This temperature ratio $f_{\rm T}$ will be used to calculate the non-equilibration values of the parameters which are determined in the remainder of this section. However, the resulting values should be taken with caution, since the temperature ratio has a large uncertainty, which is a result of the low statistics of the DEM L299 observation, and since Itoh (1978) used Galactic abundances for the ISM whereas DEM L299 is located in the LMC.

For the following equations, which were used to determine further properties of SNR B0543-68.9, the electron number density $n_{\rm e}$ of the plasma is needed as well as the mean mass per nucleus $\bar{m}_{\rm n}$ and the mean mass per free particle $\bar{m}$. Assuming cosmic abundances and that the particles in the plasma are at least singly ionized, the electron number density is given by $n_{\rm e} = n_{\rm H} + 0.1 n_{\rm H} \times (1...2) + 0.013\,\zeta_{\rm LMC} n_{\rm H} \times 1 = [(1.1...1.2) + 0.013\,\zeta_{\rm LMC}] n_{\rm H} \approx (1.11...1.21) n_{\rm H}$, with $n_{\rm H}$ being the hydrogen density and $\zeta_{\rm LMC} = 0.5$ being the metallicity of the LMC with respect to the Milky Way. The mean mass per nucleus is given as $\bar{m}_{\rm n} = 1.4 m_{\rm p}$ assuming cosmic abundances, with $m_{\rm p} = 1.67 \times 10^{-24}\,{\rm g}$ being the proton mass. The total number density of particles is the sum of the number density of nuclei $n \approx 1.1 n_{\rm H}$ and the number density of electrons $n_{\rm e}$: $n_{\rm tot} = n + n_{\rm e} \approx (2.2...2.3) n_{\rm H}$. This leads to a mean mass per free particle (including electrons) of $\bar{m} = \bar{m}_{\rm n}/n_{\rm tot} \approx (0.64...0.61) m_{\rm p}$, with $\bar{m} \approx 0.61\,m_{\rm p}$ in the case of a fully ionized plasma. In addition, the volume of the SNR is needed for the following calculations. Assuming an LMC distance of 50 kpc and a spherical symmetric shape of the remnant, the volume was determined to be $V_{\rm SNR} = (4/3)\pi R^3_{\rm SNR} = (2.53^{+1.14}_{-0.62}) \times 10^{60}\,{\rm cm}^3$, using the [S II]/H$\alpha$ flux-ratio image. The volume of the SNR and of its fitting region are assumed to be equal, since their projections are almost identical.

With these preparations, the X-ray temperature and the normalization obtained from the X-ray spectral analysis can now be inserted into the Sedov solution to determine further basic properties of the SNR.
The normalization K of the Xspec model *vpshock*, which provided the best fitting results for the SNR B0543-68.9 (as well as for the superbubble and the blowout), can be used to determine the emission measure EM with

$$EM = \int n_e n_{\rm H} dV \tag{6.1}$$

of the X-ray emitting plasma. The normalization is defined as

$$K = \frac{10^{-14}}{4\pi D_{\mathrm{LMC}}^2} \int n_{\mathrm{e}} n_{\mathrm{H}} dV \,, \tag{6.2}$$

with the distance D_{LMC} in cm and the electron and hydrogen number densities in cm^{-3}. This results in an emission measure of $EM = (2.5^{+2.7}_{-2.0}) \times 10^{58}\,\mathrm{cm}^{-3}$. The emission measure can be used to determine the pre-shock hydrogen density $n_{\mathrm{H},0}$ by using the Sedov solution and the approximation for the radial density distribution of Kahn (1975), resulting in

$$EM = 2.07 \left(\frac{n_{\mathrm{e}}}{n_{\mathrm{H}}} \right) n_{\mathrm{H},0}^2 V, \tag{6.3}$$

with V being the volume of the SNR (see e.g. Hamilton et al., 1983; Hamilton and Sarazin, 1984). With $n_{\mathrm{e}}/n_{\mathrm{H}} = 1.21$, this results in a pre-shock hydrogen density of $n_{\mathrm{H},0} = (0.063^{+0.037}_{-0.027})\,\mathrm{cm}^{-3}$. Out of this, the pre-shock density of nuclei was determined to be $n_0 \approx 1.1 n_{\mathrm{H},0} = 0.069(^{+0.041}_{-0.030})\,\mathrm{cm}^{-3}$, which is in accordance with the density expected for an H II region (e.g. McKee and Ostriker, 1977).

To obtain the shock velocity v_{S}, the following equation can be used:

$$T_{\mathrm{S}} = \frac{3\bar{m}}{16 k_{\mathrm{B}}} v_{\mathrm{S}}^2 \,, \tag{6.4}$$

with T_{S} representing the shock temperature and $k_{\mathrm{B}} = 1.38 \times 10^{-16}\,\mathrm{erg/K}$ being the Boltzmann constant. Considering that with $f_{\mathrm{T}} = T_{\mathrm{X,SNR}}/T_{\mathrm{S}} = 0.37$, temperature equilibration has been found to be not re-established yet, the shock velocity results to be $v_{\mathrm{S}} = [(16 k_{\mathrm{B}} T_{\mathrm{X,SNR}})/(3 \times 0.37 \times 0.61 m_{\mathrm{p}})]^{1/2} = (1\,200^{+1\,200}_{-700})\,\mathrm{km\,s^{-1}}$. In the case of full temperature equilibration, the X-ray temperature can be assumed to equal the shock temperature, which leads to $f_{\mathrm{T}} = 1$ and a shock velocity of $v_{\mathrm{S,TE}} = [(16 k_{\mathrm{B}} T_{\mathrm{X,SNR}})/(3 \times 0.61 m_{\mathrm{p}})]^{1/2} = (730^{+420}_{-120})\,\mathrm{km\,s^{-1}}$.
These values can now be inserted into the Sedov solution to determine the age of SNR B0543-68.9 and the initial energy of the supernova explosion. Its age t_{SNR} is given through the relation

$$v_{\mathrm{S}} = \frac{2 R_{\mathrm{SNR}}}{5 t_{\mathrm{SNR}}} \,, \tag{6.5}$$

which leads to $t_{\mathrm{SNR}} = (2R_{\mathrm{SNR}})/(5v_{\mathrm{S}}) = (8.9^{+9.2}_{-4.4})\,\mathrm{kyr}$ in the case of no re-established temperature equilibration (with $f_{\mathrm{T}} = 0.37$), while when assuming a fully re-established temperature equilibration (with $f_{\mathrm{T}} = 1$), the age of the SNR becomes $t_{\mathrm{SNR,TE}} = (15^{+9}_{-3})\,\mathrm{kyr}$.
The initial energy of the explosion E_0 can be determined using the formula

$$R_{\mathrm{SNR}} = \left(\frac{2.02 E_0 t_{\mathrm{SNR}}^2}{\bar{m}_{\mathrm{n}} n_0} \right)^{1/5} . \tag{6.6}$$

For no re-established temperature equilibration (with $f_{\mathrm{T}} = 0.37$), this results in an explosion energy of $E_0 = (1.4 m_{\mathrm{p}} n_0 R_{\mathrm{SNR}}^5)/(2.02 t_{\mathrm{SNR}}^2) = 4.3\,(< 14.0) \times 10^{51}\,\mathrm{erg}$, being in accordance with the typical value of $10^{51}\,\mathrm{erg}$. When assuming fully re-established temperature equilibration (with $f_{\mathrm{T}} = 1$), an upper limit for the explosion energy of $E_{0,\mathrm{TE}} = (1.6^{+2.6}_{-1.2}) \times 10^{51}\,\mathrm{erg}$ is obtained.

The mass M_{ISM} of the interstellar medium swept up by the shock front can be estimated out of the volume of SNR B0543-68.9 and the density of the ambient ISM as

$$M_{\mathrm{ISM}} = V_{\mathrm{SNR}}\,\rho_0 = \frac{4}{3}\pi R_{\mathrm{SNR}}^3 1.4 m_{\mathrm{p}} n_0 = (210^{+150}_{-110})\,\mathrm{M}_\odot \tag{6.7}$$

when assuming a homogeneous density of the ISM and a spherical symmetric shape of the the remnant. This large mass of swept-up ISM justifies the earlier assumption of the remnant being well into its adiabatic phase.

6.5.2 DEM L299 Superbubble and its Blowout

This section discusses the calculations performed for the superbubble and the blowout in DEM L299. These calculations are based upon the ideal gas equations, which are assumed to be adequate for the gas, since it can be considered to be in thermal equilibrium. This assumption is based upon the typically large ages of superbubbles of this size and on the absence of shocks in superbubbles, with the exception of shocks caused through supernova explosions within a superbubble.

DEM L299 Superbubble

Since both the superbubble and SNR B0543-68.9 were fitted best with the same model source component (*vpshock*), the number density of hydrogen $n_{\mathrm{H,SB}}$ for the gas inside the superbubble can again be determined out of the fitted normalization of this component. For this, Equation 6.2 holds, with the only difference that the volume has to be multiplied by the filling factor ϕ. This factor accounts for the fraction by which the superbubble is filled with the hot gas. Young interstellar bubbles can be assumed to be completely filled with hot gas, leading to a filling factor of $\phi \approx 1$ (Sasaki et al., 2011). For the volume in Equation 6.2, the volume $V_{\mathrm{SB,fit}}$ as defined by the polygonal superbubble extraction region of the X-ray spectra has to be inserted (see Fig. 6.14). To determine its volume, the polygonal region was approximated by an ellipsoid. The radii of this ellipsoid have been estimated to be $a = 153''^{+2''}_{-1''} = (37.1^{+1.2}_{-1.1})\,\mathrm{pc}$, $b = 65''^{+6''}_{-3''} = (15^{+3}_{-2})\,\mathrm{pc}$, and $c = 108'' \pm 12'' = (26.2^{+3.1}_{-3.1})\,\mathrm{pc}$, with c – representing the radius of the depth of the ellipsoid – assumed to be identical to the radius of the superbubble as determined through the Hα image (Fig. 6.5a). This leads to a volume of $V_{\mathrm{SB,fit}} = (4/3)\pi\,abc =$

$(1.8^{+0.5}_{-0.4}) \times 10^{60}\,\mathrm{cm}^3$ for the polygonal superbubble fitting region, assuming an LMC distance of 50 kpc. The volume of the whole superbubble – differing from the volume of the polygonal fitting region of the superbubble – was estimated from the Hα image to have a radius of $R_{\mathrm{SB}} = 108''^{+12''}_{-12''} = (26.2^{+3.1}_{-3.1})\,\mathrm{pc}$. This leads to a volume of $V_{\mathrm{SB}} = (4/3)\pi R_{\mathrm{SB}}^3 = (2.21^{+0.79}_{-0.79}) \times 10^{60}\,\mathrm{cm}^3$ for the whole superbubble, assuming the LMC distance and a spherical symmetric shape. The total hydrogen number density of the hot gas inside the superbubble can now be determined by using Equation 6.2, resulting in

$$n_{\mathrm{H,SB}} = \left(\frac{4\pi K D^2}{1.2 \times 10^{-14} V_{\mathrm{SB,fit}}\,\phi} \right)^{1/2} = (0.048^{+0.083}_{-0.009})\,\phi^{-0.5}\mathrm{cm}^{-3}\,. \tag{6.8}$$

The ideal gas equations can be used to calculate the pressure $p_{\mathrm{SB,i}}$ and the thermal energy content $E_{\mathrm{th,SB}}$ of the hot gas inside the superbubble. The pressure follows the ideal gas equation

$$p_{\mathrm{SB,i}} V_{\mathrm{SB}} = N_{\mathrm{tot}} k_{\mathrm{B}} T_{\mathrm{SB}}\,, \tag{6.9}$$

with the following definitions:

$p_{\mathrm{SB,i}}$: pressure in $\mathrm{g\,cm^{-1}\,s^{-2}}$,
V_{SB} : volume of the superbubble in cm^3,
N_{tot} : total number of particles,
T_{SB} : temperature in K.

The temperature T_{SB} of the superbubble can again be assumed to be $T_{\mathrm{SB}} \approx T_{\mathrm{X,SB}}$. Inserting $n_{\mathrm{tot}} = N_{\mathrm{tot}}/V_{\mathrm{SB}} = n_{\mathrm{e}} + 1.1 n_{\mathrm{H}}$ and $n_{\mathrm{e}} = (1.2 + 0.013\zeta_{\mathrm{LMC}})\,n_{\mathrm{H}}$ into Equation 6.9, it becomes

$$p_{\mathrm{SB,i}}/k_{\mathrm{B}} = 2.31 n_{\mathrm{H}} T_{\mathrm{X,SB}}\,, \tag{6.10}$$

which leads to a value of $p_{\mathrm{SB,i}}/k_{\mathrm{B}} = (9.5^{+17.2}_{-4.3}) \times 10^5 \phi^{-0.5}\,\mathrm{cm}^{-3}\,\mathrm{K}$ for the pressure of the hot gas inside the superbubble. The thermal energy content of the hot gas inside the superbubble can be described by the following equation for an ideal gas:

$$E_{\mathrm{th,SB}} = \frac{3}{2} n_{\mathrm{tot}} k_{\mathrm{B}} T_{\mathrm{X,SB}}\,\phi\,. \tag{6.11}$$

Inserting Equation 6.9 into Equation 6.11 results in a thermal energy of $E_{\mathrm{th,SB}} = (3/2) p_{\mathrm{SB,i}} V_{\mathrm{SB}} \phi = (4.3^{8.1}_{-2.6}) \times 10^{50}\,\phi^{0.5}\,\mathrm{erg}$. The mass of the hot gas inside the superbubble can be determined through the relation

$$M_{\mathrm{SB,i}} = n_{\mathrm{tot}}\,\mu\,m_{\mathrm{H}} V_{\mathrm{SB}}\,, \tag{6.12}$$

with $\mu = 0.61$ being the molecular weight of a fully ionized gas and m_{H} being the hydrogen mass. Expressing the total number of particles n_{tot} through the hydrogen density, the mass of the hot gas inside the superbubble results to be $M_{\mathrm{SB,i}} = 2.31\,n_{\mathrm{H}}\,\mu\,m_{\mathrm{H}} V_{\mathrm{SB}} = (130^{+230}_{-60})\,\phi^{0.5}\,\mathrm{M}_\odot$.

Blowout

The same calculations were performed for the blowout of the superbubble. The volume of the fitting region of the blowout (see Fig. 6.14) was approximated by an ellipsoid with radii of $a = 166''^{+2''}_{-5''} = (40.2^{+1.2}_{-1.7})$ pc, $b = 84''^{+8''}_{-9''} = (20^{+4}_{-4})$ pc, and $c = 108''^{+12''}_{-12''} = (26.2^{+3.1}_{-3.1})$ pc, assuming the LMC distance. The radius c, which is representing the depth of the ellipsoid, is again chosen as the radius of the superbubble as defined by the Hα image (Fig. 6.5a). This results in a volume of the blowout fitting region of $V_{\mathrm{BL,fit}} = (2.6^{+0.7}_{-0.7}) \times 10^{60}\,\mathrm{cm}^3$ and in a hydrogen number density of $n_{\mathrm{H,BL}} = (0.034^{+0.871}_{-0.011})\phi^{-0.5}\,\mathrm{cm}^{-3}$ for the hot gas inside the blowout. Since the spectral extraction region for the blowout has been defined in a way to include as much as possible of the X-ray emission originating from the blowout, the actual volume of the blowout is considerably smaller than its fitting region (see Fig. 6.14). Therefore, the volume of the blowout was determined separately. This was done by approximating its volume as defined by the medium X-ray image with an ellipsoid. The thus determined radii are $a = 157''^{+11''}_{-11''} = (38^{+3}_{-3})$ pc, $b = 60''^{+11''}_{-7''} = (15^{+4}_{-3})$ pc, and $c = 108''^{+12''}_{-12''} = (26.2^{+3.1}_{-3.1})$ pc, with the radius of the depth c assumed again to be equal to the superbubble radius. This leads to an approximate volume of the blowout of $V_{\mathrm{BL}} = (1.8^{+0.6}_{-0.5}) \times 10^{60}\,\mathrm{cm}^3$. With the formulae described above for the superbubble,

- a pressure of $p_{\mathrm{BL,i}}/k_{\mathrm{B}} = (0.57^{+14.50}_{-0.43}) \times 10^6 \phi^{-0.5}\,\mathrm{cm}^{-3}\,\mathrm{K}$,
- a thermal energy content of $E_{\mathrm{th,BL}} = (2.0^{+54.1}_{-1.8}) \times 10^{50} \phi^{0.5}\,\mathrm{erg}$, and
- a mass of $M_{\mathrm{BL,i}} = (70^{+1\,861}_{-36})\,\phi^{0.5}\,\mathrm{M}_\odot$

were obtained for the hot gas inside the superbubble.

DEM L299 Superbubble plus its Blowout

Summing up the values of the superbubble and of its blowout, a total mass and thermal energy content can be given. For the total mass of the hot gas inside the superbubble plus blowout, a value of $M_{\mathrm{i}} = (200^{+1\,876}_{-70})\,\phi^{0.5}\,\mathrm{M}_\odot$ was obtained, as well as a thermal energy content of $E_{\mathrm{th}} = (6.3^{+54.8}_{-3.2}) \times 10^{50} \phi^{0.5}\,\mathrm{erg}$. Although the 90 % confidence ranges for the blowout values are large due to the low statistics of the observation and the small size of the spectral extraction region, these summed up values are still given to provide an estimation for the properties of this region.

Dynamic Age of the DEM L299 Superbubble

The dynamic age of a superbubble can be estimated by using the equation:

$$R = \alpha (E_{\mathrm{th,SB}}/\rho)^{1/5} t_{\mathrm{dyn,SB}}^{2/5} \,, \tag{6.13}$$

with the following definitions:

R : radius of the outer shell in cm ($\approx R_{\mathrm{SB}}$),
$E_{\mathrm{th,SB}}$: thermal energy content of the superbubble in erg,
$t_{\mathrm{dyn,SB}}$: its dynamic age in s,
ρ : mass density of all particles of the ambient medium in g/cm^3.

The mass density can be determined through $\rho = n\,\mu\,m_{\mathrm{p}}$, with the total particle density n of the ambient medium, the mean molecular mass μ, and the proton mass m_{p}. In the formula, α is a coefficient corresponding to the stage of evolution of the interstellar bubble and is set to 0.76, according to an intermediate stage (Weaver et al., 1977). To determine the total particle density n of the ambient medium, the hydrogen density $n_{\mathrm{H,0}}$ of the ambient medium of the SNR has been used, which resulted in $n = 2.31 n_{\mathrm{H,0}} = (0.15^{+0.09}_{-0.07})\,\mathrm{cm}^{-3}$. Solving Equation 6.13 leads to a dynamic age of the superbubble of $t_{\mathrm{dyn,SB}} = (70^{+73}_{-35})\,\mathrm{kyr}$. For this calculation, the thermal energy content of only the superbubble (without the blowout) was used due to the large confidence ranges of the blowout and since this approach provides an upper limit for the dynamic age. Compared to the age of the stars which formed it, the dynamic age of the superbubble seems quite young. Too young dynamic ages have also been found for several other superbubbles, see e.g. Sasaki et al. (2011) or Cooper et al. (2004). A possible answer to this problem might be the growth-rate discrepancy, which has been observed in several superbubbles (e.g. Cooper et al., 2004; Jaskot et al., 2011), and which can explain too small observed sizes of superbubbles due to a lower growth rate than expected from the stellar wind input. More information about the growth-rate discrepancy can be found in Section 2.4.1. Out of the dynamic age, an average mass loss rate of $(1.9^{+3.9}_{-1.3}) \times 10^{-3}\,\mathrm{M}_{\odot}/\mathrm{yr}$ and an average energy input rate of $(2.0^{+4.3}_{-1.6}) \times 10^{38}\,\mathrm{erg/s}$ were determined for the superbubble (without the blowout), considering its mass and thermal energy content as obtained above.

6.5.3 Contribution of Stars

In the previous sections, the basic properties of SNR B0543-68.9 and the DEM L299 superbubble were deduced, emanating from the results of the X-ray spectral analysis. This section will now discuss how and to what extent some of these previous results – and the SNR and the superbubble themselves – are affected by the presence of stars in the vicinity of these two objects.

Population Study

To estimate the influence of these stars, the astronomical database SIMBAD[8] has been used to perform a population study for the vicinity of DEM L299, covering an area with a radius of $\sim 4\farcm5$ (65 pc) around the center of SNR B0543-68.9 as defined by the [S II]/Hα flux-ratio image. In this area, two clusters of stars, two associations of stars, and five OB-stars were found. A list of these objects is given in Table 6.4, and their positions are marked in the X-ray and optical images of Figure 6.17. Three of these objects – the two OB-stars in the south-west of DEM L299 and the association KMHK 1274 lying projected towards one of these OB-stars – are too far away from the border of the remnant ($4'$) and of the superbubble ($2'$ and $3'$, respectively) to be likely to have a great influence on them. Furthermore, this association is marked by Bica et al. (1999) to be possibly connected to the emission object LHA 120-N 164, visible as a bright region south of DEM L299 in the Hα image of Figure 6.17b.
The remaining six objects are projected close to the border of SNR B0543-68.9 and of the superbubble, including the OB-star CPD-69 513 lying in projection within the remnant, the OB-star GSC 09163-00731 which is visible at the position of the circular star-forming region at the northern rim of the superbubble, and the cluster H88 324 imaged at the intersection point of the SNR and the superbubble (see Fig. 6.17). The cluster H88 324 is marked by Bica et al. (1999) to be possibly connected to DEM L299, but unfortunately, no further information is available about this cluster. There is also no deep study of the other cluster (H88 325) and the association (BSDL 2862) projected close to the border of DEM L299, and no detailed information about the spectral types of the OB-stars could be found in SIMBAD.

Stellar Contribution to the X-ray Luminosity

In Section 6.4, the X-ray luminosity in the energy band of 0.5 – 8 keV was determined for SNR B0543-68.9 and for the superbubble. To do so, it was assumed that all X-ray point sources in this energy range were masked and that the entire remaining X-ray emission in this energy band originates from either the remnant or the superbubble. However, there are two additional types of X-ray sources

[8] SIMBAD – **S**et of **I**dentifications, **M**easurements, and **B**ibliography for **A**stronomical **D**ata: An astronomical database which is maintained by the Centre de données astronomiques de Strasbourg (CDS), France. The first online version of SIMBAD has been released in 1981. Today, it contains information about more than 3.5 million astronomical objects excluding objects from the Solar System. Beyond basic information like object type or coordinates, information needed for, e.g., cross-calibration of catalogs and bibliographic references are provided. SIMBAD hompage: `http://simbad.u-strasbg.fr/simbad/`

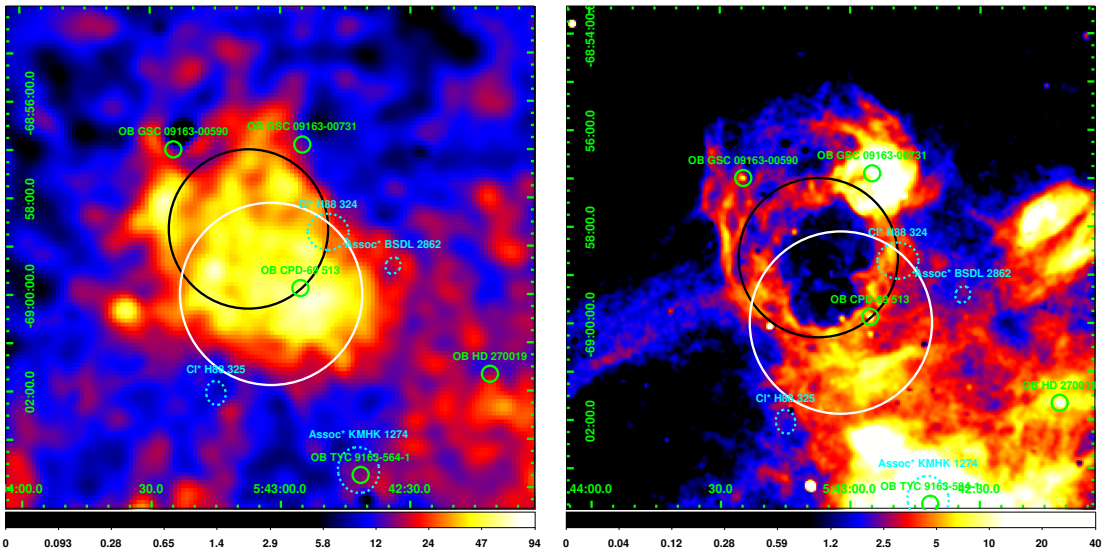

Figure 6.17: Clusters of stars, stellar associations (both indicated by blue, dashed circles), and OB-stars (marked with green circles) in the DEM L299 region as found in SIMBAD. The position and size of the clusters and associations are taken from the catalog of Bica et al. (1999). The position of SNR B0543-68.9 as found through the [S II]/Hα flux-ratio image (Fig. 6.6) and of the superbubble as defined by the Hα image (Fig. 6.5a) is marked in white and black, respectively. The objects are overlaid onto (a) the *XMM-Newton* EPIC X-ray broadband (0.3 – 8 keV) image of DEM L299, showing approximately the same area of the sky, smoothing parameters, and scale parameters as used for Figure 6.3; and (b) the DEM L299 region in Hα, with the same parameters as used for Figure 6.5.

Table 6.4: Table showing the results of the population study performed with SIMBAD for an area with a radius of $\sim 4\farcm5$ (65 pc) around the center of SNR B0543-68.9. Listed are the clusters of stars, stellar associations, and OB-stars in this region. For each object, the coordinates, the type, and the identifier are given. A possible physical connection to another object – as given by Bica et al. (1999) – is stated in the last column.

RA (J2000)	Dec (J2000)	Type	Identifier	
05:42:49	-68:58.7	Cluster	H88 324	in DEM L299
05:43:15	-69:02.0	Cluster	H88 325	
05:42:34	-68:59.4	Assoc.	BSDL 2862	
05:42:42	-69:03.7	Assoc.	KMHK 1274	in LHA 120-N 164
05:42:11.561	-69:01:39.33	OB-star	HD 270019	
05:42:41.496	-69:03:45.10	OB-star	TYC 9163-564-1	
05:42:54.93	-68:56:54.5	OB-star	GSC 09163-00731	
05:42:55.414	-68:59:52.81	OB-star	CPD-69 513	
05:43:24.67	-68:57:00.1	OB-star	GSC 09163-00590	

which can spoil these assumptions and the influence of which has to be investigated: a considerable amount of X-ray emission can be produced by OB-stars (i.e. high-mass stars) and low-mass stars.[9]

Contribution of OB-Stars

OB-stars emit X-ray emission due to shock waves in their stellar winds (Oskinova, 2005), which are generated through radiation pressure. The contribution of OB-stars to the X-ray luminosity of DEM L299 can be estimated by using the results of the population study. The OB-star CPD-69 513 is projected towards the spectral extraction region of SNR B0543-68.9, while OB-star GSC 09163-00731 is lying within the extraction region of the superbubble. Since no further information about the spectral type of these stars is available, typical soft X-ray luminosities for O-type stars of $\sim 10^{31} - 10^{33}\,\mathrm{erg\,s^{-1}}$ were used as an estimate of their X-ray luminosity (Chlebowski et al., 1989; Berghoefer et al., 1997; Sana et al., 2006). Therefore, these high-mass stars contribute $\sim 2 \times 10^{31} - 2 \times 10^{33}\,\mathrm{erg\,s^{-1}}$ to the X-ray luminosity of DEM L299. Considering the unabsorbed, local background subtracted luminosities as determined in Section 6.4, this only accounts for 0.6 % of the luminosity of the superbubble and for 0.14 % of the luminosity of SNR B0543-68.9 and is therefore negligible.

[9] In general, stars with intermediate masses produce a negligible amount of X-ray emission (Oskinova, 2005).

Contribution of Low-Mass Stars

The second source of potentially considerable, additional X-ray emission are low-mass stars. These stars produce X-ray emission due to magnetic activity, for which the presence of outer convective layers is important (Oskinova, 2005). Although each of these stars with masses $\lesssim 3\,\mathrm{M}_\odot$ has a low X-ray luminosity compared to OB-stars, the large number of low-mass stars in any stellar population may nonetheless lead to their considerable contribution to the X-ray luminosity of an area of the sky. Furthermore, if these low-mass stars are unresolved, their emission might easily be confused with diffuse X-ray emission as emitted by hot gas. When studying diffuse X-ray emission, it is therefore important to ensure that the observed emission is truly diffuse emission and not the sum of the radiation of a large number of unresolved low-mass stars.
To test this, the actual number of these low-mass stars in the observed population is needed as well as the average X-ray luminosity of these stars. Their number was estimated by creating a color-magnitude diagram of DEM L299 (see Fig. 6.18). Since there are no extensive studies about the OB-stars, the clusters, and the association projected towards DEM L299, the color-magnitude diagram was produced within the scope of this thesis by using the photometric catalog of Zaritsky et al. (2004). This catalog comprises stars in the bandpasses UBVI of the central $8^\circ \times 8^\circ$ of the Large Magellanic Cloud (Zaritsky et al., 1997). This catalog was used to create the color-magnitude diagram for a composed area of DEM L299 consisting of two circles: one circle centered around the superbubble with a radius of $2'$ and another circle around SNR B0543-68.9 with a radius of $2\farcm3$. Figure 6.18 shows the resulting color-magnitude diagram, with evolutionary tracks and isochrones taken from Lejeune and Schaerer (2001), for which the basic model set for the Johnson-Cousins-Glass photometry was used and the metallicity of $Z = 0.008$ was chosen, since – being about half of the solar value $Z_\odot = 0.02$ – it is close to the metallicity of the LMC. In order to plot the evolutionary tracks into the color-magnitude diagram, the absolute magnitude M for the V-band as given by Lejeune and Schaerer (2001) was converted into the apparent magnitude m using the distance modulus:

$$m - M = 5\,\mathrm{mag}\log(r/10\,\mathrm{pc})\,, \tag{6.14}$$

with r being the distance to the LMC in pc.

Since no information about the distance to the stars is provided in the catalog of Zaritsky et al. (1997), background and foreground stars will be present in the thus created color-magnitude diagram of DEM L299. This was considered by ignoring those stars during the further analysis which lie on a different isochrone than the most massive stars. This approach is justified since stars belonging to the same stellar population should follow the same isochrone, as they should be approximately of the same age (apart from second generation stars), and as

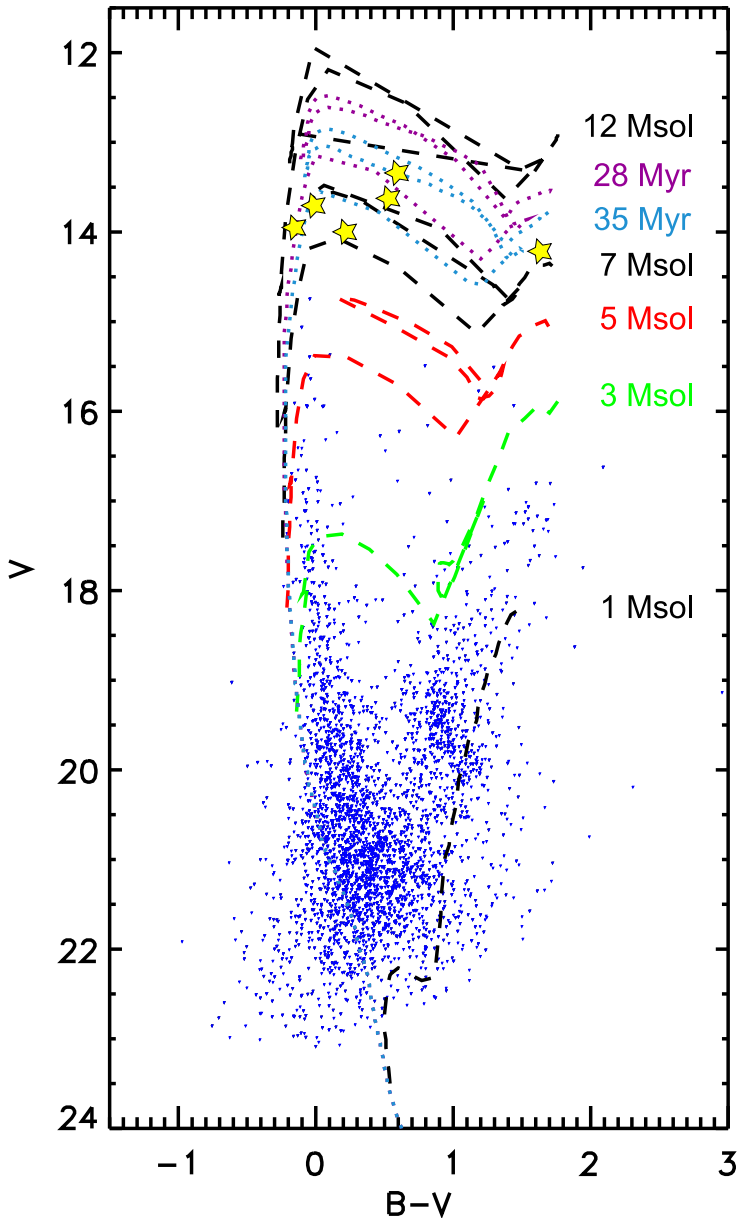

Figure 6.18: Color-magnitude diagram for the stars in the DEM L299 region created with data from the photometric catalog of Zaritsky et al. (1997). Plotted are the stars within an area with a radius of 2′.3 from the center of SNR B0543-68.9 plus stars within an area of 2′ around the center of the superbubble. Stars are plotted in blue, with the yellow star symbols marking the most massive stars. Evolutionary tracks taken from Lejeune and Schaerer (2001) are plotted as dashed lines for stars with masses of – from bottom to top – 1, 3 (green), 5 (red), 7, and 12 $M_\odot$. The two isochrones at 28 Myr and 35 Myr, which are also taken from Lejeune and Schaerer (2001), are plotted as dotted curves in purple and blue, respectively.

DEM L299, being located in a star-forming region of the LMC, is expected to harbor young stars. Following this procedure, it was assumed that all stars in the DEM L299 region originate from the same stellar population.
Since a stellar population develops along its isochrone in the color-magnitude diagram, the turn-off point of a stellar population from the main sequence can be used to determine the age of the population. Since more massive stars develop faster than low-mass stars, this turn-off point can be observed first at the high-mass end of the main sequence, moving downwards as the population gets older. Out of the created color-magnitude diagram from DEM L299, an age of $28-35\,\mathrm{Myr}$ was estimated for the DEM L299 population, since the most massive stars of this diagram (with masses between $7-12\,\mathrm{M}_\odot$) seem to follow these isochrones (see Fig. 6.18). However, since no unambiguous turn-off point can be determined and to consider possible confusion with back- and foreground stars, this age estimate should rather be treated as an upper limit.

For a population of stars which formed from the same parental molecular cloud, the initial mass function (IMF) can be used to determine the amount of stars in a certain mass bin when knowing the number of stars in any mass bin of this population. The IMF describes empirically the mass distribution of the stars of a population which they initially had during their main-sequence phase. The IMF can empirically be well described for stars with masses $m \gtrsim 1\,\mathrm{M}_\odot$ as a power law with an index of $\alpha = 2.35$ and is then called the Salpeter IMF (Salpeter, 1955) ψ with

$$\psi \propto m^{-2.35}\,, \tag{6.15}$$

where ψ gives the number of stars per volume (pc^3) with a mass between m and $m+dm$. This empirical formula shows that low-mass stars are more frequent than stars with high masses. For stars with masses $m \lesssim 1\,\mathrm{M}_\odot$, the power law index decreases. A universal description fails in this mass range and different formulae exist.
In this analysis, the Salpeter IMF was used to determine the number of stars in the mass bin of $1-3\,\mathrm{M}_\odot$ out of the color-magnitude diagram, assuming that the population of stars formed from the same parental molecular cloud. This was accomplished by first counting the number of stars in a certain mass bin in the color-magnitude diagram and then using the Interactive Data Language (IDL)[10] routine *IMF* to calculate the number of stars between $1-3\,\mathrm{M}_\odot$. This was done six times using different mass bins between $3\,M_\odot$ and $7\,M_\odot$ and then averaging the results in order to even out statistical effects and rounding procedures. Mass bins above $7\,\mathrm{M}_\odot$ were not used since some of these high-mass stars of the original population might already have become a supernova and are therefore not represented

[10] IDL – **I**nteractive **D**ata **L**anguage: an analysis and visualization software developed specifically for scientists, enabling the handling of large data sets.

in the color-magnitude diagram, which was created out of an empirical catalog. Given the low statistics of the higher mass bins, missing stars in these bins would have an enormous effect on the calculated values and therefore, only lower mass bins are used. With this procedure, a number of 306^{+58}_{-58} stars were obtained for the mass bin of $1-3\,M_\odot$. To determine the uncertainty limits, the Poissonian uncertainties of each of the six different mass bins used for normalization were applied. These upper and lower number limits were then used to determine the upper and lower number limits of the stars in the mass bin of $1-3\,M_\odot$, which were then averaged.
In addition to the number of stars in this low-mass bin, the average X-ray luminosity of stars in this mass bin is needed to estimate their contribution to the total X-ray luminosity of DEM L299. To obtain this, a method was applied which has also been used previously by e.g. Getman et al. (2006); Ezoe et al. (2006); Broos et al. (2007); Kavanagh et al. (2012) and which makes use of results of the well-studied Orion Nebula Cluster (ONC). In this method, the studied population is compared to the population of the Orion Nebula Cluster under the assumption that both populations can be described by the same IMF and differ only in age and size. The ONC, of which the OB-stars are illuminating the Orion Nebula, has been studied very thoroughly within the scope of the *Chandra* Orion Ultradeep Project (COUP, Getman et al., 2005). This project covers six *Chandra* (Weisskopf et al., 2002) observations of the ONC taken within 13.2 days in the year 2003 with a total exposure time of 838 ks, equalling 9.7 days. In the *Chandra* Orion Ultradeep Project, $\sim 1\,400$ stars were classified as associated with the Orion Nebula Cluster (Getman et al., 2005; Feigelson et al., 2005). Feigelson et al. (2005) used these observations to determine global properties of the ONC, such as for example the number of stars in different mass bins, their integrated unabsorbed X-ray luminosity in an energy band of $0.5-8$ keV, and the percentual contribution of each bin to the total X-ray luminosity of the population. These results allow the determination of an average luminosity per star for different mass bins. For the ONC, Feigelson et al. (2005) found that 70 stars lie within the mass bin of $1-3\,M_\odot$ and have an integrated X-ray luminosity of $9.12\times10^{32}\,\mathrm{erg\,s^{-1}}$. Within this thesis, this result was used to calculate an integrated luminosity for the same mass bin of DEM L299. Taking the upper limit of 364 stars within this mass bin as determined above for DEM L299 and taking the average luminosity per star of the same ONC mass bin, an integrated luminosity of $4.7\times10^{33}\,\mathrm{erg\,s^{-1}}$ was obtained for this DEM L299 mass bin. According to Feigelson et al. (2005), the luminosity of the stars within this mass bin accounts for 41 % of the total X-ray luminosity of a stellar population, with another 33 % originating from stars below $1\,M_\odot$. Using these numbers, an unabsorbed total X-ray luminosity of $8.6\times10^{33}\,\mathrm{erg\,s^{-1}}$ was calculated within the scope of this thesis for stars of the DEM L299 population with a mass of $\leq 3\,M_\odot$. This is the sought contribution of low-mass stars to the X-ray luminosity of DEM L299.

After having considered the different size of the ONC and the DEM L299 population, also their different ages have to be taken into account. Getman et al. (2005) give an age of < 1 Myr for 80 % of the stars within the central region of the ONC, i.e. within 1 pc of its center, while the star sample of Preibisch and Feigelson (2005) has an assigned age of $\lesssim 0.1 - \sim 10$ Myr. Both values are considerably lower than the upper age limit of $28 - 35$ Myr as determined for DEM L299. Since the DEM L299 population seems most likely to be older than the ONC population and since the X-ray luminosity of low-mass stars with $m < 3\,M_\odot$ decreases with time (Preibisch and Feigelson, 2005), the here determined X-ray luminosity should be considered as an upper limit for the contribution of low-mass stars. Since this value makes up for only ~ 0.5 % of the total, unabsorbed X-ray luminosity of DEM L299 of $1.79 \times 10^{36}\,\mathrm{erg\,s^{-1}}$ (i.e. the sum of the luminosity of the SNR and the polygonal superbubble-only fitting region as determined in Section 6.4 for the same energy band), the contribution of low-mass stars to the diffuse X-ray luminosity of DEM L299 seems to be negligible.

The studies performed in this section about the stellar contribution to the X-ray luminosity of DEM L299 concluded that high- and low-mass stars only account for a negligible fraction of the detected X-ray emission of DEM L299. Therefore, it can be assumed that the observed diffuse X-ray emission of DEM L299 is truly diffuse emission.

Energy and Mass Input for the DEM L299 Superbubble

Since superbubbles are created through the stellar winds and supernovae of a population of stars, the energy and mass content of a superbubble should equal this energy and mass input. However, a growth-rate discrepancy of superbubbles has been observed, which manifests itself in a too low energy content of a superbubble compared to the energy input of the stellar population which formed it (see Sect. 2.4.1 for more information). The energy content of a superbubble is the sum of its thermal energy, mainly stored in the hot gas in its interior, and its kinetic energy, mainly stored in its expanding shells of warm and cold gas. Unfortunately, not enough information about the shell of the DEM L299 superbubble is available to determine its kinetic energy in order to create a complete energy and mass budget. Nevertheless, the mass and energy input of the stellar population which formed DEM L299 can be estimated. To do so, another color-magnitude diagram was created with the same method as described in the previous section, but this time for an area within $2'$ (30 pc) around the center of the superbubble, covering only the superbubble region of DEM L299. The resulting diagram is shown in Figure 6.19, in which $\sim 1\,900$ stars are plotted. To estimate the number of already occurred supernova explosions in this stellar population, the number of high-mass

stars present in the initial stellar population with masses between $8-100\,M_\odot$ has to be determined and then compared to the observed number of stars within the same mass bin. This mass bin was chosen since only stars with initial masses above $8\,M_\odot$ can undergo a core-collaps supernova. By using again the Salpeter IMF and the same approach as described in the previous section, an average initial number of 9^{+3}_{-3} stars was obtained for this mass bin. In the color-magnitude diagram, only two stars lie within this mass bin. Thus, 7^{+3}_{-3} supernovae can be assumed to have already occurred within this DEM L299 superbubble region.

The color-magnitude diagram can further be used to determine the total initial mass of the stars in the mass bin of $1-100\,M_\odot$ and the age of the stellar population, which are both needed for the next steps of the analysis as described in the following paragraph. With the same method as described above and after the calculation of an average mass, this total initial mass of the population resulted to be $(636^{+157}_{-158})\,M_\odot$. The uncertainty limit was determined following the same method as described above, using the Poissonian error of the number of stars in six different mass bins. These upper and lower number limits were then used to calculate the number of stars in the 1-100 $M_\odot$ bin and out of this, the average mass error. The two most massive stars in the color-magnitude diagram have a mass of $7-12\,M_\odot$. Since both stars lie close to the main sequence, no turn-off point and therefore no exact age of the population can be determined, but an upper limit of $28-35$ Myr can be given. This upper limit is in agreement with the age determined above for the whole DEM L299 population and can therefore be assumed as the age of the stellar population of the superbubble.

In addition to the number of previous supernovae, the stellar wind energy input is needed to determine the total energy input for the superbubble. This input was estimated using the Starburst99[11] v6.0.4 software and data package (Leitherer et al., 1999; Vázquez and Leitherer, 2005), which allows the calculation of spectral and photometric properties of a stellar population. It was originally written for the modeling of galaxies with active star formation and predicts for example several colors, luminosities, the strength of diagnostic lines, and stellar continua of a population as well as its mass and energy return and the stellar inventory – the latter two being needed for the estimates done within the scope of this thesis. As basic input parameters, the package requires the age of the population, its total initial mass, and its IMF exponent. For the mass and age, the values determined from the magnitude-color diagram were taken. As input parameters, a Salpeter IMF exponent of 2.35 was chosen with mass limits of $1-100\,M_\odot$, a metallicity of $Z = 0.008$, and the UV spectral library for the LMC. For the remaining parameters, their default values were taken.

[11] Starburst99 homepage: `http://www.stsci.edu/science/starburst99/`

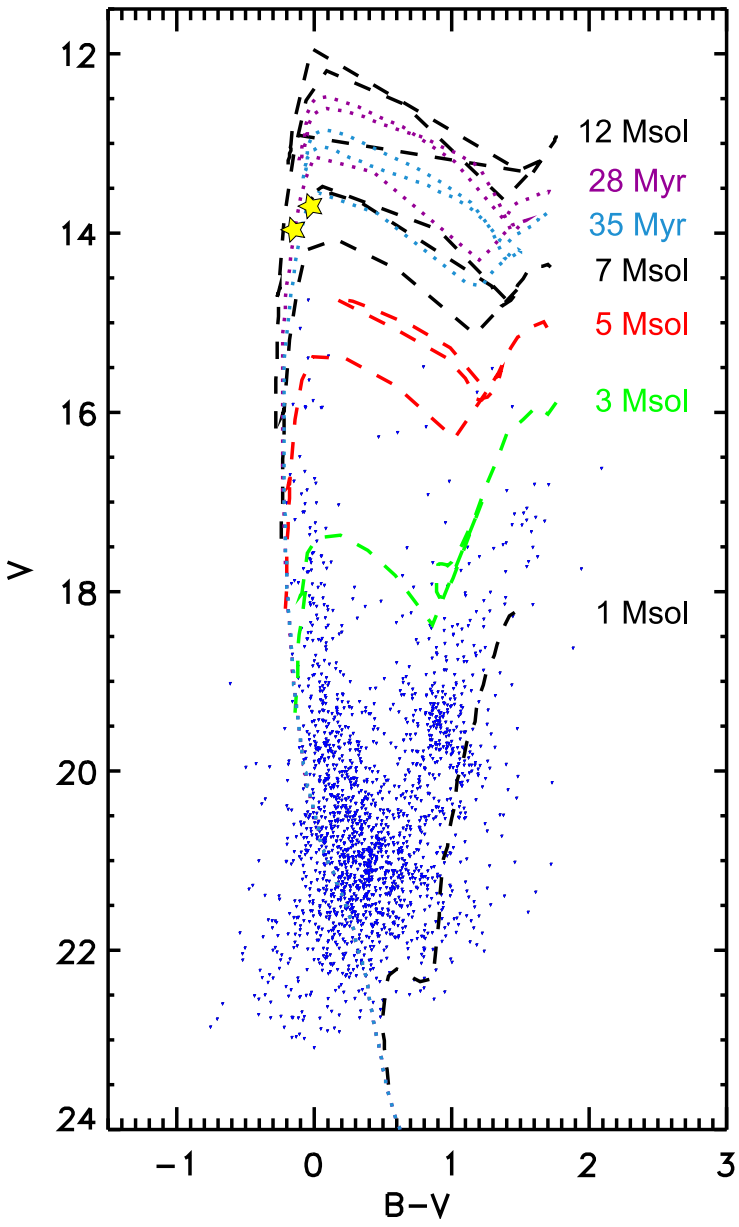

Figure 6.19: Color-magnitude diagram for the stars within a projected distance of 2′ (30 pc) around the center of the superbubble. To create this plot, the same parameters have been used as for Figure 6.18.

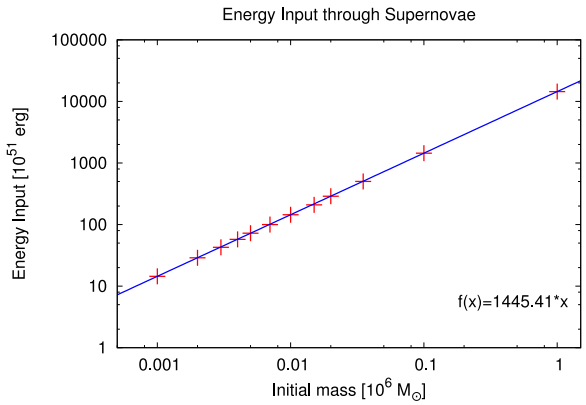

(a)

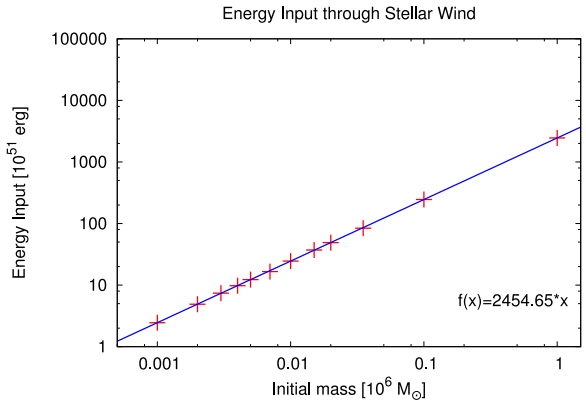

(b)

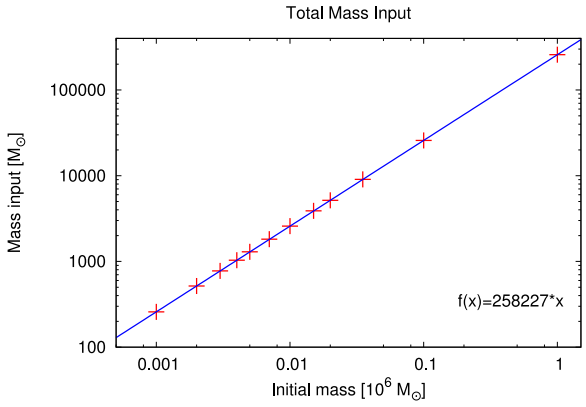

(c)

Figure 6.20: Energy input through supernovae, energy input through stellar winds, and total mass input for the DEM L299 superbubble as determined with Starburst99. Crosses are the Starburst99 simulation results for a stellar population with an age of 32 Myr. The blue line represents the linear function f(x), which has been fitted to the simulation results and was used to extrapolate the results to lower initial masses.

Since Starburst99 was written for the simulation of whole galaxies, only total initial masses down to $1 \times 10^3\,M_\odot$ are accepted by the input mask, with a minimal step size of $1 \times 10^3\,M_\odot$. Since the total initial mass for the DEM L299 superbubble population was determined to be $(636^{+157}_{-158})\,M_\odot$, it is smaller than the lowest possible initial mass to be used in Starburst99. For this reason, a series of 12 different simulations was run with initial masses between $1 \times 10^3\,M_\odot$ and $1 \times 10^6\,M_\odot$. The results were plotted as a function of initial mass and fitted to enable their extrapolation to lower masses. As an example of the results, the obtained values for the energy input through stellar winds, the energy input through supernovae, and the mass input are plotted in Figure 6.20. All three parameters have been found to decrease linearly with the initial mass. Thus, the energy input through core-collaps supernovae was extrapolated to be $\sim (9.13^{+3.07}_{-3.01}) \times 10^{51}$ erg, with uncertainties according to the upper and lower mass and time limits. This represents a second way to determine the number of already occurred supernovae, in addition to the number obtained from the color-magnitude diagram: assuming an energy input of 10^{51} erg per supernova, $\sim 9^{+3}_{-3}$ supernovae should have already occurred in this region. This number is similar to the $\sim 7^{+3}_{-3}$, although both values seem unexpectedly high. This might be a result of a possible confusion with fore- and background stars in the color-magnitude diagram - an error that would propagate to the results of Starburst99 through its input parameters, which were determined with the help of the color-magnitude diagram. The energy input through stellar winds was extrapolated to be $\sim (1.56^{+0.38}_{-0.39}) \times 10^{51}$ erg. This results in a total energy input through core-collaps supernovae and stellar winds of $\sim (1.1^{+0.3}_{-0.37}) \times 10^{52}$ erg. Furthermore, a total mass input through supernovae and stellar winds of $\sim (164^{+48}_{-46})\,M_\odot$ is estimated through Starburst99. This number is comparable to the mass of the hot gas inside the superbubble as determined in Section 6.5.2. Still, the latter mass has a very high upper limit, and the mass of a superbubble is indeed expected to be higher than the mass input through supernovae and stellar winds through evaporation of its swept-up, cooler shell (see Sect. 2.4.1 and Silich et al., 1996).

As a result, it can be stated that the contribution of the stellar population – in particular of the low- and high-mass stars – to the X-ray luminosity of DEM L299 can be neglected. The performed study about the energy and mass input through supernovae and stellar winds for the DEM L299 superbubble yielded reasonable values. To obtain smaller uncertainties of the calculated values, additional information about the OB stars, the two stellar clusters, the stellar association in the DEM L299 region, and the swept-up warm and cold shell of the superbubble would be needed, which would also enable to establish the complete energy budget of the superbubble.

6.6 Summary and Outlook

In this chapter, the detailed multi-wavelength study of DEM L299 has been presented, which has been performed within the scope of this thesis. The study includes an X-ray spectral analysis as well as morphological studies in radio, optical, and X-ray wavelengths of DEM L299.

The morphological study in optical wavelengths, which was performed using Hα, [S II], and [O III] data, showed very strong evidence for DEM L299 to be a superposition of the known supernova remnant SNR B0543-68.9 and a superbubble. This manifested itself through the created [S II]/Hα flux-ratio image. The superbubble resulted to lie further to the north than SNR B0543-68.9. The relative position of both objects to each other was studied in more detail using 21 cm radio data. In these 21 cm images, an H I shell could be recognized, which seems to enclose both objects. This indicates that the SNR and the superbubble lie close to each other and might have the same population of stars as common origin, and are not just by chance projected towards the same area of the sky. Yet, the images are ambiguous, and no final statement can be made out of these data. However, since DEM L299 lies next to an active star-forming region and since the center of SNR B0543-68.9 is projected inside the superbubble, the probability seems high that both objects are connected and that both the SNR and the superbubble originate from the same stellar association.
The exact position of SNR B0543-68.9 within DEM L299 was determined, with its center lying at RA 05:43:02.2, Dec -69:00:00.0 (J2000) and a diameter of $\sim 4'$ (~ 60 pc). All three indicators for a supernova remnant could be verified for SNR B0543-68.9: diffuse X-ray emission, an enhanced [S II]/Hα flux ratio, and a low spectral index between -0.5 – 1 as visible in the spectral index map of DEM L299, created out of radio-continuum data by Luke M. Bozzetto and Miroslav D. Filipović from the University of Western Sydney, Australia. This rather flat spectral index indicates a rather mature SNR, which is in agreement with the results of the X-ray spectral analysis. The DEM L299 superbubble has been identified through a clear shell-like structure in the Hα, [S II], and [O III] images; diffuse X-ray emission; and an H I radio shell. It is centered at RA 05:43:07.4, Dec -68:58:39.3 (J2000) with a diameter of $\sim 3'$ (~ 45 pc), as determined through the Hα image. Evidence has been found – in particular at optical wavelengths – for a blowout of the superbubble at its north-eastern rim.

In the spectral X-ray analysis, three different regions of DEM L299 were examined using archived *XMM-Newton* EPIC data: an SNR region, a superbubble-only region which is not overlapping with the remnant as indicated through the [S II]/Hα flux-ratio image, and a blowout region. For background estimation, three *XMM-Newton* EPIC observations of the South Ecliptic Pole were combined

and fitted simultaneously to the DEM L299 observation. As a verification of this background estimation, an as much as possible empty region inside the field of view of the DEM L299 observation was used as an extraction region for the local background of DEM L299, and its extracted data were fitted simultaneously to the SEP observations. The fits of the SEP and the background region are in good agreement and differ only through a slight excess of the local background spectrum. This excess can be fitted through an additional thermal component and is probably a result of the local hot ISM in the busy field of view of the DEM L299 observation. However, the spectrum of the local background extraction region has far too low statistics to be used for background estimation of the SNR, the superbubble, or its blowout. Nevertheless, this additional thermal component was considered when calculating the luminosities of the different regions.
In the model used for the spectral fits, several sources of soft X-ray fore- and backgrounds have been considered, as described in Section 5.4. To account for the superbubble contribution to the spectrum of the overlapping remnant, an additional component has been added to the SNR model. For this additional model component, the resulting parameters of the source component of the previously fitted superbubble-only spectrum were adopted and frozen. For all three spectral extraction regions, Xspec's plane-parallel shock model *vpshock* provided the best reduced χ^2. For SNR B0543-68.9, the obtained best-fit values are

- a temperature of $k_\mathrm{B}T_\mathrm{X,SNR} = (0.64^{+0.73}_{-0.20})\,\mathrm{keV}$,
- an ionization timescale of $\tau_\mathrm{SNR} = (2.1^{+1.3}_{-0.6}) \times 10^{10}\,\mathrm{s\,cm^{-3}}$, and
- a column density within the LMC of $N_\mathrm{H,LMC,SNR} = (0.66^{+0.11}_{-0.07}) \times 10^{22}\,\mathrm{cm^{-2}}$.

The superbubble was found to have

- a temperature of $k_\mathrm{B}T_\mathrm{X,SB} = (0.74^{+0.36}_{-0.30})\,\mathrm{keV}$ and
- a column density of $N_\mathrm{H,LMC,SB} = (0.30^{+0.36}_{-0.23}) \times 10^{22}\,\mathrm{cm^{-2}}$;

and for the blowout,

- a temperature of $k_\mathrm{B}T_\mathrm{X,BL} = (0.62^{+0.38}_{-0.42})\,\mathrm{keV}$ and
- a column density of $N_\mathrm{H,LMC,BL} = (0.27^{+0.93}_{-0.27}) \times 10^{22}\,\mathrm{cm^{-2}}$

were obtained. The absorbed and unabsorbed X-ray luminosities in an energy range of $0.5-8\,\mathrm{keV}$ were determined for the SNR, the superbubble, the blowout, and the local background region. The contribution of the latter was subtracted from the luminosities of the other three regions. This resulted in an unabsorbed, local background subtracted luminosity

- of $(1.5^{+1.6}_{-1.2}) \times 10^{36}\,\mathrm{erg\,s^{-1}}$ for SNR B0543-68.9,
- of $(3.4^{+7.8}_{-1.2}) \times 10^{35}\,\mathrm{erg\,s^{-1}}$ for the superbubble, and
- of $(5.6^{+286.5}_{-3.3}) \times 10^{34}\,\mathrm{erg\,s^{-1}}$ for the blowout.

The fitting results were used to calculate further properties of these objects, which are summarized in Table 6.5. For SNR B0543-68.9, the Sedov model was used to determine its age, the initial energy of the explosion, and the mass of the swept-up ISM. The method of Smith and Hughes (2010) was used to show that collisional ionization equilibrium has not yet been re-established, and the method of Itoh (1978) was used to show that also temperature equilibration is not re-established, with a temperature ratio of $f_{\mathrm{T}} = 0.37^{+0.59}_{-0.35}$. This temperature ratio was considered when calculating the SNR properties.
The ideal gas equations were applied for the DEM L299 superbubble to determine its dynamic age as well as the pressure, the thermal energy content, and the mass of the hot gas in its interior (see Table 6.5). With these parameters, the average mass loss rate and the average energy input rate were calculated for the superbubble (without the blowout). For the blowout, comparable values for the pressure, the thermal energy content, and the mass were obtained as for the superbubble, although the low statistics of the observation lead to large uncertainty ranges.

A population study of the DEM L299 region was performed to estimate the contribution of stars to the determined properties. The X-ray emission of low- and high-mass stars has been proven to be negligible when calculating the X-ray luminosity of DEM L299, accounting for $\lesssim 1.1\,\%$ of its total X-ray luminosity. Thus, it was shown that the observed diffuse X-ray emission is truly diffuse emission. A color-magnitude diagram was created for the stellar population of DEM L299, which resulted in an age of $28-35\,\mathrm{Myr}$ for this population. A second color-magnitude diagram for the stellar population of the superbubble and the Starburst99 software were used to determine the number of $4-12$ supernovae which should already have occurred in this region, and to determine the energy input through stellar winds and core-collaps supernovae for the superbubble to be $\sim (1.1^{+0.3}_{-0.37}) \times 10^{52}\,\mathrm{erg}$ and the mass input to be $\sim (164^{+48}_{-46})\ \mathrm{M}_{\odot}$.

For the creation of a complete energy budget of the superbubble, additional information is needed about the OB-stars, the clusters, the stellar association in the DEM L299 region, and about the properties of the Hα and radio shells around the superbubble. This will allow to test current models for the growth-rate discrepancy of superbubbles and will enhance the knowledge about this still not well-understood discrepancy in superbubble evolution. To supply more constrained confidence ranges for the determined properties of SNR B0543-68.9 and the superbubble, deeper X-ray observations are required for all spectral extraction regions, in particular for the blowout and for the local background region. This would lead to better confined values for, e.g., the age and the swept-up mass of the objects. In addition, a detailed X-ray analysis of the blowout of the superbubble would be possible, which can be well recognized up to now only in optical wavelengths. Higher X-ray statistics would also allow a much better estimate of the local background, which would lead to a more accurate background estimation during X-ray

spectral analysis. In addition, deeper observations would enable the fitting of elemental abundances, which can yield important information about the chemical composition of the SNR and the superbubble, allowing for a better understanding of stellar evolution and the matter cycle.

Table 6.5: Summary of the calculated properties of SNR B0543-68.9 (assuming no re-established temperature equilibrium with $f_{\mathrm{T}} = 0.37$), the DEM L299 superbubble, its blowout, and the combined values for the superbubble plus blowout.

Object	Parameter	Value	Unit
SNR B0543-68.9	Age	$8.9^{+9.2}_{-5.4}$	kyr
	Initial energy of the explosion	$4.3\,(<14)$	$\times 10^{51}\,\mathrm{erg}$
	Mass of swept-up ISM	210^{+150}_{-110}	$\mathrm{M}_{\odot}$
	Shock velocity	$1\,200^{+1\,200}_{-700}$	$\mathrm{km\,s^{-1}}$
DEM L299 Superbubble	Dynamic age	70^{+73}_{-35}	kyr
	Pressure/$\mathrm{k_B}$	$9.5^{+17.2}_{-4.3}$	$\times 10^{5}\phi^{-0.5}\,\mathrm{cm^{-3}\,K}$
	Thermal energy content	$0.43^{+0.81}_{-0.26}$	$\times 10^{51}\phi^{0.5}\,\mathrm{erg}$
	Mass of the hot gas inside the superbubble	130^{+230}_{-60}	$\phi^{0.5}\,\mathrm{M}_{\odot}$
	Average mass loss rate	$1.9^{+3.9}_{-1.3}$	$\times 10^{-3}\,\mathrm{M}_{\odot}/\mathrm{yr}$
	Average energy input rate	$2.0^{+4.3}_{-1.6}$	$\times 10^{38}\,\mathrm{erg/s}$
Blowout	Pressure/$\mathrm{k_B}$	$5.7^{+145.0}_{-4.3}$	$\times 10^{5}\phi^{-0.5}\,\mathrm{cm^{-3}\,K}$
	Thermal energy content	$0.2^{+5.41}_{-0.18}$	$\times 10^{51}\phi^{0.5}\,\mathrm{erg}$
	Mass of hot gas	$70^{+1\,861}_{-36}$	$\phi^{0.5}\,\mathrm{M}_{\odot}$
Combined Superbubble and Blowout	Thermal energy content	$0.63^{+5.48}_{-0.32}$	$\times 10^{51}\phi^{0.5}\,\mathrm{erg}$
	Mass of hot gas	$200^{+1\,876}_{-70}$	$\phi^{0.5}\,\mathrm{M}_{\odot}$

Chapter 7

Summary and Outlook

Within the scope of this thesis, a detailed analysis of the hot ISM has been performed for the LMC-SGS 2 region in the Large Magellanic Cloud. This region contains the supergiant shell LMC-SGS 2 and the H II region DEM L299. For these objects, a multi-frequency morphological and X-ray spectral analysis has been performed. During these studies, we have obtained the most detailed X-ray image of LMC-SGS 2 which exists up-to-now, and we have identified a new superbubble embedded in DEM L299.

For the studies of the supergiant shell LMC-SGS 2, a morphological analysis has been performed using X-ray, optical, and radio data. For the morphological X-ray analysis, seven observations of the *XMM-Newton* satellite have been used. The mosaicked images, created out of these data for several X-ray energy bands, show LMC-SGS 2 in unprecedented detail. This allows a better confinement and identification of individual structures of the supergiant shell and thus a better determination of its properties.
For the X-ray analysis of LMC-SGS 2, three additional *XMM-Newton* observations of the South Ecliptic Pole were processed, combined and used for the estimation of the X-ray background. A spectral analysis was performed for the supergiant shell and for the X-ray spur extending south of it. For both regions, the best fitting results have been obtained with a collisional non-equilibrium ionization (NEI) model assuming a plane-parallel shock (*vpshock*). The resulting best-fit parameters are in accordance with those expected for a supergiant shell. Individual spectra have been created for different regions of the supergiant shell and the X-ray spur: for the entire FOV of each observation as well as for smaller extraction regions. It was shown that the spectra extracted from the entire FOV are representative of the emission of LMC-SGS 2 and the X-ray spur. The results of the spectral analysis confirm those obtained through the morphological X-ray studies: a higher column density was obtained for the eastern half of LMC-SGS 2, which is in accordance with its X-ray morphology, indicating a lower apparent brightness of this eastern part.

The fitting results were used to determine further properties of LMC-SGS 2 and the X-ray spur (see Table 5.6), like the thermal energy content, the pressure, and the mass of their hot gas. The results obtained from the entire FOV are well in agreement with those obtained for the smaller extraction regions. The obtained results are consistent with those expected for a supergiant shell.

At the north-western rim of LMC-SGS 2 lies the H II region DEM L299, which harbors the supernova remnant SNR B0543-68.9. We analyzed X-ray data of the *XMM-Newton* satellite, optical data of the Magellanic Cloud Emission Line Survey, and radio 21 cm data of the Magellanic Cloud Survey. For SNR B0543-68.9, the three major indicators for a supernova remnant were found: diffuse X-ray emission, an enhanced [S II]/Hα flux ratio, and a spectral index for the radio-continuum emission indicative of a mature SNR. The morphological analysis allowed a more accurate determination of the position of the supernova remnant, which unexpectedly resulted to be shifted in respect to a shell-like structure clearly visible in Hα, [S II], and [O III] emission line data. This led to the conclusion that besides SNR B0543-68.9, a superbubble is projected towards DEM L299. Indications for a blowout has been found at the north-western rim of the superbubble, with the strongest evidence visible in the optical images. Radio 21 cm emission line data revealed a common shell-like structure of neutral hydrogen around SNR B0543-68.9 and the superbubble, indicating that both objects lie close to each other. However, the data did not allow for an unambiguous identification of their relative position.

An X-ray spectral analysis has been performed for SNR B0543-68.9, the DEM L299 superbubble, its blowout, and for a local background region within the same FOV. For SNR B0543-68.9, the contamination by the superbubble emission has been accounted for in the model used for the spectral fits. All four regions were fitted best with a plane-parallel shock NEI model (*vpshock)*. For background estimation, the combined SEP data were fitted simultaneously to the source data. The resulting best-fit parameters were conclusive for the respective objects. The local background spectra revealed a small thermal contribution to the spectra, which has been considered when determining the luminosities of SNR B0543-68.9, the DEM L299 superbubble, and its blowout.
The best-fit parameters were used to calculate further properties of the objects (see Table 6.5). Thus, for the SNR, the initial energy of the supernova explosion, the mass of the swept-up ISM, and the shock velocity were determined. For the superbubble, its dynamic age and the pressure, thermal energy content, and mass of the hot gas in its interior and in its blowout have been calculated. For SNR B0543-68.9, it was shown that neither NEI nor temperature equilibration have been re-established yet. The effects of the latter were considered when calculating the properties of the SNR.

During the population study, the diffuse X-ray emission of this region has been proven to be truly diffuse emission and to have only a negligible contribution from low- and high-mass stars. The age of the stellar population of DEM L299 has been determined to be $28-35\,\mathrm{Myr}$, and a number of $4-12$ already occurred supernovae have been calculated for this region. For the superbubble, the energy and mass input of the stellar population have been determined, which are in agreement with the results of the X-ray spectral analysis.

Both LMC-SGS 2 and DEM L299 offer the possibility of further, deeper studies, which will reveal more of their characteristics and physics. For the creation of a complete energy budget of the superbubble and of the supergiant shell, additional information about their stellar population and about their Hα and H I shells are required. This would allow to further enhance the knowledge about the growth-rate discrepancy, which has been observed for several superbubbles and which is not entirely understood yet. In addition, deeper X-ray observations are necessary to further constrain the confidence ranges of the determined parameters, and for a more precise local background estimation. A better statistics of the data would also enable a more exact analysis of the spatial dependance of its parameters. This is of particular interest for the supergiant shell, which has a huge extend and which shows a strongly varying X-ray morphology. A better statistics will also enable the examination of the chemical composition of both objects, which would reveal further information about their origin and about their physical history.

Bibliography

C. W. Allen. *Astrophysical quantities*. 1973.

P. Ambrocio-Cruz, A. Laval, M. Rosado, Y. P. Georgelin, M. Marcelin, F. Comeron, N. Delmotte, and A. Viale. The Kinematic Map of the Ionized Gas of the Supergiant Shell LMC SGS 2. *The Astronomical Journal*, 127:2145–2153, April 2004. doi: 10.1086/382093.

K. Arnaud, B. Dorman, and C. Gordon. *Xspec – An X-ray Spectral Fitting Package*. 2011a.

K. Arnaud, R. Smith, and A. Siemiginowska. *Handbook of X-ray Astronomy*. November 2011b.

K. A. Arnaud. XSPEC: The First Ten Years. In G. H. Jacoby and J. Barnes, editors, *Astronomical Data Analysis Software and Systems V*, volume 101 of *Astronomical Society of the Pacific Conference Series*, page 17, 1996.

B. Aschenbach. X-ray telescopes. *Reports of Progress in Physics*, 48:579–629, May 1985.

ATCA Users Guide. *Australia Telescope Compact Array Users Guide*. 2010.

T. W. Berghoefer, J. H. M. M. Schmitt, R. Danner, and J. P. Cassinelli. X-ray properties of bright OB-type stars detected in the ROSAT all-sky survey. *Astronomy & Astrophysics*, 322:167–174, June 1997.

E. M. Berkhuijsen. Properties of supernova remnants at known distances. I - Surface brightness and radio spectral index. *Astronomy & Astrophysics*, 166: 257–270, September 1986.

E. L. D. Bica, H. R. Schmitt, C. M. Dutra, and H. L. Oliveira. A Revised and Extended Catalog of Magellanic System Clusters, Associations, and Emission Nebulae. II. The Large Magellanic Cloud. *The Astronomical Journal*, 117:238–246, January 1999. doi: 10.1086/300687.

J. K. Blackburn. FTOOLS: A FITS Data Processing and Analysis Software Package. In R. A. Shaw, H. E. Payne, and J. J. E. Hayes, editors, *Astronomical Data Analysis Software and Systems IV*, volume 77 of *Astronomical Society of the Pacific Conference Series*, page 367, 1995.

D. J. Bomans, K. Dennerl, and M. Kurster. Diffuse X-Ray Emission from the Supergiant Shell Large Magellanic CLOUD-4 Detected with ROSAT. *Astronomy & Astrophysics*, 283:L21, March 1994.

L. G. Book, Y.-H. Chu, and R. A. Gruendl. Structure of Supergiant Shells in the Large Magellanic Cloud. *The Astrophysical Journal Supplement Series*, 175: 165–178, March 2008. doi: 10.1086/523897.

K. J. Borkowski. Nonequilibrium Ionization Models for Analysis of X-Ray Spectra of Supernova Remnants. In S. J. Arthur, N. S. Brickhouse, and J. Franco, editors, *Revista Mexicana de Astronomia y Astrofisica Conference Series*, volume 9 of *Revista Mexicana de Astronomia y Astrofisica Conference Series*, pages 288–289, May 2000.

K. J. Borkowski, W. J. Lyerly, and S. P. Reynolds. Supernova Remnants in the Sedov Expansion Phase: Thermal X-Ray Emission. *The Astrophysical Journal*, 548:820–835, February 2001. doi: 10.1086/319011.

L. M. Bozzetto, P. J. Kavanagh, P. Maggi, M. D. Filipović, M. Stupar, Q. A. Parker, W. A. Reid, M. Sasaki, F. Haberl, D. Urošević, J. Dickel, R. Sturm, R. Williams, M. Ehle, R. Gruendl, Y.-H. Chu, S. Points, and E. J. Crawford. Multifrequency study of a new Fe-rich supernova remnant in the Large Magellanic Cloud, MCSNR J0508-6902. *Monthly Notices of the Royal Astronomical Society*, 439:1110–1124, March 2014. doi: 10.1093/mnras/stu051.

P. S. Broos, E. D. Feigelson, L. K. Townsley, K. V. Getman, J. Wang, G. P. Garmire, Z. Jiang, and Y. Tsuboi. The Young Stellar Population in M17 Revealed by Chandra. *The Astrophysical Journal Supplement Series*, 169:353–385, April 2007. doi: 10.1086/512068.

J. A. Carter and S. Sembay. Identifying XMM-Newton observations affected by solar wind charge exchange. Part I. *Astronomy & Astrophysics*, 489:837–848, October 2008. doi: 10.1051/0004-6361:200809997.

J. Castor, R. McCray, and R. Weaver. Interstellar bubbles. *The Astrophysical Journal Letters*, 200:L107–L110, September 1975. doi: 10.1086/181908.

A. Caulet, L. Deharveng, Y. M. Georgelin, and Y. P. Georgelin. Dynamics of the supergiant shell LMC 2 in the Large Magellanic Cloud. *Astronomy & Astrophysics*, 110:185–197, June 1982.

L.-W. Chen, A. C. Fabian, and K. C. Gendreau. ASCA and ROSAT observations of the QSF3 field: the X-ray background in the 0.1-7 keV band. *Monthly Notices of the Royal Astronomical Society*, 285:449–471, March 1997.

T. Chlebowski, F. R. Harnden, Jr., and S. Sciortino. The Einstein X-ray Observatory Catalog of O-type stars. *The Astrophysical Journal*, 341:427–455, June 1989. doi: 10.1086/167506.

R. L. Cooper, M. A. Guerrero, Y.-H. Chu, C.-H. R. Chen, and B. C. Dunne. Energy Crisis in the Superbubble DEM L192 (N51D). *The Astrophysical Journal*, 605:751–758, April 2004. doi: 10.1086/382501.

D. P. Cox and R. J. Reynolds. The local interstellar medium. *Annual Review of Astronomy & Astrophysics*, 25:303–344, 1987. doi: 10.1146/annurev.aa.25.090187.001511.

R. D. Davies, K. H. Elliott, and J. Meaburn. The nebular complexes of the large and small Magellanic Clouds. *Royal Astronomical Society, Memoirs*, 81:89–128, 1976.

J. W. den Herder, A. C. Brinkman, S. M. Kahn, G. Branduardi-Raymont, K. Thomsen, H. Aarts, M. Audard, J. V. Bixler, A. J. den Boggende, J. Cottam, T. Decker, L. Dubbeldam, C. Erd, H. Goulooze, M. Güdel, P. Guttridge, C. J. Hailey, K. A. Janabi, J. S. Kaastra, P. A. J. de Korte, B. J. van Leeuwen, C. Mauche, A. J. McCalden, R. Mewe, A. Naber, F. B. Paerels, J. R. Peterson, A. P. Rasmussen, K. Rees, I. Sakelliou, M. Sako, J. Spodek, M. Stern, T. Tamura, J. Tandy, C. P. de Vries, S. Welch, and A. Zehnder. The Reflection Grating Spectrometer on board XMM-Newton. *Astronomy & Astrophysics*, 365:L7–L17, January 2001. doi: 10.1051/0004-6361:20000058.

K. M. Desai, Y.-H. Chu, R. A. Gruendl, W. Dluger, M. Katz, T. Wong, C.-H. R. Chen, L. W. Looney, A. Hughes, E. Muller, J. Ott, and J. L. Pineda. Supernova Remnants and Star Formation in the Large Magellanic Cloud. *The Astronomical Journal*, 140:584–594, August 2010. doi: 10.1088/0004-6256/140/2/584.

J. R. Dickel, V. J. McIntyre, R. A. Gruendl, and D. K. Milne. A 4.8 and 8.6 GHz Survey of the Large Magellanic Cloud. I. The Images. *The Astronomical Journal*, 129:790–804, February 2005. doi: 10.1086/426916.

J. M. Dickey and F. J. Lockman. H I in the Galaxy. *Annual Review of Astronomy & Astrophysics*, 28:215–261, 1990. doi: 10.1146/annurev.aa.28.090190.001243.

J. Dyson and D. Williams. *The Physics of the Interstellar Medium, Second Edition*. January 1997. doi: 10.1201/9780585368115.

Y. Ezoe, M. Kokubun, K. Makishima, Y. Sekimoto, and K. Matsuzaki. Investigation of Diffuse Hard X-Ray Emission from the Massive Star-forming Region NGC 6334. *The Astrophysical Journal*, 638:860–877, February 2006. doi: 10.1086/499120.

E. D. Feigelson, K. Getman, L. Townsley, G. Garmire, T. Preibisch, N. Grosso, T. Montmerle, A. Muench, and M. McCaughrean. Global X-Ray Properties of the Orion Nebula Region. *The Astrophysical Journal Supplement Series*, 160: 379–389, October 2005. doi: 10.1086/432512.

R. A. Fesen, W. P. Blair, and R. P. Kirshner. Optical emission-line properties of evolved galactic supernova remnants. *The Astrophysical Journal*, 292:29–48, May 1985. doi: 10.1086/163130.

J. L. A. Fordham, D. A. Bone, M. K. Oldfield, J. G. Bellis, and T. J. Norton. The MIC photon counting detector. In T. D. Guyenne and J. Hunt, editors, *Photon Detectors for Space Instrumentation*, volume 356 of *ESA Special Publication*, pages 103–106, December 1992.

H. Friedman, S. W. Lichtman, and E. T. Byram. Photon Counter Measurements of Solar X-Rays and Extreme Ultraviolet Light. *Physical Review*, 83:1025–1030, September 1951. doi: 10.1103/PhysRev.83.1025.

K. V. Getman, E. Flaccomio, P. S. Broos, N. Grosso, M. Tsujimoto, L. Townsley, G. P. Garmire, J. Kastner, J. Li, F. R. Harnden, Jr., S. Wolk, S. S. Murray, C. J. Lada, A. A. Muench, M. J. McCaughrean, G. Meeus, F. Damiani, G. Micela, S. Sciortino, J. Bally, L. A. Hillenbrand, W. Herbst, T. Preibisch, and E. D. Feigelson. Chandra Orion Ultradeep Project: Observations and Source Lists. *The Astrophysical Journal Supplement Series*, 160:319–352, October 2005. doi: 10.1086/432092.

K. V. Getman, E. D. Feigelson, L. Townsley, P. Broos, G. Garmire, and M. Tsujimoto. Chandra Study of the Cepheus B Star-forming Region: Stellar Populations and the Initial Mass Function. *The Astrophysical Journal Supplement Series*, 163:306–334, April 2006. doi: 10.1086/501453.

R. Giacconi. The Einstein X-ray Observatory. *Scientific American*, 242:80–85, February 1980.

R. Giacconi, H. Gursky, F. R. Paolini, and B. B. Rossi. Evidence for X-Rays From Sources Outside the Solar System. *Physical Review Letters*, 9:439–443, December 1962. doi: 10.1103/PhysRevLett.9.439.

R. Giacconi, H. Gursky, and J. R. Waters. Two Sources of Cosmic X-rays in Scorpius and Sagittarius. *Nature*, 204:981–982, December 1964. doi: 10.1038/204981a0.

R. Giacconi, H. Gursky, and L. P. van Speybroeck. Observational Techniques in X-Ray Astronomy. *Annual Review of Astronomy and Astrophysics*, 6:373–+, 1968. doi: 10.1146/annurev.aa.06.090168.002105.

C. Goudis and J. Meaburn. Four super-giant shells in the Large Magellanic Cloud. *Astronomy & Astrophysics*, 68:189–192, August 1978.

F. Haberl and W. Pietsch. A ROSAT PSPC catalogue of X-ray sources in the LMC region. *Astronomy & Astrophysics Supplement*, 139:277–295, October 1999. doi: 10.1051/aas:1999394.

A. J. S. Hamilton and C. L. Sarazin. X-ray emission from supernova remnants. II - The effect of remnant structure on nonequilibrium X-ray spectra. *The Astrophysical Journal*, 284:601–611, September 1984. doi: 10.1086/162443.

A. J. S. Hamilton, C. L. Sarazin, and R. A. Chevalier. X-ray line emission from supernova remnants. I - Models for adiabatic remnants. *The Astrophysical Journal Supplement Series*, 51:115–147, January 1983. doi: 10.1086/190841.

C. Heiles. Supernova Shells and Galactic X-Rays. *The Astrophysical Journal*, 140: 470, August 1964. doi: 10.1086/147941.

K. G. Henize. Catalogues of Hα-EMISSION Stars and Nebulae in the Magellanic Clouds. *The Astrophysical Journal Supplement Series*, 2:315, September 1956. doi: 10.1086/190025.

A. Hughes, L. Staveley-Smith, S. Kim, M. Wolleben, and M. Filipović. An Australia Telescope Compact Array 20-cm radio continuum study of the Large Magellanic Cloud. *Monthly Notices of the Royal Astronomical Society*, 382: 543–552, December 2007. doi: 10.1111/j.1365-2966.2007.12466.x.

H. Hugoniot. Mémoire sur la propagation des mouvements dans les corps et spécialement dans les gaz parfaits (première partie) [Memoir on the propagation of movements in bodies, especially perfect gases (first part)]. *Journal de l'École Polytechnique*, 57:3–97, 1887.

H. Hugoniot. Mémoire sur la propagation des mouvements dans les corps et spécialement dans les gaz parfaits (deuxième partie) [Memoir on the propagation of movements in bodies, especially perfect gases (second part)]. *Journal de l'École Polytechnique*, 58:1–125, 1889.

H. Itoh. Two-fluid blast-wave model for supernova remnants. *Publications of the Astronomical Society of Japan*, 30:489–498, 1978.

N. Jagoda, G. Austin, S. Mickiewicz, and R. Goddard. The UHURU X-Ray Instrument. *IEEE Transactions on Nuclear Science*, 19:579–+, February 1972.

F. Jansen, D. Lumb, B. Altieri, J. Clavel, M. Ehle, C. Erd, C. Gabriel, M. Guainazzi, P. Gondoin, R. Much, R. Munoz, M. Santos, N. Schartel, D. Texier, and G. Vacanti. XMM-Newton observatory. I. The spacecraft

and operations. *Astronomy & Astrophysics*, 365:L1–L6, January 2001. doi: 10.1051/0004-6361:20000036.

A. E. Jaskot, D. K. Strickland, M. S. Oey, Y.-H. Chu, and G. García-Segura. Observational Constraints on Superbubble X-ray Energy Budgets. *The Astrophysical Journal*, 729:28, March 2011. doi: 10.1088/0004-637X/729/1/28.

F. D. Kahn. Supernova Remnants. In *International Cosmic Ray Conference*, volume 11 of *International Cosmic Ray Conference*, page 3566, 1975.

P. J. Kavanagh, M. Sasaki, and S. D. Points. XMM-Newton view of the N 206 superbubble in the Large Magellanic Cloud. *Astronomy & Astrophysics*, 547: A19, November 2012. doi: 10.1051/0004-6361/201219532.

E. Kendziorra. *The Universe in X-rays*, pages 15–19. 2008. doi: 10.1007/978-3-540-34412-4.

S. Kim, L. Staveley-Smith, M. A. Dopita, K. C. Freeman, R. J. Sault, M. J. Kesteven, and D. McConnell. An H i Aperture Synthesis Mosaic of the Large Magellanic Cloud. *The Astrophysical Journal*, 503:674, August 1998. doi: 10.1086/306030.

S. Kim, L. Staveley-Smith, M. A. Dopita, R. J. Sault, K. C. Freeman, Y. Lee, and Y.-H. Chu. A Neutral Hydrogen Survey of the Large Magellanic Cloud: Aperture Synthesis and Multibeam Data Combined. *The Astrophysical Journal Supplement Series*, 148:473–486, October 2003. doi: 10.1086/376980.

S. Kim, E. Rosolowsky, Y. Lee, Y. Kim, Y. C. Jung, M. A. Dopita, B. G. Elmegreen, K. C. Freeman, R. J. Sault, M. Kesteven, D. McConnell, and Y.-H. Chu. A Catalog of H I Clouds in the Large Magellanic Cloud. *The Astrophysical Journal Supplement Series*, 171:419–446, August 2007. doi: 10.1086/518126.

D. Koutroumpa, M. R. Collier, K. D. Kuntz, R. Lallement, and S. L. Snowden. Solar Wind Charge Exchange Emission from the Helium Focusing Cone: Model to Data Comparison. *The Astrophysical Journal*, 697:1214–1225, June 2009. doi: 10.1088/0004-637X/697/2/1214.

K. D. Kuntz and S. L. Snowden. The EPIC-MOS particle-induced background spectra. *Astronomy & Astrophysics*, 478:575–596, February 2008. doi: 10.1051/0004-6361:20077912.

F. Lamarche and C. Leroy. Evaluation of the volume of intersection of a sphere with a cylinder by elliptic integrals. *Computer Physics Communications*, 59: 359–369, June 1990. doi: 10.1016/0010-4655(90)90184-3.

C. Leitherer, D. Schaerer, J. D. Goldader, R. M. González Delgado, C. Robert, D. F. Kune, D. F. de Mello, D. Devost, and T. M. Heckman. Starburst99: Synthesis Models for Galaxies with Active Star Formation. *The Astrophysical Journal Supplement Series*, 123:3–40, July 1999. doi: 10.1086/313233.

T. Lejeune and D. Schaerer. Database of Geneva stellar evolution tracks and isochrones for $(UBV)_J(RI)_C$ JHKLL'M, HST-WFPC2, Geneva and Washington photometric systems. *Astronomy & Astrophysics*, 366:538–546, February 2001. doi: 10.1051/0004-6361:20000214.

K. S. Long, D. J. Helfand, and D. A. Grabelsky. A soft X-ray study of the Large Magellanic Cloud. *The Astrophysical Journal*, 248:925–944, September 1981. doi: 10.1086/159222.

L. A. Maddox, R. M. Williams, B. C. Dunne, and Y.-H. Chu. Nonthermal X-ray Emission in the N11 Superbubble in the Large Magellanic Cloud. *The Astrophysical Journal*, 699:911–916, July 2009. doi: 10.1088/0004-637X/699/1/911.

J. Maíz-Apellániz. The Origin of the Local Bubble. *The Astrophysical Journal Letters*, 560:L83–L86, October 2001. doi: 10.1086/324016.

S. Malhotra, M. J. Kaufman, D. Hollenbach, G. Helou, R. H. Rubin, J. Brauher, D. Dale, N. Y. Lu, S. Lord, G. Stacey, A. Contursi, D. A. Hunter, and H. Dinerstein. Far-Infrared Spectroscopy of Normal Galaxies: Physical Conditions in the Interstellar Medium. *The Astrophysical Journal*, 561:766–786, November 2001. doi: 10.1086/323046.

K. O. Mason, A. Breeveld, R. Much, M. Carter, F. A. Cordova, M. S. Cropper, J. Fordham, H. Huckle, C. Ho, H. Kawakami, J. Kennea, T. Kennedy, J. Mittaz, D. Pandel, W. C. Priedhorsky, T. Sasseen, R. Shirey, P. Smith, and J.-M. Vreux. The XMM-Newton optical/UV monitor telescope. *Astronomy & Astrophysics*, 365:L36–L44, January 2001. doi: 10.1051/0004-6361:20000044.

D. S. Mathewson, V. L. Ford, M. A. Dopita, I. R. Tuohy, K. S. Long, and D. J. Helfand. Optical studies of supernova remnants in the Magellanic Clouds. In J. Danziger and P. Gorenstein, editors, *Supernova Remnants and their X-ray Emission*, volume 101 of *IAU Symposium*, pages 541–549, 1983.

R. McCray and T. P. Snow, Jr. The violent interstellar medium. *Annual Review of Astronomy & Astrophysics*, 17:213–240, 1979. doi: 10.1146/annurev.aa.17.090179.001241.

C. F. McKee and J. P. Ostriker. A theory of the interstellar medium - Three components regulated by supernova explosions in an inhomogeneous substrate. *The Astrophysical Journal*, 218:148–169, November 1977. doi: 10.1086/155667.

J. Meaburn. The giant and supergiant shells of the Magellanic Clouds. *Monthly Notices of the Royal Astronomical Society*, 192:365–375, August 1980.

B. Y. Mills, A. J. Turtle, A. G. Little, and J. M. Durdin. A new look at radio supernova remnants. *Australian Journal of Physics*, 37:321–357, 1984.

M. S. Oey and G. García-Segura. Ambient Interstellar Pressure and Superbubble Evolution. *The Astrophysical Journal*, 613:302–311, September 2004. doi: 10.1086/421483.

L. M. Oskinova. Evolution of X-ray emission from young massive star clusters. *Monthly Notices of the Royal Astronomical Society*, 361:679–694, August 2005. doi: 10.1111/j.1365-2966.2005.09229.x.

E. Pfeffermann. *The Universe in X-rays*, pages 5–14. 2008. doi: 10.1007/978-3-540-34412-4.

G. Pietrzyński, W. Gieren, D. Graczyk, I. Thompson, B. Pilecki, N. Nardetto, R.-P. Kudritzki, F. Bresolin, G. Bono, P. P. Moroni, P. Konorski, M. Gorski, J. Storm, R. Smolec, and P. Karczmarek. A precise and accurate distance to the Large Magellanic Cloud from late-type eclipsing-binary systems. In R. de Grijs, editor, *IAU Symposium*, volume 289 of *IAU Symposium*, pages 169–172, February 2013. doi: 10.1017/S174392131202131X.

S. D. Points, Y. H. Chu, S. Kim, R. C. Smith, S. L. Snowden, W. Brandner, and R. A. Gruendl. The Supergiant Shell LMC 2. I. The Kinematics and Physical Structure. *The Astrophysical Journal*, 518:298–323, June 1999. doi: 10.1086/307249.

S. D. Points, Y.-H. Chu, S. L. Snowden, and L. Staveley-Smith. The Supergiant Shell LMC 2. II. Physical Properties of the 10^6 K Gas. *The Astrophysical Journal*, 545:827–841, December 2000. doi: 10.1086/317865.

P. Predehl, G. Hasinger, H. Böhringer, U. Briel, H. Brunner, E. Churazov, M. Freyberg, P. Friedrich, E. Kendziorra, D. Lutz, N. Meidinger, M. Pavlinsky, E. Pfeffermann, A. Santangelo, J. Schmitt, P. Schuecker, A. Schwope, M. Steinmetz, L. Strüder, R. Sunyaev, and J. Wilms. eROSITA. In *Society of Photo-Optical Instrumentation Engineers (SPIE) Conference Series*, volume 6266 of *Society of Photo-Optical Instrumentation Engineers (SPIE) Conference Series*, July 2006. doi: 10.1117/12.670249.

T. Preibisch and E. D. Feigelson. The Evolution of X-Ray Emission in Young Stars. *The Astrophysical Journal Supplement Series*, 160:390–400, October 2005. doi: 10.1086/432094.

W.J.M. Rankine. On the thermodynamic theory of waves of finite longitudinal disturbances. *Philosophical Transactions of the Royal Society of London*, 160: 277–288, 1870. doi: 10.1098/rstl.1870.0015.

C. Reppin, W. Pietsch, J. Trümper, E. Kendziorra, and R. Staubert. *High Energy X-ray Experiment for the Saljut-Mission (HEXE)*, page 279. 1985.

W.C. Röntgen. Über eine neue Art von Strahlen (vorläufige Mitteilung). *Sonderabbdruck aus den Sitzungsberichten der Würzburger Physik.-medic. Gesellschaft 1895*, 1896.

S. C. Russell and M. A. Dopita. Abundances of the heavy elements in the Magellanic Clouds. III - Interpretation of results. *The Astrophysical Journal*, 384: 508–522, January 1992. doi: 10.1086/170893.

E. Rutherford and H. Geiger. An Electrical Method of Counting the Number of Alpha Particles from Radioactive Substances. *Proc. Roy. Soc. London*, A81: 141–161, 1908.

E. E. Salpeter. The Luminosity Function and Stellar Evolution. *The Astrophysical Journal*, 121:161, January 1955. doi: 10.1086/145971.

H. Sana, G. Rauw, Y. Nazé, E. Gosset, and J.-M. Vreux. An XMM-Newton view of the young open cluster NGC 6231 - II. The OB star population. *Monthly Notices of the Royal Astronomical Society*, 372:661–678, October 2006. doi: 10.1111/j.1365-2966.2006.10847.x.

A. Santangelo and R. Madonia. Fifty years of X-ray astronomy: A look back and into the (near) future. *Astroparticle Physics*, 53:130–151, January 2014. doi: 10.1016/j.astropartphys.2013.11.005.

M. Sasaki, F. Haberl, and W. Pietsch. ROSAT HRI catalogue of X-ray sources in the LMC region. *Astronomy & Astrophysics Supplement*, 143:391–403, May 2000. doi: 10.1051/aas:2000185.

M. Sasaki, P. P. Plucinsky, T. J. Gaetz, R. K. Smith, R. J. Edgar, and P. O. Slane. XMM-Newton Observations of the Galactic Supernova Remnant CTB 109 (G109.1-1.0). *The Astrophysical Journal*, 617:322–338, December 2004. doi: 10.1086/425353.

M. Sasaki, D. Breitschwerdt, V. Baumgartner, and F. Haberl. XMM-Newton observations of the superbubble in N 158 in the LMC. *Astronomy & Astrophysics*, 528:A136, April 2011. doi: 10.1051/0004-6361/201015866.

N. Schartel. XMM-Newton highlights . *Mem. Societa Astronomica Italiana*, 83: 97, 2012.

L. I. Sedov. *Similarity and Dimensional Methods in Mechanics*. 1959.

F. D. Seward and P. A. Charles. *Exploring the X-ray Universe*. August 2010.

I. S. Shklovskij. *Supernovae*. 1969.

S. A. Silich, J. Franco, J. Palous, and G. Tenorio-Tagle. Three-dimensional Calculations of the Evolution of Superbubbles in a Cloudy Medium. *The Astrophysical Journal*, 468:722, September 1996. doi: 10.1086/177728.

J. D. Slavin and D. P. Cox. Completing the evolution of supernova remnants and their bubbles. *The Astrophysical Journal*, 392:131–144, June 1992. doi: 10.1086/171412.

C. Smith, R. Leiton, and S. Pizarro. The UM/CTIO Magellanic Cloud Emission Line Survey (MCELS). In D. Alloin, K. Olsen, and G. Galaz, editors, *Stars, Gas and Dust in Galaxies: Exploring the Links*, volume 221 of *Astronomical Society of the Pacific Conference Series*, page 83, 2000.

R. K. Smith and J. P. Hughes. Ionization Equilibrium Timescales in Collisional Plasmas. *The Astrophysical Journal*, 718:583–585, July 2010. doi: 10.1088/0004-637X/718/1/583.

R. K. Smith, N. S. Brickhouse, D. A. Liedahl, and J. C. Raymond. Collisional Plasma Models with APEC/APED: Emission-Line Diagnostics of Hydrogen-like and Helium-like Ions. *The Astrophysical Journal Letters*, 556:L91–L95, August 2001. doi: 10.1086/322992.

S. L. Snowden and K. D. Kuntz. Analysis of XMM-Newton Data from Extended Sources and the Diffuse X-ray Background. In *American Astronomical Society Meeting Abstracts #217*, volume 43 of *Bulletin of the American Astronomical Society*, page #344.17, January 2011a.

S. L. Snowden and K. D. Kuntz. *Cookbook for Analysis Procedures for XMM-Newton EPIC MOS Observations of Extended Objects and the Diffuse Background*. 2011b.

S. L. Snowden, R. Egger, D. P. Finkbeiner, M. J. Freyberg, and P. P. Plucinsky. Progress on Establishing the Spatial Distribution of Material Responsible for the 1 4 keV Soft X-Ray Diffuse Background Local and Halo Components. *The Astrophysical Journal*, 493:715, January 1998. doi: 10.1086/305135.

S. L. Snowden, R. F. Mushotzky, K. D. Kuntz, and D. S. Davis. A catalog of galaxy clusters observed by XMM-Newton. *Astronomy & Astrophysics*, 478:615–658, February 2008. doi: 10.1051/0004-6361:20077930.

R. Staubert. *The Universe in X-rays*, pages 29–39. 2008. doi: 10.1007/978-3-540-34412-4.

L. Staveley-Smith, W. E. Wilson, T. S. Bird, M. J. Disney, R. D. Ekers, K. C. Freeman, R. F. Haynes, M. W. Sinclair, R. A. Vaile, R. L. Webster, and A. E. Wright. The Parkes 21 CM multibeam receiver. *Publications of the Astron. Soc. of Australia*, 13:243–248, November 1996.

L. Strüder and N. Meidinger. *The Universe in X-rays*, pages 51–71. 2008. doi: 10.1007/978-3-540-34412-4.

L. Strüder, U. Briel, K. Dennerl, R. Hartmann, E. Kendziorra, N. Meidinger, E. Pfeffermann, C. Reppin, B. Aschenbach, W. Bornemann, H. Bräuninger, W. Burkert, M. Elender, M. Freyberg, F. Haberl, G. Hartner, F. Heuschmann, H. Hippmann, E. Kastelic, S. Kemmer, G. Kettenring, W. Kink, N. Krause, S. Müller, A. Oppitz, W. Pietsch, M. Popp, P. Predehl, A. Read, K. H. Stephan, D. Stötter, J. Trümper, P. Holl, J. Kemmer, H. Soltau, R. Stötter, U. Weber, U. Weichert, C. von Zanthier, D. Carathanassis, G. Lutz, R. H. Richter, P. Solc, H. Böttcher, M. Kuster, R. Staubert, A. Abbey, A. Holland, M. Turner, M. Balasini, G. F. Bignami, N. La Palombara, G. Villa, W. Buttler, F. Gianini, R. Lainé, D. Lumb, and P. Dhez. The European Photon Imaging Camera on XMM-Newton: The pn-CCD camera. *Astronomy & Astrophysics*, 365:L18–L26, January 2001. doi: 10.1051/0004-6361:20000066.

G. Taylor. The Formation of a Blast Wave by a Very Intense Explosion. I. Theoretical Discussion. *Royal Society of London Proceedings Series A*, 201:159–174, March 1950. doi: 10.1098/rspa.1950.0049.

G. Tenorio-Tagle and P. Bodenheimer. Large-scale expanding superstructures in galaxies. *Annual Review of Astronomy & Astrophysics*, 26:145–197, 1988. doi: 10.1146/annurev.aa.26.090188.001045.

J. Treis, R. Andritschke, R. Hartmann, S. Herrmann, P. Holl, T. Lauf, P. Lechner, G. Lutz, N. Meidinger, M. Porro, R. H. Richter, F. Schopper, H. Soltau, and L. Strüder. Pixel detectors for x-ray imaging spectroscopy in space. *Journal of Instrumentation*, 4:3012, March 2009. doi: 10.1088/1748-0221/4/03/P03012.

J. Trümper. The ROSAT mission. *Advances in Space Research*, 2:241–249, 1982. doi: 10.1016/0273-1177(82)90070-9.

M. J. L. Turner, A. Abbey, M. Arnaud, M. Balasini, M. Barbera, E. Belsole, P. J. Bennie, J. P. Bernard, G. F. Bignami, M. Boer, U. Briel, I. Butler, C. Cara, C. Chabaud, R. Cole, A. Collura, M. Conte, A. Cros, M. Denby, P. Dhez, G. Di Coco, J. Dowson, P. Ferrando, S. Ghizzardi, F. Gianotti, C. V. Goodall, L. Gretton, R. G. Griffiths, O. Hainaut, J. F. Hochedez, A. D. Holland, E. Jourdain, E. Kendziorra, A. Lagostina, R. Laine, N. La Palombara, M. Lortholary, D. Lumb, P. Marty, S. Molendi, C. Pigot, E. Poindron, K. A. Pounds, J. N. Reeves, C. Reppin, R. Rothenflug, P. Salvetat, J. L. Sauvageot, D. Schmitt,

S. Sembay, A. D. T. Short, J. Spragg, J. Stephen, L. Strüder, A. Tiengo, M. Trifoglio, J. Trümper, S. Vercellone, L. Vigroux, G. Villa, M. J. Ward, S. Whitehead, and E. Zonca. The European Photon Imaging Camera on XMM-Newton: The MOS cameras : The MOS cameras. *Astronomy & Astrophysics*, 365:L27–L35, January 2001. doi: 10.1051/0004-6361:20000087.

A. Unsöld and B. Baschek. *Der neue Kosmos*. 1999.

G. A. Vázquez and C. Leitherer. Optimization of Starburst99 for Intermediate-Age and Old Stellar Populations. *The Astrophysical Journal*, 621:695–717, March 2005. doi: 10.1086/427866.

J. Vink. Supernova remnants: the X-ray perspective. *The Astronomy & Astrophysics Review*, 20:49, December 2012. doi: 10.1007/s00159-011-0049-1.

J. von Neumann. *Los Alamos Sci. Lab. Tech. Series*, 7, 1947.

Q. Wang and D. J. Helfand. LMC-2 as the blowout of a hot superbubble. *The Astrophysical Journal*, 379:327–337, September 1991. doi: 10.1086/170507.

Q. Wang, T. Hamilton, D. J. Helfand, and X. Wu. The detection of X-rays from the hot interstellar medium of the Large Magellanic Cloud. *The Astrophysical Journal*, 374:475–495, June 1991. doi: 10.1086/170137.

G. Warth, M. Sasaki, P. J. Kavanagh, M. D. Filipović, S. D. Points, and L. M. Bozzetto. Multi-frequency study of DEM L299 in the Large Magellanic Cloud. *Astronomy & Astrophysics*, 567:A136, July 2014. doi: 10.1051/0004-6361/201423575.

M. G. Watson, J.-L. Auguères, J. Ballet, X. Barcons, D. Barret, M. Boer, T. Boller, G. E. Bromage, H. Brunner, F. J. Carrera, M. S. Cropper, M. Denby, M. Ehle, M. Elvis, A. C. Fabian, M. J. Freyberg, P. Guillout, J.-M. Hameury, G. Hasinger, D. A. Hinshaw, T. Maccacaro, K. O. Mason, R. G. McMahon, L. Michel, L. Mirioni, J. P. Mittaz, C. Motch, J.-F. Olive, J. P. Osborne, C. G. Page, M. Pakull, B. H. Perry, M. Pierre, W. Pietsch, J. P. Pye, A. M. Read, T. P. Roberts, S. R. Rosen, J.-L. Sauvageot, A. D. Schwope, K. Sekiguchi, G. C. Stewart, I. Stewart, I. Valtchanov, M. J. Ward, R. S. Warwick, R. G. West, N. E. White, and D. M. Worrall. The XMM-Newton Serendipitous Survey. I. The role of XMM-Newton Survey Science Centre. *Astronomy & Astrophysics*, 365:L51–L59, January 2001. doi: 10.1051/0004-6361:20000067.

R. Weaver, R. McCray, J. Castor, P. Shapiro, and R. Moore. Interstellar bubbles. II - Structure and evolution. *The Astrophysical Journal*, 218:377–395, December 1977. doi: 10.1086/155692.

A. Weigert, H. J. Wendker, and L. Wisotzki. *Astronomie und Astrophysik - ein Grundkurs*. 2009.

M. C. Weisskopf, B. Brinkman, C. Canizares, G. Garmire, S. Murray, and L. P. Van Speybroeck. An Overview of the Performance and Scientific Results from the Chandra X-Ray Observatory. *Publications of the Astronomical Society of the Pacific*, 114:1–24, January 2002. doi: 10.1086/338108.

R. M. Williams and Y.-H. Chu. Supernova Remnants in the Magellanic Clouds. VI. The DEM L316 Supernova Remnants. *The Astrophysical Journal*, 635: 1077–1086, December 2005. doi: 10.1086/497681.

H. Wolter. Spiegelsysteme streifenden Einfalls als abbildende Optiken für Röntgenstrahlen. *Annalen der Physik*, 445:94–114, 1952. doi: 10.1002/andp.19524450108.

ESA: XMM-Newton SOC. XMM-Newton Users Handbook. *XMM-Newton Users Handbook*. 2013.

D. Zaritsky, J. Harris, and I. Thompson. A digital photometric survey of the magellanic clouds: First results from one million stars. *The Astronomical Journal*, 114:1002–1013, September 1997. doi: 10.1086/118531.

D. Zaritsky, J. Harris, I. B. Thompson, and E. K. Grebel. The Magellanic Clouds Photometric Survey: The Large Magellanic Cloud Stellar Catalog and Extinction Map. *The Astronomical Journal*, 128:1606–1614, October 2004. doi: 10.1086/423910.

List of Figures

List of Tables

Acronyms

AGNs	active galactic nuclei
ARF	ancillary response file
ATCA	Australia Telescope Compact Array
ATNF	Australia Telescope National Facility
CCD	charge-coupled device
CCF	current calibration file
CIE	collisional ionization equilibrium
CTIO	Cerro Tololo Inter-American Observatory
CXB	cosmic X-ray background
EPIC	European Photon Imaging Camera
ESA	European Space Agency
ESO	European Southern Observatory
FOV	field of view
FWC	filter wheel closed
FWHM	full width at half maximum
HEW	half energy width
IDL	Interactive Data Language
IMF	initial mass function
IR	infrared
ISM	interstellar medium
LMC	Large Magellanic Cloud
MCELS	Magellanic Cloud Emission Line Survey
MCS	Magellanic Cloud Survey
MOST	Molonglo Synthesis Telescope
NEI	collisional non-equilibrium ionization
ONC	Orion Nebula Cluster
P.I.	principal investigator
PSF	point spread function
QPB	quiescent particle background
RGS	Reflection Grating Spectrometer
RMF	redistribution matrix file
SAS	Scientific Analysis System
SEP	South Ecliptic Pole
SGS	supergiant shell

SN	supernova
SNe	supernovae
SNR	supernova remnant
SWCX	solar wind charge exchange
UM	University of Michigan
UV	ultraviolet
XMM-OM	Optical/UV Monitor Telescope
YSO	young stellar object

Acknowledgment

Ich möchte mich bei allen ganz herzlich bedanken, die mich während der vergangenen Jahre begleitet und unterstützt haben. Insbesondere bei:

Dr. Manami Sasaki, die mir diese vergangenen vier Jahre möglich gemacht hat, welche entscheidenden Einfluss auf mein Leben hatten und in denen ich sehr viel gelernt habe. Vielen Dank für die lückenlose Betreuung und die schöne Zeit!

Prof. Andrea Santangelo, für das Vertrauen, dass er mir zu jeder Zeit entgegen gebracht hat, was ich immer als äußerst aufbauend und motivierend empfunden habe

Dr. Patrick Kavanagh, for many helpful suggestions and his advise and help during data analysis

Dr. Chris Tenzer, für sein fortwährendes Interesse und seine Hilfe in allen Belangen, und für das „Skipper-sein“

Meinen insgesamt sieben Bürokollegen, insbesondere Beppe Distratis, für die gemeinsam verbrachten Tage

Sara Saeedi, who became much more than an office mate, for her kindness and our nice talks

Dr. Davide Vasco, for our nice cooking sessions and for his support during difficult times

our Mensa group – in particular Alejandro G., Thomas, Elias, Kendji, Sara, Alejandro M., and Francesco –, for nice and funny lunches, which always cheered up my mood, and of course for our Expedition Clubs

der nicht vergessenen Espresso-Runde, v.a. Thorsten, Stephan, Jens, Michi, Basti und Benni, für schöne Pausen und interessante Diskussionen

der Crew unseres jährlichen Instituts-Segeltörns, der zum festen Bestandteil des Sommerurlaubs geworden ist

Dr. Hanna Sickinger, mit der ich zusammen ab dem ersten Tag das Physikstudium verbracht habe und die zu jeder Zeit und in in allen Belangen immer für mich da war und ist

Michael Bölling und Viola Kohler, die immer für mich da waren, für ihre Unterstützung und Beratung in allen Belangen und für unsere schönen Ausflüge

Ruth Kowalski, Daniel Gottschall und Marc Pfeifer, die mir zugleich Freunde, Mitbewohner und Kollegen sind und waren

Saskia Kühnhold, Dr. Christian Stehle, Florian Karlewski, Henning Wende und Dr. Kai Freund, die mich durch das Physikstudium und darüber hinaus begleitet haben

Martha Swider, für unsere gemeinsamen Trainingsstunden, die gemeinsam verbrachten Tage und die schönen Café-Besuche

Steffi Heinzelmann und Silke Molitor, meine ständigen und nicht wegzudenkenden Wegbegleiter

den Familien Bayer und Zühlke, die mich so freundlich aufgenommen und empfangen haben

meinen Geschwistern Olga, Lydia, Dora und meinen Schwägern, für ihre ständige Unterstützung und für unser schönes Familienleben

meinen Nichten und Neffen, dafür, dass es sie gibt und dass sie so viel Freude in unser Leben bringen

meinen Eltern, für ihre ständige Unterstützung und Ermutigungen, und die zu Hause ein kleines Paradies für uns geschaffen haben, in das wir immer wieder zurückkehren dürfen

Jörg Bayer, der die Tage farbiger, den Regen wärmer und die Sonne strahlender macht, für die Zeit, die er mir schenkt, und für das Gefühl, heimgekommen zu sein.

I would like to thank the co-authors of the paper which resulted from this work: Manami Sasaki, Patrick Kavanagh, Miroslav Filipović, Sean Points, and Luke Bozzetto. I would also like to thank all the people helped to improve this thesis, in particular Manami Sasaki, Andrea Santangelo, Chris Tenzer, Jörg Bayer, my father, and Martha Swider.
This research has been funded by the Deutsche Forschungsgemeinschaft through the Emmy Noether Research Grant SA 2131/1-1. This work is based on observations obtained with XMM-Newton, an ESA science mission with instruments and contributions directly funded by ESA Member States and NASA. The MCELS project has been supported in part by NSF grants AST-9540747 and AST-0307613, and through the generous support of the Dean B. McLaughlin Fund at the University of Michigan, a bequest from the family of Dr. Dean B. McLaughlin in memory of his lasting impact on Astronomy. The National Optical Astronomy Observatory is operated by the Association of Universities for Research in Astronomy Inc. (AURA), under a cooperative agreement with the National Science Foundation. This research has made use of the SIMBAD database, operated at CDS, Strasbourg, France.

List of Publications

G. Warth, M. Sasaki, P. J. Kavanagh, M. D. Filipović, S. D. Points, and L. M. Bozzetto
Multi-frequency study of DEM L299 in the Large Magellanic Cloud
2014, Astronomy & Astrophysics, 567:A136 – 151

M. Sasaki, C. Heinitz, G. Warth, and G. Pühlhofer
XMM-Newton observation of the Galactic supernova remnant W51C (G49.1-0.1)
2014, Astronomy & Astrophysics, 563:A9 – 14

D. Maier, J. Dick, G. Distratis, E. Kendziorra, A. Santangelo, T. Schanz, C. Tenzer, and G. Warth
Development of fast data processing electronics for a stacked x-ray detector system with application as a polarimeter
2012, SPIE proceedings, Vol. 8443, pp. 10

C. Tenzer, G. Warth, E. Kendziorra, and A. Santangelo
Geant4 simulation studies of the eROSITA detector background
2010, SPIE proceedings, Vol. 7742